UNIVERSITY OF SOUTHAMPTON

FACULTY OF ENGINEERING, SCIENCE AND MATHEMATICS

School of Chemistry

Synthesis and Characterization of Molybdenum and Vanadium Framework Materials

by

Eleni Kotsapa

Thesis for the degree of Doctor of Philosophy

September 2010

UNIVERSITY OF SOUTHAMPTON

ABSTRACT

FACULTY OF ENGINEERING, SCIENCE AND MATHEMATICS

SCHOOL OF CHEMISTRY

Doctor of Philosophy

Synthesis and Characterization of Molybdenum and Vanadium Inorganic Framework Materials

Molybdenum and vanadium inorganic framework materials, with structures based on phosphate and arsenate tetrahedra have been synthesised by hydrothermal techniques and characterised by single crystal X-ray diffraction; additional techniques including thermogravimetric analysis, electron dispersive spectroscopy and infrared spectroscopy were carried out to fully characterise these materials. Of the molybdenum phosphates that have been synthesised, a new layer structure type has been identified. This exhibits perpendicular channels through the molybdenophosphate sheets wherein multiple guest ions, ammonium cations and free orthophosphate $(PO_4)^{3-}$ or halide (Cl^-, Br^-), are hosted. Anion exchange investigations were performed, showing the affinity of the Br^- analogue to be completely exchange with Cl^- anions. Hydrothermal syntheses with a variety of organic amines resulted in the formation of four compounds. These include three distinct cluster polyanions in addition to a ribbon structure type. The effect of fluoride ions into the synthesis of molybdenum phosphates has been investigated; this approach has led to the discovery of a new oxyfluorinated molybdenum phosphate compound templated by piperazine. Further studies were concentrated on the preparation of molybdenum phosphonate compounds. An amine templated molybdenophosphite polyanion has been obtained from reactions that involved 4,4’-bipyridine.

During investigations of the role of fluoride ions in the formation of vanadium phosphate and arsenate frameworks, four amine templated compounds have been synthesised and fully characterised. Three of these materials presented, exhibit similar but rather distinct framework topologies including two new layered structure types, which comprise flat or super-corrugated vanadoarsenate layers, and one-dimensional tubular structure. Reactions were also performed using inorganic templates, and a number of new structure types were produced with ammonium, rubidium, barium and caesium. The series of materials includes two-dimensional layer structures, and two main structural topologies have been generally observed.

During investigations into vanadium borate and phosphate compounds, a three-dimensional vanadium phosphate was discovered. Further studies on previously reported vanadium polyborate compounds have led to the isolation of the series of the analogous alkali metal templated structures.

TABLE OF CONTENTS

Chapter One: Introduction

Chapter Two: Experimental Techniques

Chapter Three: Molybdenum Phosphates

Chapter Four: Amine Templated Fluorinated Vanadium Arsenates

Chapter Five: Oxyfluorinated Vanadium Phosphates and Arsenates

Chapter Six: Vanadium Phosphate and Borate Structures

Chapter Seven: Molybdenum Phosphonates

LIST OF TABLES AND FIGURES

Chapter 1: Introduction

Chapter 2: Experimental Techniques

Chapter 3: Molybdenum Phosphates

Chapter 4: Amine Templated Oxyfluorinated Vanadium Arsenates

Chapter 5: Oxyfluorinated Vanadium Phosphates and Arsenates

Chapter 6: Vanadium Phosphate and Borate Structures

Chapter 7: Molybdenum Phosphonates

ABBREVIATIONS

Dabco	1,4-diazabicyclo[2.2.2]octane
Pip	Piperazine
En	Ethylenediamine
TMAOH	Tetramethylammonium hydroxide
TMAC	Tetramethylammonium chloride
4,4’-bipy	4,4’-bipyridine
PXD	Powder X-ray diffraction
SXD	Single crystal X-ray diffraction
TGA	Thermogravimetric analysis
DTA	Differential thermal analysis
IR	Infra-red
EDX	Energy dispersive X-ray spectroscopy
SEM	Scanning electron microscopy
BV	Bond valence
AlPO	Aluminium Phosphate
GaPO	Gallium phosphate
MoPO	Molybdenum phosphate

DECLARATION OF AUTHORSHIP

I, Eleni Kotsapa, declare that the thesis entitled

Synthesis and Characterization of Molybdenum and Vanadium Framework Materials

and the work presented in the thesis are both my own, and have been generated by me as the result of my own original research. I confirm that:

- this work was done wholly or mainly while in candidature for a research degree at this University;
- where any part of this thesis has previously been submitted for a degree or any other qualification at this University or any other institution, this has been clearly stated;
- where I have consulted the published work of others, this is always clearly attributed;
- where I have quoted from the work of others, the source is always given. With the exception of such quotations, this thesis is entirely my own work;
- I have acknowledged all main sources of help;
- where the thesis is based on work done by myself jointly with others, I have made clear exactly what was done by others and what I have contributed myself;
- parts of this work have been published as:

Kotsapa, E. and Weller, M.
$[NH_4]_{12}[(MoO_2)_2O(HPO_4)_2]_4[PO_4]X$, X = Cl, Br- new porous layer molybdenophosphates with embedded multiple anionic and cationic guests.
Dalton Transactions, 418-420, 2009

Rouse, J. Redrup, K. Kotsapa, E and Weller, M.
Controlling Dimensionality in Templated Layer, Chain and Framework Structures by Combining Metal Fluorides with oxotetrahedra.
Chemical Communications, 7209-7211, 2009

Signed:

Date:

The work was performed exclusively by the author, with the following exceptions. Neutron diffraction data for compound (1) (which is presented in Chapter 3) were collected by Professor Mark T. Weller at the D20 diffractometer situated at the Institut Laue-Langevin Neutron Source in Grenoble, and further analysed by him for carrying out the joint refinement of X-ray and neutron diffraction data. Data collection and structure refinement of compound (4) (which is presented in Chapter 4) were carried out by Dr Mark E. Light. BET measurement of the same material was performed by James Paterson from Dr. Robert Raja's research group.

ACKNOWLEDGEMENTS

I am indebted to a number of people who have helped me during the course of this research project, and it is probably impossible for me to thank every one of them individually.

Firstly, many thanks are due to my supervisor Professor Mark T. Weller for his guidance and support over the past three years.

I am extremely grateful to Mark Light for his help and crystallography advice, especially on solving a certain particularly awkward crystal structure.

Many thanks should be given to the Weller group past and present, especially to Jenny, who was an excellent proof-reader, Alexandra who provided research advice and assistance, and Rosa, Valeska, Jess, Kate, Charlie and Ben which made the last three years thoroughly enjoyable. Special mention is due for Rosa Galati and the Pilelo's family who made my life at Southampton truly memorable. Their friendship and support have been invaluable to me.

I owe many thanks to my flatmate Derya who has helped me through this journey, encouraging me and supporting me to carry on strong through hard times. Your friendship meant a lot to me Loulou mou. Also, thanks are due to Christos for his love and support.

Finally, I am most grateful to my family, my father, brothers George and Christopher and especially to my mother, for their love and support without which this would not have been possible.

Chapter One

Introduction

1.0 Introduction

The chemistry of inorganic materials is a vigorous area of research and there has been intense interest in the synthesis of new functional inorganic solids. These can be categorized into various classes of compounds, with sections on layer intercalates, complex oxide materials such as high-temperature superconductors, inorganic framework structures such as zeolites, and molecular materials. The structure of such materials, the majority of which are crystalline, has been a critical aspect in the physical and chemical properties that they show. Research into the synthesis of new materials constitutes a vital step in gaining a fundamental understanding of the formation process of these complex structures, and helps in developing new synthetic approaches that can be used to prepare crystalline structures with special characteristics and useful properties.

The framework structure of several inorganic materials can be described in terms of linked polyhedra units. These comprise a wide range of structural types varying from naturally occurring zeolite framework types, which are constructed of alternating aluminate and silicate tetrahedra, to layered oxide materials such as Ruddlesden-Popper phases which derive from layers build up from corner-sharing transition metal octahedra.

The research presented within this thesis is mainly focused on framework structures that attempt to bring together properties from these various classes of inorganic materials. Framework structures discussed in this thesis show a diverse range of structural types and bonding motifs. These are based on molybdenum or vanadium octahedra species that are linked together with TO_4^{3-} tetrahedra units, where T = As or P; fluoride can also be incorporated into the structure that offers the potential of different framework topologies.

1.1 Framework materials

In the field of functional nanoporous materials, aluminosilicate zeolites were the first inorganic crystalline materials to be recognized. They occur naturally in the earth's crust formed under hydrothermal conditions; nearly fifty various minerals have been identified in so far, whilst synthetic zeolites contribute over 150 diverse framework types according to the International Zeolite Association.[1]

Aluminosilicates can be thought of as being constructed of corner sharing silicate and aluminate tetrahedra linked together into three dimensional frameworks containing nanometer-sized pores. Whereas pure silicate minerals exhibit neutral frameworks, the introduction of the trivalent aluminium renders the framework negatively charged and thus charge balancing cations are involved. The general formula of an aluminosilicate zeolite is given as follows, $\{[M^{n+}]_{x/n}.[mH_2O\{[AlO_2]_x[SiO_2]_{1-x}\}$ where M represents the charge-compensating cation (that typically is an alkali metal or alkaline earth cation) and the other components relate to the aluminosilicate framework and the adsorbed water molecules hosted in the pores.

Varying the ratio of aluminium to silicon, with the maximum limit of 1:1 due to the Loewenstein's principle of Al-O-Al avoidance,[2] it becomes possible to control the desired properties of these materials. Thus a high degree of aluminium in the material results in a more hydrophilic character owing to the increasing negative framework charge. On the other hand this may give the material a poor acid stability, as one might expect the affinity of hydrogen protons for the highly electronegative aluminates leading to the framework collapse.

Taking into account the complex framework structures that aluminosilicates generally exhibit, the concept of describing such frameworks in terms of simple building units (denoted as SBUs) was initiated by Meier and Smith.[3] Figure 1.1 illustrates the twenty three types of SBUs that have been observed in frameworks consisted of tetrahedral units only. As can be depicted, the maximum level of tetrahedrally coordinated atoms within these SBUs reaches the sixteen atoms when taking into account that the entire framework is derived from only one type. However, it appears that many zeolites often comprise a combination of SBUs; for instance zeolite A can be thought of as being derived from the combination of 4- and 6- ring SBUs.

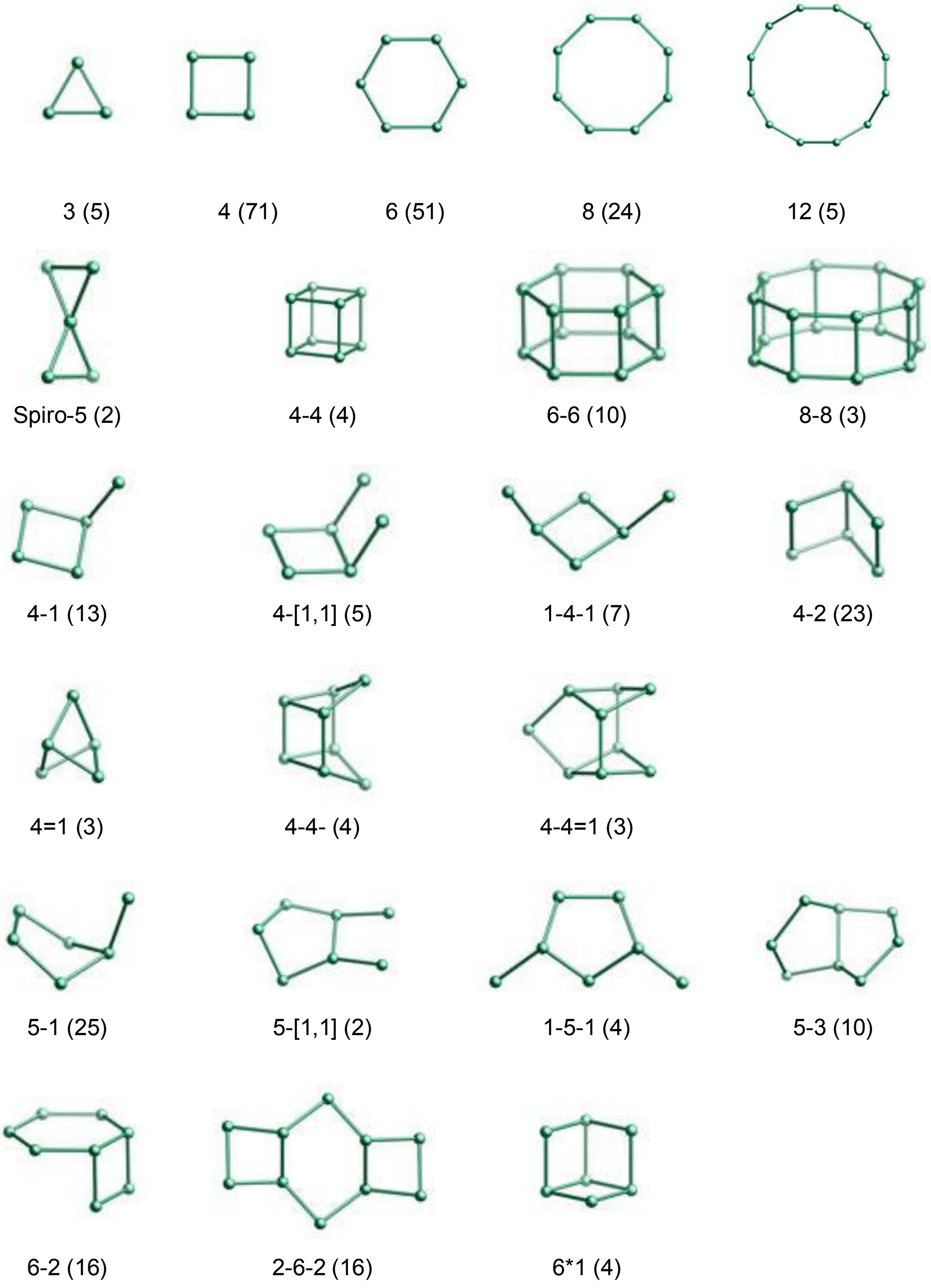

Figure 1.1: Secondary Building Units (SBUs). Each sphere represents the centre of a TO_4 tetrahedron. The number inside the brackets shows the frequency of occurrence.[4]

Unique features of these materials derive from their relatively open frameworks that are penetrated by channels and cavities. The pore openings of these frameworks can be described in terms of their characteristic cage-building units forming *n*-rings, where *n* represents the number of the TO_4 units within the ring type. Aluminosilicate zeolites can be categorized into groups based upon their common structural features including the cage type (shown in Figure 1.2), the channel system as well as the bonding motif of the fundamental building units. For example sodalite, zeolite A and faujasite are considered as being derived from the same SBU type, the truncated octahedron which has the [$4^6 6^8$] cage type constructed by six 4-rings and eight 6-rings.

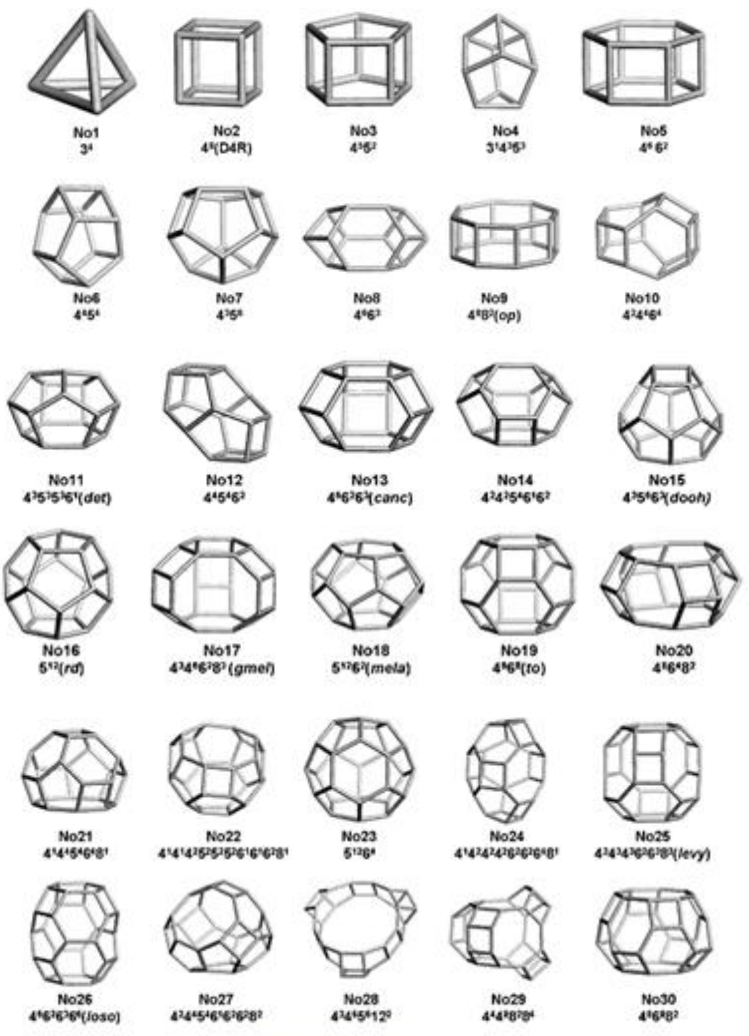

Figure 1.2: Some of the characteristic cage-building units that have been found to occur in known zeolites.[5]

Industrial interest in aluminosilicates has been arisen from their applications as ion exchangers, as well as for their use in many adsorption and catalytic processes. The charge-balancing cations, located in cavities or channels of the zeolite, interact very weakly with the framework and therefore can be readily exchanged with other metal cations. This is seen in the case of low-silica zeolites which possess high cation exchange capacity and thus they are regarded as suitable materials for use in detergents and water softeners as well as for waste remediation. Examples include sodium-zeolite A and zeolite MAP for their use in removing the hard Ca^{2+} and Mg^{2+} cations from raw water, in addition to the clinoptilolite and chabazite which are widely used in the treatment of radioactive wastes to remove the ^{90}Sr and ^{137}Cs isotopes.

Zeolites in their dehydrate form can allow small molecules to get entrapped within their porous frameworks. Owing to their high affinity for water, zeolites can be excellent drying agents such as for gases and solvents. Furthermore, the electrostatic interactions between the charge balancing cations and the sorbate molecules have been the key factor for many gas-separation applications. In fact, the variety in size and shape of the pore systems in addition to the different ways of atoms distribution in the framework has induced a broad range of molecular adsorption and separation applications.

High-silica zeolites represent an important class of powerful catalyst materials with many industrial applications including catalytic cracking, isomerization processes and hydrocarbon synthesis. There has been much research effort placed into generating stable acidic-zeolite materials, such as reactions that entail a combination of acid or ammonium exchange followed by steaming or calcination processes in order to obtain the H-zeolite form. However, research focused on the optimization of the catalytic activity of these materials does not only deal with the conversion to the acidic form but also takes into account the unique characteristics of the framework such as the size and the shape of the cavities.[6] This is the case of the shape-selective catalysis where it becomes possible to control the reagents entering the pores and thereby to direct the formation of particular products.

1.2 Phosphate frameworks

The existing applications of aluminosilicates in porous and catalysis chemistry have raised the challenge for the discovery of new inorganic framework materials that will promise new industrial applications based upon the fundamental zeolite chemistry. Based on crystal chemistry principles, research has gradually extended to metal phosphate frameworks. A large number of phosphate-based frameworks consisting of numerous main block elements and transition metal species have now been produced; most of these compounds exhibit similar framework topologies to many zeolite-type frameworks, whilst a wide range of novel structure types has been identified.

1.2.1 Aluminium phosphates

Aluminophosphate framework materials were the first area of research to be explored with the aim of producing systems related to zeolites.[7] This class of inorganic materials possess electroneutral frameworks with relatively large pore openings that follow strictly the sequence of alternating aluminate and phosphate tetrahedra. The general formula of an aluminophosphate can be described as $[(AlO_2)_x(PO_2)_x].yH_2O$, showing the strict ordering of the $AlPO_4$ frameworks with the ratio of aluminium to phosphorous always unity. Although the invariant Al/P ratio, aluminophosphates show great structural diversity. They encompass a vast number of framework architectures related to many known zeolites (such as sodalite, chabazite, zeolite A and Y) in addition to numerous new topologies that have not yet been observed in the existing zeolite chemistry.

In contrast to aluminosilicates, AlPOs must be made up of frameworks consisting of even-membered rings; in fact the majority of them embrace (4,2)-connected frameworks. The lack of negative charge within their framework structures implies the no need for counterbalanced cations and therefore does not allow ion exchange reactions. On the other hand, the wide range of pore openings that those materials exhibit makes them suitable candidates for many adsorption applications, giving rise to a new class of molecular sieves. Among this enhanced family of compounds, the most striking example was the discovery of VPI-5 (VFI) aluminophosphate.[8] Its framework structure can be best considered as derived from one dimensional extraopened channels (having an approximately diameter of 12 Å) built up from 18 tetrahedral units.

Despite their excellent adsorption properties, pure aluminophosphates exhibit relatively poor catalytic activity. In attempts to tailor the catalytic properties of such materials, much research effort has been placed into modifying the composition of the AlPOs frameworks by incorporating other elements with different oxidation states so as to generate active catalytic sites. The phosphor sites could be partially substituted by silicon, whereas aluminium sites could be replaced with many divalent (Mg, Mn, Zn, Fe and Co) and trivalent cations (B, Cr, Fe), leading to the generation of new series of AlPOs materials denoted as SAPO-*n*, MAPO-*n*, and MAPSO-*n*.[9]

From a general point of view, aluminium phosphate-based compounds constitute an important class in the field of nanoporous materials. Thus, they have dramatically expanded the family of traditional aluminosilicate zeolites in terms of both structural and compositional diversity. In this enormous field, metal substituted aluminophosphates brought about increased interest, thus besides their widespread applications, they have led to a new concept in materials chemistry concerning the chemical design of new functional materials.

It was this preliminary work in metal aluminophosphates that showed the potential to combine a wide range of properties and functionalities in the same crystalline solid by introducing various metal elements with different valence states and coordination geometries. Nowadays, there has been much synthetic work on producing phosphate-based compounds consisting exclusively of transition metal centres, giving rise to a diverse range of new framework architectures with fascinating properties owing to the redox abilities and magnetic nature of the *d* block elements.

1.2.2 Transition metal phosphates

In the expanded field of transition metal phosphates, a diverse range of framework structures from one dimensional chains or ladders, layer structures to three dimensional porous frameworks, has been identified. Looking at the one dimensional chain and ladder compounds, it would appear as they commonly exhibit basic SBUs which can spontaneously self-assemble into layered frameworks. Examples involve the types of ID chains and ladders, shown in Figures 1.3a and 1.3b, which have been frequently observed in many layered structures.[10] This type of chains can be best thought of as being derived from four membered rings of alternating metal-oxo polyhedra units and phosphate tetrahedra, having a bonding motif related to that occurs in mineral natisite. Depending on the transition metal involved (V,[10b] Cu,[10g] Nb,[10f] Zn,[10a] Ti[10c]), different coordination geometries can be preferentially adopted such as tetrahedral, square pyramidal coordination and octahedral. Concerning the latter, the increase of the coordination number of the metal implies an extended polyhedral connectivity and thus the related ladder structure type is more favorable to be formed.

Another example is the type of chain illustrated in Figure 1.3c. This type has been often observed in 2D frameworks based on several transition metals such as titanium, vanadium and iron.[11] This family of compounds exhibits frameworks which derive from –M-O-M-O-M- infinite chains of corner-sharing metal octahedra capped on both sites by phosphate groups through di-μ-(O,O')PO_4 bridges; this bonding motif resembles the mineral tancoite. An increase of the ratio of metal to phosphor gives rise to further polymerization and leads to a diverse connectivity of the polyhedra units through edge- and face-sharing. The most common building unit is the tetrameric block, shown in Figure 1.3d, which is constructed of edge-shared bioctahedral units capped on both sides by two different phosphate groups. This type of building blocks has been frequently found in many two dimensional structures, where such tetramers share common corners so as to form various layer topologies penetrated by channel systems.[12]

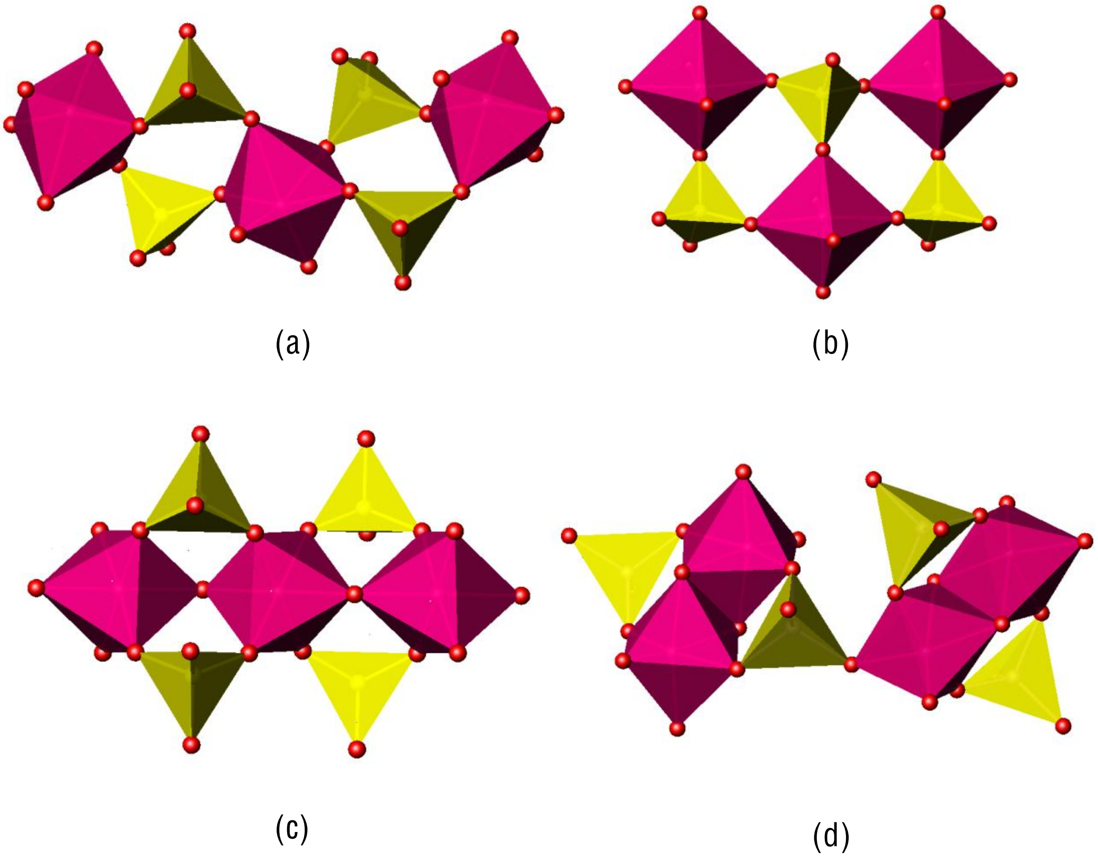

Figure 1.3: Schematic showing some of the building blocks which have been frequently observed in the field of 1D and 2D phosphate based compounds. Pink polyhedra represent the MO_6 octahedra and yellow polyhedra show the phosphate.

In the search for new open-framework metal phosphates the family of iron phosphate has attracted considerable attention because of the diverse range of porous architectures and the rich magnetic properties observed in these materials. Iron phosphates occur frequently in nature, with the most striking example being the discovery of the mineral cacoxenite which exhibits channels of an approximately 14 Å diameter.[13] The first synthetic iron phosphates were the analogous structures of the minerals hureaulite and alluaudite prepared from the group of Corbin et al.[14] Subsequently, several groups have attempted to synthesize open-framework iron phosphates. Much of this work has been carried out from the group of Ferey,[15] who produced the series of the ULM-porous oxyfluorinated iron phosphates, and the group of Lii and co-workers who mainly investigated the formation of amine-templated structures with large pore sizes.[16] It appears that these ferrophosphate open-frameworks exhibit antiferromagnetic behaviour with relatively low Neel temperatures, giving rise to the generation of a new class of nanoporous materials that attempts to combine the fundamental applications of the porous-zeolites with magnetic properties.

Another important subclass is the open-framework zinc phosphates. The main interest in these materials concerns the ability of zinc to adopt tetrahedral coordination geometry, allowing a number of zeolite-type frameworks to be formed. In addition, there are few zincphosphate compounds which exhibit very unusual bonding motifs resulting from the presence of Zn-O-Zn linkages;[17] therefore very different topologies could occur from those reported with the alumino-silicate/phosphate systems. Recent investigations of zincphosphate phases have shown that low-dimensional structures consisting of linear chains or ladders can self assemble to form 2D layers and 3D framework structures.[18] This was seen in the case of the one-dimensional ladder structure $[C_6N_4H_{22}]_{0.5}$ $[Zn(HPO_4)_2]$ which was successfully converted in a three-dimensional framework when heated in water, whereas its reaction with other amines resulted in different high dimensional structures.[18a] In a similar vein, the two-dimensional layer structure of $[C_5N_3H_{18}][Zn_2(PO_4)(HPO_4)_2].H_2O$ was transformed to the three-dimensional channel structure $[C_5N_3H_{18}][Zn_3(PO_4)(HPO_4)_3]$ by simply heating in water.[19] Such studies have traced a new concept in materials chemistry, as they can offer a better understanding of the building-up process of the high-dimensional complex architectures.

I. Molybdenum phosphates

In a domain where the challenge is to synthesise new metal phosphate frameworks that contain additional structural motifs beyond the tetrahedral co-ordination, molybdenum has been a particularly attractive target because of its ability to adopt many different oxidation states and coordination geometries. Since the discovery of $MoOPO_4$ by Kierkegaard and Westerlund,[20] much research effort has been placed into producing reduced molybdenum phosphates using solid state techniques. The

Raveau and Haushalter groups produced a large number of condensed molybdenum phosphate frameworks in the presence of charge balancing inorganic cations.[21]

Classification of these framework structures according to the connectivity mode of the molybdenum polyhedra was suggested by Costentin et al.[21a] According to them, the family of compounds formed at high-temperatures can be divided into three main classes. Class A represents the largest family among the three series. It encompasses a diverse range of framework topologies with the Mo/P ratios = 1/2 and 2/3. Framework structures within this class exhibit isolated MoO_6 octahedra which share five corners with different phosphate groups, whilst their sixth apical contributes a terminal M=O oxo group. Class B involves framework structures which derive from infinite chains of corner sharing MoO_6 octahedra capped in up and down orientations by phosphate groups, implying the non free available apices in the molybdenum coordination sphere. Finally, class C includes molybdenum phosphate compounds that exhibit Mo/P ratios > 1. This family is characterised by edge- and face-shared molybdenum polymeric units, thus one might expect further condensation of the MoO_6 octahedra to occur as the Mo/P ratio is increased. The most common building unit within this family is the complex $Mo_4P_6O_{29}$ block shown in Figure 1.4a. It may be described as $Mo_4O_8^{4+}$ cube blocks built up from four edge-shared molybdenum octahedra; each face of the cube is capped by a phosphate group that serves to connect adjacent cubes together through di-μ-(O,O') bridges.

Although these materials have been shown to form a wide range of framework architectures with diverse bonding motifs, they exhibit relatively dense frameworks which show poor ion exchange properties. Subsequently, hydrothermal routes were followed in order to tailor the synthesis of more open frameworks in presence of larger removable cations. During this development, a large variety of two dimensional layer structures[22] and three dimensional porous frameworks[23] was successfully synthesized. Consideration of these layered frameworks obtained via mild hydrothermal routes demonstrates that they generally exhibit Mo/P ratios > 1. Their building units are often constructed of corner or edge-shared molybdenum bioctahedral units which are grafted by phosphate groups. More complex building units have been also identified, for example the cube blocks (shown in Figure 1.4b) which are very similar to those mentioned above with the main difference being the reduced number of the phosphate linkers.

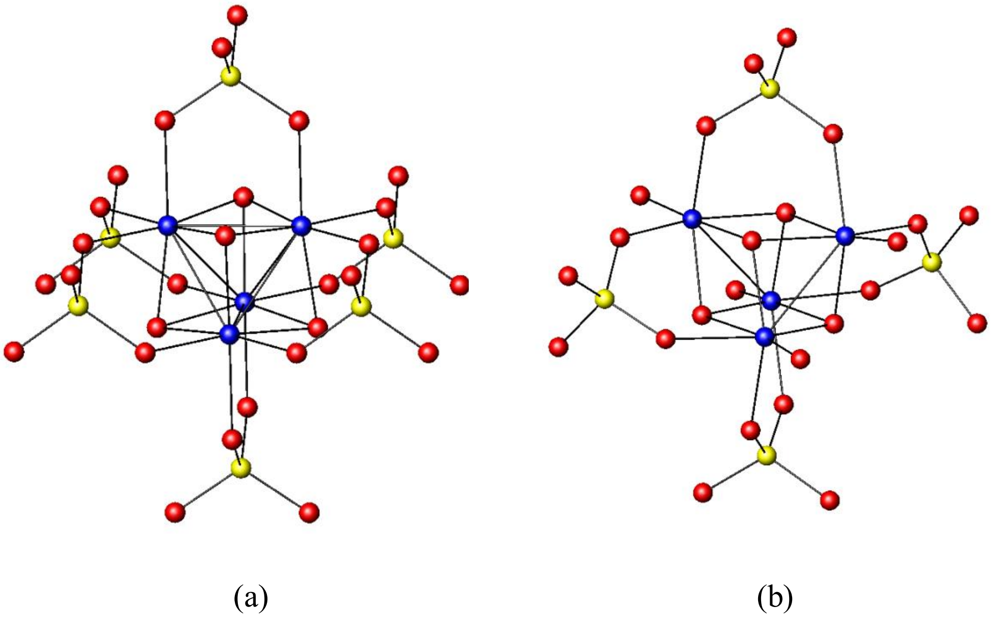

Figure 1.4: Schematic showing details of the $Mo_4O_8^{4+}$ cube building blocks. Molybdenum atoms: small blue spheres, phosphorus atoms: yellow spheres and oxygen atoms: red spheres.

By utilizing hydrothermal routes it was demonstrated that it was possible to obtain three dimensional molybdenum phosphate frameworks with significant internal micropore volume. This is the case for a new series of open framework solids which were prepared from hydrothermal treatments of MoO_3/Mo molybdenum sources with phosphoric acid in presence of various amines. $(Me_4N)_{1.3}(H_3O)_{0.7}[Mo_4O_8(PO_4)_2].2H_2O$ was the first three dimensional molybdenum phosphate to be synthesised with 25 vol % void space.[23a] Its framework structure can be best considered as derived from $Mo_4O_8^{4+}$ cubes connected together in a three dimensional network by the up and down alteration of phosphate groups . Identical $Mo_4O_8^{4+}$ cubes blocks have been observed in the previously discussed layered compounds and it is remarkable that such building blocks can exhibit different bonding motifs, forming a number of distinct framework architectures with various cavity diameters.

Another example of a microporous material is the $Mo_8O_{12}(PO_4)_4(HPO_4)_2.13H_2O$ shown in Figure 1.5.[23c] This material can be regarded as the first example of an electroneutral molybdenum phosphate constructed of previously unknown tetrameric units and which shows the largest internal void volume (35 vol %) achieved in the family of molybdenum phosphate-based materials. Its channel system is filled with only water molecules and allows reversible adsorption to take place. Finally, one other framework topology has been identified.[23d, 24] It may be described as layers consisting of alternating corner-sharing molybdenum octahedra and phosphate tetrahedra; bridging phosphate groups serve to connect these layers by generating the three dimensional porous framework with 25 vol % void space.

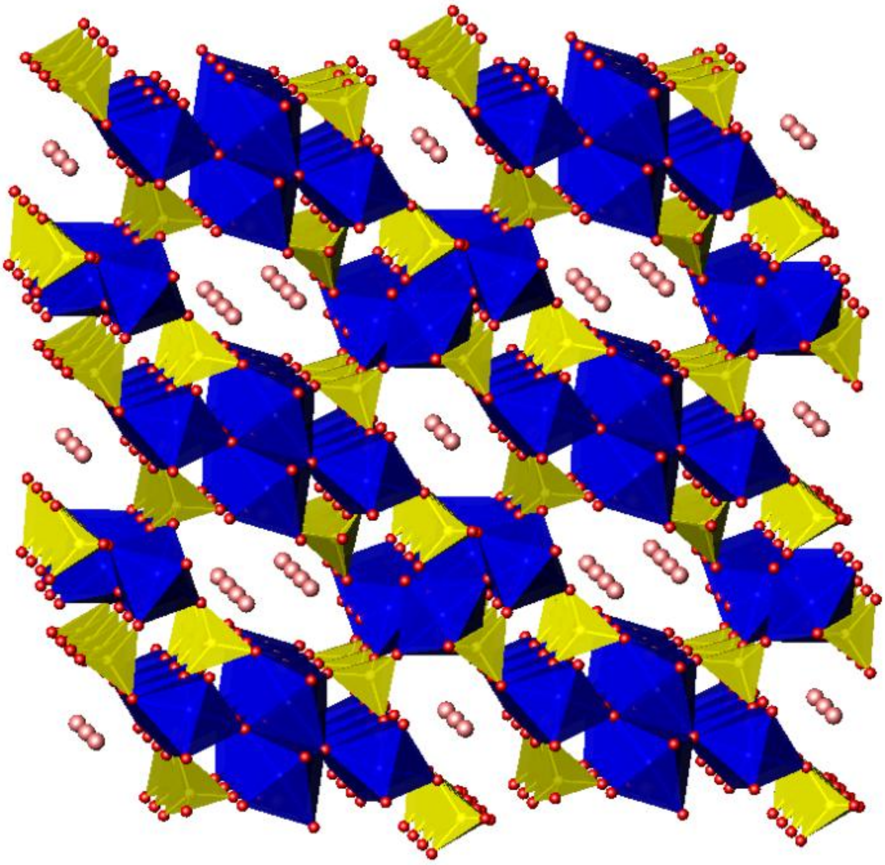

Figure 1.5: A view of the structure of the $Mo_8O_{12}(PO_4)_4(HPO_4)_2.13H_2O$ which exhibits large internal void spaces filled with just water molecules. Blue octahedra represent the MoO_6 and yellow tetrahedra show the PO_4; pink spheres show the water molecules.

From a general point of view, the family of molybdenum phosphates has shown the potential for the design numerous framework topologies consisting of linked octahedra and tetrahedra by the use of both solid state reactions with inorganic cations and hydrothermal routes with organic amines acting as templates. The three-dimensional molybdenum phosphates, obtained *via* hydrothermal routes, have received considerable attention due to their relatively defect-free porous frameworks. However, such materials have shown poor adsorption properties concerning the hydrocarbon sized molecules; there is still much work to be done in order to address this problem.

II. Vanadium phosphates

Vanadium phosphate framework materials have been extensively studied for several years, with a vast number of structural types being produced. Interest in such materials was instigated by the discovery of the $(VO)_2P_2O_7$ and its potential catalytic use in the selective oxidation of butane to maleic anhydride.[25] Similar to the molybdenum phosphates discussed above, early investigations concentrated on producing vanadium phosphates using solid state synthesis. Much of this work has been undertaken by four groups: the groups of Raveau, Haushalter and Jacobson, Lii and Beltran-Porter. Numerous framework topologies consisting of different coordination geometries of the vanadium metal, such as tetrahedral, square pyramidal, trigonal bipyramidal and octahedral, combined with varied coordination modes of the phosphate linkers have been identified.

Boudin et al. has recently suggested a classification of these materials according to the connectivity of the vanadium polyhedra.[26] The first class includes frameworks consisting of isolated vanadium polyhedra which can either adopt one type of polyhedron or a combination of them; for example the combination of vanadium octahedra and vanadium square pyramids has been frequently observed in this class of materials. The second class includes frameworks constructed of vanadium polymeric units. Examples involve simple building units such as corner-, edge- or face-shared bioctahedral units (V_2O_{11}, V_2O_{10} and V_2O_9 respectively) as well as more complex polyhedral units such as the tetrameric V_4O_{20} units. These tetramers are composed of a central edge-shared bioctahedral unit on to which is grafted, on two sides, two vanadium octahedra. Finally, the third class involves structures which exhibit infinite chains of VO_n polyhedra. Most examples include corner-sharing vanadium octahedral or square pyramidal units, whereas there are few cases in which polyhedra exhibit connectivity through common edges.

Following the successful preparation of the microporous molybdenum phosphates *via* hydrothermal routes, investigations were then carried out on the vanadium system with the aim of synthesizing vanadium phosphates with larger pore sizes. The groups of Haushalter[27] and Ferey[28] have produced a number of different framework topologies; remarkable examples include the discovery of an inorganic double helix in the structure of $[(CH_3)_2NH_2]K_4\,[V_{10}O_{10}(H_2O)_2(OH)_4(PO_4)_7].4H_2O$[27] (shown in Figure 1.6) and the two open frameworks[29], $Cs_3[V_5O_9(PO_4)_2].xH_2O$ and $[HN(C_2H_4)_3NH]K_{1.35}[V_5O_9(PO_4)_2]\ .xH_2O$ (shown in Figure 1.7) which exhibit giant voids. The former can be best considered as derived from spirals constructed of V_5P_5 oligomeric units which are intertwined so as to form the two strands of the double helix. These previously unknown oligomeric units are built up from a trimer of three corner-sharing vanadium octahedra which share two outer edges with two different vanadium square pyramids. There are four different phosphate groups grafted on each trimer which serve to connect the two strands together, forming this three dimensional double-helix compound.

In the two $Cs_3[V_5O_9(PO_4)_2].xH_2O$ and $[HN(C_2H_4)_3NH]K_{1.35}[V_5O_9(PO_4)_2].xH_2O$ compounds, the fundamental building units consist of very unusual pentameric units which are capped on sites by phosphate tetrahedra. These pentamers are composed of a central VO_5 square pyramid which shares its four basal edges with four different square pyramids, forming a cross-shaped building unit. Phosphate tetrahedra serve to connect together five adjacent pentameric units, forming extremely large cavities with an approximately diameter of 13 Å. These channels are filled in a remarkable complex, self-assembled manner, showing two channel types distinguished by their content. The one channel type is filled by dabco and water molecules while the other type hosts only potassium cations.

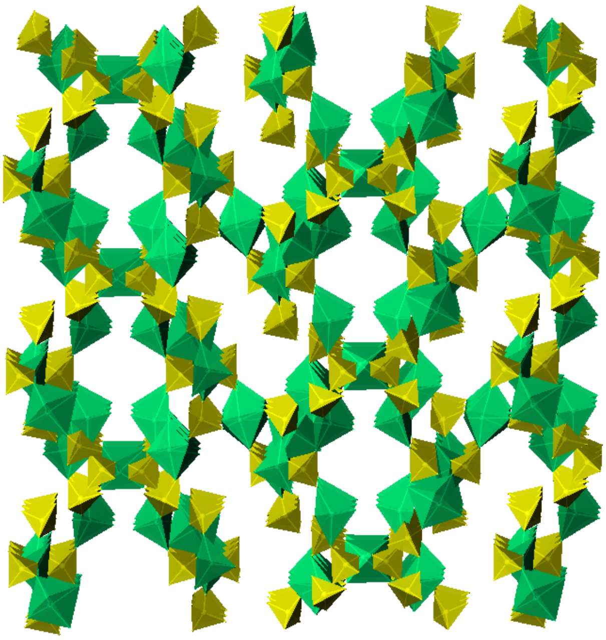

Figure 1.6: A perspective view of the three dimensional framework of $[(CH_3)_2NH_2]K_4$ $[V_{10}O_{10}(H_2O)_2(OH)_4(PO_4)_7].4H_2O$ showing the presence of the double helix. Green polyhedra represent the VO_6 and VO_5 units and yellow tetrahedra show the PO_4.

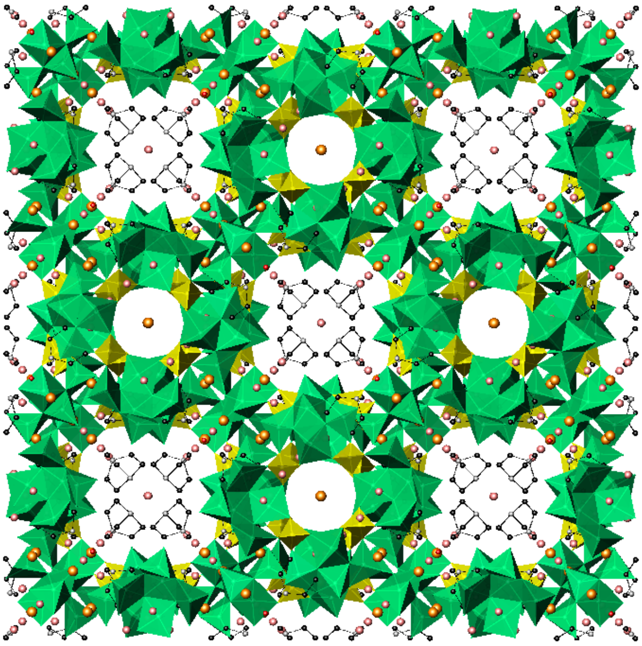

Figure 1.7: A view of the three dimensional framework of $[HN(C_2H_4)_3NH]K_{1.35}$ $[V_5O_9(PO_4)_2].xH_2O$ showing details of the giant channels. Green polyhedra represent the VO_6 and VO_5 units and yellow tetrahedra show the PO_4.

1.2.3 Borophosphates

From a structural point of view, BPO_4 can be regarded as III-V heterotype of quartz as it exhibits the same condensed structures to those identified in silica polymorphs and aluminophosphates.[30] Whereas aluminosilicates and the related AlPOs have been extensively investigated for many decades, borophosphates have only few years. Early work concentrated on borophosphate glasses with respect to their ionic conductivity and nonlinear optical properties, while research into crystalline framework materials begun in the mid-1990s.[31]

The group of Kniep and co-workers has produced a large number of borophosphate framework materials.[32] In general, borophosphates are indicated as intermediate compounds obtained from systems M_xO_y-B_2O_3-P_2O_5(-H_2O), where M = metal from the main group or *d* block, or ammonium cation. These materials exhibit a rich structural diversity resulting from the multi co-ordinate linking ability of the boron which can either adopt tetrahedral geometry or three-fold planar coordination. Examples include single chains of alternating borate and phosphate polyhedra,[33] open- and cyclo-branched chains,[34] layer structures[35] as well as three dimensional frameworks[36]. Depending on the B: P ratio, particular bonding motifs may be favoured. Hence, similarly to aluminophosphates, borophosphates do not exhibit P-O-P linkages and therefore an increase of the phosphor composition generally leads to open-branched bonding motifs consisting of terminal phosphate groups.

Metalloborophosphate frameworks have been also investigated.[37] This family is characterized by framework structures consisting of exclusively tetrahedral units. They possess three dimensional frameworks which comprise metallate/borate/phosphate tetrahedra in the ratio = 1/1/2. An exception with M/B/P ratio = 2/1/3 was identified in the series of the $(NH_4)_{16}[M_{16}B_8P_{24}O_{96}]$ compounds (where M = Zn, $Zn_{1-x}Co_{x}$).[38] Metalloborophosphate framework structures can be thought of as being derived from corner-shared four-, six- or eight-membered rings consisting of alternating borate or metallate units which are only connected to phosphate tetrahedra, thus linkage modes such as B-O-B, M-OM, P-O-P and M-O-B have not been observed. Nevertheless, this family of compounds exhibits a wide range of framework topologies resulting from the varied ring motifs. There are few striking compounds which exhibit zeolite-type frameworks. Examples include the $NH_4[(Zn_{1-x}Co_x)BP_2O_8$,[39] which shows a framework topology analogous to gismondine, and the two borophosphate compounds $KBeBP_2O_8.0.33H_2O$[40] and $(NH_4)_{16}[Zn_{16}B_8P_{24}O_{96}]$[38] which have analcime type frameworks.

Though borophosphate frameworks have not been under prolonged investigation, numerous new framework topologies have been identified. Several main block metals and transition metal species have been successfully incorporated into those anionic frameworks, giving rise to new structure types consisting of polyhedra units with varied coordination geometries, such as the tetrahedral geometry of phosphate and borate units, the trigonal planar geometry of boron in addition to the octahedral geometry of the metal centers.

1.2.4 Organophosphonates

The quest for new three-dimensional open frameworks has led to the use of phosphonate anions to link inorganic oxide units into extended framework structures. The proof of concept was first given by Alberti et al. with the successful preparation of a series of zirconium layer structures by introducing monophosphate linkers to enhance the interlayer spacing.[41] Following this approach, a number of organically pillared materials were produced using various diphosphonate linkers. Examples include most zirconium phosphonates, with a wide range of corrugated[42] and flat porous-layer structures[43] to three-dimensional channel frameworks[44] being formed. Since then, the family of metal phosphonates has been dramatically expanded and is no longer limited to pillared materials associated with only bifunctional linkers. Thus, the relatively easy synthesis of various rigid and flexible ligands consisting of different functional groups offers the potential of a diverse range of new framework architectures.[45]

More recent studies appear to be focused on transition metal containing frameworks. The groups of Zubieta[46], Bujoli[44a] and Ferey[47] have produced a number of three-dimensional metal phosphonates. Striking examples include the two analogous structures, $[M(O_3PCH_2NH(C_2H_4)_2NHCH_2PO_3)].H_2O$[46] where M = Mn, Co, and the vanadium containing framework $[NH_4]_4[(VO_3)(O_3PCH_2PO_3)_4(H_2O)_4].4H_2O$ (which is denoted as MIL-2).[47a] The framework structure of the former can be best considered as derived from tetrameric building blocks built up from two corner-sharing metal tetrahedra units and two phosphate tetrahedra which are connected together to form eight-membered rings; diphosphonate ligands serve to link these ring-units together by generating larger ellipsoidal 44-membered rings. The latter exhibits a three-dimensional framework structure consisting of 14-membered rings. Vanadium octahedra and square pyramids alternate with phosphate tetrahedra to form these clover-like rings which are further interconnected to the diphosphonate anions, forming a three-dimensional framework structure.

1.3 Arsenate frameworks

Following recent interest in the potential applications of phosphate-based materials, research has been directed towards the exploration of other oxotetrahedral and framework building units, such as arsenate in combination with transition metal species. The use of alternative primary building units offers the potential of different framework topologies from those found with the more conventional phosphate systems. Though arsenate and phosphate anions exhibit related structural patterns based upon tetrahedral motifs, they do exhibit very different chemistry in aqueous solution. In comparing the standard potentials of the two acids it can be observed that the former exhibits a diverse range of stable anionic species in acidic and basic media which might further undergo different polycondensation processes under hydrothermal conditions.[48] In addition, considering the larger size of the AsO_4^{3-} anion and thereby its softer character compared to phosphate PO_4^{3-}, one might expect the different bonding affinity of the former, leading to different fundamental building units.

Early studies were concentrated on the alumino- and galloarsenate frameworks,[49] whereas research has recently begun shifted towards the investigations of framework structures based on transition metals such as vanadium, iron, and zinc, giving rise to the discovery of novel framework topologies. Examples mainly include a number of one-dimensional chains or ladders amine templated-vanadoarsenate structures,[12b, 50] a large family of iron arsenate-oxalates which has been shown to exhibit transformations phenomena of the low-dimensional structures to the related 2D and 3D channel frameworks,[51] in addition to a broad family of alkali metal-templated zincarsenates[52] which shows a wide structural diversity based upon tetrahedral, trigonal bipyramidal and octahedral coordination motifs.

Though research work into arsenate-based frameworks has been relatively limited, the materials reported so far show rich structural diversity having bonding motifs that have not yet been observed in the phosphates domain. The rapidly development of this family of materials shows the potential of numerous novel topologies yet to be discovered.

1.4 Fluoride incorporation in frameworks

Interest in incorporation of fluoride ions in the synthesis of inorganic framework materials was initiated at the end of the 1980s by Flanigen and Patton with the discovery of a novel crystalline silica polymorph prepared in a fluoride medium.[53] Since then, the fluoride route has been extensively applied for the elaboration of many silica-based zeolites as well as for the development of phosphate microporous compounds, with great attention paid to alumino- and gallophosphate systems.

Guth and Kessler were the first to demonstrate that aluminosilicate zeolites can be also prepared from gels in the presence of fluoride media, providing new routes in the field of zeolite synthesis.[54] Their systematic studies were aimed at incorporating fluoride into zeolite synthesis, as an alternative mineralizer to OH^-, in an effort to maintain zeolite formation in neutral or even slightly acidic conditions. Thus, the solubility of silica species significantly increases in a fluoride medium by formation of SiF_6^{2-} complexes which further undergo hydrolysis and polycondensation processes to form the crystalline zeolite structure. As a result, many zeolites have been successfully obtained and remarkably these materials tend to grow as large crystals and exhibit relatively low density structures with few lattice defects.

Besides the mineralizing effect that the fluoride anion exhibits, it appears to have a structure directing role as well. Fluoride anions exhibit a great tendency to get entrapped within small cages, providing stabilization of the zeolite structure through the formation of five-coordinated $[SiO_{4/2}F]^-$ elongated trigonal bipyramids.[55] The major benefit of this is the formation of silica-based materials that exhibit lower defective structures and thus, they have higher hydrophobic character compared to those materials prepared in hydroxide media.[56] Hence, the ability of the entrapped fluoride anions to balance the charge-compensating organic templates, in addition to the low concentration of $Si\text{-}O^-$ or Si-OH species that generally occur in low pH synthesis, significantly limits the formation of connectivity defects in the structure. Owing to this highly hydrophobic character arising from defect-free structures, pure silica materials are very interesting candidates in the field of energetics for their use as molecular springs or bumpers,[57] whilst aluminosilicate catalysts are suitable materials for catalyzing reactions in systems that contain reactants with different polarities.[58] An additional advantage is the crystallization of zeolites in polar noncentrosymmetric space groups, giving rise to active nonlinear optical materials. This is seen in the case of the zeolite IFR which exhibits a non centrosymmetric space group and thus a polar character when crystallised from a fluoride medium, although the topological symmetry is centrosymmetric.[59] Hence, the preferential location of fluoride ions at specific sites in $[SiO_{4/2}F]^-$ units generates ordering of the organic templates due to the strong electrostatic interactions between fluorides and the amino parts of the template, leading to a change of symmetry.

A remarkable feature in this context is the stabilization of double-four-ring units (D4R) with incorporated fluoride anions, leading to the discovery of novel framework topologies that have not yet been observed through the typical zeolite synthesis performed in hydroxide media. Notable examples include the successful formation of the novel silica-based zeolites, ITQ-7,[60] ITQ-12[61] and ITQ-13,[62] which exhibit structural building units mainly constructed of D4R units. Similar D4R cube-like octameric blocks built up from corner-sharing tetrahedra with an occluded fluoride anion have also been observed in a number of alumino- and gallophosphate microporous compounds. Examples include the GaPO-LTA,[63] $AlPO_4$-16(AST),[64] ULM-18[65] compounds and a series of materials called Mu-*n*,[66] but the most eye-catching discovery has been the extremely large porous gallophosphate cloverite.[67] This new GaPO molecular sieve exhibits a channel system related to the FAU zeolite type built up from 20 $[TO_4]$ tetrahedra and has a pore diameter of approximately 13.2 Å. It appears that the D4R building units are rather distorted due to the presence of entrapped fluorides which exhibit weak Ga-F distances in the range of 2.3-2.6 Å, leading to five-coordinate gallium atoms (distorted trigonal bipyramids).

Alternatively, fluoride can be incorporated more directly into the gallium or aluminium coordination sphere, leading to a diverse range of structural patterns based on five- or sixfold co-ordinations alongside the typical tetrahedral geometry. Fluoride can adopt both terminal and bridging coordination geometries. Terminal-bonded fluorides have been identified in the case of Al/$GaPO_4$ CJ2 compounds in which both six- and five-fold coordinated MO_5F and MO_5 (M = Al or Ga) polyhedra alternate with phosphate groups to form these three-dimensional microporous frameworks.[68] When fluoride is involved in bridging bonds, more complex polymeric building units generally occur. The most common fundamental units can be either tetramers [69] or hexamers [70]. Tetrameric units are built up from a metal-bioctahedral unit (M = Al, Ga) capped on two poles by two different phosphate groups; fluoride anions are usually located in the shared corners or edges of the dimer. Hexamers are built up from a central Al or Ga octahedron that shares two *cis*-corners with two trigonal bipyramids through fluorine and are capped by three phosphate groups.

Nowadays, this field is no longer limited to Al and Ga phosphate-based materials, whilst research has begun to shift towards the investigation of framework structures based on early transition metals such as Ti,[71] Fe,[72] Zr,[73] Nb,[74] and V[75], giving rise to the discovery of new functional materials. Non-centrosymmetric structures based upon d^0 metals, for which out-of-centre octahedral distortions are frequently found, are of great interest owing to their potential piezoelectric, ferroelectric and non-linear optical applications. Incorporation of fluoride into octahedral geometries of such materials has been a key aspect in terms of both structural diversity and functionality, as it becomes possible to direct the extended bond network in a non-centrosymmetric arrangement by generating nucleophilic sites in acentric octahedra units. Earlier investigations were concentrated on structures constructed by linked $[MOxF_{6-x}]^{2-}$ (where $x = 1$ for M: V^{V}, Nb^{V}, Ta^{V} and $x = 2$ for M: Mo^{VI}, W^{VI})[76], with respect to their optical effects; one might expect the great challenge for expanding this new field into the phosphate-based compounds where both anionic species (F^{-}, PO_4^{-3}) are combined together to connect transition metal centres.

1.5 Scope of work

The aim of this project is to synthesise and characterise new framework materials. The framework structures are produced with the aim of expanding the range of structural types and bonding motifs available. The materials to be investigated will be produced using molybdenum and vanadium metal centres combined with a variety of anionic units, such as phosphate, arsenate, borate and fluoride anions. The presence of such elements should give additional structure motifs beyond tetrahedral co-ordination, such as trigonal bipyramidally, square pyramidally or octahedrally coordinated metal atoms. This diverse range of structural building units should help to obtain new framework topologies with the potential for industrial applications.

Chapter Two describes the experimental methods and theory applied in order to carry out this research project.

Chapter Three discusses a number of molybdenum phosphate framework structures. Whilst exploring this extensively studied area, new approaches are investigated such as the incorporation of borate or fluoride anions into the framework structure.

Chapters Four and Five describe a variety of oxyfluorinated vanadium phosphate and arsenate frameworks, highlighting the rich structural diversity of these materials.

Chapter Six details some vanadium phosphate and borate structures. The products have been investigated with X-ray diffraction methods and compared to previously reported compounds.

Chapter Seven presents synthetic efforts in producing molybdenum organophosphonate frameworks during a three month placement at the University of Kiel (Germany).

1.6 References

[1] H.Gies, R.Kirchner, H. v. Koningsveld and M.Treacy, *Proceedings of the 12th International Zeolite Conference* 1999, 2999.

[2] W. Loewenstein, *Annual Meeting of the Society at Porto Alegre* 1952, 92-96.

[3] a) J. V. Smith, *Chemical Reviews* 1988, *88*, 149-182; b) W.M.Meier, D.H.Olson and C.Baerlocher, *Atlas of Zeolite Structure Types, Elsevier, London* 1996.

[4] Original drawing from http://izasc.ethz.ch/fmi/xsl/iza-sc/SBUList.htm.

[5] R. Xu, W. Pang and J. Yu in *Chemistry of zeolites and related porous materials, Vol. page 25* (Ed. Wiley-Interscience), 2007.

[6] M.Weller, 1999, Oxford University Press,Oxford.

[7] S. T. Wilson, B. M. Lok, C. A. Messina, T. R. Cannan and E. M. Flanigen, *Journal of the American Chemical Society* 1982, *104*, 1146-1147.

[8] M. E. Davis, C. Saldarriaga, C. Montes, J. Garces and C. Crowder, *Nature* 1988, *331*, 698-699.

[9] a) E. M. Flanigen, B. M. Lok, R. L. Patton and S. T. Wilson, *Pure and Applied Chemistry* 1986, *58*, 1351-1358; b) B. M. Lok, C. A. Messina, R. L. Patton, R. T. Gajek, T. R. Cannan and E. M. Flanigen, *Journal of the American Chemical Society* 1984, *106*, 6092-6093.

[10] a) A. A. Ayi, S. Neeraj, A. Choudhury, S. Natarajan and C. N. R. Rao, *Journal of Physics and Chemistry of Solids* 2001, *62*, 1481-1491; b) Z. Bircsak, A. K. Hall and W. T. A. Harrison, *Journal of Solid State Chemistry* 1999, *142*, 168-173; c) C. Chen, Y. L. Yang, K. L. Huang, Z. H. Sun, W. Wang, Z. Yi, Y. L. Liu and W. Q. Pang, *Polyhedron* 2004, *23*, 3033-3042; d) R. K. Chiang, *Journal of Solid State Chemistry* 2000, *153*, 180-184; e) A. Choudhury, S. Natarajan and C. N. R. Rao, *Journal of the Chemical Society-Dalton Transactions* 2000, 2595-2598; f) G. Z. Liu, S. T. Zheng and G. Y. Yang, *Inorganic Chemistry* 2007, *46*, 231-237; g) S. Neeraj, T. Loiseau, C. N. R. Rao and A. K. Cheetham, *Solid State Sciences* 2004, *6*, 1169-1173.

[11] a) Y. H. Guo, Z. Shi, J. H. Yu, J. D. Wang, Y. L. Liu, N. Bai and W. Q. Pang, *Chemistry of Materials* 2001, *13*, 203-207; b) L. M. Liu, X. Q. Wang, R. Bontchev, K. Ross and A. J. Jacobson, *Journal of Materials Chemistry* 1999, *9*, 1585-1589; c) S. Mahesh, M. A. Green and S. Natarajan, *Journal of Solid State Chemistry* 2002,

165, 334-344; d) S. Mandal, M. A. Green and S. Natarajan, *Journal of Solid State Chemistry* 2004, *177*, 1117-1126; e) Y. P. Zhang, C. J. Warren, A. Clearfield and R. C. Haushalter, *Polyhedron* 1998, *17*, 2575-2580.

[12] a) F. Gagnard, C. Reisner and W. Tremel, *Inorganic Chemistry* 1997, *36*, 352-355; b) A. H. Liu and S. L. Wang, *Inorganic Chemistry* 1998, *37*, 3415-+; c) S. L. Wang and C. Y. Cheng, *Journal of Solid State Chemistry* 1994, *109*, 277-280.

[13] P. B. Moore and J. Shen, *Nature* 1983, *306*, 356-358.

[14] D. R. Corbin, J. F. Whitney, W. C. Fultz, G. D. Stucky, M. M. Eddy and A. K. Cheetham, *Inorganic Chemistry* 1986, *25*, 2279-2280.

[15] a) M. Cavellec, J. M. Greneche, D. Riou and G. Ferey, *Microporous Materials* 1997, *8*, 103-112; b) M. Cavellec, D. Riou, J. M. Greneche and G. Ferey, *Inorganic Chemistry* 1997, *36*, 2187-2190; c) M. Cavellec, D. Riou, C. Ninclaus, J. M. Greneche and G. Ferey, *Zeolites* 1996, *17*, 250-260.

[16] a) K. H. Lii, *Journal of the Chemical Society-Dalton Transactions* 1996, 819-822; b) K. H. Lii and C. Y. Huang, *Journal of the Chemical Society-Dalton Transactions* 1995, 571-574; c) K. H. Lii and Y. F. Huang, *Chemical Communications* 1997, 839-840; d) L. Y. Na, Y. L. Liu, W. Q. Pang and R. R. Xu, *Chinese Journal of Inorganic Chemistry* 2000, *16*, 287-292; e) V. Zima, K. H. Lii, N. Nguyen and A. Ducouret, *Chemistry of Materials* 1998, *10*, 1914-1920.

[17] X. H. Bu, P. Y. Feng and G. D. Stucky, *Journal of Solid State Chemistry* 1996, *125*, 243-248.

[18] a) A. Choudhury, S. Neeraj, S. Natarajan and C. N. R. Rao, *Journal of Materials Chemistry* 2001, *11*, 1537-1546; b) C. N. R. Rao, M. Dan and J. N. Behera, *Pure and Applied Chemistry* 2005, *77*, 1655-1674.

[19] S. Natarajan, *Chemical Communications* 2002, 780-781.

[20] P. Kierkegaard and M. Westerlund, *Acta Chemica Scandinavica* 1964, *18*, 2217-2225.

[21] a) G. Costentin, A. Leclaire, M. M. Borel, A. Grandin and B. Raveau, *Reviews in Inorganic Chemistry* 1993, *13*, 77; b) R. C. Haushalter and L. A. Mundi, *Chemistry of Materials* 1992, *4*, 31-48.

[22] a) E. W. Corcoran, *Inorganic Chemistry* 1990, *29*, 157-158; b) R. C. Haushalter and L. A. Mundi in *THE HYDROTHERMAL SYNTHESIS OF LAYERED MOLYBDENUM PHOSPHATES WITH OCTAHEDRAL-TETRAHEDRAL LAYERS*,

Vol. 233 Eds.: R. L. Bedard, T. Bein, M. E. Davis, J. Garces, V. A. Maroni and G. D. Stucky), Materials Research Soc, Pittsburgh, 1991, pp. 255-265; c) L. A. Mundi and R. C. Haushalter, *Inorganic Chemistry* 1990, *29*, 2879-2881.

[23] a) R. C. Haushalter, K. G. Strohmaier and F. W. Lai, *Science* 1989, *246*, 1289-1291; b) H. E. King, L. A. Mundi, K. G. Strohmaier and R. C. Haushalter, *Journal of Solid State Chemistry* 1991, *92*, 1-7; c) L. A. Mundi, K. G. Strohmaier, D. P. Goshorn and R. C. Haushalter, *Journal of the American Chemical Society* 1990, *112*, 8182-8183; d) L. A. Mundi, K. G. Strohmaier and R. C. Haushalter, *Inorganic Chemistry* 1991, *30*, 153-154.

[24] L. A. Mundi, L. Yacullo and R. C. Haushalter, *Journal of Solid State Chemistry* 1991, *95*, 283-288.

[25] H. Seeboth, B. Kubias, H. Wolf and B. Lucke, *Chemische Technik* 1976, *28*, 730-734.

[26] S. Boudin, A. Guesdon, A. Leclaire and M. M. Borel, *International Journal of Inorganic Materials* 2000, *2*, 561-579.

[27] V. Soghomonian, Q. Chen, R. C. Haushalter, J. Zubieta and C. J. Oconnor, *Science* 1993, *259*, 1596-1599.

[28] T. Loiseau and G. Ferey, *Journal of Solid State Chemistry* 1994, *111*, 416-421.

[29] M. I. Khan, L. M. Meyer, R. C. Haushalter, A. L. Schweitzer, J. Zubieta and J. L. Dye, *Chemistry of Materials* 1996, *8*, 43-53.

[30] G.E.R.Schulze, *Zeitschrift für Physikalische Chemie* 1934, *24*, 215.

[31] a) B. Ferreira, E. Fargin, J. P. Manaud, G. Le Flem, V. Rodriguez and T. Buffeteau, *Journal of Non-Crystalline Solids* 2004, *343*, 121-130; b) A. Magistris, G. Chiodelli and M. Duclot, *Solid State Ionics* 1983, *9-10*, 611-616.

[32] B. Ewald, Y. X. Huang and R. Kniep, *Zeitschrift Fur Anorganische Und Allgemeine Chemie* 2007, *633*, 1517-1540.

[33] R. Kniep, G. Gozel, B. Eisenmann, C. Rohr, M. Asbrand and M. Kizilyalli, *Angewandte Chemie-International Edition in English* 1994, *33*, 749-751.

[34] C. H. Park and K. Bluhm, *Zeitschrift Fur Naturforschung Section B-a Journal of Chemical Sciences* 1995, *50*, 1617-1622.

[35] S. C. Sevov, *Angewandte Chemie-International Edition in English* 1996, *35*, 2630-2632.

[36] C. Hauf and R. Kniep, *Zeitschrift Fur Naturforschung Section B-a Journal of Chemical Sciences* 1997, *52*, 1432-1435.

[37] a) M.Yang, J.Yu, L.Shi, P.Chen, G.Li and R.Xu, *Chemistry of Materials* 2006, *18(2)*, 476-481; b) A.Yilmaz, X.Bu, M.Kizilyalli and G.Stucky, *Chemistry of Materials* 2000, *12(11)*, 3243-3245; c) R.Bontchev and A.Jacobson, *Materials Research Bulletin* 2002, *37(12)*, 1997-2005.

[38] M. Yang, J. H. Yu, P. Chen, J. Y. Li, Q. R. Fang and R. R. Xu, *Microporous and Mesoporous Materials* 2005, *87*, 124-132.

[39] G. Schafer, H. Borrmann and R. Kniep, *Microporous and Mesoporous Materials* 2000, *41*, 161-167.

[40] H. Y. Zhang, Z. X. Chen, L. H. Weng, Y. M. Zhou and D. Y. Zhao, *Microporous and Mesoporous Materials* 2003, *57*, 309-316.

[41] G. Alberti, M. Casciola, U. Constantino and G. Levi, *Journal of Membrane Science* 1978, *32-4*, 179-190.

[42] D. M. Poojary, B. L. Zhang and A. Clearfield, *Chemistry of Materials* 1999, *11*, 421-426.

[43] G. Alberti, U. Costantino, F. Marmottini, R. Vivani and P. Zappelli, *Angewandte Chemie-International Edition in English* 1993, *32*, 1357-1359.

[44] a) S. Drumel, P. Janvier, P. Barboux, M. Bujolidoeuff and B. Bujoli, *Inorganic Chemistry* 1995, *34*, 148-156; b) S. Drumel, P. Janvier, D. Deniaud and B. Bujoli, *Journal of the Chemical Society-Chemical Communications* 1995, 1051-1052; c) G. B. Hix, A. Turner, B. M. Kariuki, M. Tremayne and E. J. MacLean, *Journal of Materials Chemistry* 2002, *12*, 3220-3227.

[45] a) B. A. Adair, N. Guillou, M. Alvarez, G. Ferey and A. K. Cheetham, *Journal of Solid State Chemistry* 2001, *162*, 347-353; b) G. Bonavia, R. C. Haushalter, C. J. O'Connor, C. Sangregorio and J. Zubieta, *Chemical Communications* 1998, 2187-2188; c) A. Distler and S. C. Sevov, *Chemical Communications* 1998, 959-960; d) D. M. Poojary, A. Cabeza, M. A. G. Aranda, S. Bruque and A. Clearfield, *Inorganic Chemistry* 1996, *35*, 1468-1473; e) D. M. Poojary, D. Grohol and A. Clearfield, *Angewandte Chemie-International Edition in English* 1995, *34*, 1508-1510; f) D. Riou and G. Ferey, *Journal of Materials Chemistry* 1998, *8*, 2733-2735; g) D. Riou, C. Serre, J. Provost and G. Ferey, *Journal of Solid State Chemistry* 2000, *155*, 238-242; h) M. Riou-Cavellec, M. Sanselme and G. Ferey, *Journal of Materials*

Chemistry 2000, *10*, 745-748; i) M. Riou-Cavellec, M. Sanselme, M. Nogues, J. M. Greneche and G. Ferey, *Solid State Sciences* 2002, *4*, 619-625; j) V. Soghomonian, Q. Chen, R. C. Haushalter and J. Zubieta, *Angewandte Chemie-International Edition in English* 1995, *34*, 223-226; k) A. Turner, P. A. Jaffres, E. J. MacLean, D. Villemin, V. McKee and G. B. Hix, *Dalton Transactions* 2003, 1314-1319.

[46] R. LaDuca, D. Rose, J. R. D. DeBord, R. C. Haushalter, C. J. Oconnor and J. Zubieta, *Journal of Solid State Chemistry* 1996, *123*, 408-412.

[47] a) D. Riou, O. Roubeau and G. Ferey, *Microporous and Mesoporous Materials* 1998, *23*, 23-31; b) F. Serpaggi and G. Ferey, *Journal of Materials Chemistry* 1998, *8*, 2749-2755.

[48] D.Shriver, P.Atkins and C.Langford, 1994, Oxford University Press, Oxford.

[49] a) J. S. Chen, L. Li, G. D. Yang and R. R. Xu, *Journal of the Chemical Society-Chemical Communications* 1989, 1217-1218; b) G. D. Yang, L. Li, J. S. Chen and R. R. Xu, *Journal of the Chemical Society-Chemical Communications* 1989, 810-811.

[50] R. C. Haushalter, Z. W. Wang, L. M. Meyer, S. S. Dhingra, M. E. Thompson and J. Zubieta, *Chemistry of Materials* 1994, *6*, 1463-1464.

[51] a) S. Chakrabarti, M. A. Green and S. Natarajan, *Solid State Sciences* 2002, *4*, 405-412; b) S. Chakrabarti and S. Natarajan, *Angewandte Chemie-International Edition* 2002, *41*, 1224-+; c) S. B. Wiggin, R. W. Hughes, D. J. Price and M. T. Weller, *Dalton Transactions* 2007, 2935-2941.

[52] a) X. H. Bu, T. E. Gier and G. D. Stucky, *Chemical Communications* 1997, 2271-2272; b) T. R. Jensen, P. Norby, J. C. Hanson, O. Simonsen, E. M. Skou, P. C. Stein and H. A. Boye, *Journal of Materials Chemistry* 1998, *8*, 969-975; c) T. M. Nenoff, W. T. A. Harrison, T. E. Gier, J. C. Calabrese and G. D. Stucky, *Journal of Solid State Chemistry* 1993, *107*, 285-295; d) R. M. Yeates and W. T. A. Harrison, *Journal of Materials Chemistry* 2002, *12*, 1103-1106; e) S. B. Wiggin and M. T. Weller, *Chemical Communications* 2006, 1100-1102.

[53] E. Flanigen and R. Patton, *US Patent 4,073,865* 1978.

[54] J. Guth, H. Kessler, P. Caullet, J. Hazm, A. Merrouche and J. Patarin, *Proc. of the 9th Int'l Zeolite Conf. Montreal* 1993, p. 215.

[55] a) P. A. Barrett, M. A. Camblor, A. Corma, R. H. Jones and L. A. Villaescusa, *Journal of Physical Chemistry B* 1998, *102*, 4147-4155; b) M. A. Camblor, M. J. Diaz-Cabanas, J. Perez-Pariente, S. J. Teat, W. Clegg, I. J. Shannon, P. Lightfoot, P.

A. Wright and R. E. Morris, *Angewandte Chemie-International Edition* 1998, *37*, 2122-2126; c) L. A. Villaescusa, P. S. Wheatley, I. Bull, P. Lightfoot and R. E. Morris, *Journal of the American Chemical Society* 2001, *123*, 8797-8805.

[56] M. A. Camblor, L. A. Villaescusa and M. J. Diaz-Cabanas, *Topics in Catalysis* 1999, *9*, 59-76.

[57] P. Caullet, J. L. Paillaud, A. Simon-Masseron, M. Soulard and J. Patarin, *Comptes Rendus Chimie* 2005, *8*, 245-266.

[58] M. A. Camblor, A. Corma, S. Iborra, S. Miquel, J. Primo and S. Valencia, *Journal of Catalysis* 1997, *172*, 76-84.

[59] I. Bull, L. A. Villaescusa, S. J. Teat, M. A. Camblor, P. A. Wright, P. Lightfoot and R. E. Morris, *Journal of the American Chemical Society* 2000, *122*, 7128-7129.

[60] L. A. Villaescusa, P. A. Barrett and M. A. Camblor, *Angewandte Chemie-International Edition* 1999, *38*, 1997-2000.

[61] P. A. Barrett, T. Boix, M. Puche, D. H. Olson, E. Jordan, H. Koller and M. A. Camblor, *Chemical Communications* 2003, 2114-2115.

[62] A. Corma, M. Puche, F. Rey, G. Sankar and S. J. Teat, *Angewandte Chemie-International Edition* 2003, *42*, 1156-1159.

[63] A. Simmen, J. Patarin and C. Baerlocher, *Proc. 9th Int. Zeolite Conf. Montreal* 1993, p. 443.

[64] L. Schreyeck, P. Caullet, J. C. Mougenel, J. Patarin and J. L. Paillaud, *Microporous Materials* 1997, *11*, 161-169.

[65] F. Taulelle, A. Samoson, T. Loiseau and G. Ferey, *Journal of Physical Chemistry B* 1998, *102*, 8588-8598.

[66] a) S. Kallus, J. Patarin and B. Marler, *Microporous Materials* 1996, *7*, 89-95; b) A. Matijasic, J. L. Paillaud and J. Patarin, *Journal of Materials Chemistry* 2000, *10*, 1345-1351; c) P. Reinert, B. Marler and J. Patarin, *Chemical Communications* 1998, 1769-1770; d) P. Reinert, J. Patarin, T. Loiseau, G. Ferey and H. Kessler, *Microporous and Mesoporous Materials* 1998, *22*, 43-55; e) T. Wessels, L. B. McCusker, C. Baerlocher, P. Reinert and J. Patarin, *Microporous and Mesoporous Materials* 1998, *23*, 67-77.

[67] M. Estermann, L. B. McCusker, C. Baerlocher, A. Merrouche and H. Kessler, *Nature* 1991, *352*, 320-323.

[68] a) G. Ferey, T. Loiseau, P. Lacorre and F. Taulelle, *Journal of Solid State Chemistry* 1993, *105*, 179-190; b) L. Yu, W. Pang and L. Li, *Journal of Solid State Chemistry* 1990, *87*, 241-244.

[69] a) T. Loiseau and G. Ferey, *Journal of the Chemical Society-Chemical Communications* 1992, 1197-1198; b) J. L. Paillaud, B. Marler and H. Kessler, *Chemical Communications* 1996, 1293-1294.

[70] a) T. Loiseau, R. Retoux, P. Lacorre and G. Ferey, *Journal of Solid State Chemistry* 1994, *111*, 427-436; b) C. Sassoye, T. Loiseau, F. Taulelle and G. Ferey, *Chemical Communications* 2000, 943-944; c) X. T. Yin and L. F. Nazar, *Journal of the Chemical Society-Chemical Communications* 1994, 2349-2350.

[71] a) Y. L. Fu, Y. L. Liu, Z. Shi, Y. C. Zou and W. Q. Pang, *Journal of Solid State Chemistry* 2001, *162*, 96-102; b) C. Serre and G. Ferey, *Journal of Materials Chemistry* 1999, *9*, 579-584.

[72] M. Cavellec, C. Egger, J. Linares, M. Nogues, F. Varret and G. Ferey, *Journal of Solid State Chemistry* 1997, *134*, 349-355.

[73] a) E. Kemnitz, M. Wloka, S. Trojanov and A. Stiewe, *Angewandte Chemie-International Edition in English* 1996, *35*, 2677-2678; b) D. M. Poojary, B. L. Zhang and A. Clearfield, *Journal of the Chemical Society-Dalton Transactions* 1994, 2453-2456; c) M. Wloka, S. I. Troyanov and E. Kemnitz, *Journal of Solid State Chemistry* 2000, *149*, 21-27.

[74] a) X. Q. Wang, L. M. Liu, H. D. Cheng, K. Ross and A. J. Jacobson, *Journal of Materials Chemistry* 2000, *10*, 1203-1208; b) X. Q. Wang, L. M. Liu and A. J. Jacobson, *Journal of Materials Chemistry* 2002, *12*, 1824-1827.

[75] a) E. Alda, B. Bazan, J. L. Mesa, J. L. Pizarro, M. I. Arriortua and T. Rojo, *Journal of Solid State Chemistry* 2003, *173*, 101-108; b) G. Bonavia, R. C. Haushalter and J. Zubieta, *Journal of Solid State Chemistry* 1996, *126*, 292-299; c) D. Riou and G. Ferey, *Journal of Solid State Chemistry* 1994, *111*, 422-426.

[76] a) H. K. Izumi, J. E. Kirsch, C. L. Stern and K. R. Poeppelmeier, *Inorganic Chemistry* 2005, *44*, 884-895; b) J. E. Kirsch, H. K. Izumi, C. L. Stern and K. R. Poeppelmeier, *Inorganic Chemistry* 2005, *44*, 4586-4593; c) M. R. Marvel, J. Lesage, J. Baek, P. S. Halasyamani, C. L. Stern and K. R. Poeppelmeier, *Journal of the American Chemical Society* 2007, *129*, 13963-13969; d) M. E. Welk, A. J.

Norquist, C. L. Stern and K. R. Poeppelmeier, *Inorganic Chemistry* 2001, *40*, 5479-+.

Chapter Two

Experimental Techniques

2.0 Introduction

The work included in this thesis is mainly concerned with the synthesis and characterization of new inorganic framework materials. The primary synthetic technique employed in this project was the hydrothermal synthetic method, and this involves reaction mixtures heated in presence of aqueous solvent within Teflon lined autoclaves. High-temperature synthetic routes were also employed by undertaking few experiments in a platinum crucible.

A range of appropriate analytical techniques was used for the characterization of the inorganic materials prepared in this work. Single crystal X-ray diffraction was the main method of identification employed, allowing a methodical structural characterization to be performed. Powder X-ray diffraction was carried out to assess the phase purity of the products obtained. Neutron diffraction was used as a supplementary technique to locate hydrogen atoms present in the framework structure.

Thermogravimetric and differential thermal analysis were used to study the thermal behavior of selected samples. This was of particular use for frameworks consisting of lattice water molecules, ammonium cations or amine templates. Energy-dispersive X-ray spectroscopy was used for the identification of the elemental composition of the samples; particularly this was useful for samples consisting of near isoelectronic species, such as oxide and fluoride ions. Infrared spectroscopy was used to investigate the characteristic vibrational modes of the functional groups, and mainly to identify any hydroxide groups within the framework structure.

2.1 Synthetic methods

One key objective of the research included in this thesis has been to produce new inorganic framework materials using low temperature routes that favour kinetic metastable products rather than thermodynamic products, since open frameworks with high surface area and large pores are more likely to be high-energy products. Hydrothermal and solvothermal synthetic routes have demonstrated significant improvements in materials chemistry, and have been extensively used in the synthesis of a large number of functional inorganic materials, such as zeolites and related microporous and porous materials, composite materials and many inorganic compounds with special characteristics and useful properties. Another technique rarely used in this work was the flux growth method. This can be classified as a high-temperature approach, widely used for the growth of single crystals from a molten flux.

2.1.1 Hydrothermal synthesis

Hydrothermal synthesis refers to the chemical reactions conducted at elevated temperature and pressure conditions in aqueous solvent. These are typically performed in specially closed vessels; in almost all cases, synthetic reactions within this work were performed on Teflon-lined stainless steel autoclaves of internal volume of 23 mL (supplied by the Parr Instrument Company).[1] Such autoclaves can be used up to a maximum temperature of 523K (250 °C) and operating pressure of ~ 8000 kPa (1200 psig). In this work, few experiments were carried out in a custom-made high-throughput reactor system[2] (consisted of 48 PTFE inserts with a maximum volume of 300 μL), allowing a systematic study of compositional and process parameters.

Compared with ambient conditions, the properties of the aqueous solvent will be markedly changed under high temperature and pressure conditions. For instance, the ion product and vapor pressure will be rapidly increased, whereas the viscosity and the polarity of water will be decreased. As a result, the solvation ability of water can be much enhanced, allowing practically water-insoluble reagents to become more reactive.

Hydrothermal synthesis approach offers many advantages over the solid-state reaction synthesis route. The main difference between the two techniques is based on the reactivity. Synthesis under hydrothermal conditions offers increased mobility of the reagents in the liquid phase, whereas the solid-state synthesis requires quite high temperatures to overcome difficulties associated with lack of ion mobility in order to achieve transportation of the reactants to the sites of the reactions. Another benefit of the greater ion mobility is that perfect and large single crystals may normally be formed, suitable for further diffraction analysis, than the microcrystalline powders typically obtained from solid state reactions. A wide range of new compounds which would be difficult to obtain *via* solid state methods have been successfully prepared using hydrothermal methods. More importantly, inorganic materials with special structures and properties such as high surface area or large pore size can usually be formed, since metastable kinetic products are generally favored under hydrothermal conditions.

The technique is not necessarily limited to chemical reactions conducted in the presence of water. A large number of organic solvents which have different properties can also be used in the system, giving rise to the synthesis and preparation of new compounds such as products whose precursors may be sensitive to water. In recent years, there has been a trend towards the mixed-solvent systems. The use of mixed aqueous-organic solvents offers the potential of new crystalline materials. It appears that the properties of reaction media can strongly affect the solubility of the reactants as well as the diffusion and the crystallization processes.

Hydrothermal and solvothermal synthesis reactions do show several problems, the foremost of which is the lack of a comprehensive understanding of any mechanistic step. Reactions take place in a closed system and thus many factors can affect the synthesis process. Factors such as the time and temperature of the reaction, the pH and concentration of source materials might all play significant roles in the process. In addition, as the pressure is generated by the reaction mixture, the degree of filling will also be significant. In many cases, one factor might influence other factors, and there it becomes very difficult to investigate the affect of each factor on the chemical reaction. The lack of any mechanistic information cannot elucidate this further, and only trial and error experiments can be alternatively considered.

2.1.2 Flux growth

Flux growth technique was rarely used in this project. The technique can be categorized as a high-temperature solution method, most commonly used to produce single crystals by the slow cooling process of a liquid flux. A typical flux-growth experiment is started by the thorough grinding of material sources in a pestle and mortar in order to obtain a well homogenized mixture; this is then transferred into a crucible and heated to a temperature at which one or more of the reagents melt. Reactions within this work took place in a platinum crucible which is usually preferred because it is chemically inert and has a high melting point. Crystals can be naturally formed during the slow cooling process. The temperature is decreased to a sufficient step so as to allow for crystal nucleation to be occurred. Once the nucleation stage has begun, the crystal growth can then proceed. The latter depends on the level of supersaturation which can be controlled by the cooling rate. A relatively low cooling rate and thus a low degree of supersaturation generally cause a slow crystal growth.

2.2 X-ray diffraction

Single crystal X-ray diffraction was the primary technique used in characterizing the inorganic materials obtained in this work. Powder diffraction was carried out to further verify the phase purity of the products.

2.2.1 Diffraction theory

Few years after the discovery of X rays by Wilhelm Rontgen in 1895, Max von Laue was the first to demonstrate that crystals can be used as natural diffraction gratings for X- rays.[3] Taking into account the wave nature of X-rays, it was proven that X-rays have a wavelength of the same order of magnitude as the interatomic distances in crystals (d ~ 1 Å). Crystals were able to reflect the incoming X-ray beam only at certain allowed directions, like the diffraction gratings for the visible light.

Crystals can be regarded as solids consisting of atoms arranged in a three-dimensional periodic pattern. The simplest unit of a crystalline structure that translates itself in three dimensions is referred to as the unit cell, and is defined by the three side lengths a, b and c, and the angles between adjacent sides α, β, and γ. Symmetry operations may take place, thus similarly to finite molecules crystals frequently possess a combination of symmetry elements, leading to the seven crystal systems shown in Table 2.1. These can be divided further into fourteen Bravais lattices, resulting from the combinations of the crystal system and the lattice type. The latter includes four distinct types. The simplest type is the primitive (P) which has lattice points in all of the corners of the unit cell, the second type is known as body centered (I) and involves the addition of a lattice point at the cell centre, and finally in the remaining two types the lattice points are located at the centre of all the unit cell faces (F) or selectively at one of the faces (A, B or C). As can be depicted in Table 2.1, in case of the triclinic system there are no symmetry restrictions and therefore a primitive cell can always be selected, leading to two triclinic classes P1 and $P\bar{1}$ with the main difference being the presence of a centre of symmetry. Looking at the other crystal systems, it would appear that body- or face-centered cells are frequently chosen, giving a total of thirty-two crystal classes that eventually leads to a list of 230 space groups when taking into account the translational symmetry elements.

Table 2.1: The seven crystal systems and the Bravais lattices.[4]

Crystal class	Unit cell dimensions	Point group	Bravais lattices
Cubic	a = b = c $\alpha = \beta = \gamma = 90^\circ$	23, $m3$, 432, $\bar{4}3m$, $m3m$	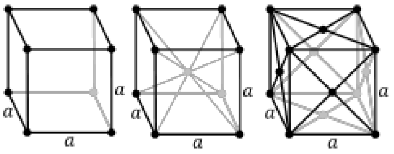
Tetragonal	a = b ≠ c $\alpha = \beta = \gamma = 90$ °	4, $\bar{4}$, $4/m$, 422, $4mm$, $\bar{4}2m$, $4/mmm$	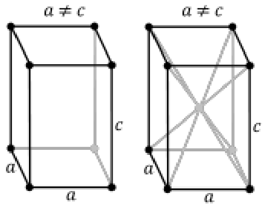
Orthorhombic	a ≠ b ≠ c $\alpha = \beta = \gamma = 90^\circ$	222, $mm2$, mmm	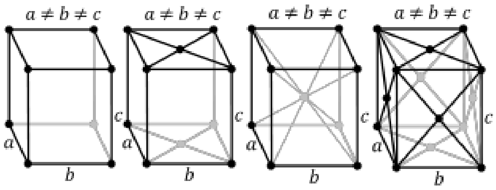
Monoclinic	a ≠ b ≠ c $\alpha = \gamma = 90^\circ$ $\beta \neq 90^\circ$	2, m, $2/m$	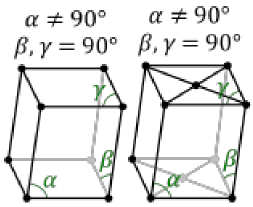
Triclinic	a ≠ b ≠ c $\alpha \neq \beta \neq \gamma \neq 90^\circ$	1, $\bar{1}$	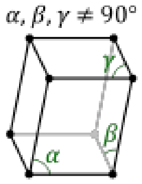
Hexagonal	a = b ≠ c $\alpha = \beta = 90^\circ$ $\gamma = 120^\circ$	6, $\bar{6}$, $6/m$, 622, $6mm$, $\bar{6}m2$, $6/mmm$	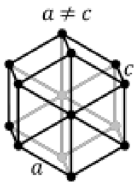
Trigonal/ Rhombohedral	a = b = c $\alpha = \beta = \gamma \neq 90^\circ$	3, $\bar{3}$, 32, $3m$, $\bar{3}m$	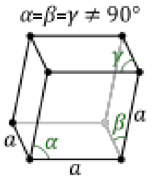

The periodic arrangement of lattice points in a crystalline structure allows one to assume the existence of parallel and regularly spaced planes of atoms, where each plane represents a layer of atoms and each parallel set shows the stacking of these layers. Lattice planes intercept the unit cell axes in fractional parts and the reciprocals of these constitute the Miller indices, which are given the symbols h, k, l. Each atom of the same set of lattice planes acts as a point scatterer. The incoming coherent beam of X-rays interacts with the electron density present in atoms; this will cause excitement of electrons to a higher energy level where then atoms can emit X-rays in all directions. Interference can occur between scattered rays, resulting in observed intensities at maxima and minima.

Constructive interference will only occur if the difference in path lengths is equal to an integral number of wavelengths, and this is known as the Bragg's Law.[5] Figure 2.1 illustrates the X-ray scattering by a set of parallel lattice planes. The incoming beam of X-rays strikes the atomic planes at an angle θ where then is reflected at the same angle θ, as typically occurs in an optical reflection. The reflected waves from different points of a parallel set will be in phase only if the path difference AB+BC is equal to a whole number of wavelengths. This can be expressed by the following equation: $2d_{hkl}.\sin\theta = n\lambda$, where d_{hkl} is known as the d-spacing between adjacent planes of a parallel set and n is an integer which can always be taken as unity.

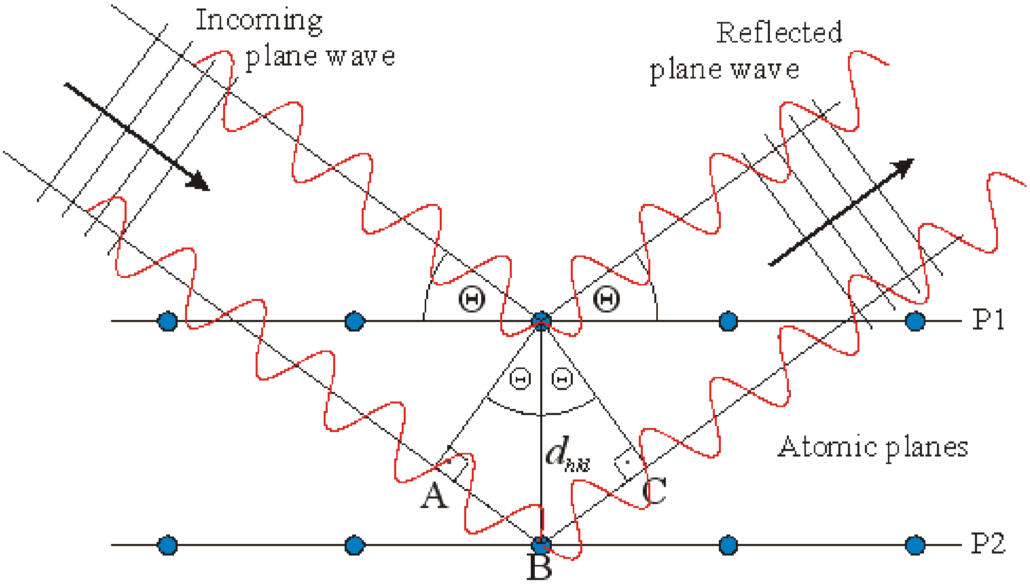

Figure 2.1: Schematic representation of Bragg's Law.[6]

The unit cell of a crystalline structure can be determined from a set of diffraction maxima in the X-ray diffraction pattern. Using the Bragg equation, the diffraction angles θ of various reflections can give the d-spacing. The unit cell parameters can then be deduced from the equations given in Table 2.2, which represent the relationship between the d_{hkl}, the lattice parameters and the Miller indices for each crystal system. In order to determine the Bravais lattice, the systematic absences of reflections must be encountered. These generally occur because each lattice type may impose restrictions on reflections of a certain type. For example, a face centered lattice will have reflections corresponding to indices which are all even or all odd integers, and thus planes such as (210) or (221) will be absent from the diffraction pattern. Consequently, a number of possible space groups can readily be obtained. However, much more information is required to determine the entire crystal structure. The intensities of the Bragg reflections can help to decrease this choice further.

Table 2.2: Equations for d_{hkl} for the seven crystal systems.

Crystal system	Equation for d_{hkl}
Cubic	$\frac{1}{d^2} = \frac{h^2 + k^2 + l^2}{a^2}$
Tetragonal	$\frac{1}{d^2} = \frac{h^2 + k^2}{a^2} + \frac{l^2}{c^2}$
Orthorhombic	$\frac{1}{d^2} = \frac{h^2}{a^2} + \frac{k^2}{b^2} + \frac{l^2}{c^2}$
Monoclinic	$\frac{1}{d^2} = \frac{1}{sin^2\theta}\left(\frac{h^2}{a^2} + \frac{k^2 sin^2\theta}{b^2} + \frac{l^2}{c^2} - \frac{2hlcos\beta}{ac}\right)$
Triclinic	Complex expression
Hexagonal and Rhombohedral	$\frac{1}{d^2} = \frac{4}{3}\left(\frac{h^2 + hk + k^2}{a^2}\right) + \frac{l^2}{c^2}$

The intensities of the X-ray beams reflected from the lattice planes can be obtained by measuring the densities of the diffraction spots from photographic films or either using a detector. The occurrence of diffraction spots in a typical experiment can be explained by means of the Ewald's sphere. As can be depicted in the Figure 2.2, the crystal resides at the center of the sphere of radius 1/λ. The incoming beam is incident on the crystal, where the unaffected beam cuts off the surface of the sphere at the lattice point 000. Further diffraction effects from various lattice planes will produce more reciprocal lattice points; of these, some will lie on the Ewald's sphere and will have a distance from the 000 lattice point equal to $1/d_{hkl}$. By rotating the crystal, more lattice points will then be shifted into the surface of the sphere, allowing a fully characterization of the crystalline structure. The intensities of the diffraction spots mainly depend on the atomic scattering factors of all the atoms in the unit cell which are related to the electron densities. These can also be affected by the crystal size and the thermal vibration effect, as well as by the phase factor. The latter results from the different period of time that X-rays will take to scatter from different lattice planes.

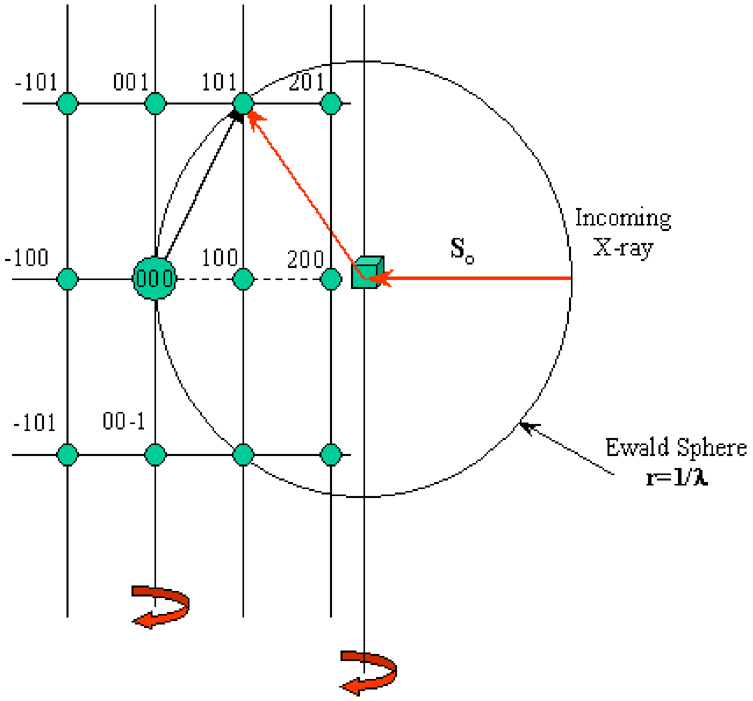

Figure 2.2: Representation of the Ewald sphere showing how the reciprocal lattice points can intercept the surface of this sphere by rotating the crystal.[7]

All the atomic scattering factors can be combined to compute the structure factor F_{hkl} (given in Equation 2.1). When the structure factor and the phases of the reflections are known, the electron density distribution in the unit cell can be estimated by means of Equation (2.2) and so the atomic positions can be determined. The problem occurs as the intensity of the reflected beam is proportional to the square of the structure factor, $I_{hkl} \propto F_{hkl}^2$, and thus the structure factor may take positive or negative values. This is known as the phase problem in the field of crystallography.

$$F_{hkl} = \sum_n f_n \exp\,[2\pi i(hx_n + ky_n + lz_n\,] \qquad (2.1)$$

$$\rho(xyz) = \sum_h \sum_k \sum_l |F_{hkl}| cos[2\pi(hx + ky + lz) - \alpha_{hkl}] \qquad (2.2)$$

It might seem possible to overcome the phase problem by using Direct or Patterson methods to solve the structure. Direct methods involve trial-and-error solutions by evaluating the Fourier transform of the diffraction pattern for all possible combinations of signs. The concept is based on the fact that the electron density cannot take negative values, and therefore the sum of waves must produce only positive regions and cancel out the negative ones. Once the approximate reflection phases are obtained, the refinement can then proceed, allowing determination of atomic positions.

The Patterson method is known as the heavy-atom method since it becomes more effective in structures consisting of atoms of large atomic numbers. It involves the Fourier transform of the measured intensities by using values of F_{hkl}^2 as coefficients in order to derive a Patterson map. This represents a map of vectors between pairs of atoms, rather than the actual atoms. Every peak is proportional to the electron density present in atoms, and therefore pairs consisting of heavy atoms can be easily distinguished. Once the heaviest atoms are located, a partial structure factor can then be calculated. Using the phases obtained from the F_{hkl}^{heavy} values, the electron density map is obtained where the light atom positions can be found.

Atomic positions are normally optimized by the least-squares refinement which automatically adjusts the atomic coordinates so as to minimize the function, where w_{hkl} is the weight for the F_{hkl} values:

$$D = \sum_{hkl} w_{hkl} \left(|F^{o}_{hkl}| - |F^{c}_{hkl}|\right)^2 \tag{2.3}$$

The accuracy of the model can be measured in terms of the residual factor (R-factor) or the weighted R-factor given in Equations 2.4 and 2.5, respectively. This involves a measure of the level of discrepancy between the observed (F_o) and calculated structure factors (F_c). A correct structure should show good agreement, indicated by an R value below 0.10.

$$R = \frac{\sum\big||F_o| - |F_c|\big|}{\sum|F_o|} \times 100\% \tag{2.4}$$

$$R_W = \frac{\sum w_{hkl}\big||F_o| - |F_c|\big|}{\sum w_{hkl}|F_o|} \times 100\%$$

2.2.2 Single crystal X-ray diffraction

The University of Southampton operates two Bruker-Nonius Kappa CCD diffractometers. Both instruments run from a single Bruker-Nonius FR591 rotating anode X-ray generator with a molybdenum target (λ = 0.71703 Å). One diffractometer has a graphite monochromator and an automatic sample changing robot, whereas the other has a confocal focusing mirror instead. The latter allows a much greater flux (about six times greater) and thus data collection time may become shorter, but large crystals cannot be collected with the more focused beam. Both devices have low and high temperature capabilities in the range of 80-500 K, using a pair of Oxford cryostreams. In a typical diffraction experiment, diffraction data is collected using a 95 mm CCD camera. The crystal is normally mounted on a glass fibre attached in a brass pip using amorphous silicon grease, before being placed in the goniometer.

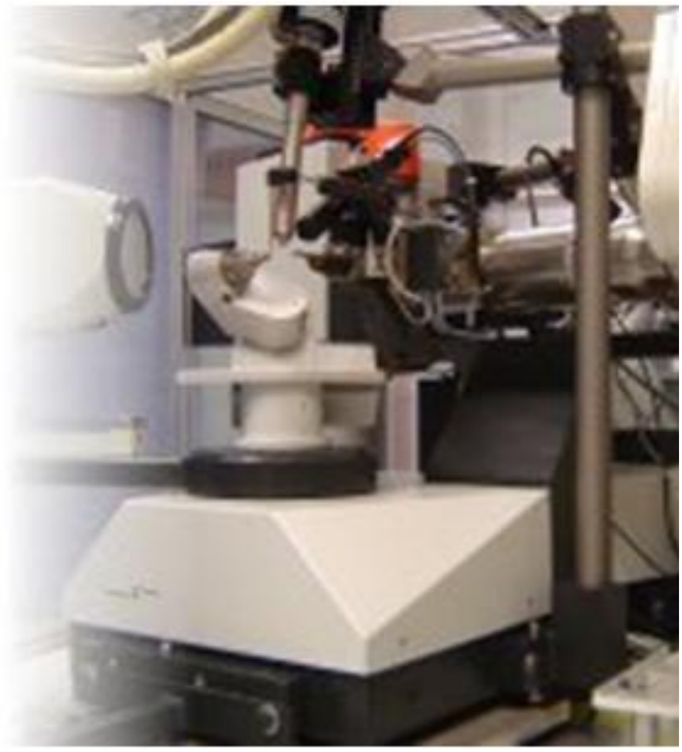

Figure 2.3: Photograph of a Bruker-Nonius Kappa CCD. The CCD detector is to the left of the picture; the goniometer is at the centre surrounded by the positioning camera and the cryostream. The rotating anode X-ray source assembly is shown on the right.[8]

For a typical collection procedure, a quick scan (approximately 10-20 sec) is initially set up to check the quality of the diffraction pattern. Lack of diffraction spots within the pattern implies that the sample is amorphous, whereas rings of density indicate that the sample consists of a crystalline powder rather than a single crystal; the presence of blurred or doubled diffraction spots may be attributed to twinned crystals. Once, a good quality crystal sample is selected, a series of eight phi/chi scans is made to identify the unit cell. Using the program DirAx,[9] a list of possible unit cell is obtained with an indication of how well these models fit with the collected data. A comparison of the given unit cell with the database of known cells[10] is suggested before data collection begins. Data collection can be achieved by using the software package COLLECT[11] which automatically calculates the number of frames required and suggests a data collection time. During the collection procedure, this program attempts to obtain 100% data completeness with further redundancies, giving rise to a greater level of statistical accuracy to the results. Once the collection is completed, absorption corrections can then be applied to the data using the SORTAV[12] system. This program is responsible for measuring the amount of X-ray absorption undergone by the crystal using the information, given by the user, about the crystal size and composition. If there is no available information about the composition, the absorption correction can be quite approximate. Data analysis carried out to determine the crystal structures presented in this thesis by using the WinGX set of packages[13] (version 1.70.01) including XPREP[14] and SHELX-97[15].

2.2.3 Powder X-ray diffraction

The fundamental principles of the powder X-ray diffraction are the same as single crystal diffraction. The powder diffraction technique relies on a monochromatic X-ray beam striking the sample. Powders are polycrystalline samples consisting of many small and randomly oriented crystallites. With random orientations one might expect different atomic planes within the grains; many of these will be oriented in such a way as to satisfy the Bragg's Law, giving rise to various diffraction cones. Each cone can be described as a ring made up from small spaced dots which represent the diffraction maxima from the single crystallites. The conical angle is equal to the Bragg 2θ angle and this can be measured by using a photographic film or an X-ray detector.

The University of Southampton operates two powder diffractometers, the Siemens D5000 and Bruker D8. Both instruments use a copper source and a Ge(111) single crystal monochromator to generate the monochromatic beam with a wavelength of $\lambda = 1.54056$ Å. The incident radiation is collimated through aperture slits before interaction with the sample which is normally mounted in an alumina or a plastic sample holder. The sample rotates at a constant angular velocity, and the detector correspondingly rotates with the sample at precisely double the given angular velocity in such a way as the diffraction angle to be always fixed at 2θ and the glancing angle at θ. The schematic diagram of the D5000 diffractometer is illustrated in Figure 2.4.

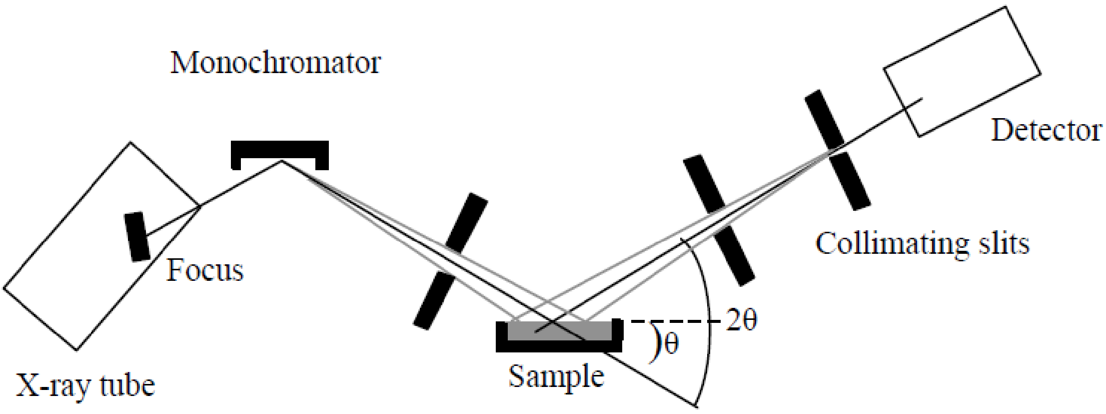

Figure 2.4: Schematic diagram of D5000 diffractometer.

A further application of the powder X-ray diffraction is the variable temperature diffraction. This can be set up only at the Bruker D8 diffractometer which has a fitted Paar HTK-1200 furnace stage, allowing diffraction to be occurred at temperatures up to 1200 °C. The furnace contains a sealed sample chamber which can be placed under vacuum. During the experiment, the incoming and diffracted beams are passing through Kapton polymide windows which exhibit low X-ray absorption and scattering capabilities. The 2θ range and the temperature range as well as the diffraction time can be set up by the user via the PC which is connected to the device.

2.3 Thermal analysis

In the course of this work, samples were investigated using a Polymer Laboratories STA 1500 simultaneous thermal analysis system. This is capable of performing thermogravimetric analysis (TGA) and differential thermal analysis (DTA) measurements in order to determine the weight- and temperature-changes that may occur as the sample is heated at a specific temperature range.

In a typical experiment, approximately 10 mg of sample were placed on a crucible which was then transferred on the furnace equipment and allowed to be heated to 800 °C at a rate of 10 °C/min. The mass loss of the sample was recorded as a function of the temperature. This can provide information about the composition and thermal stability of the sample; dehydration and decomposition processes can be indicated. The DTA analysis involved heating the sample against an inert reference such as alumina and measuring the temperature difference between the two samples. This can be recorded as either change in temperature or change in energy against time.

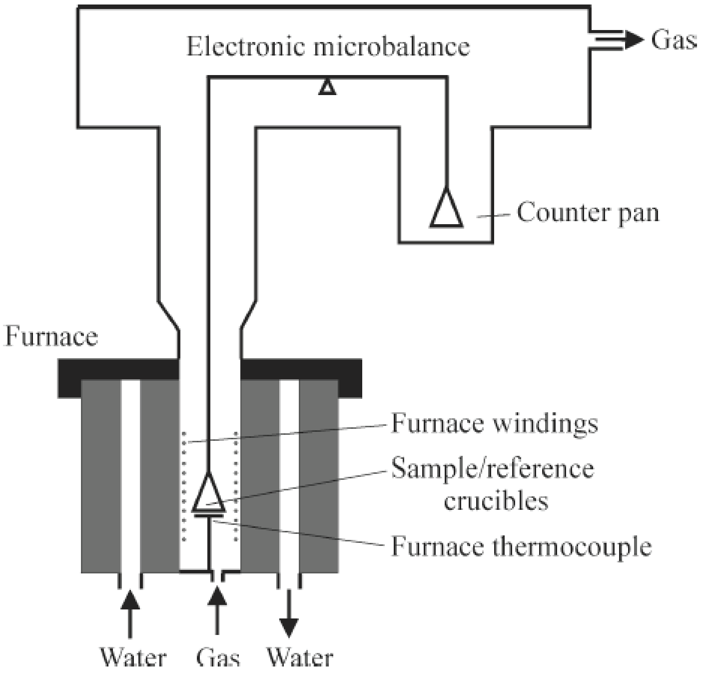

Figure 2.5: Schematic diagram of STA 1500-TGA/DTA equipment.

DTA analysis provides information about thermal events such as phase changes, or decomposition of the compound. For example, the compound under study would show temperature increase if an endothermic process occurred and temperature decrease in presence of an exothermic process. It is suggested to record both TGA and DTA analysis simultaneously. This can be useful in identifying whether the thermal events are accompanied with a change in sample mass, and especially in cases of the phase changes that do not involve weight loss and thus they cannot be observed by TGA analysis.

Inorganic framework materials with large surface areas are more likely to be metastable products, and one might expect the framework structure to collapse or transform into another structure type instead of decomposing at quite high temperatures. For framework structures that can be suitable for ion exchange or catalytic applications, the template must be removed; ideally, organic-amine templates would be decomposed at high temperatures without the collapse of the framework.

2.4 Energy dispersive analysis-Scanning electron microscopy

Energy-dispersive X-ray spectroscopy is an analytical method that is used for the identification of the elemental composition of a sample. It relies on the examination of a sample through interactions between a high-energy beam of electrons and the sample being studied. During this operation, an electron beam generated by high voltage is targeted at the sample. This will cause excitement of an electron from an inner shell to a higher energy level, leaving an electron hole. An electron from an outer shell may then be released to the position just vacated, and the energy difference emitted would be in the form of an X-ray photon. The characteristic X-rays emitted from the sample can be used to identify and determine the different elements present in the sample.

Scanning electron microscopy involves scanning over the surface of the sample with the primary electron beam. Different signals can normally be obtained, and these carry information about the morphology, the surface appearance as well as the chemical composition of the sample under study. The most common types of signal produced by SEM analysis are the secondary and back-scattered electrons. The former refers to the low-energy beam of electrons which is produced when the primary electron beam interacts with electrons of atoms located at the surface of the sample, whereas the latter includes the electrons generated by the elastic scattering of the incident primary beam. Images of the sample surface can be obtained from analysis of the secondary electrons, thereby allowing topographic information of the sample. Signals of back-scatter electrons are characteristic of the atomic number and therefore they can be used to determine the chemical composition of the sample.

Scanning electron microscopy (SEM) and energy dispersive X-ray Spectroscopy (EDS) were combined together to investigate the elemental content of the samples produced within this work, as well as to study their morphology. Experiments were performed on a JOEL JSM-5910 Scanning Electron Microscope which has a fitted Oxford Instruments Inca Energy 300 Energy-Dispersive X-ray Spectroscopy analysis system.

2.5 Infrared spectroscopy

Infrared spectroscopy was performed on all samples to identify and determine structural informations, mainly concerning water molecules or hydroxide groups and organic templates within the framework structure. The instrument used in this work was a Perkin-Elmer Spectrum one, and this is capable of collecting data in either transmission or reflection mode. Samples were prepared by pressing a small quantity of the powdered material with potassium bromide into translucent dicks. Infrared spectra were collected in the transmission mode between 4000-450 cm^{-1}.

The fundamental principle of the technique relies on the ability of molecules to absorb radiation at specific frequencies that are characteristic of their functional groups present within the framework structure. In particular, each bond in a molecule vibrates always at a specific frequency, and this depends upon the vibrating masses and the strength of the bond between them. When an incoming beam of infrared light strikes the sample this will absorb at these frequencies that match with the vibrational frequencies of all the bonds. The transmitted ray shows information about the absorbed energy at each value of wavelength. The percent transmittance (%T) is plotted against the wavelength ($\bar{v}$) at which specific molecular vibrations occur, allowing identification of the types of functional groups present in the sample.

2.6 References

[1] Parr Instrument Company, 211 Fifty Third Street, Moline, Illinois 61265-9984 USA.

[2] N. Stock and T. Bein, *Angewandte Chemie-International Edition* 2004, *43*, 749-752.

[3] Max Von Laue, *Nobel Lecture* November 12, 1915.

[4] Original drawing from: http://en.wikipedia.org/wiki/Crystal_system.

[5] W. L. Bragg, *Proceedings of the Cambridge Philosophical Society* 1913, *17*, 43-57.

[6] Original drawing from: http://www.xenocs.com/technology-braggs-law-and-multilayer-reflection.htm.

[7] Original drawing from: http://chemistry.bd.psu.edu/jircitano/ewald.html.

[8] Original drawing from: http://www.southampton.ac.uk/xray/instrument/kappaccd.html.

[9] a) A. J. M. Duisenberg, *Journal of Applied Crystallography* 1992, *25*, 92-96; b) A. J. M. Duisenberg, R. W. W. Hooft, A. M. M. Schreurs and J. Kroon, *Journal of Applied Crystallography* 2000, *33*, 893-898.

[10] D. A. Fletcher, R. F. McMeeking and D. Parkin, *Journal of Chemical Information and Computer Sciences* 1996, *36*, 746-749.

[11] R.Hooft, *COLLECT data collection software* 1998, Nonius B.V.

[12] R. H. Blessing, *Acta Crystallographica Section A* 1995, *51*, 33-38.

[13] L.J. Farrugia, *Journal of Applied Crystallography* 1999, *32(4)*, 837-838.

[14] XPREP Bruker AXS Inc., Madison, Wisconsin, USA.

[15] G.Sheldrick, SHELX-97 [Includes SHELXS97, SHELXL97], Programs for Crystal Structure Analysis (Release 97-2), 1997 University of Cottingen, Cottingen, Germany.

Chapter Three

Molybdenum Phosphates

3.0 Molybdenum phosphate materials

Following the successful incorporation of transition metals into the zeolitic AlPOs and GaPOs, recent research has explored new phosphate based frameworks that also contain in their structures transition metal based oxopolyhedra. The presence of such metals gives additional structure motifs beyond tetrahedral co-ordination, such as trigonal bipyramidally, square pyramidally or octahedrally coordinated metal atoms. Molybdenum has been a particularly attractive target for such frameworks because of its ability to adopt many different oxidation states and coordination geometries. Since the discovery of $MoOPO_4$ by Kierkegaard and Westerlund,[1] a number of molybdenum phosphates have been synthesised using both high-temperature solid state reactions (often with charge balancing by extra-framework inorganic cations) and hydrothermal techniques (using large removable organic cations as templates). Examples include compounds with infinite chains,[2] layers[3] and tunnel structures[4] as well as three dimensional frameworks with significant internal micropore volume.[3c, 5]

Research included in this chapter has mainly focussed on investigating new aspects of the molybdenum phosphate based compounds. Initial synthetic work was directed towards the investigations of incorporating boron into the $MoPO_4$ frameworks, thus one might expect that boron would offer the potential of structural diversity in the framework resulting from its multi co-ordinate linking ability. A series of hydrothermal reactions involving molybdenum, phosphate and borate reagents with a variety of templating agents were carried out. It appears as incorporation of boron into the framework was unsuccessful, however the system yielded a number of molybdenum phosphate compounds whose particular structural features are discussed here. These include a new layer structure type that also has perpendicular channels through the molybdenophosphate sheets wherein multiple guest ions are hosted (detailed in Section 3.1), and four organically templated structures that comprise previously reported molybdenum phosphate polyanions (detailed in Section 3.2).

Investigations were then concentrated on preparing molybdenum phosphate compounds *via* high temperature flux-growth methods. This approach has led to the discovery of a new rubidium templated compound (detailed in Section 3.3). Finally, research reported here has aimed at investigating the formation of molybdenum containing frameworks where both the anionic units, PO_4^{3-} and F^-, have been used together to link molybdenum metal centres. A synthesis including the templating agent piperazine yielded a new oxyfluorinated molybdenum phosphate, and this is detailed in Section 3.4.

3.1 $[NH_4]_{12}[(MoO_2)_2O(HPO_4)_2]_4[PO_4]X$, ($X$ = Cl, Br)

In the course of the investigation of molybdenum borophosphate framework materials, new porous layer molybdenophosphates with embedded multiple anionic and cationic guests have been successfully obtained. They are constructed from molybdenophosphate layers of unique topology that are penetrated by channels containing perfectly ordered, alternating ammonium cations and free orthophosphate $(PO_4)^{3-}$ or halide (Cl^-, Br^-) anions. Further investigations of possible functionality of these compounds through anion exchange reactions have shown the Br-analogue to act as an anion-exchanger.

3.1.1 Experimental

I. Synthesis

- ✓ Synthesis of $[NH_4]_{12}[(MoO_2)_2O(HPO_4)_2]_4[PO_4]Cl$ (1)

The title compound was prepared from a mixture of $Na_2MoO_4.2H_2O$ (1.210 g, 5 mmol), $(NH_4)H_2PO_4$ (3.451 g, 30 mmol), H_3BO_3 (1.850 g, 30 mmol), NH_4Cl (1.337 g, 25 mmol) and distilled water (3 mL) in a molar ratio of 1:6:6:5:33. The reaction mixture (having a final pH ~ 4) was first stirred to homogeneity and then transferred to a 23 mL Teflon lined steel autoclave and heated under autogenous pressure for four days at 140 °C. Once cool the product was filtered, washed with distilled water and air dried. The product consisted of colourless crystals and microcrystalline powder of the new compound.

- ✓ Synthetic plans aimed at exchanging the anionic/cationic guest species

Initial reactions involved reproduction of the synthesis of compound (1) but using NH_4Br (2.449 g, 25 mmol) or K^+ sources [KH_2PO_4 (4.083 g, 30 mmol) and KCl (1.864 g, 25 mmol)], in an effort to synthesise the analogous bromide or potassium compounds respectively. Further reactions focussed on anion exchange reactions that entailed dispersion of X-phase powder (0.2 g) into concentrated solutions of NH_4X' (the concentration of the solution was varied from 1M to 5M) with stirring at room temperature (where X, X' = Cl^- or Br^-). Ion-exchange reactions, in the absence of water, were finally carried out and entailed well mixing of X-phase powder (0.25 g) with the NH_4*X'* (0.5 g) in a pestle and mortar before being placed in a 23 mL Teflon lined steel autoclave and heated to 448 K for 6 hours.

II. Characterization

- ✓ X-ray diffraction studies

Single crystal X-ray diffraction data for each crystal structure were collected on a Bruker Nonius KappaCCD diffractometer (Mo Kα radiation, $\lambda = 0.71073$ Å) at 120 K. Refinements of the structures were carried out using the WinGX system and SHELX-97 (by following direct methods).

- ✓ Neutron diffraction

Powder neutron diffraction data were obtained using the D20 instrument at ILL, Grenoble, France over a period of 3 hours. A joint refinement combining these data together with the single crystal X-ray diffraction data was performed using the GSAS suite with EXPGUI graphical interface.

- ✓ Thermogravimetric (TGA) analysis

TGA and DTA data were collected on a Polymer Laboratories STA 1500 system. Samples (mass ~ 10 mg) were heated in flowing air from room temperature to 600 °C at a range of 10° C min^{-1}. Weight loss and heat flow were recorded as a function of temperature.

- ✓ Infra-red (IR) analysis

Samples were first mixed with KBr and then pressed into thin pellets. IR spectra were collected using a Perkin Elmer Spectrum system over the range 4000-500 cm^{-1}.

- ✓ Electron microscopy

Energy-dispersive X-ray spectroscopy and Scanning electron microscopy studies completed on a JOEL JSM-5910 SEM fitted with an Oxford Inca 300 energy dispersive X-ray spectroscopy analysis system.

- ✓ Bond Valence calculations

Bond valence calculations were completed at each atom site using the equation below. The theory behind the equation refers to the valence sum rule for which the valence (V) of each atom must be equal to the sum of its individual bond valences (V_i). The corresponding (V_i) values were calculated using the experimental bond lengths (R) and (R_0, b) parameters from the Tables compiled by Brown and Altermatt.[6]

$$V = \Sigma\,(V_i),\ \text{where}\ V_i = \exp\,[(R_0-R)/b]$$

3.1.2 Results and discussion

I. Characterization of $[NH_4]_{12}[(MoO_2)_2O(HPO_4)_2]_4[PO_4]Cl$ (1)

Compound (1) crystallised from reactions that were targeted at synthesizing molybdenum borophosphate framework structures in presence of NH_4^+ template. However, single crystal X-ray crystal analysis of the crystalline phase revealed a structure that lacks borate moieties but is rather constructed from molybdenophosphate layers of unique topology with embedded multiple anionic and cationic guests. Crystal and diffraction data are given in Table 3.1.

The slightly undulating $[(MoO_2)O(HPO_4)_2]_\infty$ layers run along the *c* axis, showing an ABAB stacking type. This stacking arrangement produces two types of interlayer space with walls formed either from just molybdenyl $(MoO_2)O_4$ octahedra or solely hydrogenphosphate HPO_4 groups. As can be seen in Figure 3.1, this arrangement produces two different interlayer fillings; one, separating the molybdenyl $(MoO_2)O_4$ layers, consisting of ammonium cations, while between the hydrogenphosphate layers is an ordered arrangement of free phosphate tetrahedra, chloride anions and ammonium cations.

The molybdenophosphate layers are constructed from previously unknown tetrameric units built up from Mo_2O_{11} binuclear units capped on both sides by HPO_4 groups. As shown in Figure 3.2, each octahedral MoO_6 unit share one corner with the crystallographically equivalent octahedron and three corners with different phosphate groups, whilst two apices are terminal oxo groups. The two crystallographically independent Mo atoms (Mo1, Mo2) show interactions with oxygen comparable to those reported in other Mo(VI) phosphates. They exhibit the classic distorted octahedral geometry with two adjacent short Mo-O distances (1.707(4)-1.799(4) Å) forming a molybdenyl group, with opposite longer Mo-O bonds (2.125(4)-2.197(4) Å) and two additional bonds of intermediate length (1.916(13)-2.021(4) Å).

The HPO_4 tetrahedra show three P-O bonds in the range 1.514(3)-1.538(4) Å and one slightly longer P-O distance (~ 1.56 Å) that constitutes a P-OH bond. All the bond lengths and bond valence calculations are given in Table 3.2. All non-hydrogen positions were located and refined with anisotropic atomic displacement parameters using the SXD data. The hydrogen atoms attached to the molybdenophosphate layers and some ammonium hydrogen atoms were also located with these data. The majority of the remaining hydrogen atom positions were located in the joint refinement.

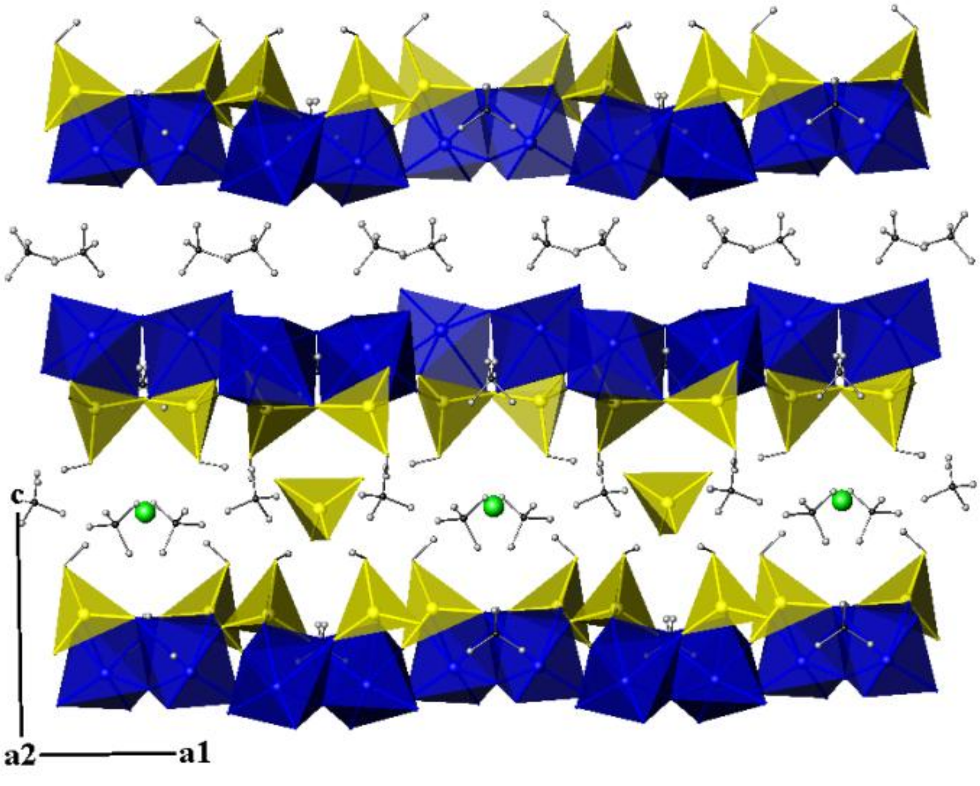

Figure 3.1: A perspective view of the structure of compound (1) showing the ABAB stacking type. Blue polyhedra represent the molybdenum octahedra and yellow polyhedra show the phosphate. Nitrogen atoms: small black spheres, hydrogen atoms: small grey spheres and chloride anions: medium green spheres.

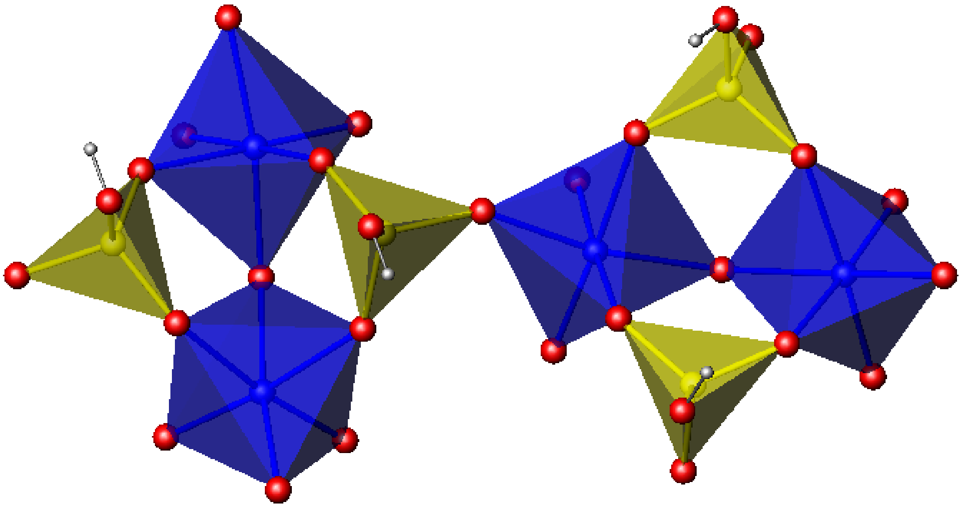

Figure 3.2: The two topologically similar tetrameric secondary building units found in compound (1).

Table 3.1: Crystal and diffraction information for compound (1).

Empirical formula	$H_{56}N_{12}Mo_8P_9Cl_1O_{56}$
Formula weight	2202.27
Temperature (K)	120(2)
Appearance	colourless plate
Wavelength	0.71073 Å (Mo K_{α})
Crystal system	Tetragonal
Space group	$P\bar{4}$
Unit cell dimensions	a = 9.7148(1) Å, c =14.5615(3) Å
Volume	1374.28 (3) $Å^3$
Z	1
D_c (g.cm^{-3})	2.661
Θ range for data collection	3.28°-27.49°
Reflections collected	10374
Independent reflections	3113
Data/Restraints/Parameters	3113/26/239
R indices	R_1 = 0.0265 wR_2 = 0.0633

A further unique structural feature is the tunnels running along the direction perpendicular to the $[(MoO_2)O(HPO_4)_2]_\infty$ layers (shown in Figure 3.3). These channels are filled in a remarkable complex, self-assembled manner, showing two perfectly ordered channel types distinguished by their content. Both channels contain ammonium cations NH_4^+, but one channel type is additionally filled by isolated PO_4^{3-} groups while the other type hosts only chloride anions. Within their particular channels the chloride and phosphate units alternate with ammonium cations along the direction of the channel.

In the mixed anion/cation interlayer region a simple two dimensional sheet (shown in Figure 3.4), of stoichiometry $[(NH_4)_4ClPO_4]$ and overall neutral charge, exists. The PO_4^{3-} groups and chloride anions are centred with respect to the channel axis. The isolated phosphate group is an almost regular tetrahedron with equal P-O distances (1.528(4) Å) and O-P-O angles between 108.5(4)° and 111.5(4)°. This isolated phosphate tetrahedron is located only in the hydrogenphosphate-lined channels/interlayer spaces, where hydrogen bonds exist between the framework attached hydrogen atoms and the free phosphate anions and therefore provide stabilization of this usual tri-negative anion (Figure 3.5a). The structure also exhibits a complex network of H-bonding in which the ammonium cations are involved. The hydrogen atoms of the NH_4 groups are within H-bonding distance of a number of the framework oxygen atoms with the N(H)···O distances ranging from 2.91 to 3.44 Å (shown in Figure 3.5b).

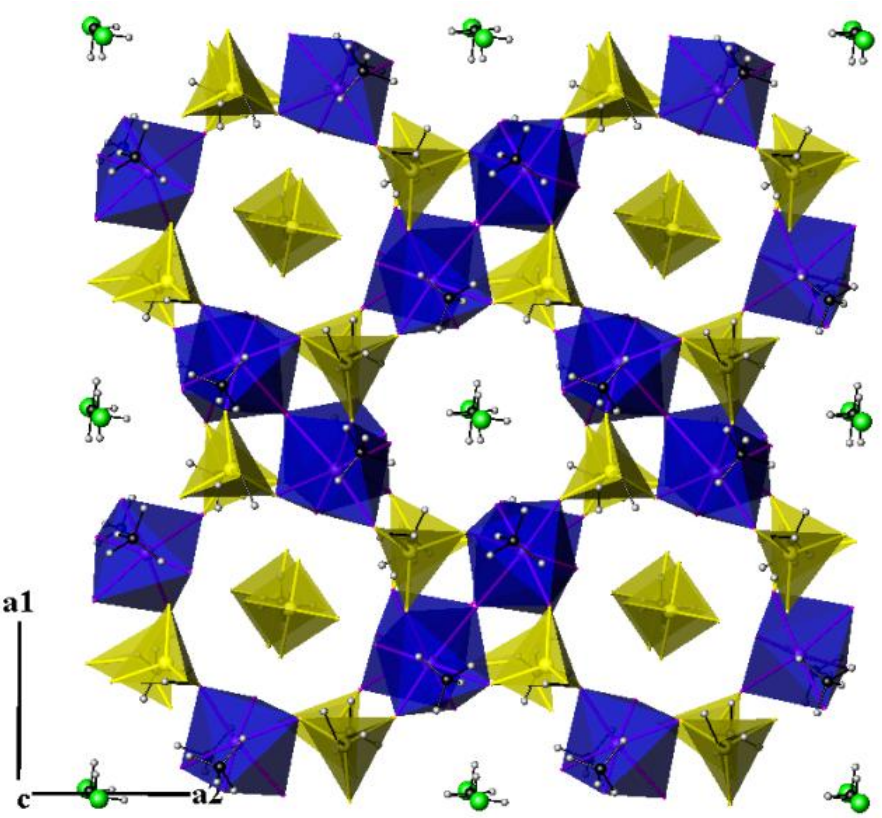

Figure 3.3: The view along the *c* axis shows details of the channels in compound (1). Blue polyhedra represent the molybdenum octahedra and yellow polyhedra show the phosphate. Nitrogen atoms: small black spheres, hydrogen atoms: small grey spheres and chloride anions: medium green spheres.

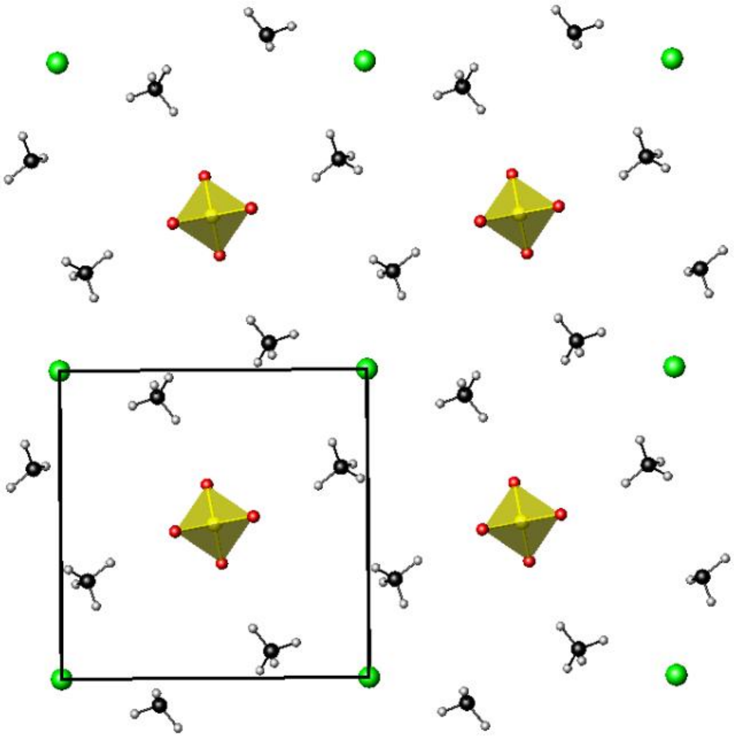

Figure 3.4: Distribution of guest species in the mixed anion/cation interlayer region of compound (1). Nitrogen atoms: small black spheres, hydrogen atoms: small grey spheres, chloride anions: medium green spheres and free PO_4^{3-}: yellow tetrahedra.

Table 3.2: Selected bond lengths (Å) and bond valences for compound (1).

Polyhedra	Bond lengths	Σs_{ij}	Polyhedra	Bond lengths	Σs_{ij}
$Mo(1)O_6$			$HP(1)O_4$		
Mo(1)-O(13)	1.707(4)	1.731	P(1)-O(2)	1.514(3)	1.321
Mo(1)-O(11)	1.710(4)	1.703	P(1)-O(1)	1.515(4)	1.317
Mo(1)-O(18)	1.916(13)	0.976	P(1)-O(3)	1.536(4)	1.245
Mo(1)-O(3)	2.021(4)	0.735	P(1)-O(4)	1.567(3)	1.145
Mo(1)-O(5)	2.189(3)	0.467			**ΣP1 = 5.03**
Mo(1)-O(6)	2.201(4)	0.452			
		ΣMo1 = 6.06	$HP(2)O_4$		
			P(2)-O(5)	1.518(4)	1.307
$Mo(2)O_6$			P(2)-O(6’)	1.519(4)	1.303
Mo(2)-O(9)	1.799(4)	1.339	P(2)-O(7)	1.538(4)	1.238
Mo(2)-O(12)	1.716(4)	1.676	P(2)-O(8)	1.555(4)	1.182
Mo(2)-O(10)	1.935(13)	0.927			**ΣP2 = 5.03**
Mo(2)-O(7’)	2.013(4)	0.751			
Mo(2)-O(1)	2.125(4)	0.555	$P(3)O_4$		
Mo(2)-O(2’)	2.197(4)	0.457	P(3)-O(14)	1.528(4)	1.272
		ΣMo2 = 5.70	P(3)-O(14’)	1.528(4)	1.272
			P(3)-O(14’)	1.528(4)	1.272
			P(3)-O(14’)	1.528(4)	1.272
					ΣP3 = 5.09

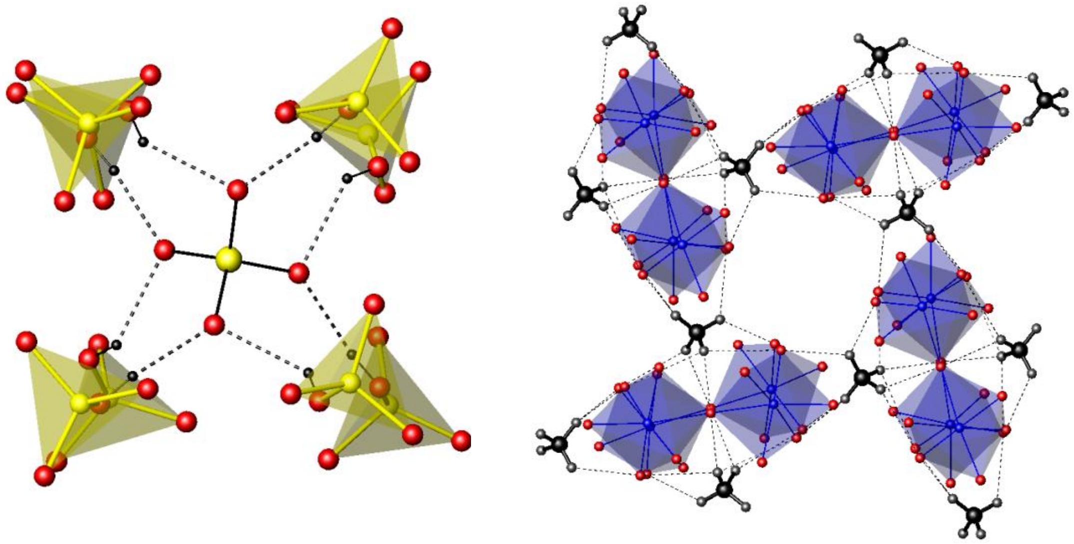

Figure 3.5: The local coordination geometry of the free PO_4^{3-} ion (LHS), Schematic showing the arrangement of ammonium cations between the molybdeno-sheets (RHS).

Compound (1) was further characterised by IR spectroscopy and TGA analysis. The infrared spectrum of compound (1), shown in Figure 3.6, exhibits an inseparable broad band at 3200-2400 cm^{-1} region attributed to the stretching modes of the NH_4^+ groups and the HPO_4 groups. The present IR spectrum shows overlap of broad bands in this region. Bands in the high frequency region (~ 3206 cm^{-1} and 3013 cm^{-1}) belong to N-H groups, whilst weak bands in the low frequency region (~2780 cm^{-1}, 2416 cm^{-1}) are attributed to the stretching modes of (P)O-H groups. Regarding the deformation vibrations modes, these can be readily distinguished; N-H groups show a very characteristic strong band at 1409 cm^{-1}, whereas the observation of two weak bands at 1638 cm-^{1} and 1296 cm^{-1} is an indication of having protonated HPO_4 groups.[7]

The absorption bands of PO_4^{3-} and Mo=O groups can be detected at lower frequencies. There is a broad intense band well resolved into three components: one doublet band at 1040/1002 cm^{-1}, one doublet band at 902/886 cm^{-1} and one singlet band at 736 cm^{-1}.[8] The first band is assigned to a mixture of P-O and Mo=O stretching modes whilst the following two bands correspond to the $\nu 3$ and $\nu 1$ stretching vibrations of the phosphate groups respectively. As it can be observed, there is a relatively splitting of the $\nu 3$ band, implying the presence of more than two types of site symmetry for the phosphate groups. Additionally, the presence of the *v*1 band indicates the reduction in symmetry for the HPO_4^{2-} ions.

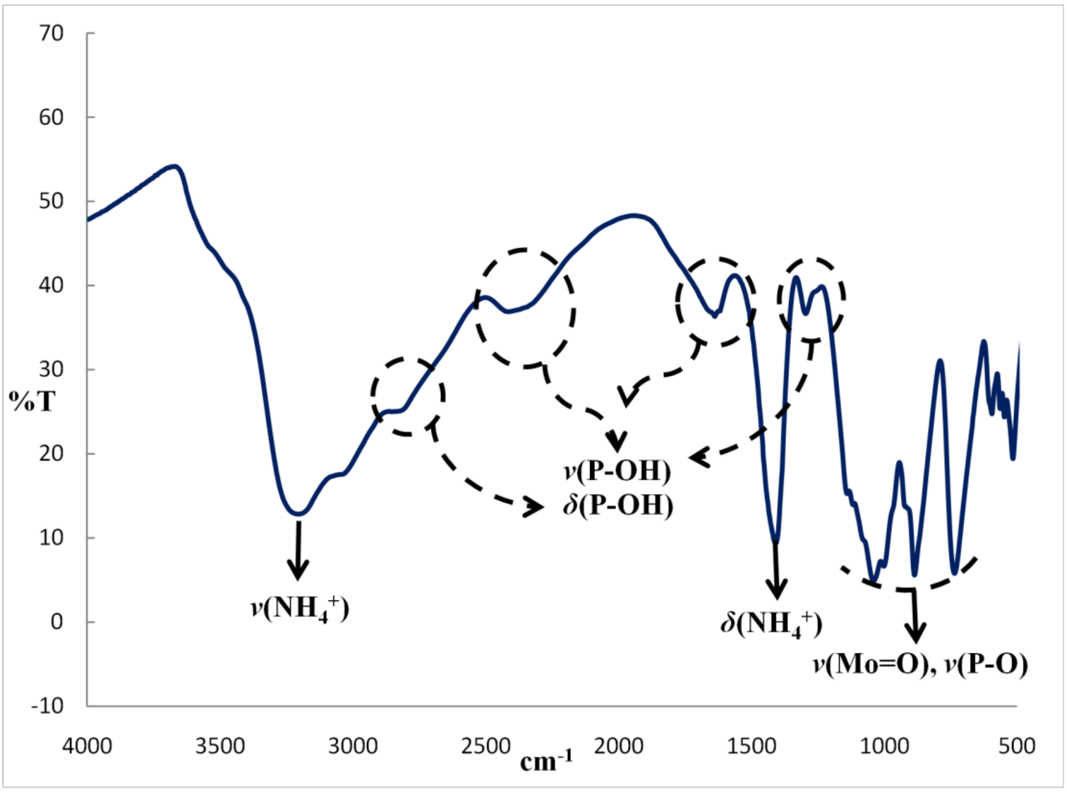

Figure 3.6: Infrared spectrum of compound (1) showing the characteristic bands for each group.

Figure 3.7 shows analysis of compound (1) (11.752 mg) by TGA. A small mass loss (~3.31 %) occurred in the region of 80-115 °C, followed by a sharp decrement of mass barely observed in four steps in the region of 115-280 °C (total mass of the four small continued steps ~ 4.92 %). Both steps indicate the evaporation of the twelve ammonium molecules from one molecule of compound (1), as the total mass loss of 8.23% is in good agreement with the calculated value (9.81 %). The mass continues decreasing up to 520 °C with a total mass loss estimated to be ~ 17.09 %. As can be depicted in the figure above (Fig: 3.7), DTA analysis of compound (1) shows one sharp exothermic peak at 110 ° C and two rather weak exothermic peaks at the temperatures 160 and 215 °C, indicating the release of energy. Exothermic peaks may be attributed to the collapse of the framework structure and the formation of the inorganic residue, suggesting the essential role of ammonium cations to stabilize this unique structure *via* strong hydrogen bonding.

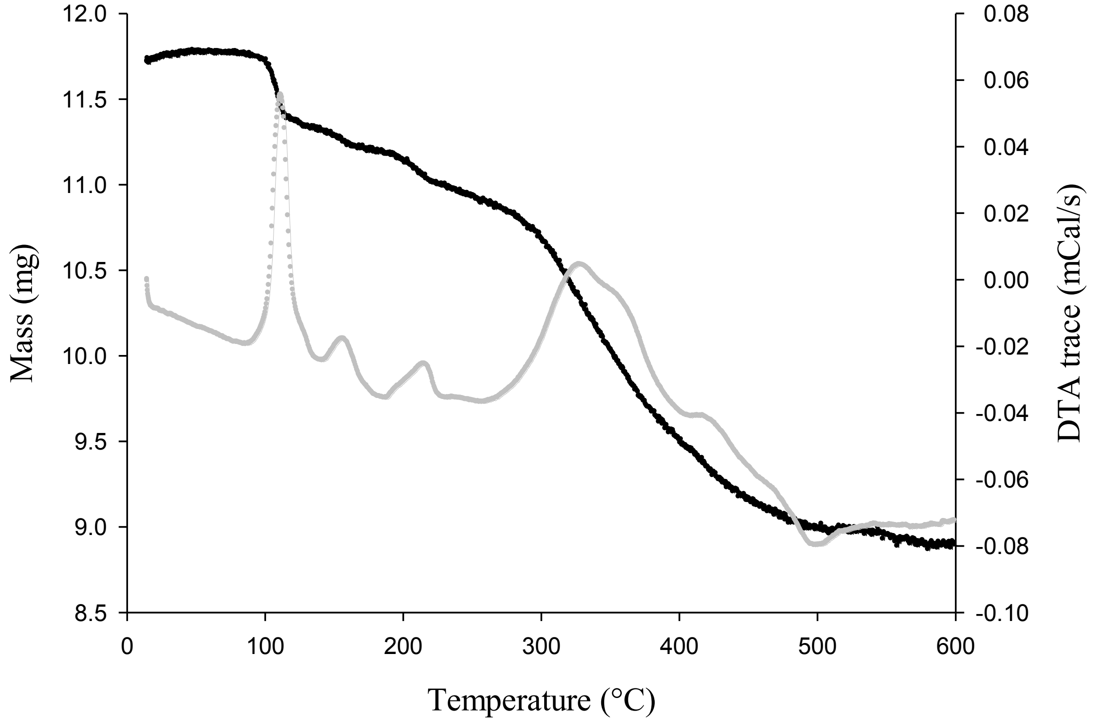

Figure 3.7: TGA pattern of compound (1). Mass loss was recorded as a function of temperature and is shown by the black line. DTA trace is the grey line.

II. Ion exchange investigations of compound (1)

Reproduction of the synthesis of compound (1) $[NH_4]_2[(MoO_2)_2O(HPO_4)_2]_4[PO_4]Cl$ but substituting NH_4Cl source for NH_4Br afforded the analogue product phase. The isotypic Br-phase was identified using single crystal X-ray diffraction. The unit cell found to be slightly expanded compared to the previously obtained compound (1) (a = 9.729(3), c = 14.628(11) Å). Bromide content was confirmed from EDS analysis and the determined atomic ratios were in line with the chemical formula sum (Mo/P/Br = 1:0.99:0.12).

In attempts to replace NH_4HPO_4 and NH_4Cl starting materials with the analogous potassium sources proved to be unsuccessful, leading to a distinct product phase whose structure still remains unidentified. K^+ and NH_4^+ cations are rather similar in terms of charge and size, and one might expect the potassium to exhibit similar templating effect. However, it appears that the layered framework of compound (1) is not templating around the potassium, suggesting the essential role of ammonium cations in the framework formation. A reasonable explanation might be the strong hydrogen bonding that NH_4^+ cations are greatly involved and which provides stabilisation of the structure of (1).

Given the channel and layer like nature of this structure type compound and the possible direct synthesis of both the chloride and bromide analogues, a possible functionality of this compound would be through anion exchange reactions. A series of experiments were performed that involved dispersion of the Cl and Br analogues in concentrated solutions of NH_4Br and NH_4Cl respectively, in attempts to exchange the Cl anions in the structure for Br anions and vice versa. Under these conditions, only very low levels of anion incorporation were observed when the concentration of NH_4X solution was 2M. Anion exchange in more concentrated solutions (C_{NH4X}: 3-6M) did not occur, as the solid compound was dissolved after a period of time (~6-8 h).

Due to solubility problems encountered in the latter case, further ion-exchange reactions took place in the absence of water. Following a similar procedure reported for previously known molybdenum phosphates,[9] solid homogeneous mixtures consisting of the *X*-analogue and the NH_4X' salt were placed in 23 mL Teflon lined steel autoclaves and heated to 448 K. As a result, Br^- anions were successfully exchanged with Cl^- anions, but not the other way round. X-ray powder diffraction analysis completed on the exchanged product phase, identified the isotypical Cl-analogue, whilst additional EDS analysis clearly showed only the presence of chloride within the crystalline phase and the determined atomic ratios were in line with the chemical formula sum (Mo/P/Cl = 1:1.04:0.14).

3.1.3 Conclusions

The unusual layered molybdenum phosphates $[NH_4]_{12}[(MoO_2)_2O(HPO_4)_2]_4[PO_4]X$ (where $X = Cl^-, Br^-$) with embedded multiple anionic and cationic guests have been successfully synthesised *via* mild hydrothermal routes. The framework structure is of particular interest as it encompasses previously unknown tetrameric units, constructed from Mo_2O_{11} binuclear units capped on both sides by HPO_4 groups, forming two perfectly ordered channel types distinguished by their content. Both channels contain ammonium cations NH_4^+, but one channel type is additionally filled by isolated PO_4^{3-} groups while the other channel hosts only halide anions (either Cl^- or Br^-). Given the channel and layer like nature of this structure type compound and the possible direct synthesis of both the chloride and bromide analogues, a possible functionality of this compound would be through anion exchange reactions. Ion exchange investigations carried out, and showed the affinity of the Br-analogous to be completely exchanged with Cl^- anions but not vice versa.

3.2 Amine templated molybdenophosphates

This section of research includes a series of hydrothermal reactions involving molybdenum, phosphate and borate reagents with a variety of organic templating agents. Thus, it was thought that amines would act as suitable templates in the formation of molybdenum borophosphate frameworks. However, reactions resulted in previously known molybdenum phosphate compounds mostly consisting of polyoxometalate anions. Three distinct cluster polyanions templated by different amines are discussed here, in addition to a ribbon-like structure consisted of one-dimensional molybdenophosphate chains.

3.2.1 Experimental

I. Synthesis

The general procedure consisted of the hydrothermal treatment of sodium molybdate dehydrate $Na_2MoO_4.2H_2O$ with a phosphorus source (either orthophosphoric acid H_3PO_4 or $(NH_4)H_2PO_4$) and boric acid H_3BO_3 in the presence of water. Finally an organic amine was added to the mixture and in some cases the preparation of the precursor was also followed by the addition of HCl. Reaction mixtures were first stirred to homogeneity (for ~1h) and then transferred to a 23 mL Teflon lined steel autoclave and heated at 413 K for four days under autogenous pressure. Once cool the products were filtered, washed with distilled water and air dried.

The following organic amines were introduced into the system: methylamine hydrochloride, tetramethylammonium chloride, ethylenediamine, dabco and piperazine. In each case, reaction mixtures were performed by varying the molar concentration of the amine (X = 1-5, where X = 1 corresponds to 5 mmol) in mixtures with Mo/P/B/H_2O/amine molar ratio = 1/6/6/33/X. All products were characterised as described in the previous Section 3.1.1.

✓ Detailed reaction conditions for the compounds isolated within this work

$\{(C_6H_{14}N_2)\}\{MoO_2(HPO_4)_2\}.H_2O$ (2): $Na_2MoO_4.2H_2O$ (1.210 g, 5 mmol), 85% orthophosphoric acid solution (2.09 mL, 30 mmol), H_3BO_3 (1.854 g, 30 mmol), dabco (1.1217 g, 10 mmol) and distilled water (3 mL). The final reaction mixture had a pH value = 2.60. Heated to 413 K and held for 4 days. Product occurred as colourless plate like crystals.

$Na_3(dabco)_2\{Mo_5O_{15}(PO_4)_2.(H_2O)_6$ (3): $Na_2MoO_4.2H_2O$ (1.210 g, 5 mmol), $(NH_4)H_2PO_4$ (3.451 g, 30 mmol), H_3BO_3 (1.854 g, 30 mmol), dabco (2.2434 g, 20 mmol), HCl four drops of concentrated 37% hydrochloric acid solution and distilled water (3 mL). The final reaction mixture had a pH value of 4.12. Heated to 413 K and held for 4 days. Product occurred as colourless plate like crystals.

$[(CH_3)_4N]_3[PMo_{12}O_{40}]$ (4): $Na_2MoO_4.2H_2O$ (1.210 g, 5 mmol), 85% orthophosphoric acid solution (2.09 mL, 30 mmol), H_3BO_3 (1.854 g, 30 mmol) and distilled water (3 mL). The final reaction mixture had a pH value of 2.20. Heated to 413 K and held for 4 days. Product occurred as pale orange fragments.

$\{C_2H_4(NH_3)_2\}_2Na\{Mo_6O_{15}(PO_4)_4\}_2.(H_2O)_{12.8}$ (5): $Na_2MoO_4.2H_2O$ (1.210 g, 5 mmol), $(NH_4)H_2PO_4$ (3.451 g, 30 mmol), H_3BO_3 (1.854 g, 30 mmol), ethylenediamine (1.62 mL, 25 mmol) and distilled water (3 mL). The final reaction mixture had a pH value of 6.30. Heated to 413 K and held for 4 days. Product crystallised as blue plate like crystals.

3.2.2 Results and discussion

I. Synthesis overview

As part of an attempt to discover new framework topologies as well as to investigate the templating effect of organic amines in the formation of molybdenum borophosphate frameworks, we set out a programme of work in systems that entailed mild hydrothermal reactions of molybdenum, phosphate and borate reagents with a variety of organic templating agents. Three main systems were prepared, and each of them involved different starting material sources.

The first system aimed at investigating reactions performed under alkaline conditions (pH ~ in the range 6-9) by introducing the phosphate source $(NH_4)H_2PO_4$, whilst the second system entailed the use of H_3PO_4 instead, in order to examine the reactivity under quite acidic conditions (pH values ~ < 3). In the case of dabco, reaction mixtures (within the pH range 6-8) resulted in the previously reported borophosphate compound $Na_5B_2P_3O_{13}$,[10] whereas in presence of H_3PO_4 and under very acidic conditions (pH ~ 2) the compound $\{(C_6H_{14}N_2)\{MoO_2(HPO_4)_2\}.H_2O$ (2) was successfully obtained. Further decrease on the pH resulted in the formation of amorphous phases. Using tetramethylammonium chloride as the organic template, the system yielded compound $[(CH_3)_4N]_3[PMo_{12}O_{40}]$ (4), which was stable formed under acidic conditions. When the pH was allowed to increase to any value greater than five, the system formed only amorphous slurry. In the case of ethylenediamine, compound (5) was obtained from quite alkaline mixtures, whereas acidic conditions produced only clear solutions or glassy phases. Finally, the cases of piperazine and methylamine remain very ambiguous since the latter gave no solid products and the former resulted in unidentified product phases. Unfortunately the lack of large enough crystals, suitable for single crystal X-ray diffraction, within the product phases and the unsuccessful attempts to identify the resulting phases using X-ray powder diffraction could not help to elucidate this further.

The third system involved similar synthetic procedures to those described above, with the main difference being the addition of HCl in order to adjust the pH at ~ 4. This study aimed at investigating the formation of compound (1), (details of which are given in the earlier section 3.1.2) in the presence of an organic templating agent. Thus, the successful preparation of that unusual layered compound $[NH_4]_{12}[(MoO_2)_2O(HPO_4)_2]_4[PO_4]Cl$ (1) and the great tendency of ammonium cations to stabilise that unique framework topology has incited the challenge to investigate the templating effect of alkyl-substituted amines.

This investigation has demonstrated that none of the organic amines succeeded in getting entrapped into the layers of compound (1) but rather tended to direct the formation of the previously reported compound $NaMo(H_2O)O_2PO_4$.[11] This consists of layers built up from alternating $Mo^{(VI)}O_6$ octahedra and PO_4 tetrahedra which form four- and eight- membered ring channels. It appears that organic amines do not participate in the crystalline structure, but rather sodium cations are located in the interlayer space. An exception occurred only in case of dabco which favoured the formation of compound (3), a structure that comprises $[Mo_5O_{15}(PO_4)_2]^{6-}$ cluster anions templated by sodium cations and dabco molecules.

II. Characterization of $\{(C_6H_{14}N_2)\}\{MoO_2(HPO_4)_2\}.H_2O$ (2)

Compound (2) crystallises in the monoclinic $P2_1/c$ space group and its structure is shown in Figure 3.8. Single crystal X-ray diffraction of compound (2) (details of which are summarized in Table 3.3) has shown the structure to consist of discrete $[MoO_2(HPO_4)_2]_\infty$ ribbons, diprotonated dabco molecules and water molecules. As depicted in Figure 3.8, molybdenophosphate ribbons are arranged in block-units, forming an out sphere of solely hydrogenphosphate groups HPO_4^{2-}. This creates anchoring points for the dabco and water molecules, allowing adjacent ribbons to be linked together *via* strong hydrogen bonding. These ribbons constitute $[MoO_2(HPO_4)_2]_\infty^{2-}$ chains built up from a repeating four-connected net of alternating molybdenum octahedra and phosphate tetrahedra (shown in Figure 3.9).

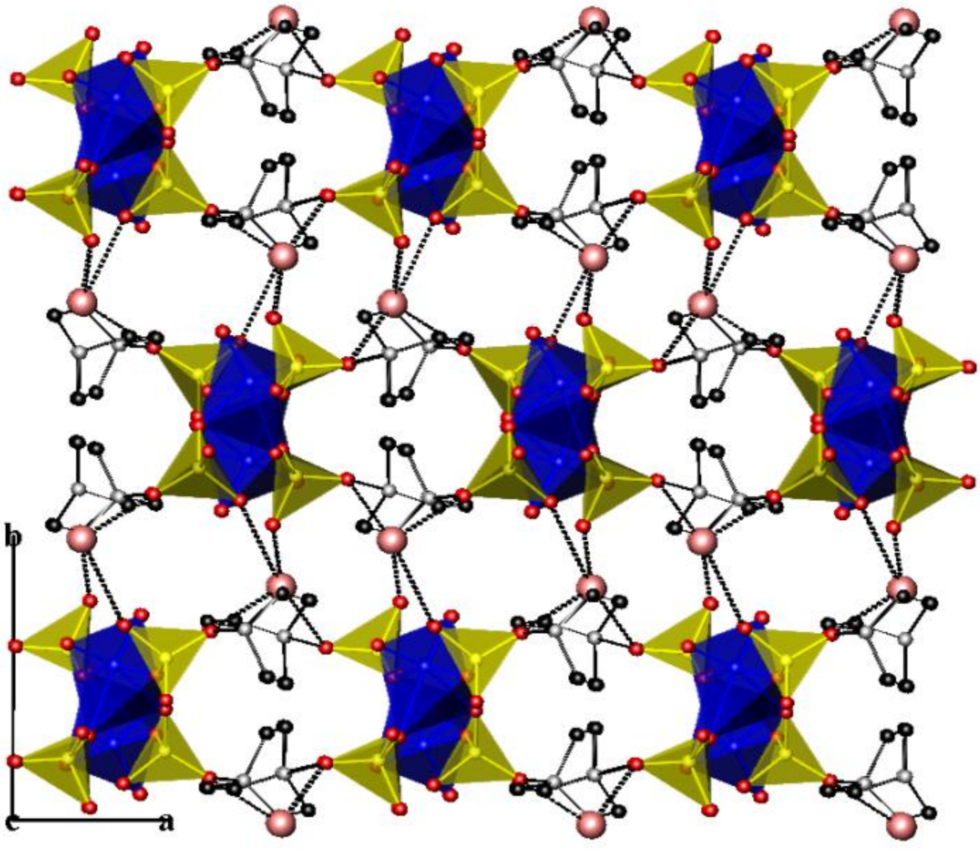

Figure 3.8: A perspective view of the structure of compound (2) showing the arrangement of the $[MoO_2(HPO_4)_2]_\infty$ ribbons. Blue polyhedra represent the molybdenum octahedra and yellow polyhedra show the phosphate. Pink spheres show lattice water; grey-black linked spheres comprise the dabco molecules.

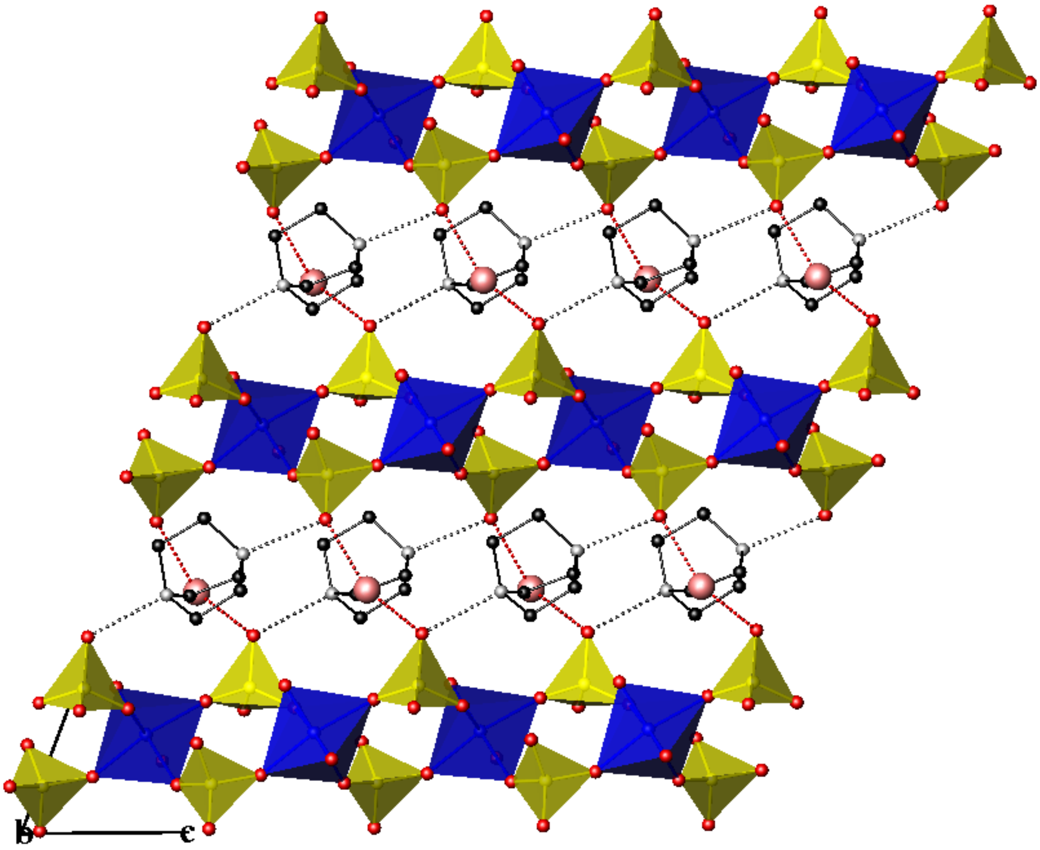

Figure 3.9: Projection of a single layer in the structure of (2) (along the *b* axis) showing how adjacent $[MoO_2(HPO_4)_2]_\infty^{2-}$ chains are linked together through hydrogen bonding interactions with dabco cations and water molecules. Blue polyhedra represent the molybdenum octahedra and yellow polyhedra show the phosphate. Pink spheres show lattice water; grey-black linked spheres comprise the dabco molecules.

The bonding motif identified in compound (2) resembles the $MoOPO_4$ compound discovered by Kierkegaard and Westerlund[1]. This exhibits layers based on a related structural pattern of alternating polyhedra, with the main difference being the connectivity of MoO_6 octahedra through common oxygen vertices to form a three-dimensional framework structure. In the structure reported here, there is one crystallographically distinct molybdenum site, Mo(1) which shares four oxygen corners with four different phosphate tetrahedra, whereas the two remaining apices are occupied by terminal oxo groups. Bond valence calculations completed on Mo(1) site showed this molybdenum site to adopt the +6 oxidation state. Mo(1) exhibits the classic distorted octahedral geometry with two adjacent short Mo-O distances (1.692(10)-1.702(10) Å) forming molybdenyl groups Mo=O, with opposite longer Mo-O bonds (1.976(10)-2.001(11) Å) and two additional bonds of intermediate length (2.124(10)-2.239(10) Å). Selected bond lengths and the bond valences for compound (2) are given in Table 3.4.

Regarding the phosphate tetrahedra, there are two crystallographically independent P atoms which exhibit identical coordination environments. Each P atom shares two corners with two different molybdenum octahedra MoO_6, whilst the rest of the apices remain unshared and pendant. Looking at the bond lengths of these PO_4 tetrahedra, it would appear that both groups show intermediate P-O bonds for all the bridging oxygen atoms (~ 1.54 Å), in addition to a pair of one relatively longer P-O distance (~1.56 Å) and one shorter bond (~1.50 Å) attributed to a P-OH bond and a P=O terminal oxo groups, respectively. The two hydrogens attached to phosphate oxygens were identified in the difference map and from bond elongation, these were then fixed in calculated positions, treated as riding on the parent atom and the torsion angle allowed to refine.

Table 3.3: Crystal and diffraction information of compound (2).

Empirical formula	$C_6H_{18}N_2MoP_2O_{11}$
Formula weight	449.96
Temperature	120(2) K
Appearance	colourless plate
Wavelength	0.71073 Å (Mo K_α)
Crystal system	Monoclinic
Space group	$P2_1/c$
Unit cell dimensions	a = 9.5485(5) Å, b = 16.2487(8) Å c = 9.6588(4) Å, β = 111.218(3)°
Volume	1396.98(12) Å^3
Z	4
D_c (g.cm^{-3})	2.15
Θ range for data collection	3.38°-25.03°
Reflections collected	14127
Independent reflections	2459
Data/Restraints/Parameters	2459/88/177
R indices	$R_1 = 0.0967$ $wR_2 = 0.1767$

Viewing down the *b* axis (shown in Figure 3.9) it can be seen how diprotonated dabco cations and water molecules serve to bridge adjacent $[MoO_2(HPO_4)_2]_\infty^{2-}$ chains, through strong hydrogen bonding, by generating layers running along the direction parallel to *bc* plane. The nitrogen atoms of dabco molecules act as H-bond donors for the terminal P=O oxo groups of adjacent chains with the N(1)···O(5) and N(2)···O(9) distances 2.6008 and 2.5913 Å, respectively.

There is one unique water molecule, and this is within hydrogen bonding distance of the four distinct terminal oxygens O(9), O(6) and O(5), O(7) of the $P(1)O_4$ and $P(2)O_4$ groups, respectively. This causes enhanced interconnectivity between adjacent layers, producing the three-dimensional array shown in Figure 3.10. $O_w(1)$ adopts a four-fold coordination geometry, acting as H-bond donor for the O(9) and O(5) [$O_w(1)$···O(9) = 2.6803 Å, $O_w(1)$···O(5) = 2.6871 Å, O(9)-Ow-O(5)$_{\text{bond angle}}$ = 108.12°] and as H-bond acceptor for the O(6) and O(7) atom sites [$O_w(1)$···O(6) = 3.1784 Å, $O_w(1)$···O(7) = 2.544 Å), O(6)-Ow-O(7) = 76.68°].

Table 3.4: Selected bond lengths (Å) and bond valences for compound (2).

Octahedra	Bond Lengths	Σs_{ij}	Tetrahedra	Bond Lengths	Σs_{ij}
$Mo(1)O_6$			$P(1)O_4$		
Mo(1)-O(3)	1.692 (10)	1.788	P(1)-O(9)	1.509(11)	1.339
Mo(1)-O(1)	1.702(10)	1.740	P(1)-O(8)	1.541(10)	1.228
Mo(1)-O(2)	1.976(10)	0.830	P(1)-O(2)	1.543(10)	1.222
Mo(1)-O(4)	2.001(11)	0.776	P(1)-O(6)	1.555(10)	1.182
Mo(1)-O(8)	2.124(10)	0.556			**ΣP1**=4.97
Mo(1)-O(10)	2.239(10)	0.408			
		ΣMo1=6.09	$P(2)O_4$		
			P(2)-O(5)	1.507(11)	1.346
			P(2)-O(4)	1.540(11)	1.231
			P(2)-O(10)	1.547(10)	1.208
			P(2)-O(7)	1.555(11)	1.182
					ΣP1=4.97

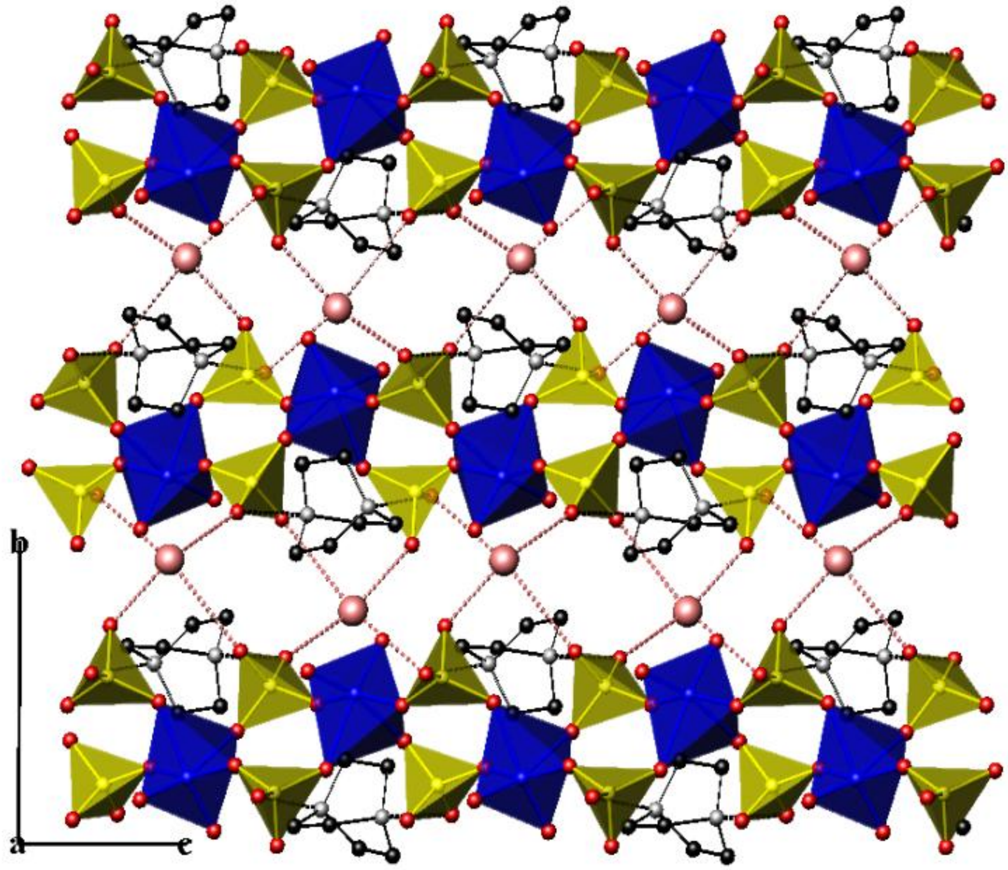

Figure 3.10: The view along the *a* axis shows the connectivity of layers into a three dimensional array through hydrogen bonding interactions with water molecules.

III. Characterization of $Na_3(dabco)_2\{Mo_5O_{15}(PO_4)_2\}.(H_2O)_6$ (3)

Compound (3), $Na_3(dabco)_2\{Mo_5O_{15}(PO_4)_2\}.(H_2O)_6$, crystallises in the triclinic $P\bar{1}$ space group and its structure is shown in Figure 3.12. Single crystal X-ray diffraction of compound (3) (details of which are summarized in Table 3.5) has shown the structure to consist of the previously reported $[Mo_5O_{15}(PO_4)_2]^{6-}$ cluster anions connected with sodium cations and dabco molecules through intricate intermolecular bonding, forming a pseudo three-dimensional framework structure. The previously reported $[Mo_5O_{15}(PO_4)_2]^{6-}$ cluster anion [12] (shown in Figure 3.11) is build up from five MoO_6 octahedra that share four common edges and one corner through oxygen atoms to form a five-membered molybdenum which is capped on both poles by two different phosphate tetrahedra.

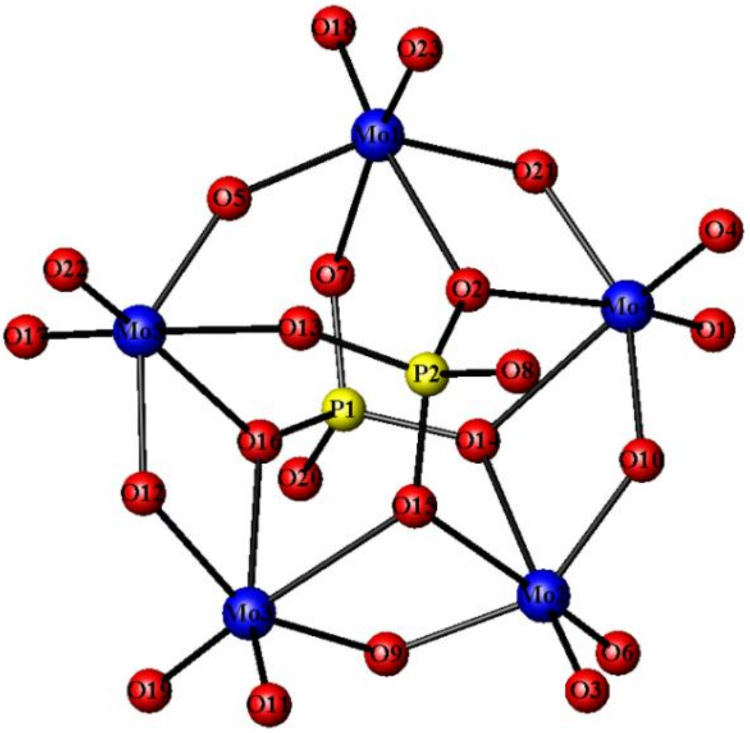

Figure 3.11: Schematic showing the $[Mo_5O_{15}(PO_4)_2]^{6-}$ cluster polyanion. Molybdenum atoms are shown as blue spheres, phosphorous atoms as yellow spheres and oxygens as red spheres.

Table 3.5: Crystal and diffraction information of compound (3).

Empirical formula	$C_{12}H_{39}N_4Na_3Mo_5P_2O_{29}$
Formula weight	1313.77
Temperature	120(2) K
Appearance	colourless block
Wavelength	0.71073Å (Mo K_α)
Crystal system	Triclinic
Space group	$P\bar{1}$
Unit cell dimensions	$a = 11.3809(5)$ Å, $b = 12.3725(5)$ Å
	$c = 12.6954(6)$ Å, $\alpha = 86.976(3)°$
	$\beta = 87.582(3)°$, $\gamma = 81.285(3)°$
Volume	1763.48(9) $Å^3$
Z	2
D_c	2.475 $g.cm^{-3}$
Θ range for data collection	3.34-25.03
Reflections collected	21966
Independent reflections	6130
Data/Restraints/Parameters	6130/270/412
R indices	$R_1 = 0.0850$, $wR_2 = 0.1737$

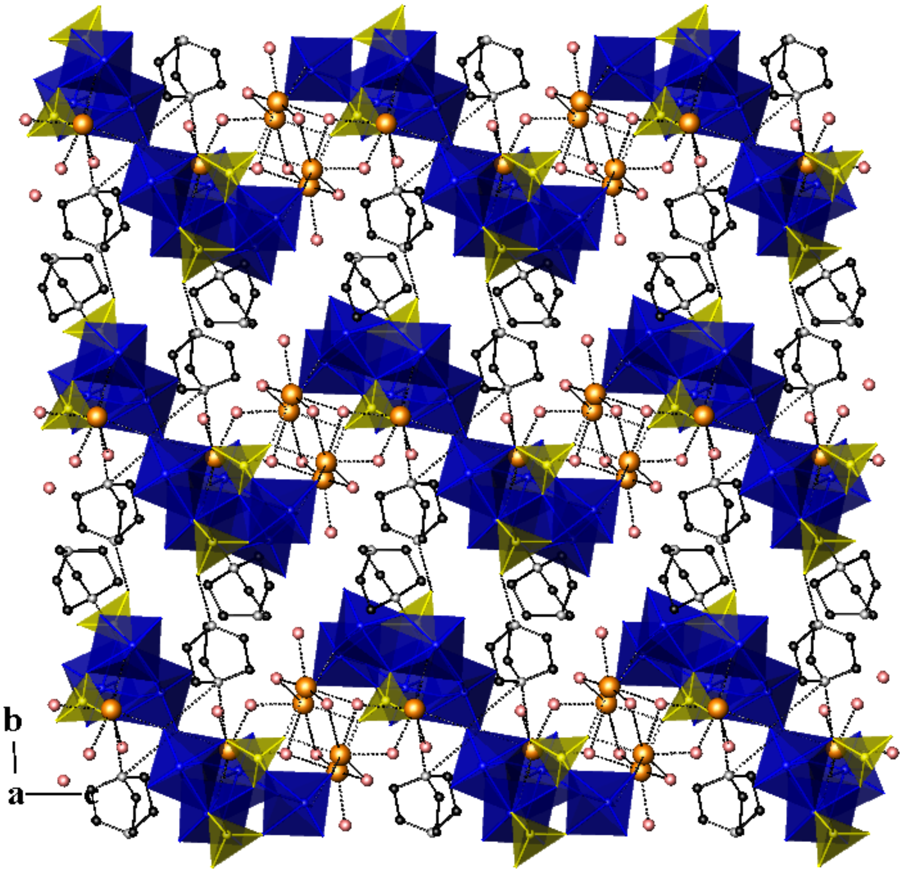

Figure 3.12: A perspective view of the structure of compound (3) along the *a* axis. Blue polyhedra represent the molybdenum octahedra and yellow polyhedra show the phosphate. Pink spheres show lattice water; grey-black linked spheres comprise the dabco molecules. Sodium cations are shown as orange spheres.

There are five crystallographically independent molybdenum sites forming a five-membered ring built up from [MoO_6] octahedral units. Bond valence calculations completed on each molybdenum site showed all the Mo sites to adopt the +6 oxidation state. All exhibit the classic distorted octahedral geometry with two adjacent short Mo-O distances (1.696(10)-1.734(10) Å) forming a molybdenyl group, with opposite longer Mo-O bonds (2.187(9)-2.369(11) Å) and two additional bonds of intermediate length (1.884(10)-1.961(10) Å).

The two distinct PO_4 tetrahedra share three corners with the five-membered ring, whilst their fourth apices remain unshared and pendant. The P(1)O_4 tetrahedron exhibits two rather long P-O bonds (~ 1.570 Å) and one slightly shorter P-O distance (~ 1.518(10) Å) for the bridging oxygen atoms (P-O-Mo), whilst the P(2)O_4 group shows three P-O bonds in the range 1.564(10)-1.572(10) Å. It is noticeable that the terminal oxygens in both phosphate tetrahedra exhibit relatively shorter bonds (P(1)-O(20): 1.530(10) Å, P(2)-O(8): 1.506(10) Å) compared to the bridging oxygens. Whereas, the terminal oxo group in P(1) is within H-bonding distance of a nearby dabco molecule, the oxygen in P(2) interacts strongly with a sodium cation. Therefore, P(1)O$_4$ shows a relatively longer P-O distance for its terminal oxygen, suggesting a possible hydrogen delocalization between this oxygen site and dabco. When comparing the bond lengths of phosphate tetrahedra in similar cluster polyanions,[8b, 12-13] it can clearly be seen that much longer terminal P-O distances generally occur (~1.57 Å) where the phosphate group constitutes a P-OH bond.

Table 3.6: Selected bond lengths (Å) and bond valences for compound (3).

Polyhedra	Bond lengths	Σs_{ij}	Polyhedra	Bond lengths	Σs_{ij}
Mo(1)O$_6$			Mo(4)O$_6$		
Mo(1)-O(18)	1.708(10)	1.712	Mo(4)-O(1)	1.700 (10)	1.750
Mo(1)-O(23)	1.724(10)	1.640	Mo(4)-O(4)	1.700(11)	1.750
Mo(1)-O(5)	1.920(9)	0.965	Mo(4)-O(21)	1.929(10)	0.950
Mo(1)-O(21)	1.944(10)	0.905	Mo(4)-O(10)	1.947(10)	0.900
Mo(1)-O(7)	2.234(10)	0.413	Mo(4)-O(2)	2.187(9)	0.469
Mo(1)-O(2)	2.320(10)	0.328	Mo(4)-O(14)	2.369(11)	0.287
		ΣMo1=5.96			**ΣMo4=6.10**
Mo(2)O$_6$			Mo(5)O$_6$		
Mo(2)-O(6)	1.713(10)	1.689	Mo(5)-O(17)	1.722(10)	1.649
Mo(2)-O(3)	1.734(10)	1.596	Mo(5)-O(22)	1.727(10)	1.627
Mo(2)-O(9)	1.894(10)	1.036	Mo(5)-O(5)	1.884(10)	1.064
Mo(2)-O(10)	1.918(10)	0.971	Mo(5)-O(12)	1.895(10)	1.033
Mo(2)-O(14)	2.257(10)	0.388	Mo(5)-O(16)	2.269(10)	0.376
Mo(2)-O(15)	2.278(10)	0.367	Mo(5)-O(13)	2.330(9)	0.319
		ΣMo2=6.05			**ΣMo5=6.06**
Mo(3)O$_6$			P(1)O$_4$		
Mo(3)-O(19)	1.696(10)	1.769	P(1)-O(7)	1.518(10)	1.307
Mo(3)-O(11)	1.718(10)	1.667	P(1)-O(20)	1.530(10)	1.265
Mo(3)-O(9)	1.928(10)	0.945	P(1)-O(14)	1.570(11)	1.135
Mo(3)-O(12)	1.961(10)	0.864	P(1)-O(16)	1.570(9)	1.135
Mo(3)-O(16)	2.222(9)	0.427			**ΣP1=4.84**
Mo(3)-O(15)	2.316(10)	0.331			
		ΣMo3=6.00	P(2)O$_4$		
			P(2)-O(8)	1.506(10)	1.350
			P(2)-O(15)	1.558(11)	1.173
			P(2)-O(13)	1.564(10)	1.154
			P(2)-O(2)	1.572(10)	1.129
					ΣP2=4.81

Projection of the structure along *a* axis shows how adjacent $[Mo_5O_{15}(PO_4)_2]^{6-}$ anions are connected together by sodium cations to form a 2D network of slightly undulating layers (Figures 3.11 and 3.13). There are three crystallographically-distinct sodium atoms within the crystalline structure of (3). Unlike related structures consisting of $[Mo_5P_2O_{23}]^{6-}$ anions[12], where sodium cations preferentially adopt octahedral coordination geometries, in the structure reported here sodium cations are found to adopt irregular geometries with the coordination number varying from five to seven. Na(1) is coordinated by four water molecules and three framework oxygens, Na(2) exhibits an octahedral coordination geometry defined by four water molecules and two framework oxygens, and Na(3) exhibits a five-fold coordination sphere with four water molecules and only one framework oxygen. The average bond distances for each cation site are: $d_{av}(Na(1)\cdots O)$ = 2.525 Å, $d_{av}(Na(2)\cdots O)$ = 2.435 Å, $d_{av}(Na(3)\cdots O)$ = 2.341 Å. View of a single layer down the *b* axis (Figure 3.13) shows how these distinct sodium cations are couple together into a complex array by sharing common edges and corners through water molecules with Na⋯Na distances varying between 3.185 and 3.922 Å.

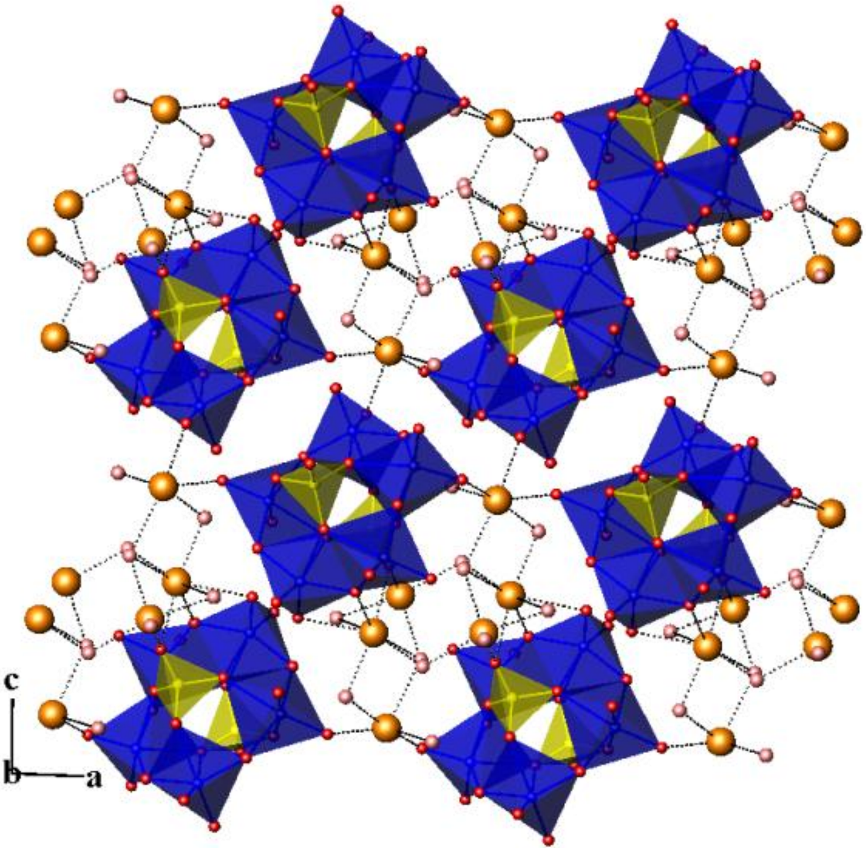

Figure 3.13: Projection of a single layer in the structure of (3) (along the *b* axis).

Protonated dabco molecules serve to bridge $[Mo_5O_{15}(PO_4)_2]^{6-}$ cluster anions of adjacent layers through an extensive hydrogen bonding, giving rise to a pseudo-three dimensional network. There are two crystallographically independent dabco molecules within the crystalline structure of compound (3) and each molecule contains two distinct nitrogen donors. As illustrated in Figure 3.14, both nitrogen atoms of dabco molecules (of type I) are within hydrogen bonding distance to one bridging and one terminal oxygen of the PO_4 tetrahedra ($N(1)\cdots O(13)$ = 2.75 Å, $N(4)\cdots O(20)$ = 2.44 Å) , whereas dabco molecules (of type II) make only one hydrogen bond link with one bridging oxygen atom of the cluster anions ($N(3)\cdots O(7)$ = 2.77 Å), suggesting that the latter should be mono-protonated. As a result, dabco molecules have an overall charge of three which is also in good agreement with the required positive charge of the formula.

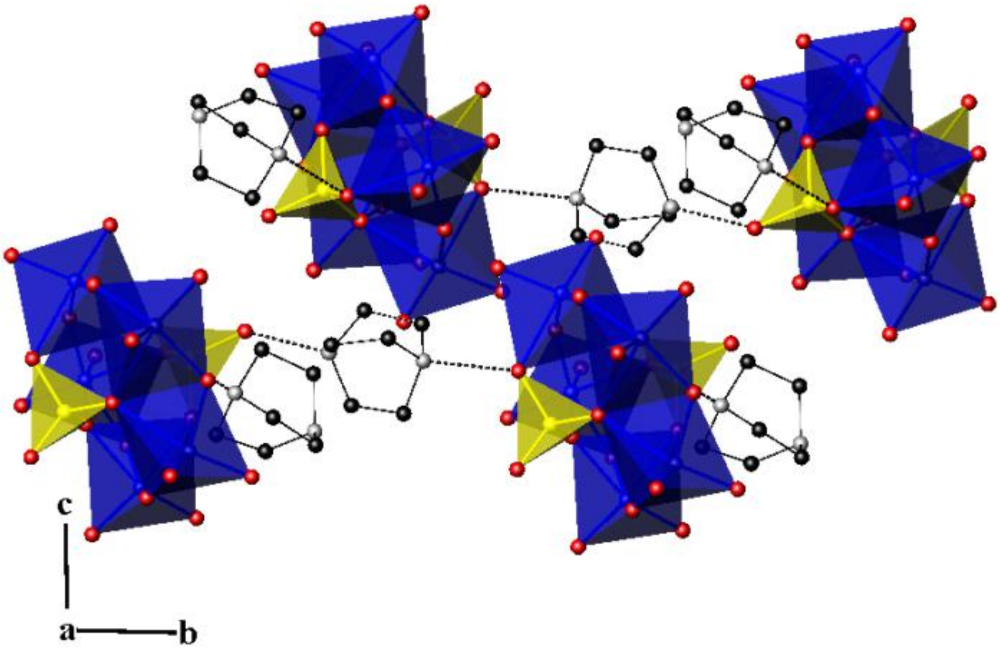

Figure 3.14: Schematic showing the different hydrogen bond links occurred between dabco molecules and the $[Mo_5O_{15}(PO_4)_2]^{6-}$ cluster polyanions.

IV. Characterization of $[(CH_3)_4N]_3[PMo_{12}O_{40}]$ (4)

Compound (4) $[(CH_3)_4N]_3[PMo_{12}O_{40}]$ crystallises in the Orthorhombic *Cmca* space group and its structure is shown in Figure 3.15. Single crystal X-ray diffraction of compound (4) (details of which are summarized in Table 3.7) has shown the structure to consist of the well known *α*-keggin type $[PMo_{12}O_{40}]^{3-}$ discrete polyanions counterbalanced by tetramethyl ammonium cations.

The crystal structure of the 12-molybdophosphoric acid $H_3Mo_{12}PO_{40}(H_2O)_n$ was first characterised by Strandberg and it can be thought of as being derived from Mo_3O_{13} triads of edge-shared MoO_6 octahedra that share common corners with a central PO_4 group to form a spherical arrangement of twelve MO_6 groups with a caged phosphate anion.[14] In the case reported here, compound (4) consists of the common distorted 'pseudo-keggin' polyanions in which molybdenum atoms are randomly distributed around the central phosphate anion. Molybdenyl groups Mo=O are not pointing towards the oxygen atoms of the phosphate anion, as typically occurs in the Keggin anion, but they are directed to the central phosphate atom by forming an angle of ~ 160° with the opposite trans Mo-O ligand. Therefore, the central phosphate group is rotationally disordered and exhibits two possible orientations that are related to each other through a four-fold rotational axis, having a cube-octahedral geometry with the oxygens distributed on eight atom sites of half occupancy.

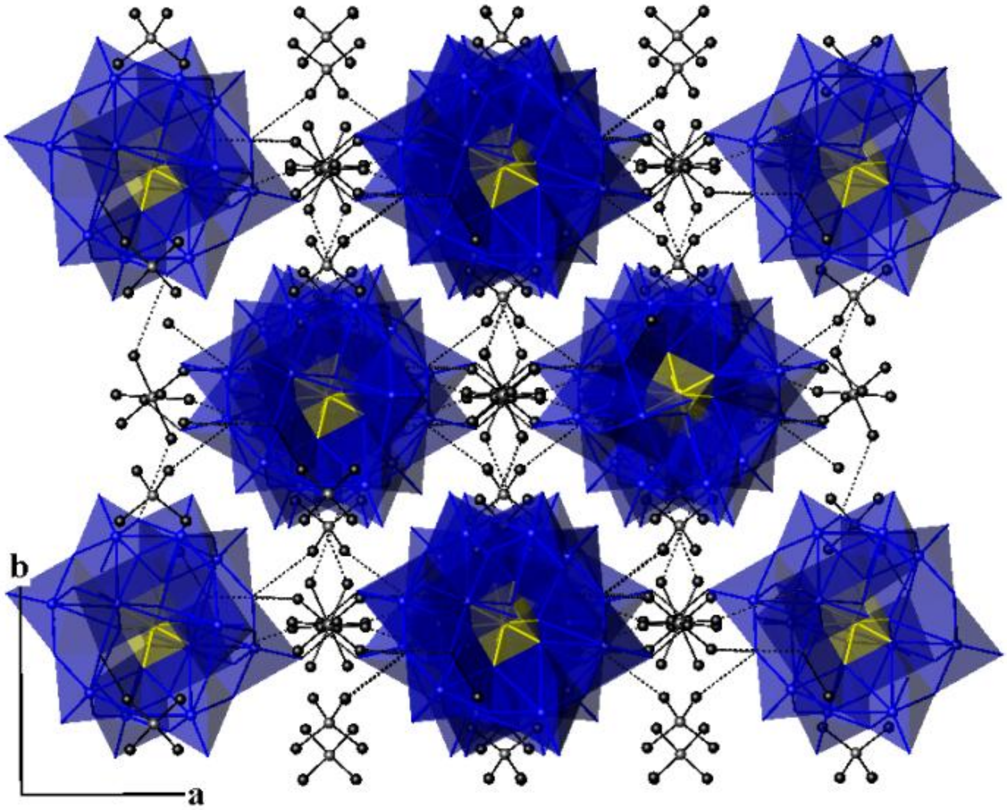

Figure 3.15: A perspective view of the structure of compound (4). Blue polyhedra represent the molybdenum octahedra and yellow polyhedra show the phosphate. Grey-black linked spheres comprise the tetramethylammonium cations.

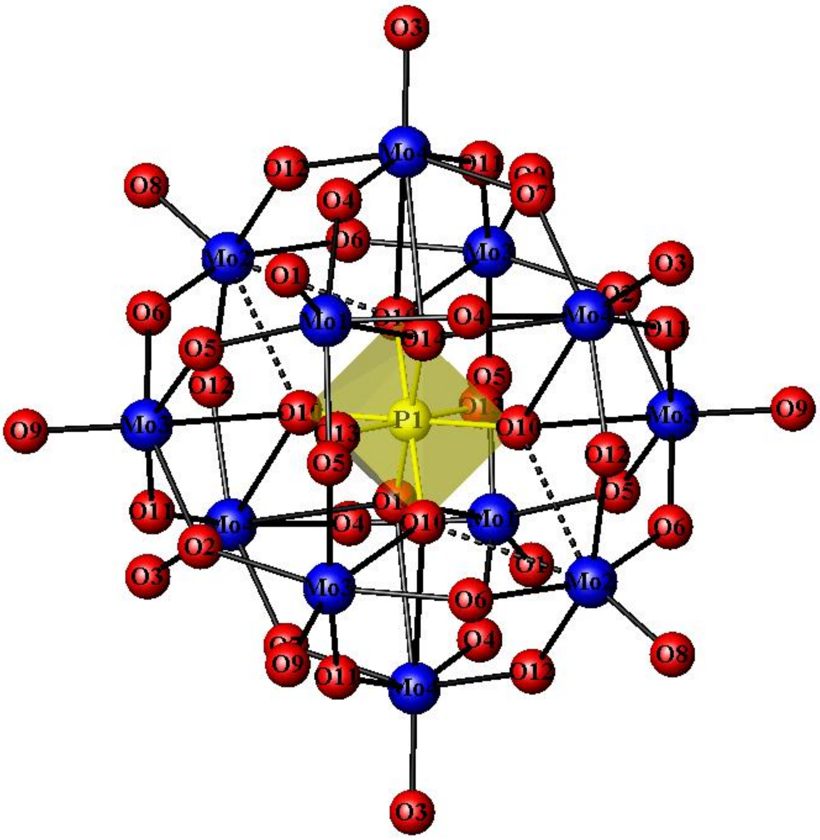

Figure 3.16: Schematic showing the pseudo Keggin $[PMo_{12}O_{40}]^{3-}$ polyanion in compound (4). The yellow cube-like octahedron represents the disordered phosphate anion.

Table 3.7: Crystal and diffraction information of compound (4).

Empirical formula	$C_{12}H_{36}N_3Mo_{12}PO_{40}$
Formula weight	2044.69
Temperature	120(2) K
Appearance	pale orange fragment
Wavelength	0.71073Å (Mo K_α)
Crystal system	Orthorhombic
Space group	*Cmca*
Unit cell dimensions	*a* = 19.7613(9) Å, *b* = 15.5441(9) Å *c* = 15.0147(9) Å,
Volume	4612.1(4) $Å^3$
Z	4
D_c	2.945 $g.cm^{-3}$
Θ range for data collection	2.95-28.64
Reflections collected	41061
Independent reflections	2099
Data/Restraints/Parameters	2099/0/185
R indices	$R_1 = 0.0586$ $wR_2 = 0.1482$

Table 3.8: Selected bond lengths (Å) and bond valences for compound (4).

Polyhedra	Bond lengths	Σs_{ij}	Polyhedra	Bond lengths	Σs_{ij}
$Mo(1)O_6$			$Mo(4)O_6$		
Mo(1)-O(1)	1.633(11)	2.097	Mo(4)-O(3)	1.650 (7)	2.003
Mo(1)-O(4)	1.898(9)	1.025	Mo(4)-O(4)	1.857(10)	1.145
Mo(1)-O(4’)	1.898(9)	1.025	Mo(4)-O(12)	1.864(9)	1.123
Mo(1)-O(5)	1.898(8)	1.025	Mo(4)-O(11)	1.900(10)	1.019
Mo(1)-O(5’)	1.898(8)	1.025	Mo(4)-O(7)	1.961(5)	0.864
Mo(1)-O(14)	2.426(18)	0.246	Mo(4)-O(14)	2.509(12)	0.098
		ΣMo1=6.44	Mo(4)-O(10)	2.511(13)	0.097
					ΣMo4=6.34
$Mo(2)O_6$					
Mo(2)-O(8)	1.628(12)	2.126	$P(1)O_4$		
Mo(2)-O(12)	1.895(8)	1.033	P(1)-O(13)	1.439(17)	0.809
Mo(2)-O(12’)	1.895(8)	1.033	P(1)-O(13)	1.439(17)	0.809
Mo(2)-O(6)	1.895(10)	1.033	P(1)-O(10)	1.514(13)	0.660
Mo(2)-O(6’)	1.895(10)	1.033	P(1)-O(10)	1.514(13)	0.660
		ΣMo2=6.26	P(1)-O(10)	1.514(13)	0.660
			P(1)-O(10)	1.514(13)	0.660
$Mo(3)O_6$			P(1)-O(14)	1.523(18)	0.645
Mo(3)-O(9)	1.642(8)	2.047	P(1)-O(14)	1.523(18)	0.645
Mo(3)-O(5)	1.855(8)	1.151			**ΣP1=5.51**
Mo(3)-O(6)	1.863(10)	1.126			
Mo(3)-O(11)	1.924(9)	0.955			
Mo(3)-O(2)	1.965(5)	0.855			
Mo(3)-O(10’)	2.414(12)	0.254			
		ΣMo3=6.39			

Figure 3.16 illustrates the pseudo-keggin polyanion found in compound (4). There are four crystallographically independent molybdenum sites which adopt the classic distorted octahedral geometry of Mo(VI) and show interactions with oxygens comparable to those reported in related structures consisting of the $[PMo_{12}O_{40}]^{3-}$ keggin polyanions.[8d, 14-15] Oxygen atoms may be divided into three main groups according to the coordination mode they adopt. First group includes the terminal oxygens connected to molybdenum centres. These have short Mo-O bond distances in the range of 1.628(12) – 1.650(7) Å. The second group involves the bridging oxygens between two Mo centres which exhibit intermediate distances in the range of 1.855(8)-1.965(5) Å, whereas the third group includes the oxygens of the central phosphate group that are triply bonded to three Mo atoms of Mo_3O_{13} units and show significantly lengthened bond distances in the range of 2.414(12)-2.511(13) Å.

Within the latter group, there is one oxygen atom O(10) located at a much longer distance from the corresponding molybdenum site (Mo(2)-O(10) ~2.56Å), and thus an elongated octahedral geometry can be suggested for this molybdenum site.

Discrete cluster anions are packed in a pseudo-3D network by generating voids where tetramethyl ammonium cations are hosted inside (shown in Figure 3.17). In fact, adjacent cluster polyanions of compound (4) are well separated from each other and they show relatively long distances between their terminal molybdenyl oxo groups (O(9)-O(8) = 3.919 Å, O(8)-O(3) = 3.859 Å, O(9)-O(3) = 4.103 Å, O(1)-O(3) = 4.151 Å. Hydrogen bonding interactions occurr between the methyl groups of $(CH_3)_4N^+$ cations and a number of framework oxygens with the C(H)···O distances ranging from 3.12 to 3.26 Å.

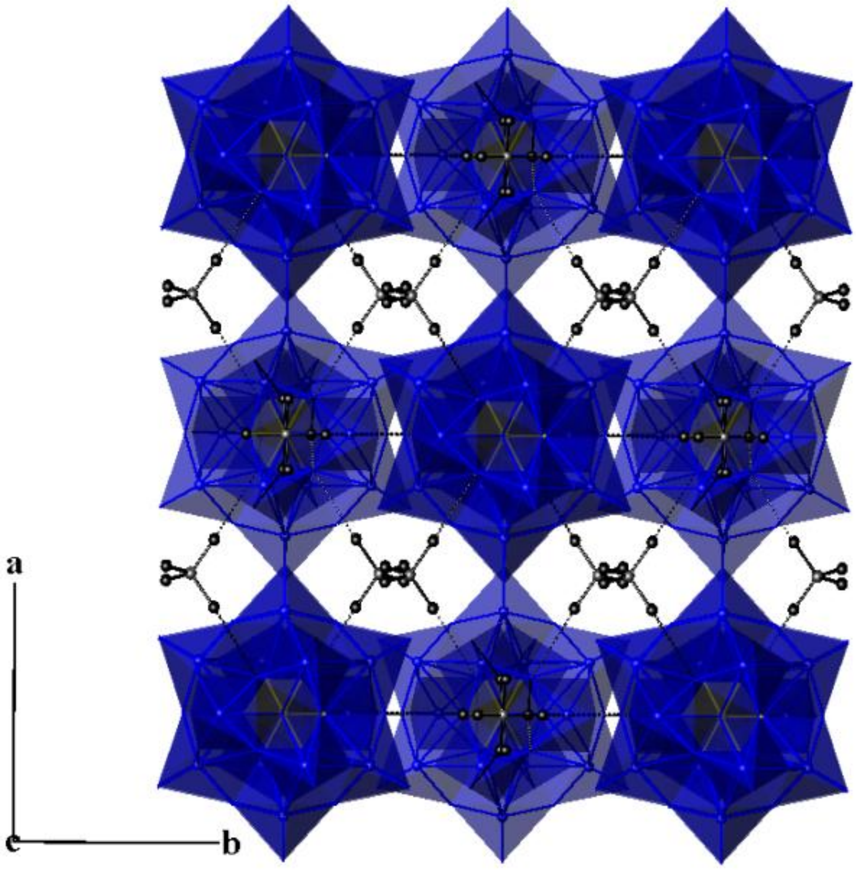

Figure 3.17: View of compound (4) along the *c* axis shows how discrete cluster anions are packed in a pseudo-3D network. Blue polyhedra represent the molybdenum octahedra and yellow polyhedra show the phosphate. Grey-black linked spheres comprise the tetramethylammonium cations.

V. Characterization of $\{C_2H_4(NH_3)_2\}_2Na\{Mo_6O_{15}(PO_4)_4\}_2.(H_2O)_{12.8}$ (5)

Compound (5) crystallised from initial reactions aimed at investigating the templating role of ethylenediamine in the current system. X-ray structural analysis of the crystalline phase revealed a structure consisted of discrete $\{Na[Mo_6P_4O_{31}]_2\}^{n-}$ polyanions, ethylenediamine cations and water molecules. Crystal and diffraction data are given in Table 3.9.

The previously reported $\{Na[Mo_6P_4O_{31}]_2\}^{n-}$ cluster polyanion[16] (shown in Figure 3.18) is built up from two identical $\{Mo_6P_4O_{31}\}^{n-}$ units that are connected together by a central sodium cation. The $[Mo_6P_4O_{31}]^{n-}$ cluster units may be considered as a coplanar ring composed of six edge-shared MoO_6 octahedra that show alternating single bonds Mo-Mo and non-bonding Mo···Mo interactions. There are three different phosphate groups that serve to cap the non-bonding Mo_2O_{10} bioctrahedral units of the $[Mo_6P_4O_{31}]^{n-}$ cluster through di-μ-(O,O')-phosphate bridges, in addition to one distinct phosphate group that is encapsulated in the centre of this Mo_6-ring and shares three corners with the three non-bonding Mo_2O_{10} dimeric units. The $P(1)O_4$ from the peripheral phosphate groups was modelled as disordered over two parts by a tilt pivoted on the two Mo bound oxygens.

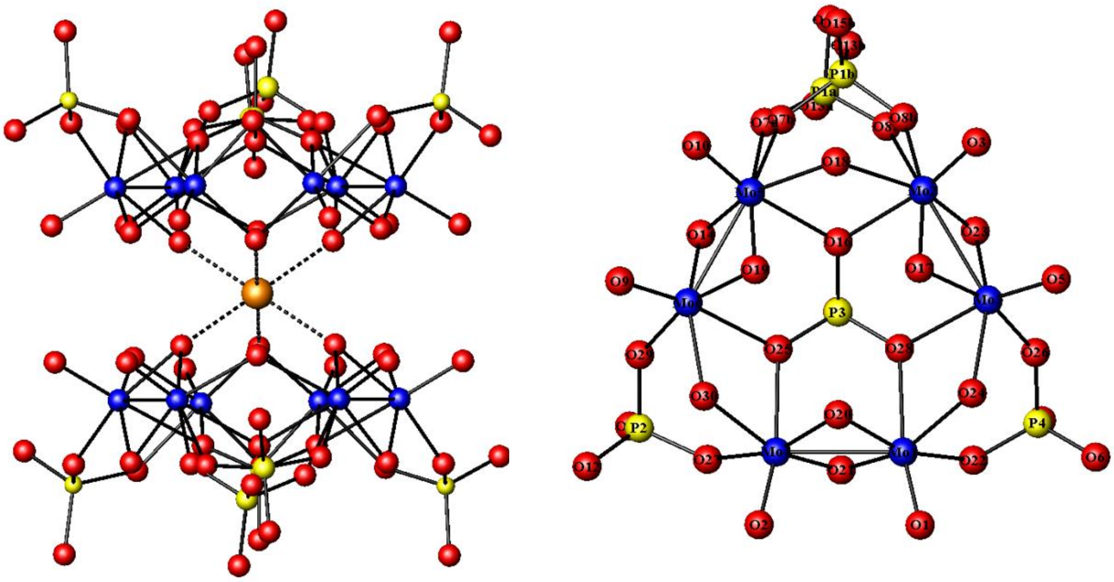

Figure 3.18: Schematic showing parts of the building unit of compound (5), $\{Na[Mo_6P_4O_{31}]_2\}.^{n-}$ cluster polyanion (LHS), $\{Mo_6P_4O_{31}\}^{n-}$ units (RHS). Molybdenum atoms are shown as blue spheres, phosphorous atoms as yellow spheres, oxygen atoms as red spheres and sodium cations as orange spheres.

Table 3.9: Crystal and diffraction information of compound (5).

Empirical formula	$C_4H_{20}N_4NaMo_{12}P_8O_{74.8}$
Formula weight	2743.07
Temperature	120(2) K
Appearance	Blue block
Wavelength	0.71073 Å (Mo K_α)
Crystal system	Monoclinic
Space group	$C2/c$
Unit cell dimensions	a = 24.8352(8) Å, b = 21.3667(7) Å c = 14.8070(4) Å, β = 111.593(2)°
Volume	7305.9(4) Å^3
Z	4
D_c	2.494 g.cm^{-3}
F(000)	5222
Θ range for data collection	2.92°-25.03°
Reflections collected	33908
Independent reflections	6441
Data/Restraints/Parameters	6441/300/450
R indices	R_1 = 0.0957, wR_2 = 0.1962

Bond valence calculations completed on the molybdenum sites have shown all the Mo centres to adopt the reduced +5 oxidation state (shown in Table 3.11). Each molybdenum centre of the $\{Mo_6P_4O_{31}\}^{n-}$ units exhibits the classic distorted octahedral geometry due to the presence of the characteristic short bond which can be attributed to the Mo=O oxo group, opposite to a significantly lengthened Mo-O bond ~2.3 Å. Additionally, each Mo site is involved in Mo-Mo bonding and the corresponding metal-metal distances are the followings: Mo(1)-Mo(4) = 2.588(2) Å, Mo(2)-Mo(3) = 2.591(2) Å, Mo(5)-Mo(6) = 2.584(2) Å.

Looking at the four remaining equatorial Mo-O distances, these would be divided into three groups. The first group involves the bridging oxygens, between MoO_6 and PO_4 groups, which are within the expected intermediate range (Mo-O = 1.985(34)-2.047(10) Å, BV(O) = 1.56-1.86). The second group includes the bridging oxygens which are located at the common edges of the M-M bonding Mo_2O_{10} bioctrahedral units and show intermediate bonds of similar length (Mo-O = 1.917(12)-1.957(10) Å, BV(O) = 1.91-1.76). Finally the third group includes the bridging oxygens, located at the common edges of the non bonding Mo_2O_{10} bioctrahedral units, which exhibit slightly longer distances than the expected intermediate length (Mo-O = 2.119(11)-2.134(10), BV(O) = 1.162-1.091). Looking at the latter group, it would appear that it exhibits considerably lower bond valence values compared to the rest groups, suggesting the lack of electron density around these oxygen sites.

Investigation of the bond lengths in phosphate tetrahedra (summarised in Table 3.10) has shown that the terminal oxygens in both types of phosphate groups show relatively shorter bonds (P-O$_t$ = 1.500(16)-1.532(16) Å, BV(O)$_t$ = 1.37-1.26) compared to the bridging oxygens (P-O$_b$ = .1.531-1.566(13) Å). When comparing the bond lengths of the phosphate groups with related previously reported polyanions [8c, 16-17], it can clearly be seen that much longer P-O distances usually occur (P-O ~ 1.57Å, BV(O) ~ 1.14) when the phosphate constitutes a P-OH bond and much shorter distances (P-O~ 1.48 Å,BV(O) ~ 1.45) occur when the phosphate comprises an oxo group. In the structure reported here, the corresponding P-O$_t$ bond lengths seem to be in between those two ranges, showing that there can exist a possible hydrogen delocalization between terminal oxygen atoms and guest species.

Table 3.10: Selected bond lengths (Å) and bond valences for PO$_4$ in compound (5).

Tetrahedra PO$_4$	Bond lengths	**Σs**$_{ij}$	Tetrahedra PO$_4$	Bond lengths	**Σs**$_{ij}$
P(1A)O$_4$			P(2)O$_4$		
P(1A)-O(13A)	1.503(18)	1.361	P(2)-O(12)	1.502(17)	1.365
P(1A)-O(15A)	1.508(17)	1.343	P(2)-O(11)	1.532(16)	1.258
P(1A)-O(8A)	1.533(15)	1.255	P(2)-O(27)	1.552(12)	1.192
P(1A)-O(7A)	1.565(16)	1.151	P(2)-O(29)	1.566(13)	1.150
		ΣP1$_A$ = 5.11			**ΣP2 = 4.97**
P(1B)O$_4$			P(3)O$_4$		
P(1B)-O(13B)	1.500(16)	1.372	P(3)-O(31)	1.509(12)	1.339
P(1B)-O(15B)	1.517(17)	1.310	P(3)-O(25)	1.531(11)	1.262
P(1B)-O(8B)	1.531(14)	1.262	P(3)-O(16)	1.540(11)	1.231
P(1B)-O(7B)	1.561(15)	1.163	P(3)-O(28)	1.541(12)	1.228
		ΣP1$_B$ = 5.11			**ΣP3 = 5.06**
			P(4)O$_4$		
			P(3)-O(6)	1.502(12)	1.365
			P(3)-O(4)	1.515(10)	1.317
			P(3)-O(26)	1.538(10)	1.238
			P(3)-O(22)	1.558(10)	1.173
					ΣP4 = 5.09

Table 3.11: Selected bond lengths (Å)-bond valences for MoO_6 in compound (5).

Octahedra MoO_6	Bond lengths	Σs_{ij}	Octahedra MoO_6	Bond lengths	Σs_{ij}
Mo(1)O_6			Mo(4)O_6		
Mo(1)-O(1)	1.686(10)	1.817	Mo(4)-O(2)	1.679(10)	1.852
Mo(1)-O(21)	1.929(11)	0.942	Mo(4)-O(20)	1.932(10)	0.935
Mo(1)-O(20)	1.942(10)	0.909	Mo(4)-O(21)	1.938(11)	0.919
Mo(1)-O(22)	2.047(10)	0.685	Mo(4)-O(27)	2.029(11)	0.719
Mo(1)-O(24)	2.128(10)	0.550	Mo(4)-O(30)	2.123(11)	0.558
Mo(1)-O(28)	2.298(10)	0.348	Mo(4)-O(25)	2.262(10)	0.383
		ΣMo=5.25			**ΣMo4=5.36**
Mo(2)O_6			Mo(5)O_6		
Mo(2)-O(3)	1.694(12)	1.778	Mo(5)-O(10)	1.681(11)	1.842
Mo(2)-O(23)	1.945(11)	0.902	Mo(5)-O(14)	1.917(12)	0.973
Mo(2)-O(17)	1.950(10)	0.890	Mo(5)-O(19)	1.940(10)	0.915
Mo(2)-O(18)	2.116(10)	0.568	Mo(5)-O(16)	2.299(11)	0.347
Mo(2)-O(16)	2.285(12)	0.360	Mo(5)-O(18)	2.097(11)	0.598
Mo(2)-	2.212(27)	0.219	Mo(5)-O(7A)	1.985(34)	0.405
O(8A)	1.968(21)	0.424	Mo(5)-O(7B)	2.121(25)	0.280
Mo(2)-O(8B)		**ΣMo2**=5.14			**ΣMo5=5.36**
Mo(3)O_6			Mo(6)O_6		
Mo(3)-O(5)	1.675(12)	1.872	Mo(6)-O(9)	1.687(12)	1.812
Mo(3)-O(23)	1.956(11)	0.876	Mo(6)-O(14)	1.930(12)	0.939
Mo(3)-O(17)	1.957(10)	0.874	Mo(6)-O(19)	1.942(11)	0.909
Mo(3)-O(26)	2.042(10)	0.694	Mo(6)-O(29)	2.040(12)	0.698
Mo(3)-O(24)	2.134(10)	0.541	Mo(6)-O(30)	2.119(11)	0.564
Mo(3)-O(28)	2.306(12)	0.340	Mo(6)-O(25)	2.301(11)	0.345
		ΣMo3=5.20			**ΣMo5=5.27**

Projection of the structure along the *c* axis shows how $\{Na[Mo_6P_4O_{31}]_2\}^{n-}$ polyanions are packed in a complex layered network (Figure 3.19). This arrangement produces two different space fillings: one separating the layers consisting of water molecules, while between adjacent $\{Na[Mo_6P_4O_{31}]_2\}^{n-}$ polyanions is an intricate arrangement of ethylenediamine cations and water molecules. Figure 3.20 illustrates the projection of one single layer along *α* axis where bulky blocks, consisted of densely packed $\{Na[Mo_6P_4O_{31}]_2\}^{n-}$ polyanions, are surrounded by the guest species. An intricate network of hydrogen bonding is present within these layers, such that all the N and O atoms from ethylenediamine cations and water molecules respectively act as H-bond donors, providing stabilization of the framework structure. All the donors are within hydrogen bonding distance of a number of the framework O atoms with the N(H)···O distances ranging from 2.7695 to 3.1980 Å and the $O_w(H)\cdots O$ distances in the range of 2.5278-3.1995 Å).

At this stage it is worth mentioning that locating hydrogen atoms within the crystalline structure of compound (5) was difficult. Thus, compound (5) contains relatively heavy atoms and thereby many difficulties were encountered in locating hydrogens due to the high difference in relative X-ray scattering factors. In addition, numerous possible hydrogen locations exist, including the bridging oxygens located at the common edges of the Mo_2O_{10} bioctrahedral units of the polyanion, the terminal oxygen sites of the phosphate groups, in addition to the ten crystallographically distinct water molecules of which some are expected to form hydronium ions H_3O^+. Consequently, the structure effectively adopts an average of these positions and the problem becomes location of a fraction of a hydrogen atom.

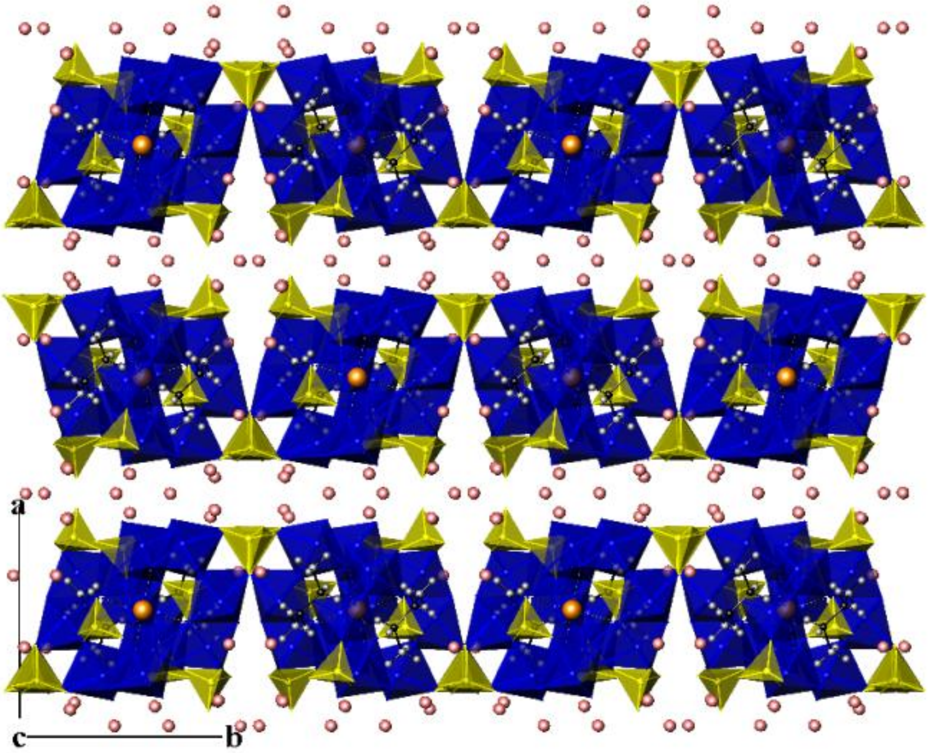

Figure 3.19: A perspective view of the structure of compound (5) showing the packing arrangement of $\{Na[Mo_6P_4O_{31}]_2\}^{n-}$ polyanions along the *c* axis. Blue polyhedra represent the molybdenum octahedra and yellow polyhedra show the phosphate. Pink spheres show the water molecules and grey-black linked spheres comprise the ethylenediamine cations.

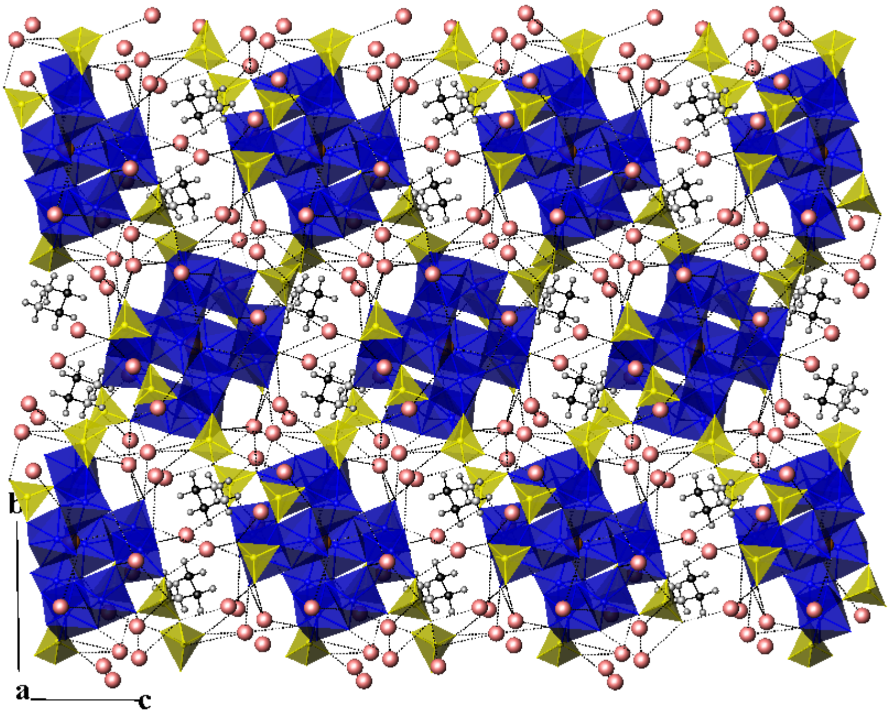

Figure 3.20: Projection of a single layer in the structure of (5) (along the *a* axis) shows how adjacent polyanions are linked together through water molecules and ethylenediamine cations.

3.2.3 Conclusions

Synthetic work in this chapter was aimed at investigating the templating effect of organic amines in systems that involved hydrothermal treatment of a molybdenum source with phosphate and borate sources. Most reactions resulted in glassy product phases or either yielded clear solutions. In cases of isolated crystalline products, single crystal X-ray diffraction revealed various structural units composed of linked molybdenum octahedra and phosphate tetrahedra. Borate units did not participate in these framework structures, assuming that the polymerization of borate with phosphate units was very unfavourable. Three cluster polyanions in addition to a ribbon-like structure were investigated. Common structural features involve the polyhedral connectivity of MoO_6 octahedra through common edges to form different types of molybdenum rings grafted by phosphate tetrahedra. The ribbon-like structure exhibits a simple building unit consisting of corner sharing MoO_6 octahedra and PO_4 tetrahedra. In all cases, organic amines are involved in strong hydrogen bonding interactions, allowing further stabilisation of the framework structure.

3.3 Molybdenophosphates *via* high temperature techniques

Investigations of inorganic-templated molybdenum phosphates *via* high temperature routes resulted in the successful preparation of a new rubidium templated structure, $Rb(MoO_2)_2(P_3O_{10})$, which contains chains of alternating MoO_6 octahedra and PO_4 tetrahedra connected into layers by phosphate bridges. This compound is reported here so as to present its particular structural features and allow comparisons between related compounds obtained *via* different synthetic routes.

3.3.1 Experimental

I. Synthesis

The reaction mixture: RbH_2PO_4 (0.073 g, 0.4 mmol), $NH_4H_2PO_4$ (0.046 g, 0.4 mmol) and MoO_3 (0.087 g, 0.6 mmol) was ground together in a pestle and mortar before being transferred to a platinum crucible and heated to 823 K for 12 hours. The reaction mixture was then cooled down slowly to 673 K and quenched to room temperature by removing the crucible from the furnace. Once cool the product was washed with hot water and filtered, leaving a mixed product phase consisted of colourless crystals of compound (6) and an amorphous powder.

3.3.2 Results and discussion

$Rb(MoO_2)_2(P_3O_{10})$ (6) was successfully synthesised during the investigation of preparing molybdenum phosphate frameworks *via* high temperature flux-growth methods. Compound (6) crystallises in the monoclinic $P2_1$ space group and crystal and diffraction data are given in Table 3.12. Its framework structure (shown in Figure 3.21) can be best considered as derived from chains of alternating MoO_6 octahedra and PO_4 tetrahedra which are connected together by bridging phosphate groups, generating a two-dimensional layered structure. Rubidium cations are located in between these anionic molybdenophosphate layers, allowing interlinking of adjacent layers along the third axes.

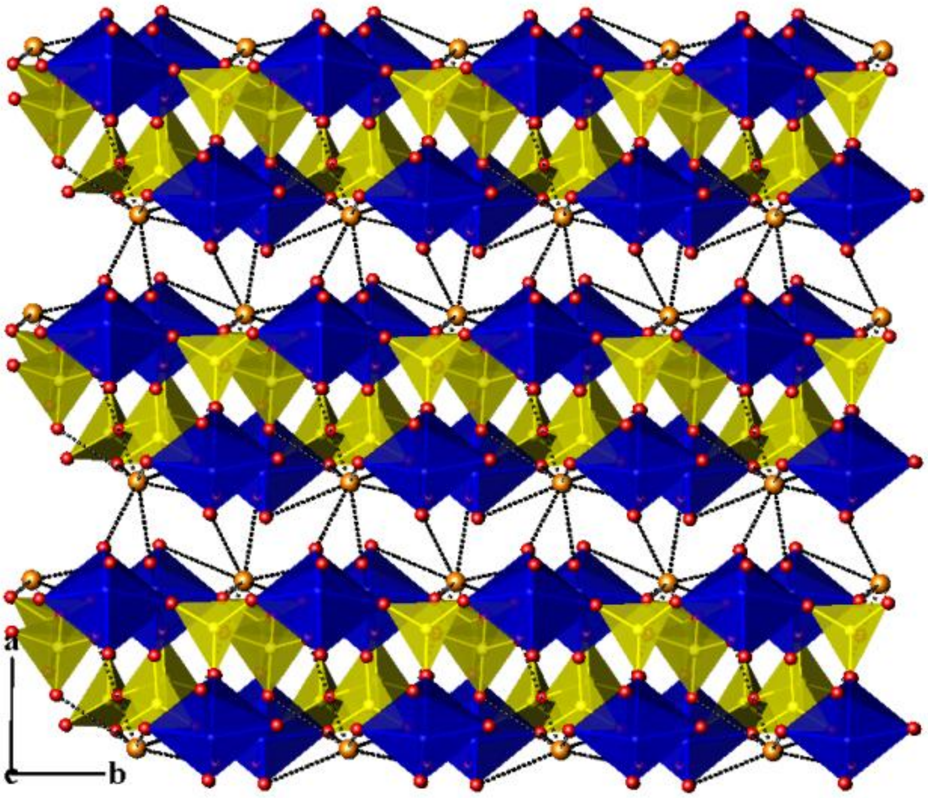

Figure 3.21: Layered structure of compound (6) viewed down the *c* axis. Blue polyhedra represent the molybdenum octahedra and yellow polyhedra show the phosphate. Orange spheres show the rubidium cations.

Table 3.12: Crystal and diffraction information of compound (6).

Empirical formula	$RbMo_2P_3O_{14}$
Formula weight	601.71
Temperature	120(2) K
Appearance	Colourless block
Wavelength	0.71073 Å (Mo K_α)
Crystal system	Monoclinic
Space group	$P2_1$
Unit cell dimensions	a = 7.9797(5) Å, b = 6.3152(4) Å c = 11.8716(7) Å, β = 96.215(4)°
Volume	594.73(6) $Å^3$
Z	2
D_c	1.659 $g.cm^{-3}$
Θ range for data collection	2.93°-27.55°
Reflections collected	5745
Independent reflections	1882
Data/Restraints/Parameters	1882/85/182
R indices	$R_1 = 0.0535$ $wR_2 = 0.1389$

There are two types of chains, $[Mo(1)P(2)O_7]_\infty$ and $[Mo(2)P(3)O_7]_\infty$, which exhibit identical bonding motifs based on a repeating four-connected net of alternating MoO_6 octahedra and PO_4 tetrahedra (illustrated in the Figures 3.22 and 3.23). Each molybdenum site [Mo(1), Mo(2)] of the chains is coordinated to two cis terminal oxo groups, three oxygen donors from three different phosphate groups whilst the fourth apical is occupied by an oxygen donor from the bridging $P(1)O_4$ tetrahedron. The two crystallographically independent Mo atoms (Mo1, Mo2) show interactions with oxygen comparable to those reported in other Mo(VI) phosphates. They exhibit the classic distorted octahedral geometry with two adjacent short Mo-O distances (1.687(12)-1.699(13) Å) forming a molybdenyl group, with opposite longer Mo-O bonds (1.998(16)-2.017(15) Å) and two additional bonds of intermediate length (2.147(15)-2.245(13) Å). The tetrahedral geometry of the two distinct phosphate groups [P(2), P(3)] is defined by three oxygen donors from three different Mo octahedra, whereas the fourth apical is occupied by an oxygen donor from the bridging $P(1)O_4$ tetrahedron. Investigations of the P(2)/(3)-O bond lengths has shown that both phosphate tetrahedra pose very characteristic bond distances for all the bridging oxygen donors from MoO_6 octahedra (1.486(13)-1.512(15) Å), however, they show slightly longer bond distances (~1.6 Å) for the oxygens shared with the bridging $P(1)O_4$ tetrahedra. All the bond lengths and bond valence calculations are summarised in Table 3.13).

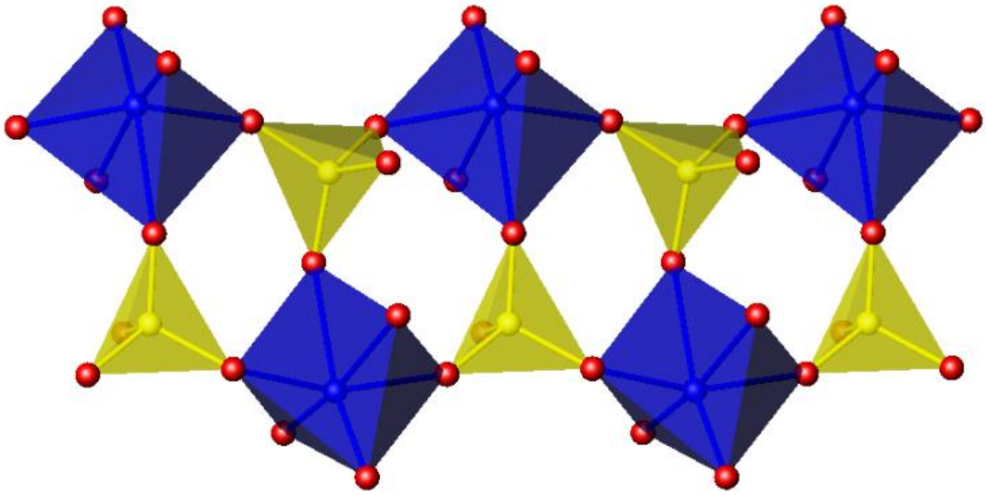

Figure 3.22: Schematic showing the bonding motif of the $[Mo(1)P(2)O_7]_\infty$ and $[Mo(2)P(3)O_7]_\infty$,chains in compound (6).

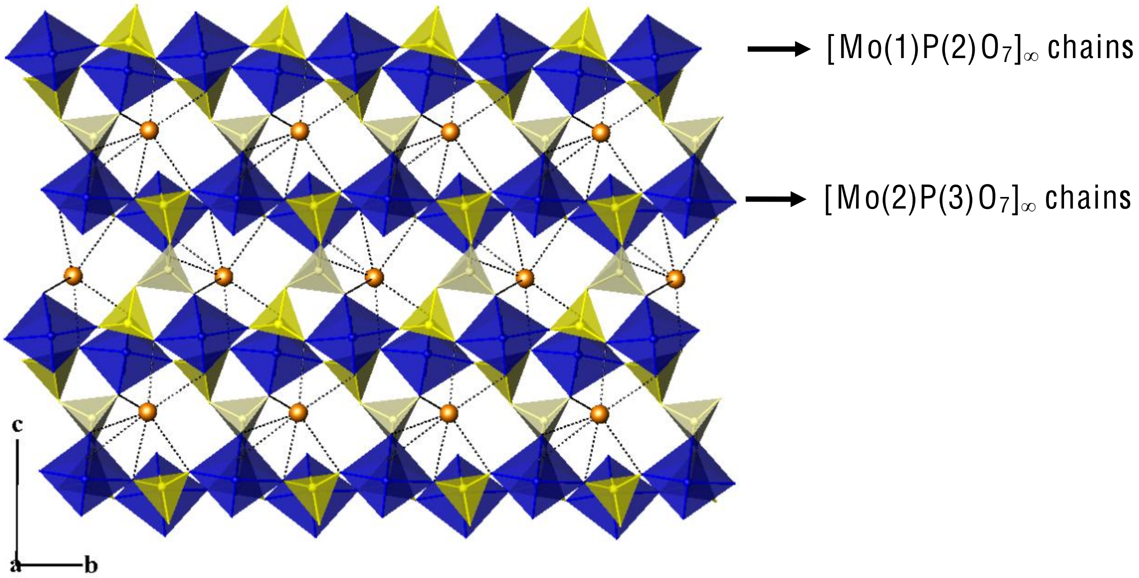

Figure 3.23: The view along the *a* axis shows details of the channels in the structure of compound (6). Molybdenum octahedra and phosphate tetrahedra from the chains are shown here as blue and yellow respectively, whereas the bridging $P(1)O_4$ type tetrahedra are shown in pale yellow. Orange spheres present the rubidium cations.

Viewing down the *a* axis (Figure 3.23), it can be seen that these two distinct chains, $[Mo(1)P(2)O_7]_\infty$ and $[Mo(2)P(3)O_7]_\infty$, are related to each other by a two-fold rotation axis and therefore they can be thought of as being enantiomers. $P(1)O_4$ bridging tetrahedra serve to link these chains together through di-μ-(O,O') bridges, leading to a relative displacement of the chains such as that related atoms of adjacent chains are not pointing exactly towards each other. Such polyhedral connectivity mode generates seven membered-rings with a channel system running along the direction perpendicular to the molybdenophosphate layers.

Rubidium cations are located slightly off centre of the channel and occupy preferentially sites which are very close to the molybdenophosphate anionic layers (shown in Figures 3.21, 3.23). There is only one crystallographically independent site Rb(1) that adopts an irregular geometry and its coordination sphere is defined by two terminal Mo=O oxo groups and five bridging oxygens from the same layer in addition to two terminal Mo=O oxo groups from an adjacent layer ($d_{av}(Rb\cdots O)$ = 3.082, $BV(Rb)_{av}$ = 1.12).

Table 3.13: Selected bond lengths (Å) and bond valences for compound (6).

Polyhedra	Bond lengths	Σs_{ij}	Polyhedra	Bond lengths	Σs_{ij}
Mo(1)O$_6$			P(2)O$_4$		
Mo(1)-O(7)	1.687(12)	1.812	P(2)-O(14)	1.486 (13)	1.425
Mo(1)-O(6)	1.698(12)	1.759	P(2)-O(3)	1.501(15)	1.368
Mo(1)-O(13)	1.998(16)	0.782	P(2)-O(13)	1.511(16)	1.332
Mo(1)-O(3)	2.012(14)	0.753	P(2)-O(11)	1.599(12)	1.050
Mo(1)-O(14)	2.163(13)	0.501			**ΣP2 = 5.18**
Mo(1)-O(10)	2.245(13)	0.401			
		ΣMo1 = 6.01	P(3)O$_4$		
			P(3)-O(12)	1.477(16)	1.460
Mo(2)O$_6$			P(3)-O(1)	1.482(15)	1.440
Mo(2)-O(4)	1.691(13)	1.793	P(3)-O(2)	1.512(15)	1.328
Mo(2)-O(5)	1.699(13)	1.754	P(3)-O(8)	1.607(12)	1.027
Mo(2)-O(1)	2.005(13)	0.767			**ΣP3 = 5.26**
Mo(2)-O(2)	2.017(15)	0.743			
Mo(2)-O(12)	2.157(15)	0.509	Rb(1)···O$_9$		
Mo(2)-O(9)	2.184(12)	0.473	Rb(1)···O(4)	2.800(14)	0.234
		ΣMo2 = 6.04	Rb(1)···O(6)	2.883(13)	0.187
			Rb(1)···O(5)	2.935(16)	0.163
P(1)O$_4$			Rb(1)···O(2)	3.025(12)	0.128
P(1)-O(10)	1.465(14)	1.508	Rb(1)···O(10)	3.062(14)	0.115
P(1)-O(9)	1.487(13)	1.421	Rb(1)···O(3)	3.063(13)	0.115
P(1)-O(11)	1.589(13)	1.079	Rb(1)···O(13)	3.194(14)	0.081
P(1)-O(8)	1.606(13)	1.030	Rb(1)···O(7)	3.271(14)	0.066
		ΣP1 = 5.04	Rb(1)···O(9)	3.512(13)	0.034
					ΣRb1 = 1.12

From a structural point of view, $Rb(MoO_2)_2(P_3O_{10})$ (6) can be thought of as being derived from the three-dimensional framework $MoOPO_4$.[1] There are several previously-reported compounds which can be regarded as derivatives of the $MoOPO_4$ compound; these were obtained from high temperature reactions in evacuated quartz ampoules.[18] They exhibit relatively dense layer structures, templated by inorganic cations such as K^+, Ba^{2+}, Cs^+, Rb^+; and their framework structures can be described in terms of layers built up from identical chains to those discussed here. However different bonding motifs have been identified, concerning the bridging manner of adjacent chains. In the structure discussed here the difference derives from the presence of bridging phosphate tetrahedra that exhibit two di-μ-(O,O') coordination links with the adjacent chains. Looking at the two previously reported three-dimensional frameworks: $CH_3NH_3[Mo_2O_2(PO_4)_2\ (H_2PO_4)]$[19] and $Cs(H_3O)[Mo_2O_2(PO_4)_2\ (HPO_4)]$,[5d] it would appear as they consist of layers which show identical bonding motif to that observed in compound (6). However, in those compounds layers are connected together through bridging H_2PO_4 groups to form three-dimensional porous frameworks. Taking into account that those compounds were obtained by low-temperature hydrothermal routes, one might expect the phosphate linkers to become protonated and thereby to allow connectivity only through *trans*-corner sharing in such a way as to generate large void spaces between adjacent layers.

3.3.3 Conclusions

The rubidium templated molybdenum phosphate compound $Rb(MoO_2)_2(P_3O_{10})$ (6) was obtained *via* high temperature flux-growth methods and characterised by single crystal X-ray diffraction. Its framework structure embraces chains of alternating MoO_6 octahedra and PO_4 tetrahedra, linked together by bridging phosphate tetrahedra. A further structural feature is the presence of seven membered-rings that generate a channel system, filled with rubidium cations, running along the direction perpendicular to the layers. From a general point of view, compound (6) can be categorised in the family of compounds which derived from the $MoOPO_4$. This family includes a number of condensed layered structures which were obtained under similar high temperature methods as well as three dimensional microporous frameworks which were successfully prepared under mild hydrothermal conditions.

3.4 Oxyfluorinated molybdenum phosphates

Research shifted towards the investigation of the role of fluoride in molybdenophosphate frameworks formation. Different fluoride sources were investigated as well as a number of organic templating agents. The first oxyfluorinated molybdenum phosphate compound has been successfully obtained under mild hydrothermal routes in presence of piperazine acting as a templating agent. This new framework structure comprises of layers built up from alternating MoO_5F octahedra and PO_4 tetrahedra with embedded piperazine cations and water molecules.

3.4.1 Experimental

Two synthetic routes were followed which differ in the fluoride source used. Brief descriptions of synthetic procedures for preparing the reaction mixtures are given here. Isolated compounds were characterised by single crystal X-ray diffraction, TGA and IR analysis (as described previously in Section 3.1.1). In addition, EDS analysis and Bond Valence calculations were carried out in order to clarify the location of near isoelectronic species, such as oxide and fluoride ions.

I. Synthesis

- ✓ Synthetic route *via* FPO_3H_2 source

$$MoO_3 \, / \, (NH_4)_2MoO_3F_2 + FPO_3H_2 + \text{organic amine} + H_2O$$

The general procedure entailed hydrothermal treatment of a molybdenum source (MoO_3 or $(NH_4)_2MoO_3F_2$) with fluorophosphoric acid (FPO_3H_2 70 wt % in H_2O) in presence of a templating agent (piperazine, dabco, ethylenediamine). A series of reactions was carried in which the molar composition of the phosphorus source (P/Mo_{ratio} = any integer value in the range of 1-6) was varied in mixtures of constant $Mo/amine/H_2O_{molar\ ratios}$ = 1/1/520 or 1/2/520 (where $n_{moles,x=1}$ = 0.32 mmol) and a wide range of pH was achieved. Final reaction mixtures were stirred for about one hour at room temperature before being added to a 23 mL Teflon-lined steel autoclave. The reaction temperature was varied from 413 K (held for 4 days) to 453 K (held for 2 days).

Note that all starting materials were commercially available, except for the $(NH_4)_2MoO_3F_2$ which was prepared from the stoichiometric mixture of NH_4F (0.822 g, 0.022 mol), MoO_3 (0.533 g, 0.037 mol) and distilled water (10 mL, 0.555 ml). The corresponding reaction mixture was slowly heated up until a clear solution is obtained (70 °C) and was continued heating up to ~ 90 °C where finally the product phase precipitated as white crystalline powder.

- ✓ Synthetic route *via* HF source

$$MoO_3 + H_3PO_4 + HF + \text{organic amine} + H_2O$$

The general procedure consisted of addition of molybdenum oxide source (MoO_3) and phosphoric acid (H_3PO_4 85 wt % in H_2O) in distilled water. Then the required amount of hydrofluoric acid (HF 48 wt % in H_2O) was added to the mixture (*Caution!* HF is highly toxic and corrosive, do not use without taking professional advice), followed by the addition of the organic amine. A series of reactions were performed by varying the molar composition of the phosphorous source (P/Mo_{ratio} = any integer value in the range of 1-6) in mixtures of constant $Mo/HF/amine/H_2O_{molar\ ratios}$ = 1/2/1/290 or 1/2/2/290 (where $n_{moles,x=1}$ = 0.32 mmol). Final reaction mixtures were stirred for about one hour at room temperature before being added to a 23 mL Teflon-lined steel autoclave. The reaction temperature was varied from 413 K (held for 4 days) to 453 K (held for 2 days).

3.4.2 Results and discussion

I. Synthesis overview

During this investigation, a unique oxyfluorinated molybdenophosphate $[H_2N(C_2H_4)_2NH_2]_{0.5}\{MoO[PO_4]F\}.H_2O_{0.5}$ (7) has been successfully synthesised, whereas non-fluorinated product phases varied considerably. The pH appeared to be the main key factor for the formation of these products. Reactions that entailed incorporation of piperazine were very successful, leading to the isolation of compound (7) whose structural features are discussed here. Compound (7) was successfully obtained *via* the FPO_3H_2 route from mixtures consisting either MoO_3 or $(NH_4)_2MoO_3F_2$ molybdenum sources. In the case of MoO_3, this was stably formed when $Mo/P/piperazine_{molar\ ratio}$ = 1/6/2 or 1/4/1, where the pH of the reaction was maintained in the range of 2-4. When the pH was increased to any value greater than four, the system tended to form the previously reported pseudo Keggin polyanion $(pip)_{1.5}[PMo_{12}O_{40}].21H_2O$ (details of which are given in Section 3.2.2).[14] In the presence of $(NH_4)_2MoO_3F_2$, compound (7) occurred in the pH region ~ 2-4 (for the range of Mo/P/piperazine$_{\text{molar ratio}}$ = 1/1/2-1/4/2), whereas the rest of the reaction mixtures resulted in having no products in their solutions. Following the second synthetic route (*via* HF), compound (7) was isolated from a wide range of Mo/P$_{\text{molar ratio}}$ = 1/1 - 1/5, but in those cases the product yields were relatively low. Using this route, compound (7) could be rapidly formed at higher temperatures and in rather shorter reaction times (180° C, 2 days) compared to the first route (140 °C, 4 days).

To investigate the templating effect of the amine, additional experiments took place in the presence of dabco and ethylenediamine. When dabco was introduced into the system, many difficulties were encountered in forming a solid product, since the majority of the reactions led to clear solutions. Although a wide range of reactions took place and especially under acidic conditions (pH 2-4), a crystalline product was only achievable from one unique combination. Whilst following the first synthetic route, a reaction mixture consisting of $(NH_4)_2MoO_3F_2/FPO_3H_2$/ dabco in a 1/1/2 ratio with a pH~3.5 (heated to 175 °C and held for 4 days) resulted in a minor crystalline phase. Few crystals were enough to be characterised by single crystal X-ray diffraction, revealing a structure isotypical to compound (7). However, due to the twinned nature of the crystals the structure obtained has relatively high R values.

On the other hand, reactions in presence of ethylenediamine template were fruitless. Similarly to dabco, reactions *via* FPO_3H_2 route resulted in clear solutions. Reactions *via* HF route formed only glassy phases at the very high temperatures (180 °C, 2 days), but a crystalline product was successfully obtained when lower temperatures and longer reaction times were applied (140 °C, 4 days). Single crystal X-ray diffraction of the crystalline product revealed a structure which consists of the previously reported $[Mo_5O_{15}(PO_4)_2]^{6-}$ cluster anions templated by sodium cations and ethylenediamine cations (the analogous dabco-templated structure was described earlier in Section 3.2.2-III).[12a]

II. Characterization of $[H_2N(C_2H_4)_2NH_2]_{0.5}\{MoO[PO_4]F\}.H_2O_{0.5}$ (7)

Single crystal X-ray diffraction of compound (7) (details of which are summarized in Table 3.14) has shown the structure to consist of layers of alternating molybdenum octahedra and phosphate tetrahedra with embedded piperazine cations and water molecules (Figure 3.24). There is only one crystallographically distinct molybdenum site Mo1 which shares its four equatorial oxygen atoms with four different phosphate tetrahedra by generating a repeating four-connected net (demonstrated in Figure 3.25). The octahedral geometry of molybdenum is completed by a terminal oxo group opposite to a fluoride ligand which are always perpendicular to the layers and alternate in up and down orientations.

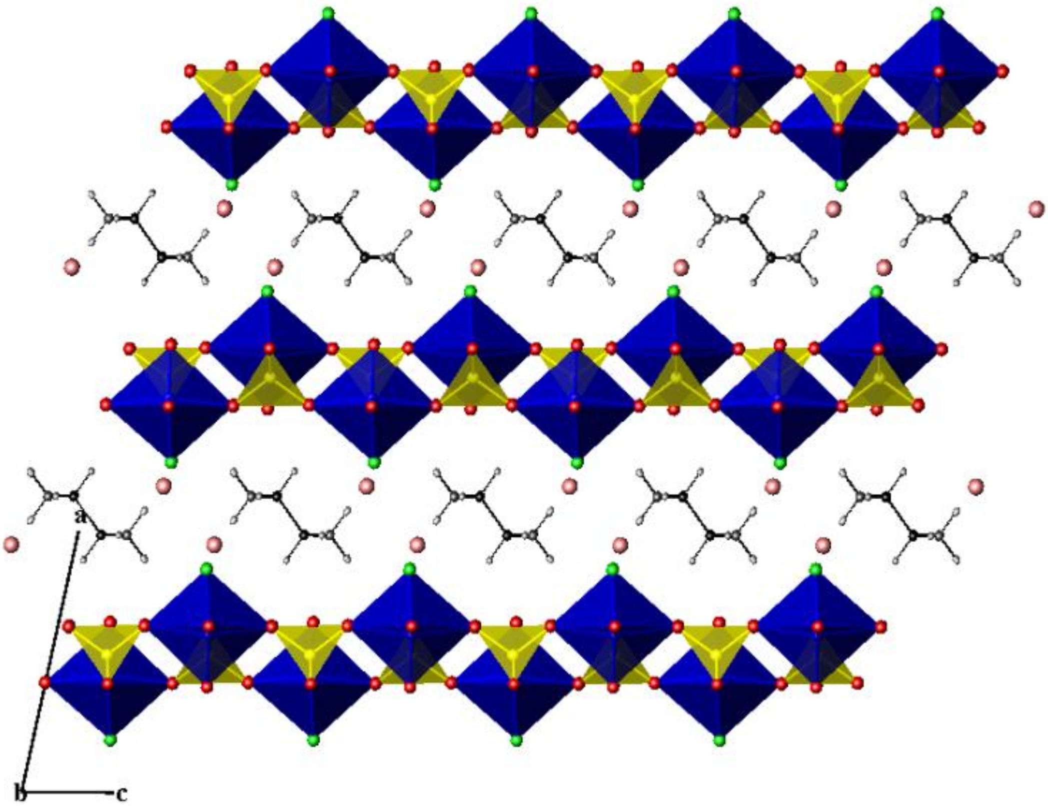

Figure 3.24: Layered structure of compound (7) viewed down the *b* axis. Blue polyhedra represent molybdenum octahedra and yellow polyhedra represent the phosphate. Framework oxygen and fluorine atoms are distinguished by red and green colours respectively. Pink spheres show lattice water and grey-black linked spheres comprise the piperazine molecules.

Mo(1) adopts the reduced +5 oxidation state (BV(Mo) = 4.82), and therefore exhibits the classic distorted octahedral geometry by having a short Mo=O oxo group (Mo(1)-O(2): 1.622(15) Å) *trans* to the fluoride ligand, whilst the four remaining equatorial Mo-O distances are intermediate bonds of similar length (Mo-O: 2.015(17)-2.062(17) Å). Bond valence calculations performed on all atom sites and showed the expected values BV(O)s ~ 2 for all the bridging oxygens in addition to a rather low BVS at the F1 site (BV(F) = 0.509, BV(O) = 0.661), below the expected unity, suggesting the strong hydrogen bonding interactions to this site. The presence of fluoride within the structure was verified by energy dispersive X-ray microanalysis and the determined atomic ratios were in line with the chemical formula sum (Mo/P/F = 1:0.94:1.03). Selected bond distances and bond valence calculations for compound (7) are given in Table 3.15.

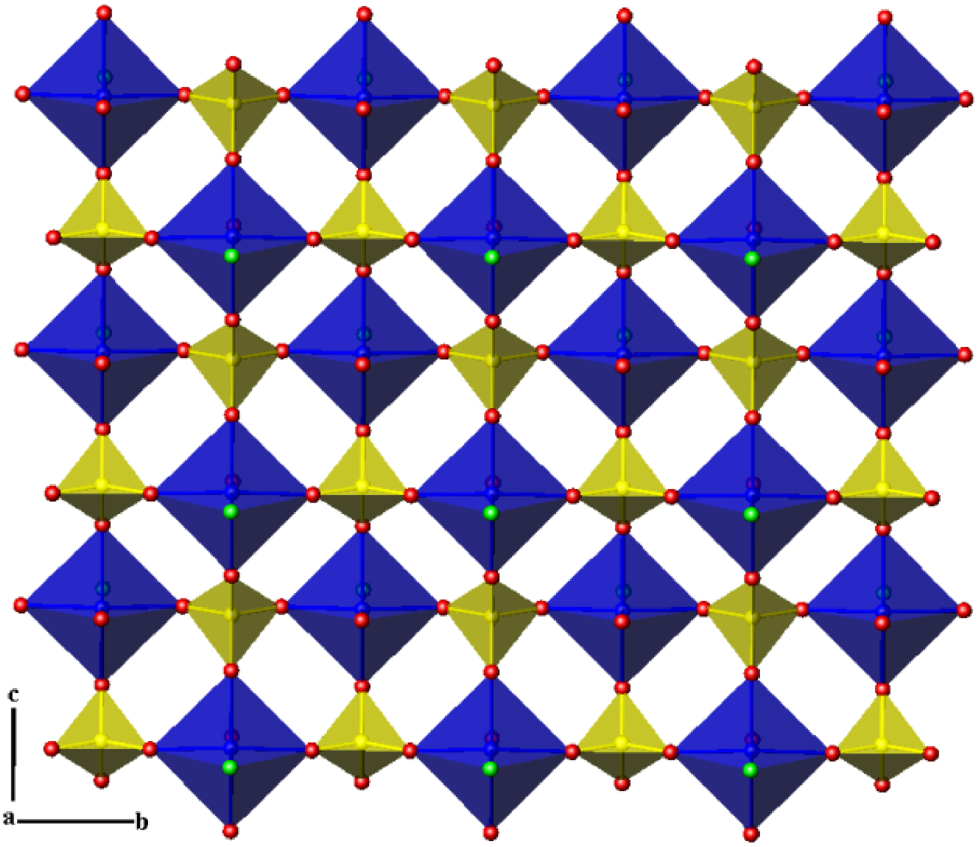

Figure 3.25: View of the layer type in compound (7) showing the repeating four-connected net of alternating molybdenum and phosphate polyhedra. Framework oxygen and fluorine atoms are distinguished by red and green colours, respectively.

Table 3.14: Crystal and diffraction information of compound (7).

Empirical formula	$C_2H_7NMoPFO_{5.5}$
Formula weight	279.01
Temperature	120(2) K
Appearance	Light yellow plate
Wavelength	0.71073Å (Mo K_α)
Crystal system	Monoclinic
Space group	$C2/m$
Unit cell dimensions	a = 18.060(2) Å, b = 6.447(6) Å
	c = 6.453(6) Å, β= 102.297(9)°
Volume	734.07(13) $Å^3$
Z	2
D_c	2.524 $g.cm^{-3}$
Θ range for data collection	3.23°-24.94°
Reflections collected	5623
Independent reflections	713
Data/Restraints/Parameters	713/24/40
R indices	R_1 = 0.1039, wR_2 = 0.2533

Table 3.15: Selected bond lengths (Å) and bond valences for compound (7).

Polyhedra	Bond Lengths	Σs_{ij}	Polyhedra	Bond Lengths	Σs_{ij}
$Mo(1)O_5F$			$P(1)O_4$		
Mo(1)-O(1)	2.015(17)	0.747	P(1)-O(1)	1.512(17)	1.328
Mo(1)-O(2)	1.662(15)	1.939	P(1)-O(3)	1.528(12)	1.272
Mo(1)-O(3)	2.023(12)	0.731	P(1)-O(3')	1.528(12)	1.272
Mo(1)-O(3')	2.023(12)	0.731	P(1)-O(4)	1.494(17)	1.394
Mo(1)-O(4)	2.062(17)	0.658			**ΣP1=5.27**
Mo(1)-F(1)	2.060(13)	0.509			
		ΣMo1=4.82			

The layered topology discussed here resembles the $MoOPO_4$ compound discovered by Kierkegaard and Westerlund.[1] Its framework structure can be best considered as derived from identical layers to those discussed here, but the MoO_6 octahedra share common oxygen vertices to form chains of corner sharing MoO_6 along the c axis, leading to a three-dimensional framework structure. What distinguishes the structure described here is the participation of fluoride into the molybdenum sphere that creates terminator points, resulting in a decrease of the dimensionality. Layers are now well separated and they become negatively charged, allowing intercalation of charge compensating cations. Indeed, diprotonated piperazine cations are located in between adjacent layers of compound (7) surrounded by lattice water molecules. As illustrated in Figure 3.26, terminal fluoride ligands create anchoring points for the NH_2- groups of the piperazine, providing further stabilization of the structure through strong hydrogen bonding (N(H)···F = 1.75-2.04 Å). Additionally, the one unique crystallographically water molecule is within hydrogen bonding distance of the framework oxygens, forming two hydrogen bond links with the bridging oxygens of type O(3) (O_w(H)···O(3) = 2.84Å).

Compound (7) can be regarded as the first example of an oxyfluorinated molybdenum phosphate compound. To the best of our knowledge, only relatively little work has been done in halide containing molybdenum phosphates; these oxychloride phases *A*$MoOPO_4Cl$ (where *A* = K, Rb) were obtained by high temperature methods.[20] The oxyfluoride compound reported here was prepared under mild hydrothermal routes and remarkable is that both compounds exhibit identical framework topologies.

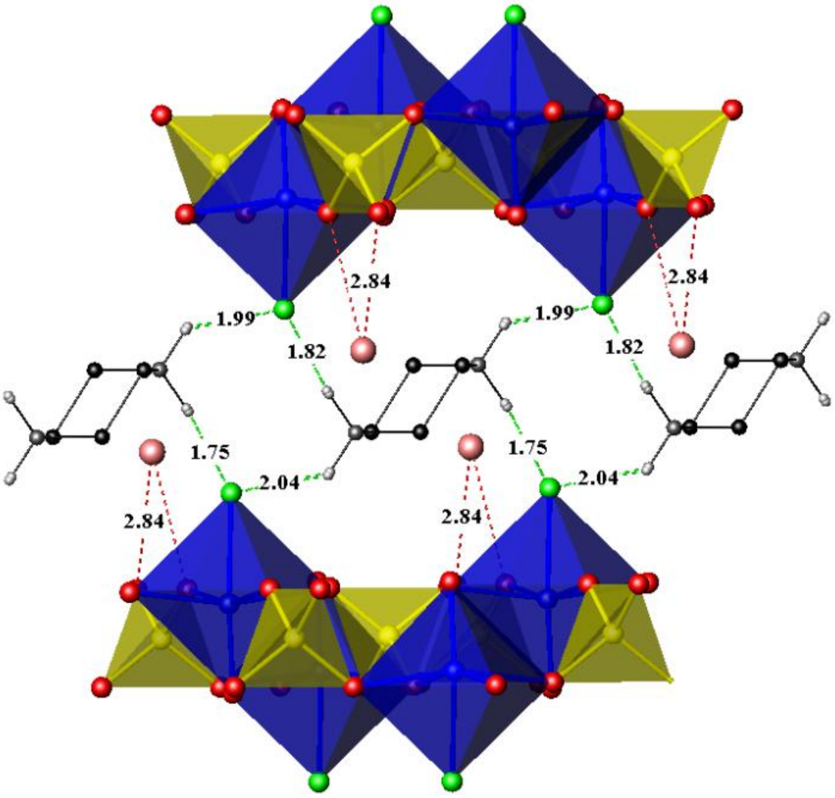

Figure 3.26: Schematic showing the extensive hydrogen bonding in between adjacent layers. Framework oxygen and fluoride atoms are distinguished by red and green colours respectively. Pink spheres show lattice water and grey-black linked spheres present the piperazine molecules.

Compound (7) was further characterised by Infrared spectroscopy and TGA analysis. The infrared spectrum, illustrated in Figure 3.27, exhibits an inseparable broad band in the 3500-2800 cm^{-1} region assigned to the hydroxyl stretching modes (antisymmetric and symmetric stretching) of the lattice water in addition to the stretching modes of the N-H and C-H groups of piperazine cations. Since this IR spectrum shows overlap of broad bands in this region, it can only be demonstrated that bands in the high frequency region (3500-3200 cm^{-1}) are assigned to the water molecule and to the amino groups of the protonated piperazine cations, whereas bands in the low frequency region (3100-2800 cm^{-1}) are attributed to the stretching modes of C-H groups of the piperazine ring. The band detected at 1612 cm^{-1} can be assigned to the corresponding H-O-H bending mode of the water molecule, whilst the following broad band occurred in the region 1460-1380 cm^{-1} can be attributed to the very characteristic modes of the piperazine ring.[7a, 21] This includes the stretching vibration of C-C and C-N bonds in combination with the deformation vibration of C-N-H groups. The absorption bands of PO_4^{3-} and Mo=O groups appear in lower frequencies. The intense broad band detected at ~ 990 cm^{-1} can be assigned to a mixture of the P-O and Mo=O stretching modes.[8]

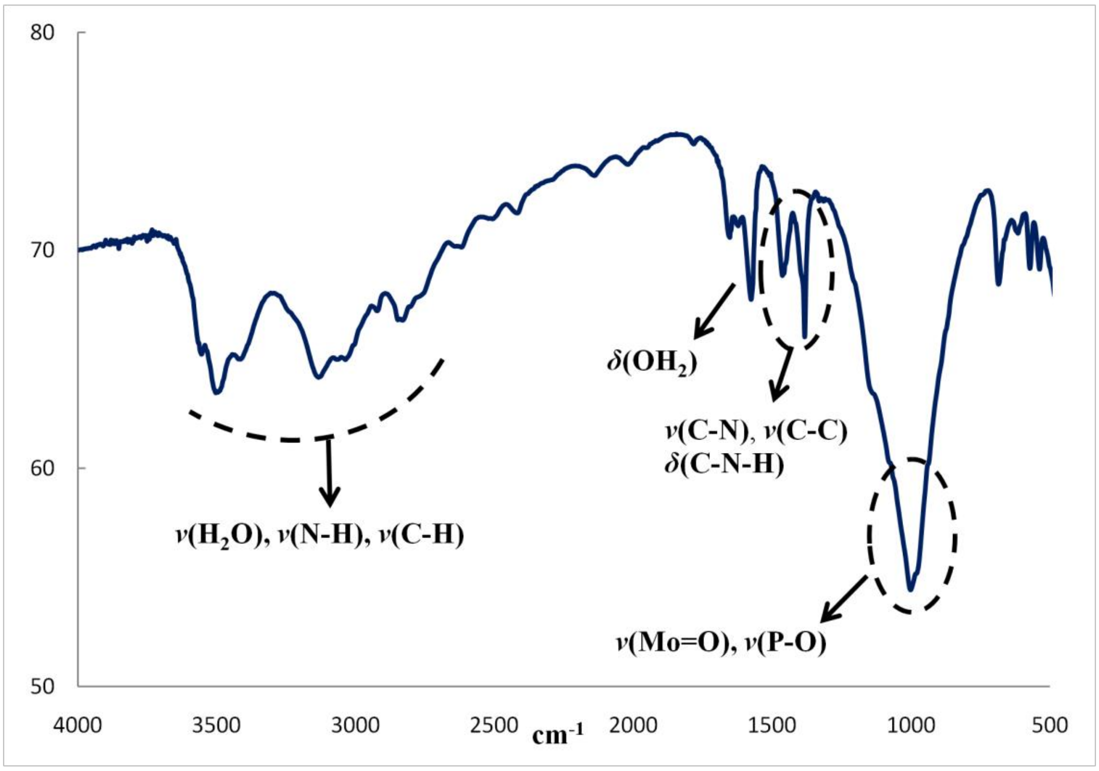

Figure 3.27: Infrared spectrum of compound (7).

The TGA pattern (shown in Figure 3.28) exhibits mass loss in two main steps followed by the endothermic peaks. The endothermic peaks are attributed to the energy for breaking all the hydrogen bonds as well as for the evaporation of the water molecules, the calcination of the piperazine cations and the elimination of the fluoride ligand. The first sharp decrement of mass (loss ~ 20.27%) occurred in the region of 80-520 °C because of the evaporation of half a mole of water molecules and half a mole of piperazine molecules from one molecule of the compound (7) (calculated value 19.02%). The second obvious decrease of mass occurred in the region of 540-670°C and can be assigned to the elimination of the fluorine ligand, as the observed mass loss (~ 7.13%) is consistent with the calculated value (9.13%).

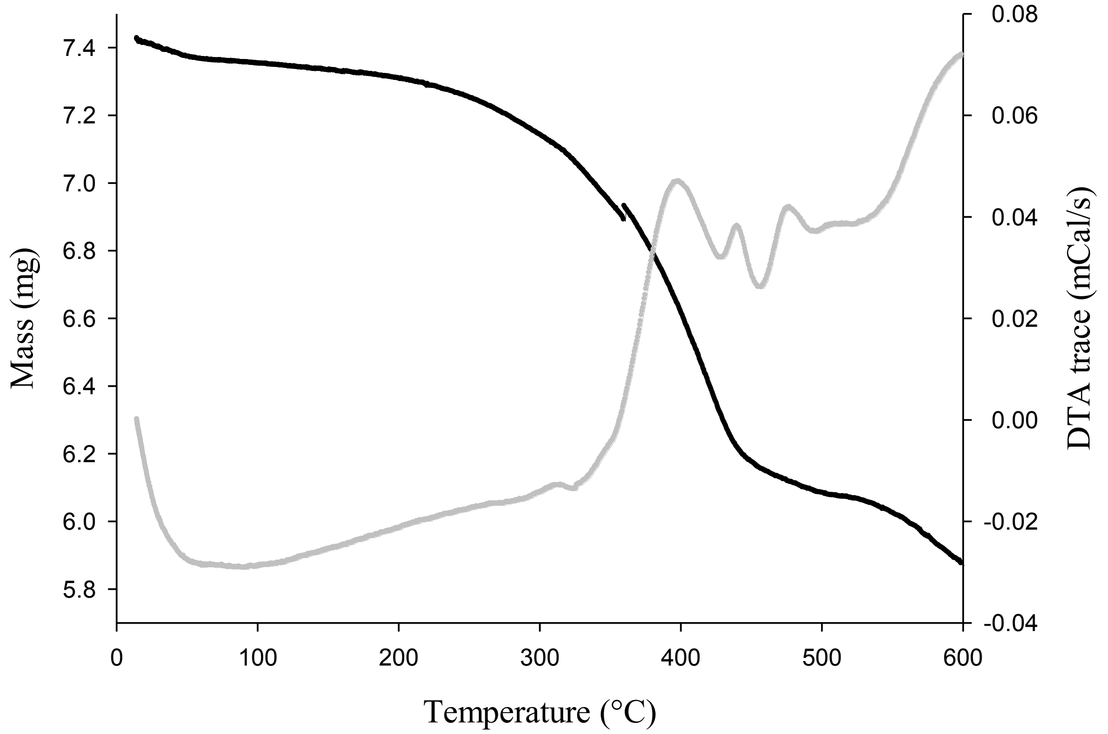

Figure 3.28: TGA pattern of compound (7). Mass loss was recorded as a function of temperature and is shown by the black line. DTA trace is the grey line.

3.4.3 Conclusions

Synthetic work in this part aimed at investigating the role of fluoride in the molybdenophosphate frameworks formation. Looking at the products isolated from this approach, it would appear that one unique oxyfluorinated molybdenum phosphate has been stably formed within a wide range of compositional and process parameters, whereas non-fluorinated products varied considerably. The former was successfully obtained using mild hydrothermal routes in the presence of piperazine and under quite acidic conditions. Two previously reported oxychloride molybdenum phosphates which show identical layered topology to the one discussed here were prepared *via* high temperature routes, showing the possibility of introducing halide anions into molybdenum containing frameworks by using varied synthetic techniques and different templating agents.

3.5 Overview

The research included in this chapter was concentrated on developing new molybdenum phosphate compounds. At the first stage, synthetic plans were focused on incorporating borate building blocks into molybdenum phosphate frameworks, with the aim of increasing structural diversity. This approach led to the discovery of the ammonium templated molybdenum phosphate $[NH_4]_{12}[(MoO_2)_2O(HPO_4)_2]_4[PO_4]Cl^-$ (1), rather than a boron containing framework structure. Compound (1) is of particular interest as it comprises molybdenophosphate layers of unique topology that are penetrated by channels containing perfectly ordered alternating ammonium cations and free orthophosphate $(PO_4)^{3-}$ or halide (Cl^-, Br^-) anions. Further investigations of possible functionality of this compound through anion exchange reactions have shown this material to act as an anion-exchanger.

A series of hydrothermal reactions in the presence of different organic amines produced a variety of crystalline structures including the one-dimensional ribbon structure of (2) and the three molybdenophosphate polyanions: the $[Mo_5O_{15}(PO_4)_2]^{6-}$ cluster units (3), the typical pseudo keggin polyanion $[PMo_{12}O_{40}]^{3-}$ (4) and the $\{Mo_6P_4O_{31}\}^{n-}$ polyanion (5). These polyanions exhibit polyhedral connectivity through oxygen edge-sharing, forming different types of molybdenum *n*-membered rings capped by di-μ-(O)PO_4 phosphate bridges. Further structural features involve the particular packing of discrete polyanions, in such a way as to generate pseudo two- and three-dimensional networks as a result of strong hydrogen bonding between the organic amines, the water molecules and the framework oxygens.

Synthetic efforts were then concentrated on producing alkali metal templated molybdenum phosphates *via* high temperature flux-growth methods. Compound $Rb(MoO_2)_2(P_3O_{10})$ (6) was crystallized from reactions aimed at incorporating rubidium into the framework structure. Its framework structure can be considered as derived from layers built up from alternating linked molybdenum octahedra and phosphate tetrahedra. Finally, synthetic efforts were placed into producing oxyfluorinated molybdenum phosphates. Compound (7) was successfully obtained under mild hydrothermal routes in the presence of piperazine, and this may be regarded as the first example of an oxyfluorinated molybdenum phosphate compound. Its framework structure derives from layers built up from alternating linked polyhedra, with fluoride anions occupying terminal sites of the metal coordination spheres.

Table 3.16: Summary of the compounds characterised in this investigation.

Formula	Structural features
$[NH_4]_{12}[(MoO_2)_2O(HPO_4)_2]_4[PO_4]Cl$ (1)	2D layers built up from $H_2Mo_2P_2O_{15}$ tetrameric units (→ $2Mo^{(VI)}{}_2O_{11}$ capped on both sides by HPO_4) with embedded NH_4^+, Cl^- and free PO_4^{3-}.
$\{(C_6H_{14}N_2)\}\{MoO_2(HPO_4)_2\}.H_2O$ (2)	1D chains of alternating $Mo^{(VI)}O_6$ and PO_4. Dabco cations and H_2O molecules interleaved.
$Na_3(dabco)_2\{Mo_5O_{15}(PO_4)_2\}.(H_2O)_6$ (3)	Discrete $[Mo_5O_{15}(PO_4)_2]^{6-}$ cluster anions (→ a five-membered ring of edge- and corner- shared $Mo^{(VI)}O_6$, capped on both poles by PO_4). Na^+, H_2O and dabco cations interleaved.
$[(CH_3)_4N]_3[PMo_{12}O_{40}]$ (4)	Discrete pseudo-keggin polyanions (→ three $Mo^{(VI)}{}_3O_{13}$ triads of edge-shared MoO_6 with an encapsulated PO_4). Templated by tetramethylammonium cations.
$\{C_2H_4(NH_3)_2\}_2Na\{Mo_6O_{15}(PO_4)_4\}_2.(H_2O)_{12.8}$ (5)	Discrete $\{Na[Mo_6P_4O_{31}]_2\}^{n-}$ cluster anions (→ $2[Mo_6P_4O_{31}]_2$, a coplanar ring of six $Mo^{(IV)}O_6$ three peripheral and one encapsulated PO_4, connected by Na^+). Ethylenediamine cations and water molecules interleaved.
$Rb(MoO_2)_2(P_3O_{10})$ (6)	2D layers built up from chains of alternating $Mo^{(VI)}O_6$ and PO_4 connected by bridging PO_4. Rb^+ interleaved.
$[H_2N(C_2H_4)_2NH_2]_{0.5}\{MoO[PO_4]F\}.H_2O_{0.5}$ (7)	2D Layers of alternating $Mo^{(IV)}O_5F$ and PO_4. Piperazine cations and H_2O interleaved.

3.6 References

[1] P. Kierkegaard and M. Westerlund, *Acta Chemica Scandinavica* 1964, *18*, 2217-2225.

[2] R. C. Haushalter and F. W. Lai, *Inorganic Chemistry* 1989, *28*, 2904-2905.

[3] a) E. W. Corcoran, *Inorganic Chemistry* 1990, *29*, 157-158; b) K. H. Lii and R. C. Haushalter, *Journal of Solid State Chemistry* 1987, *69*, 320-328; c) L. A. Mundi and R. C. Haushalter, *Inorganic Chemistry* 1990, *29*, 2879-2881.

[4] a) R. C. Haushalter, *Journal of the Chemical Society-Chemical Communications* 1987, 1566-1568; b) R. C. Haushalter and F. W. Lai, *Journal of Solid State Chemistry* 1988, *76*, 218-223; c) R. C. Haushalter and F. W. Lai, *Journal of Solid State Chemistry* 1989, *83*, 202-206; d) A. Leclaire, J. C. Monier and B. Raveau, *Journal of Solid State Chemistry* 1983, *48*, 147-153; e) A. Leclaire and B. Raveau, *Journal of Solid State Chemistry* 2007, *180*, 2734-2739; f) K. H. Lii, D. C. Johnston, D. P. Goshorn and R. C. Haushalter, *Journal of Solid State Chemistry* 1987, *71*, 131-138; g) K. H. Lii and C. C. Wang, *Journal of Solid State Chemistry* 1988, *77*, 117-123.

[5] a) R. C. Haushalter, K. G. Strohmaier and F. W. Lai, *Science* 1989, *246*, 1289-1291; b) H. E. King, L. A. Mundi, K. G. Strohmaier and R. C. Haushalter, *Journal of Solid State Chemistry* 1991, *92*, 1-7; c) R. C. Haushalter and L. A. Mundi in *THE HYDROTHERMAL SYNTHESIS OF LAYERED MOLYBDENUM PHOSPHATES WITH OCTAHEDRAL-TETRAHEDRAL LAYERS*, *Vol. 233* Eds.: R. L. Bedard, T. Bein, M. E. Davis, J. Garces, V. A. Maroni and G. D. Stucky), Materials Research Soc, Pittsburgh, 1991, pp. 255-265; d) L. A. Mundi, L. Yacullo and R. C. Haushalter, *Journal of Solid State Chemistry* 1991, *95*, 283-288.

[6] I. D. Brown and D. Altermatt, *Acta Crystallographica Section B-Structural Science* 1985, *41*, 244-247.

[7] a) D. G. Tuck, *Progr. Inorg. Chem* 1968, *9*, 161; b) T. C. Waddington, *Journal of the Chemical Society* 1958, 4340-4344.

[8] a) E. Dumas and S. C. Sevov, *Inorganic Chemistry* 2002, *41*, 144-+; b) X. He, P. Zhang, T. Y. Song, Z. C. Mu, J. H. Yu, Y. Wang and J. N. Xu, *Polyhedron* 2004, *23*, 2153-2159; c) X. Z. Liu, B. Z. Lin, L. W. He, X. F. Huang and Y. L. Chen, *Journal*

of Molecular Structure 2008, *877*, 72-78; d) J. P. Wang, J. Li and J. Y. Niu, *Journal of Coordination Chemistry* 2005, *58*, 1639-1651.

[9] E. W. Corcoran, R. C. Haushalter and W. Y. F. Lai, *US Patent 4,956,483* 1990.

[10] C. Hauf, T. Friedrich and R. Kniep, *Zeitschrift Fur Kristallographie* 1995, *210*, 446-446.

[11] R. Millini and A. Carati, *Journal of Solid State Chemistry* 1995, *118*, 153-157.

[12] a) B. Hedman, *Acta Chemica Scandinavica* 1973, *27*, 3335-3354; b) R. Strandberg, *Acta Chemica Scandinavica* 1973, *27*, 1004-1018.

[13] Q. Sun, *Acta crystallographica Section E* 2003, *59*, 729-730.

[14] R. Strandberg, *Acta Chemica Scandinavica Series a-Physical and Inorganic Chemistry* 1975, *29*, 359-364.

[15] a) P. Armand, D. Granier and A. van der Lee, *Acta Crystallographica Section E-Structure Reports Online* 2007, *63*, I191-U165; b) S. X. Liu, C. M. Wang, H. J. Zhai and D. H. Li, *Journal of Molecular Structure* 2003, *654*, 215-221; c) H. Y. Ma, X. D. Wang, F. P. Wang and L. Z. Wu, *Crystal Research and Technology* 2008, *43*, 455-460; d) J. Y. Niu, J. P. Wang, B. Yan, D. B. Dang and Z. Y. Zhou, *Journal of Chemical Crystallography* 2000, *30*, 43-48; e) C. D. Wu, C. Z. Lu, X. Lin, W. B. Yang, H. H. Zhuang and J. S. Huang, *Acta Crystallographica Section E-Structure Reports Online* 2001, *57*, m390-m392; f) Y. Xu, J. Q. Xu, G. Y. Yang, G. D. Yang, Y. Xing, Y. H. Lin and H. Q. Jia, *Acta Crystallographica Section C-Crystal Structure Communications* 1998, *54*, 9-11.

[16] R. C. Haushalter and F. W. Lai, *Angewandte Chemie-International Edition in English* 1989, *28*, 743-746.

[17] a) L. A. Meyer and R. C. Haushalter, *Inorganic Chemistry* 1993, *32*, 1579-1586; b) Y. H. Sun, X. B. Cui, J. Q. Xu, L. Ye, Y. Li, J. Lu, H. Ding and H. Y. Bie, *Journal of Solid State Chemistry* 2004, *177*, 1811-1816.

[18] a) T. Hoareau, A. Leclaire, M. M. Borel, A. Grandin and B. Raveau, *Journal of Solid State Chemistry* 1995, *116*, 87-91; b) A. Leclaire, M. M. Borel, J. Chardon and B. Raveau, *Journal of Solid State Chemistry* 1995, *116*, 364-368; c) A. Leclaire, A. Guesdon, M. M. Borel, F. Berrah and B. Raveau, *Solid State Sciences* 2001, *3*, 877-882; d) A. Leclaire and B. Raveau, *Acta Crystallographica Section C-Crystal Structure Communications* 1988, *44*, 226-229; e) S. Ledain, A. Leclaire, M. M. Borel, J. Provost and B. Raveau, *Journal of Solid State Chemistry* 1996, *125*, 147-

152; f) S. Ledain, A. Leclaire, M. M. Borel, J. Provost and B. Raveau, *Materials Research Bulletin* 1998, *33*, 401-408; g) D. Riou, A. Leclaire, A. Grandin and B. Raveau, *Acta Crystallographica Section C-Crystal Structure Communications* 1989, *45*, 989-991.

[19] L. A. Mundi, K. G. Strohmaier and R. C. Haushalter, *Inorganic Chemistry* 1991, *30*, 153-154.

[20] M. M. Borel, A. Leclaire, J. Chardon, J. Provost and B. Raveau, *Journal of Solid State Chemistry* 1998, *137*, 214-217.

[21] S.Gunasekaran and B.Anita, *Indian Journal of Pure & Applied Physics* 2008, *46*, 833.

Chapter Four

Amine Templated Oxyfluorinated Vanadium Arsenates

4.0 Introduction

Following the success with the oxyfluorinated aluminum and gallium phosphate systems, research activity was extended to transition metal phosphates, giving rise to a diverse range of new framework topologies with fascinating properties resulting from the redox abilities and magnetic nature of the *d* block elements.[1],[4] The research included in this chapter has been mainly focused on investigating the role of fluoride ions in the formation of vanadium containing frameworks. The vanadium system still remains quite unexplored, as relatively little work has been reported for the oxyfluorinated vanadium phosphates.[1] The combination of hydrofluoric acid and organic amines has been a commonly used method for preparing these fluorinated materials. Different organic amines have been introduced into the synthesis in order to achieve an increase of the pH of the reaction mixture, while also to facilitate directional interactions between the amino groups of the organic amine and the framework F and O atoms as a result of strong hydrogen bonding.

Synthetic work within this chapter has aimed at expanding this family of compounds by introducing alternative primary building units such as oxotetrahedral arsenate species. Hence due to the larger size of the arsenate anion AsO_4^{3-} and its softer character compared to phosphate PO_4^{3-}, one might expect different framework topologies from those found with the more conventional phosphate system. Following the typical HF route, two oxyfluorinated vanadium arsenate compounds have been prepared in presence of piperazine acting as a templating agent (detailed in Section 4.1). Investigations were then targeted at introducing vanadium fluoride in the system as an alternative fluoride ion source, instead of the more commonly used HF. Two amine templated vanadoarsenate compounds have been successfully obtained and characterized, as described in Section 4.2.

4.1 Oxyfluorinated vanadoarsenates (*via* the HF route)

Research work in this section involves the preparation of fluorinated vanadoarsenate compounds by following similar synthetic routes to those used for the previously reported phosphate based compounds. Two similar but rather distinct compounds have been successfully synthesised and further described in detail here, $[H_2N(C_2H_4)_2NH_2]_{1.5}\{[(VO)_2(AsO_4)F_2]O[(VO)(HAsO_4)F]\}.H_2O$ (1) and $[H_2N(C_2H_4)_2NH_2]_{1.5}\{[(VO)_3(AsO_4)F_4][VF_3(AsO_4)]\}.4H_2O$ (2). Both exhibit new layered structure types comprising flat and super corrugated layers respectively, with embedded piperazine cations and water molecules.

4.1.1 Experimental

I. Synthesis

The general procedure entailed dissolution of the vanadium oxide source (V_2O_5) and arsenic acid (H_3AsO_4) in distilled water. HF was then added to the mixture, followed by the addition of the organic amine (*Caution!* HF is highly toxic and corrosive, do not use without taking professional advice). The reaction mixture was then sealed to a 23 mL Teflon-lined steel autoclave and heated to 418 K for four days.

Three main series of experiments were performed based upon different organic amines: piperazine, ethylenediamine and dabco. Reactions mixtures were prepared by varying the molar ratio of amine/HF in the final solution, in order to achieve a range of acidic, neutral and basic conditions. Isolated compounds have been characterised by single crystal X-ray diffraction, TGA and IR analysis. Energy-dispersive X-ray spectroscopy was used for the identification of the elemental composition of the compounds isolated; Bond Valence calculations were carried out to clarify the location of near isoelectronic species, such as oxide and fluoride ions.

- ✓ Detailed reaction conditions for the compounds isolated within this work

$[H_2N(C_2H_4)_2NH_2]_{1.5}[(VO)_2(AsO_4)F_2]O[(VO)(HAsO_4)F].H_2O$ (1): Vanadium(V) oxide (0.1046 g, 0.575 mmol), 85% orthophosphoric acid solution (0.04 mL, 0.575 mmol), 48% hydrofluoric acid solution (0.05 mL, 1.38 mmol), piperazine (0.0991 g, 1.15 mmol) and distilled water (3 mL, 166.6 mmol). The final reaction mixture had a pH value = 5.24. Heated to 418 K and held for 4 days. Product crystallised as dark blue fragments.

$[H_2N(C_2H_4)_2NH_2]_{1.5}[(VO)_3(AsO_4)F_4][VF_3(AsO_4)].4H_2O$ (2): Vanadium(V) oxide (0.1046 g, 0.575 mmol), 85% orthophosphoric acid solution (0.04 mL, 0.575 mmol), 48% hydrofluoric acid solution (0.1 mL, 2.76 mmol), piperazine (0.0991 g, 1.15 mmol) and distilled water (3mL, 166.6 mmol). The final reaction mixture had a pH value = 3.28. Heated to 418 K and held for 4 days. Product occurred as green plates.

II. Characterization

- ✓ X-ray diffraction studies

Single crystal X-ray diffraction data for each crystal structure were collected on a Bruker Nonius KappaCCD diffractometer (Mo Kα radiation, λ = 0.71073 Å) at 120 K. Refinements of the structures were carried out using the WinGX system and SHELX-97 (by following direct methods). Disordered solvent and template molecules and their contribution to the scattering wave removed using PLATON SQUEEZE.[2]

- ✓ Thermogravimetric (TGA) analysis

TGA and DTA data were collected on a Polymer Laboratories STA 1500 system. Samples (mass ~ 10 mg) were heated in flowing air from room temperature to 600 °C at a range of 10° C min^{-1}. Weight loss and heat flow were recorded as a function of temperature.

- ✓ Infra-red (IR) analysis

Samples were first mixed with KBr and then pressed into thin pellets. IR spectra were collected using a Perkin Elmer Spectrum system over the range 4000-500 cm^{-1}.

- ✓ Electron microscopy

Energy-dispersive X-ray spectroscopy and Scanning electron microscopy completed on a JOEL JSM-5910 SEM fitted with an Oxford Inca 300 energy dispersive X-ray spectroscopy analysis system.

- ✓ Bond Valence calculations

Bond valence calculations were completed at each atom site using the below equation. The theory behind the equation refers to the valence sum rule for which the valence (V) of each atom must be equal to the sum of its individual bond valences (V_i). The corresponding (V_i) values were calculated using the experimental bond lengths (R) and (R_0, b) parameters from the Tables compiled by Brown and Altermatt.[3]

$$V = \Sigma\,(V_i),\ \text{where}\ V_i = \exp\,[(R_0-R)/b]$$

4.1.2 Results and discussion

I. Synthesis overview

As part of an attempt to discover new framework topologies, as well as to investigate the role of fluoride in framework formation, we set out a programme of work in systems that entailed mild hydrothermal treatment of vanadium metal source (V_2O_5) with arsenate source (H_3AsO_4) in presence of an organic amine, performed in HF fluoride medium. Organic amines used in this project (piperazine, ethylenediamine and dabco) seemed to exhibit a strong structure directing effect, yielding a diverse range of framework topologies.

Compounds (1) and (2) were successfully prepared under mild hydrothermal routes in presence of piperazine acting as a templating agent. These were obtained from similar reaction mixtures with the main difference being the amount of HF added to the mixture (pH value ~5 and 3 for compounds (1) and (2) respectively). A further increase in pH (basic conditions with a pH range ~8-10) resulted in the unsuccessful incorporation of fluoride into the framework, but rather the formation of known polyoxovanadium cluster polyanions.[4] Reactions that involved ethylenediamine and dabco were less fruitful. Using ethylenediamine as the amino template, the system resulted in the previously reported compound [5] $En_{0.5}[(VO)(HAsO_4)F]$ which was reproducibly formed under acidic conditions between the pH range 1-4. When the pH was allowed to increase to any value greater than six, only amorphous products were obtained. In the case of dabco, the system remains very ambiguous. Under acidic conditions, reactions resulted in having no solid products in their solutions, whilst under basic reactions the system tended to form two distinct but unidentified product phases. Unfortunately the lack of large enough crystals, suitable for single crystal X-ray diffraction analysis, within the isolated products and the unsuccessful attempts to identify the resultant phases using X-ray powder diffraction could not help to elucidate this further.

I. Characterization of compound (1)

Single crystal X-ray diffraction of compound (1) (details of which are summarized in Table 4.1) has shown the structure to derive from [$V_2As_2O_{12}F_2$] tetramers built up from F-F edge-shared [$V_2O_8F_2$] bioctahedral units which are capped on both sides by di-μ-(O,O')-arsenate bridges. Such topologically identical bioctrahedral units have been also identified in two previously reported compounds,[5] however those structures exhibit different bonding motifs, leading to totally different framework topologies from the one described here. From a general structural point of view, such tetramers strongly resemble many oxyfluorinated aluminium and gallium phosphate frameworks that are based on related F-F edge shared Al or Ga bioctahedral units.[6]

In the structure reported here, there are three crystallographically independent vanadium atoms, forming [VO_4F_2] octahedra that share one edge with the symmetry equivalent octahedron *via* bridging F atoms. The coordination sphere of vanadium centres of type V1, V2 is completed with a terminal oxo group and two oxygen donors from two arsenate groups, whilst the fourth apex comprises a bridging oxygen shared between adjacent vanadium bioctrahedral units so as to form chains of corner sharing [$V_2As_2O_{12}F_2$] tetramers.V3 exhibits similar octahedral geometry, but the fourth apex makes a bond linkage with an arsenate group instead, enhancing the polyhedral connectivity into a 2-D network of flat layers parallel to the *ab* plane, as shown in Figure 4.1.

Each vanadium site adopts the classic distorted octahedral geometry due to the presence of a short V=O bond opposite to a significantly lengthened V-F bond. In the case of V(2) and V(3), the four equatorial bond lengths are intermediate bonds of similar length, whilst V(1) exhibits one exceptionally short equatorial bond in addition to the other intermediate equatorial distances, suggesting the d^1 and d^0

electronic configurations for these site, respectively. Investigation of the As-O bond lengths has shown that both unique arsenate tetrahedra exhibit very characteristic bond distances for all the bridging oxygen atoms. Additionally, $As(2)O_4$ has its fourth oxygen (O6) unshared pointing towards the 10-ring channels. The hydrogen attached to this oxygen site was identified in the difference map and from bond elongation, this was then fixed in calculated positions, treated as riding on the parent atom and the torsion angle allowed to refine. Bond valence calculations and EDS analysis were carried out to clarify the location of near isoelectronic species, such as oxide and fluoride ions. Indeed, BV calculations showed very low (close to unity as expected for a monovalent ion) and similar bond valence values for the three distinct fluoride sites (BV(O): F1 = 0.96, F2 = 0.87, F3 = 1.04; BV(F): F1 = 0.73, F2 = 0.66, F3 = 0.79).

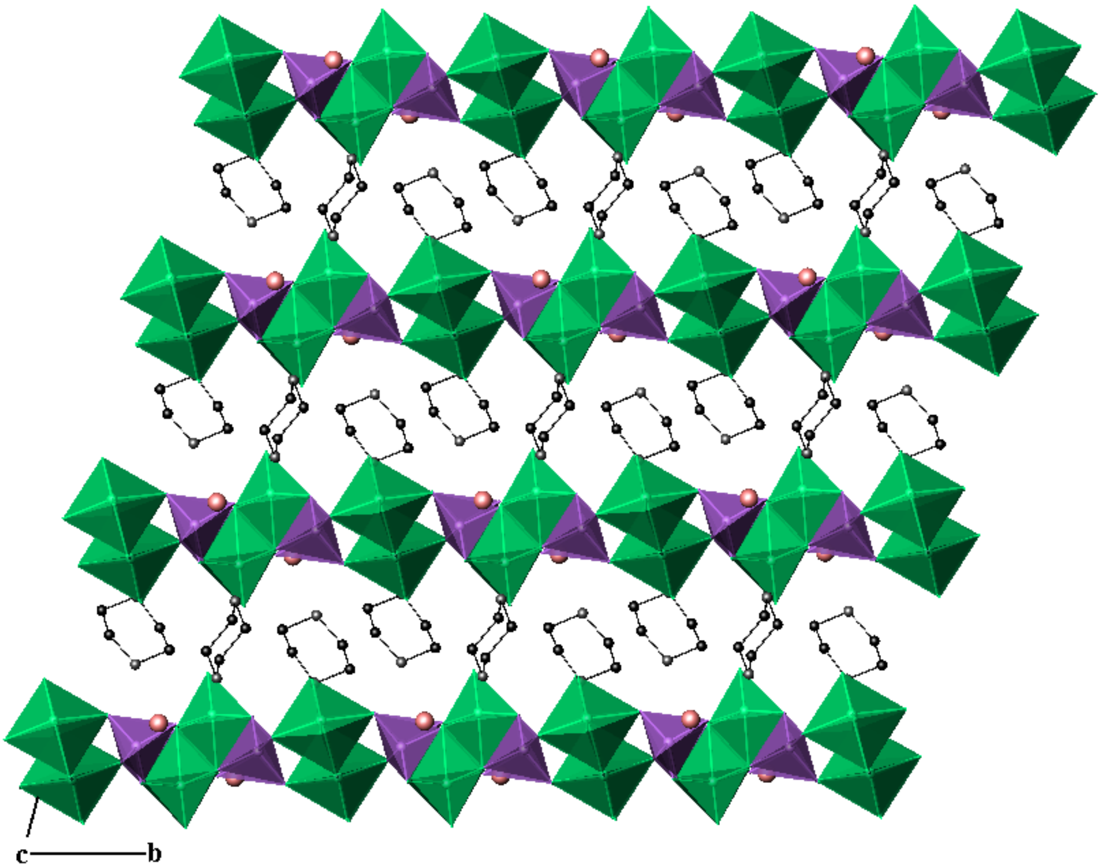

Figure 4.1: Structure of compound (1) viewed down the *c* axis. Green polyhedra represent vanadium octahedra; purple polyhedra represent the arsenate tetrahedra. Pink spheres show lattice water; grey-black linked spheres comprise the piperazine.

Table 4.1: Crystal and diffraction information of compound (1).

Empirical formula	$C_6H_{21}N_3V_3As_2F_3O_{13}$
Formula weight	702.92
Temperature	120(2) K
Appearance	dark blue
Wavelength	0.71073 Å (Mo K_α)
Crystal system	Triclinic
Space group	$P\bar{1}$
Unit cell dimensions	a = 8.5594(2) Å, b = 10.8001(2) Å c = 12.0616(2) Å, α = 65.5917(14)° β= 79.8934(13)°, c = 72.0654(14)°
Volume	964.51(3) $Å^3$
Z	2
D_c	2.420 $g.cm^{-3}$
Θ range for data collection	2.91°-27.48°
Reflections collected	15708
Independent reflections	3397
Data/Restraints/Parameters	3397/0/271
R indices	R_1 = 0.0291 wR_2 = 0.0621

Table 4.2: Selected bond lengths (Å) and bond valences for compound (1).

Polyhedra	Bond lengths	Σs_{ij}	Polyhedra	Bond lengths	Σs_{ij}
$V(1)O_4F_2$			$V(3)O_4F_2$		
V(1)-O(5)	1.723(3)	1.241	V(3)-O(1)	2.014(3)	0.537
V(1)-O(8)	1.954(3)	0.665	V(3)-O(3)	1.606(3)	1.618
V(1)-O(9)	1.980(3)	0.620	V(3)-O(7)	1.992(3)	0.570
V(1)-O(11)	1.600(3)	1.731	V(3)-O(12)	1.995(3)	0.565
V(1)-F(2)	2.050(3)	0.388	V(3)-F(3)	1.940(3)	0.523
V(1)-F(2’)	2.185(3)	0.270	V(3)-F(3’)	2.188(3)	0.267
		ΣV1=4.91			**ΣV3=4.08**
$V(2)O_4F_2$			$As(1)O_4$		
V(2)-O(2)	1.605(3)	1.622	As(1)-O(1)	1.685(3)	1.251
V(2)-O(4)	2.017(3)	0.533	As(1)-O(7)	1.700(2)	1.195
V(2)-O(5)	1.930(3)	0.674	As(1)-O(8)	1.697(2)	1.212
V(2)-O(10)	2.010(3)	0.543	As(1)-O(9)	1.693(3)	1.225
V(2)-F(1)	1.978(3)	0.472			**ΣAs1=4.88**
V(2)-F(1’)	2.207(3)	0.254			
		ΣV2=4.09	$HAs(2)O_4$		
			As(2)-O(4)	1.681(3)	1.265
			As(2)-O(6)	1.720(3)	1.132
			As(2)-O(10)	1.693(3)	1.225
			As(2)-O(12)	1.665(3)	1.317
					ΣAs2=4.94

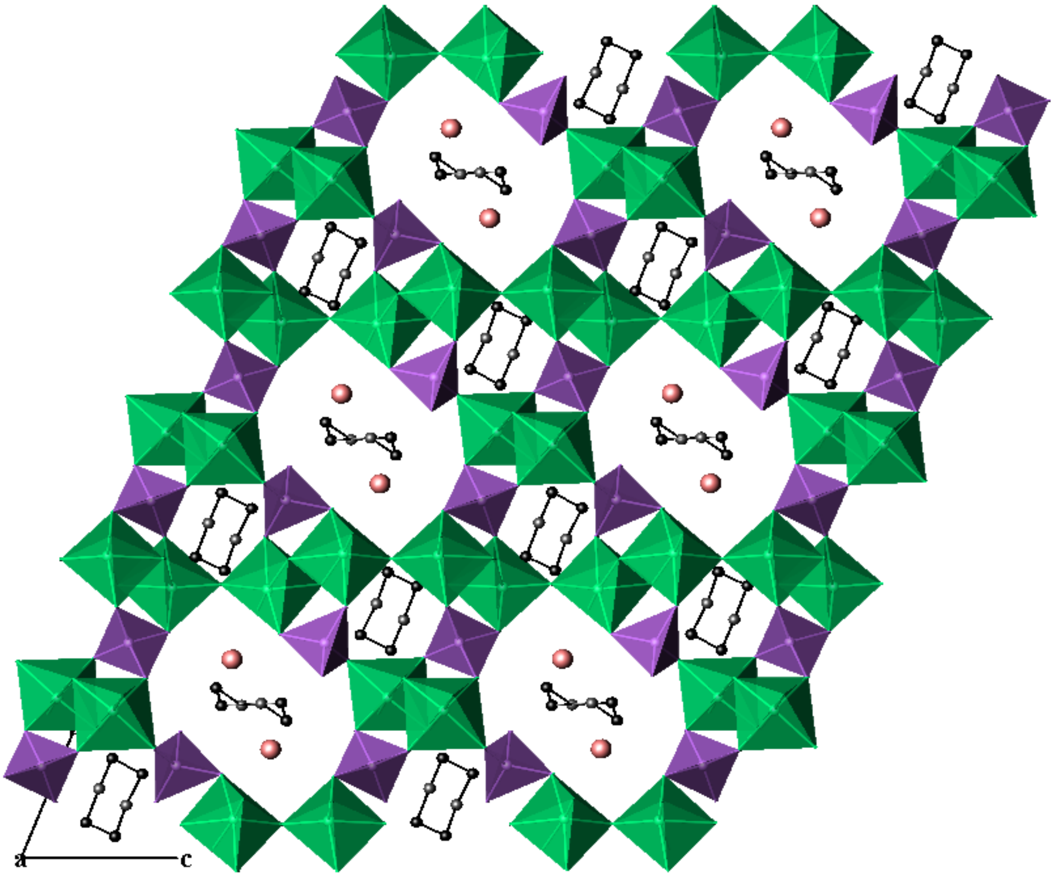

Figure 4.2: The view along the *a* axis shows details of the channels in the structure of (1). Green polyhedra represent vanadium octahedra; purple represent the arsenate. Pink spheres show lattice water; grey-black linked spheres present the piperazine molecules.

A further unique structural feature is the two types of tunnels running along the direction perpendicular to the vanadoarsenate layers, as shown in Figure 4.2. The first type involves the five-ring channel system consisting of three VO_4F_2 octahedra and two AsO_4 tetrahedra which are linked together through oxygen atoms to form pentagonal windows running along the *a* axis. Diprotonated piperazine cations are hosted inside and thus, they are involved in a strong hydrogen bonding network with the fluoro vanadoarsenate sheets. As can be illustrated in Figure 4.3, piperazine cations $[H_2N(C_2H_4)_2NH_2]^{2+}$ contain two crystallographically independent nitrogen atoms. The nitrogen atom N(1) makes two hydrogen bond links with the framework, connecting to F(1) and F(2), whilst N(2) is connected with one fluorine anion F(3) and one oxygen donor O(4). The second type involves the bigger 10-membered channel constructed of six VO_4F_2 units and four AsO_4 groups with water molecules and piperazine cations hosted inside. In this case, $[H_2N(C_2H_4)_2NH_2]^{2+}$ cations are sitting on the inversion centre, posing a special chair conformation and exhibit hydrogen bonding interactions with oxygen anions. The one crystallographically distinct water molecule adopts a three-fold coordination geometry, acting as H-bond donor for the O(8) and O(10) sites and as H-bond acceptor for the N(3) atom.

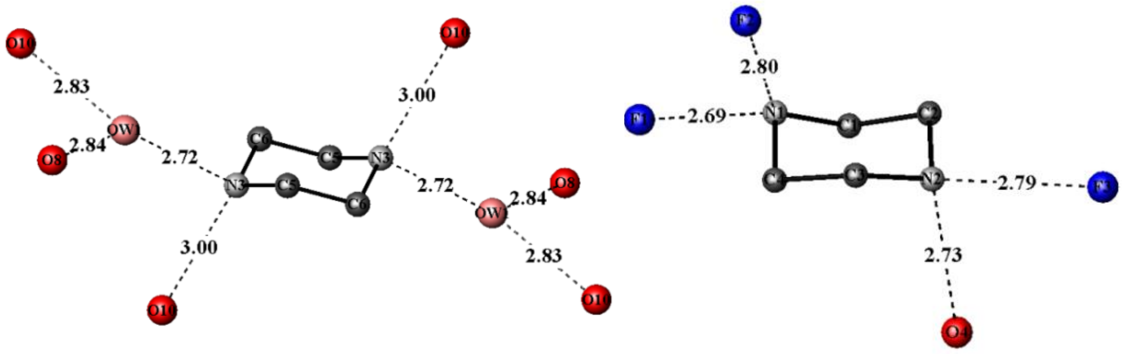

Figure 4.3: LHS and RHS show the coordination environment of the diprotonated piperazine cations located in channel type (1) and (2), respectively. Hydrogen atoms are assured to lie on the dotted lines. Bond lengths are shown in Angstrom units

The presence of lattice water and piperazinium cations was clearly seen by IR spectroscopy and was further confirmed by TGA analysis. As depicted in Figure 4.4, the infrared spectrum of compound (1) exhibits an inseparable intense broad band in the 3400-2400 cm^{-1} region attributed to the hydroxyl stretching modes (antisymmetric and symmetric stretching) of lattice water and $HAsO_4$ groups in addition to the stretching modes of the N-H and C-H groups of piperazinium cations. Since the hydroxyl bands of $HAsO_4$ groups lie in the same region as the stretching vibrations of water and amine groups, it was quite difficult to use this region for identifying any protonated arsenate groups. Therefore, assignment of these groups was based on the different deformation band frequencies which are known to be very specific for each group. The deformation vibration of the lattice water is generally observed in the region 1630-1600 cm^{-1}, whilst any deformation vibration of the T-OH group (where T = any metal atom) is expected to occur in lower frequency regions ~ 700-1300 cm^{-1}.[7] In the present IR spectra, the two strong bands detected at 1618 cm^{-1} and 1180 cm^{-1} can be assigned to the $\delta(OH_2)$ and δ(As-OH) groups, respectively.

The broad band occurring in the region (1460-1380 cm^{-1}) can be attributed to the very characteristic modes of the piperazine ring.[8] These include the stretching vibration of C-C and C-N bonds in combination with the deformation vibration of C-N-H groups. In the low frequency region, the stretching mode of the V=O group is observed at 972 cm^{-1}, followed by the stretching vibrations bands of As-O bonds.[9] The latter consist of a broad intense band well resolved into three components: one single band at 859 cm^{-1}, one doublet band at 817/825 cm^{-1} ($\nu_3(T_2)$ stretching type) and another singlet at 749 cm^{-1} ($\nu_1(A_1)$ stretching type). The splitting of the $\nu_3(T_2)$ band and the presence of the $\nu_1(A_1)$ stretching vibrations implies the presence of more than two types of site symmetry for the arsenate groups.

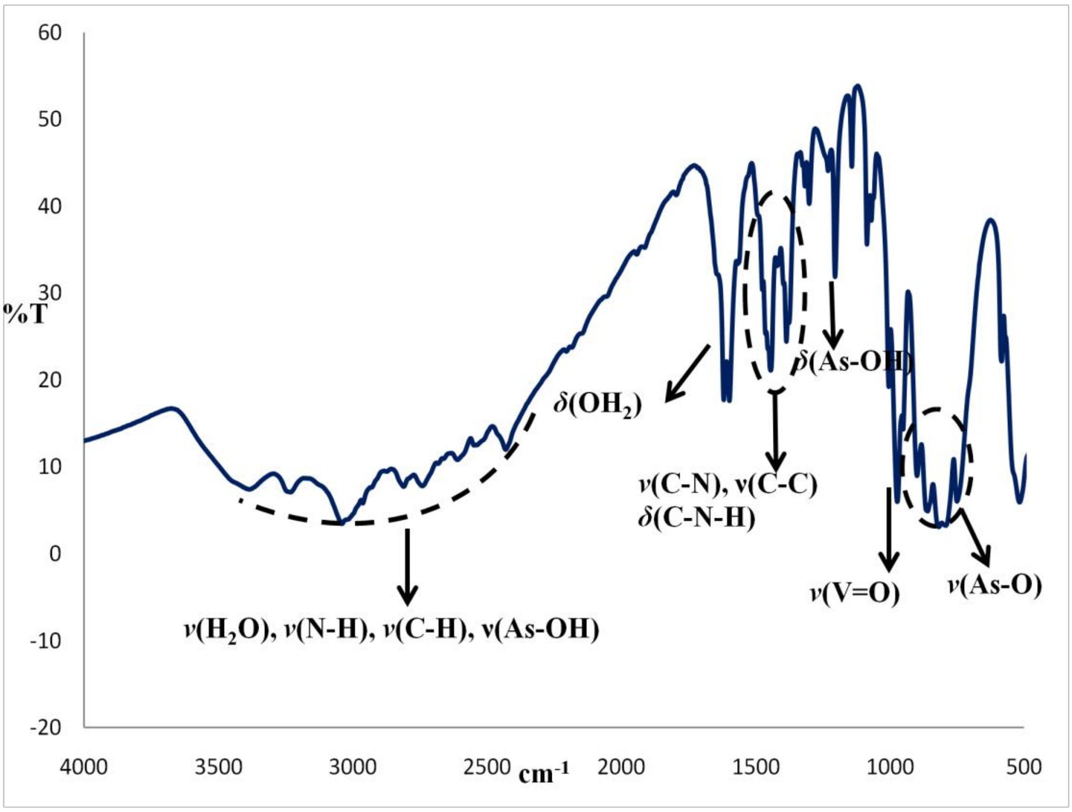

Figure 4.4: Infrared spectrum of compound (1) showing the characteristic bands for each group.

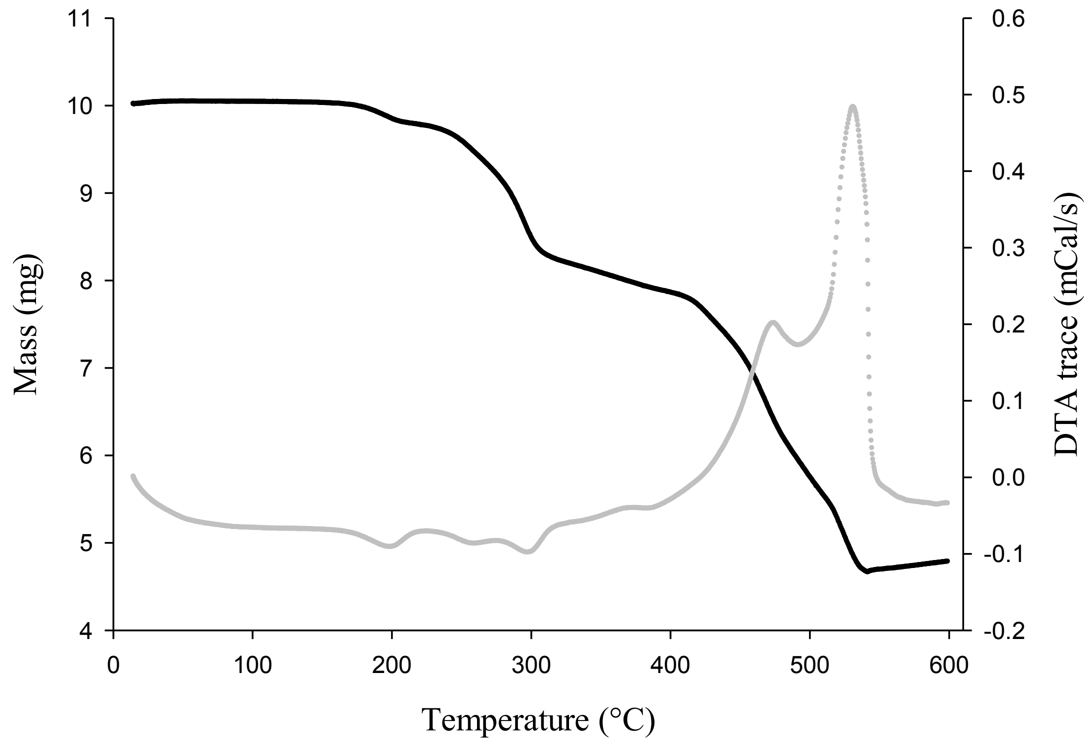

Figure 4.5: TGA pattern of compound (1). Mass loss was recorded as a function of temperature and is shown by the black line. DTA trace is the grey line.

Figure 4.5 shows TGA/DTA analysis of compound (1) (10.014 mg). A small mass loss (~2.43%) occurred in the region of 100-220 °C because of the evaporation of one water molecule from one molecule of compound (1) (calculated mass loss is 2.56%). Between 220-310 °C there is a large mass loss of approximately 15.63%, followed by a small loss of ~5.49% up to 415 °C where the framework then collapses. Both final steps indicate the calcinations of 1.5 molecules of piperazine cations and the elimination of the fluoride anions, and the total mass loss of 21.12% is in a good agreement with the calculated value (22.6%). The presence of the corresponding exothermic peak at 520 °C is consisted with the collapsing of the framework structure and the formation of the inorganic residue. X-ray powder diffraction on the decomposed product showed the presence of a mixed phase mostly consisting of V_2O_5 and As_2O_5 solids and some additional peaks that could not be identified.

II. Characterization of compound (2)

Compound (2) crystallises in the monoclinic $P2_1c$ space group as green plate crystals. Crystal and diffraction data are given in Table 4.3. Compound (2) comprises an extensive network of [$V_2As_2O_8F_6$] and [$V_6As_2O_{20}F_8$] building units in which vertices are shared to form this very unusual super-corrugated layered structure. As can be seen in Figure 4.6, layers are stacked one over the other along the *a* axis with piperazine cations and water molecules are hosted in between.

The [$V_2As_2O_8F_6$] building blocks consist of similar F-F edge shared bioctahedral units to those described earlier in compound (1), however these reported here exhibit no terminal oxo groups but rather two fluoride ligands. Bond valence calculations confirmed these sites to be fluoride based on the resulting low BVSs values (BV(O): F5 = 0.92, F6 = 1.22, F7 = 1.06; BV(F): F5 = 0.74, F6 = 0.98, F7 = 0.84). If these sites were assigned as oxide anions, BVS values close to 2 would be expected. The possibility of these being aqua ligands instead of fluorides was excluded in this case, since very low BVS values near 0.25 would have been expected. However, the case of having hydroxyl groups instead of fluorides could not be elucidated using the BV method and so investigations were concentrated on the distances between possible hydrogen-bond donors and hydrogen-bond acceptors. Indeed, fluoride ligands are within reasonable hydrogen bonding distance to a number of lattice water molecules and nitrogen atoms of piperazine molecules, and therefore a negative charge should accompany these sites. ($F(5)\cdots N_P$ = 2.65 Å, $F(6)\cdots O_W$ = 3.01-3.18 Å, $F(7)\cdots O_W$ = 2.64-3.14 Å). The presence of fluoride within the framework structure of (2) was further verified by EDS analysis.

The complex [$V_6As_2O_{20}F_8$] units are composed of two isotypical [$V_3As_1O_{11}F_4$] groups; each of them contains one doubly-bridged arsenate group and a cube-like vanadium block. The latter is composed of three VO_3F_3 octahedra connected in a triangular arrangement that share edges and faces *via* doubly and triply bonded F atoms. BV calculations showed consistently low (close to unity as expected for a monovalent ion) bond valence values for the four distinct fluoride sites (BV(O): F1 = 1.09, F2 = 1.14, F3 = 0.90, F4 = 0.88; BV(F): F1 = 0.87, F2 = 0.91, F3 = 0.72, F4 = 0.70).

The four distinct vanadium atoms present in the crystalline structure of (2) are preferentially occupied by the reduced +4 oxidation states. Each vanadium centre of the [$V_3As_1O_{11}F_4$] units exhibits the classic distorted octahedral geometry due to the presence of the VO^{+2} oxo group. All the V-F bonds *trans* to the short V=O bond are significantly lengthened and exhibit bond distances in the range of 2.123(5)-2.198(5) Å, while the remaining four equatorial distances are within the expected intermediate range. [$V_2As_2O_8F_6$] and [$V_3As_1O_{11}F_4$] building units are illustrated in Figure 4.7. The corresponding bond distances and bond valence calculations are given in Table 4.4.

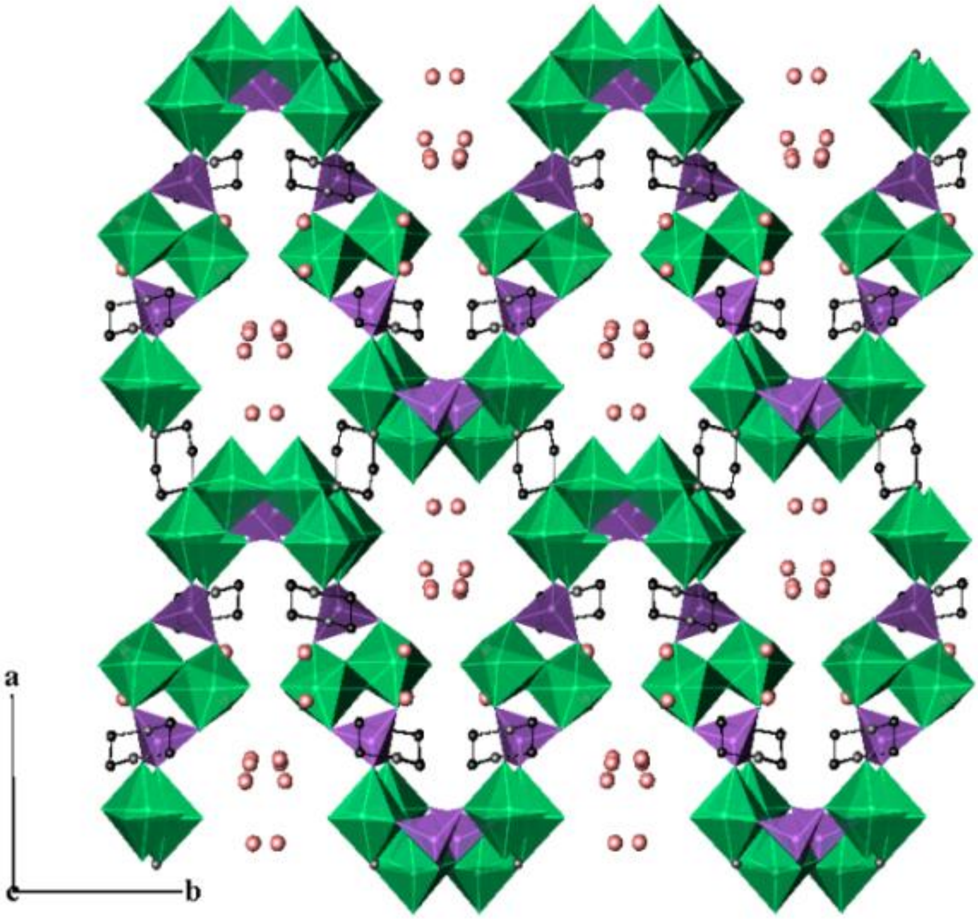

Figure 4.6: View along the *c* axis shows the super-corrugated layered character of compound (2). Green polyhedra represent vanadium octahedra; purple show the arsenate. Pink spheres show lattice water and grey-black linked spheres comprise the piperazine molecules.

Table 4.3: Crystal and diffraction information for compound (2)

Empirical formula	$C_6H_{26}N_3V_4As_2F_7O_{15}$
Formula weight	866.90
Temperature	120(2) K
Appearance	Pale green
Wavelength	0.71073Å (Mo K_α)
Crystal system	Monoclinic
Space group	$P2_1c$
Unit cell dimensions	a = 16.8763(6) Å, b = 14.1659(5) Å c = 10.7198(4) Å, β= 93.894(2)°
Volume	2556.84(16) Å^3
Z	4
D_c	2.252g.cm^{-3}
Θ range for data collection	3.12°-25.03°
Reflections collected	25614
Independent reflections	4513
Data/Restraints/Parameters	4513/0/322
R indices	R_1 = 0.0676, wR_2 = 0.1845

Table 4.4: Selected bond lengths (Å) and bond valences for compound (2).

Polyhedra	Bond lengths	Σs_{ij}	Polyhedra	Bond lengths	Σs_{ij}
$V(1)O_3F_3$			$V(4)O_3F_3$		
V(1)-O(3)	1.619(7)	1.562	V(4)-O(4)	1.964(7)	0.615
V(1)-O(9)	1.968(7)	0.608	V(4)-O(8)	1.989(6)	0.575
V(1)-O(11)	1.971(7)	0.603	V(4)-O(10)	1.608(7)	1.609
V(1)-F(2)	2.000(7)	0.444	V(4)-F(1)	2.027(6)	0.413
V(1)-F(3)	2.005(7)	0.439	V(4)-F(2)	1.985(6)	0.463
V(1)-F(4)	2.198(5)	0.260	V(4)-F(3)	2.169(5)	0.282
		ΣV1=3.92			**ΣV3=3.96**
$V(2)O_2F_4$			$As(1)O_4$		
V(2)-O(2)	1.974(7)	0.598	As(1)-O(5)	1.700(6)	1.199
V(2)-O(12)	1.985(7)	0.581	As(1)-O(7)	1.688(6)	1.238
V(2)-F(5)	2.041(6)	0.398	As(1)-O(8)	1.703(6)	1.189
V(2)-F(5')	2.102(6)	0.337	As(1)-O(11)	1.674(6)	1.286
V(2)-F(6)	1.709(9)	0.976			**ΣAs1=4.91**
V(2)-F(7)	1.763(9)	0.843			
		ΣV2=3.73	$As(2)O_4$		
			As(2)-O(2)	1.693(7)	1.221
$V(3)O_3F_3$			As(2)-O(4)	1.688(6)	1.238
V(3)-O(5)	1.976(6)	0.595	As(2)-O(9)	1.681(6)	1.262
V(3)-O(6)	1.619(7)	1.562	As(2)-O(12)	1.688(7)	1.238
V(3)-O(7)	1.973(7)	0.600			**ΣAs2=4.96**
V(3)-F(1)	1.991(6)	0.455			
V(3)-F(3)	2.123(5)	0.319			
V(3)-F(4)	2.003(7)	0.441			
		ΣV3=3.97			

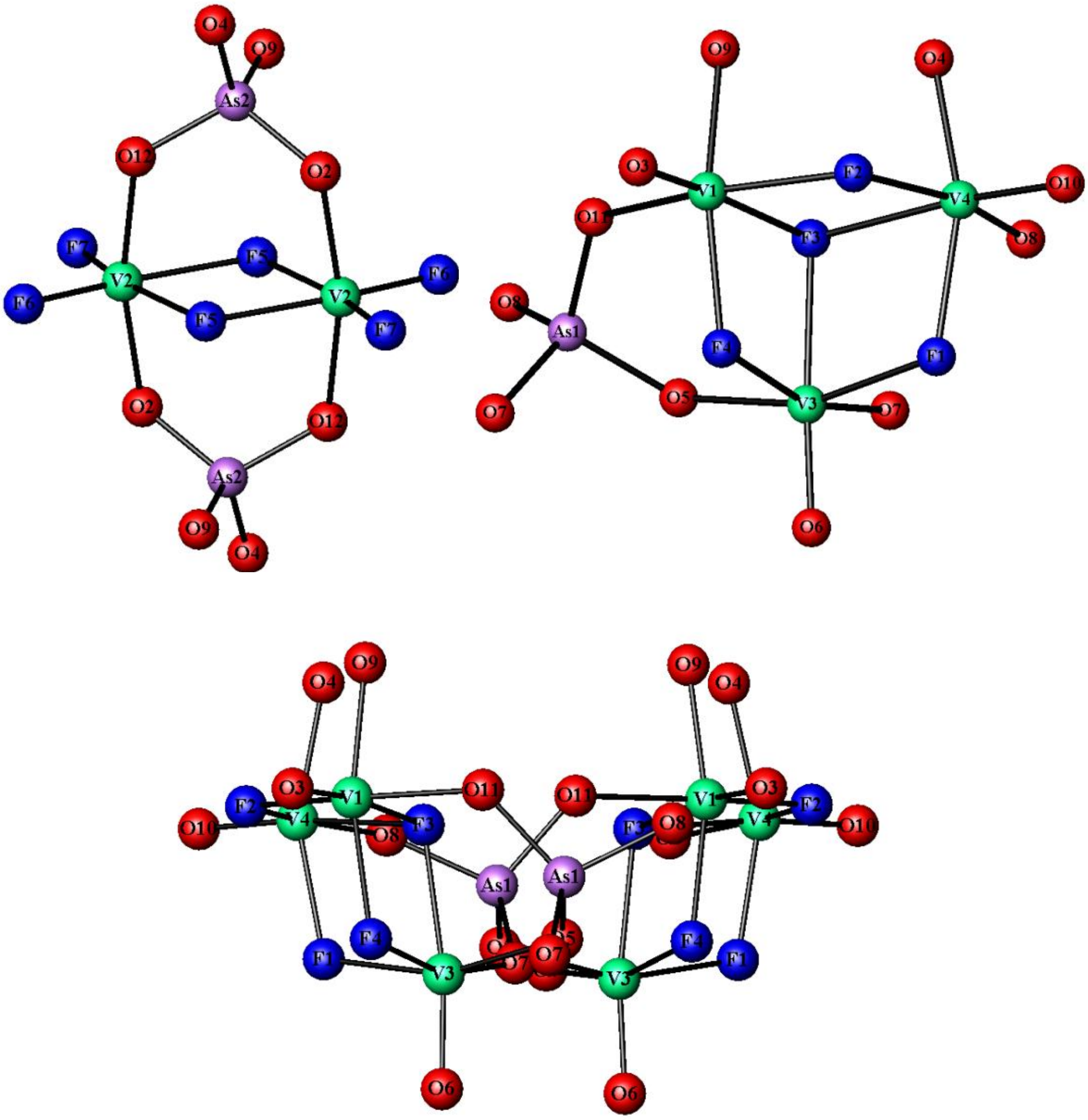

Figure 4.7: Schematic showing parts of the building unit for compound (2), [$V_2As_2O_8F_6$] unit (top left), [$V_3As_1O_{11}F_4$] unit (top right), [$V_6As_2O_{20}F_8$] unit (bottom).

Projection of the structure along the *a* axis shows how the polyhedra form complex channels filled with diprotonated piperazine cations and water molecules (Figure 4.8). [$V_6As_2O_{20}F_8$] units alternated in up and down orientations, and are connected through the As(2)O_4 tetrahedra of [$V_2As_2O_8F_6$] units to form the sinusoidal sheets. A complex network of hydrogen bonding is present within the channels, such that all the N and O atoms from the piperazine cations and water molecules respectively act as H-bond donors, providing stabilization of the framework structure. All the donors are within reasonable hydrogen bonding distances of a number of the framework O and F atoms with the N(H)···O distances ranging from 2.7559 to 2.8626 Å, the N(H)···F = 2.6471 Å, and O_W(H)···O and O_W(H)···F distances in the range 2.6362-3.0841 Å and 2.7544-3.0834 Å, respectively.

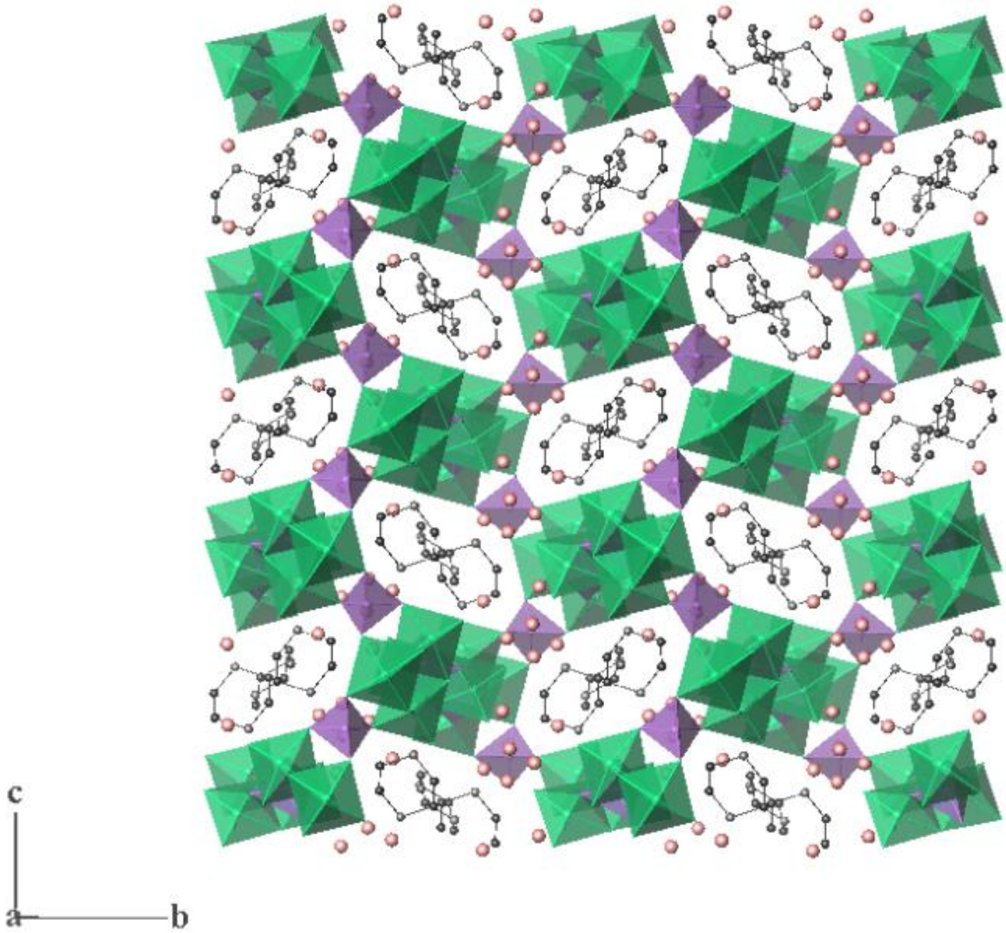

Figure 4.8: View along the *a* axis shows details of the sinusoidal sheets in the structure of (2). Green polyhedra represent vanadium octahedra; purple show the arsenate. Pink spheres show lattice water and grey-black linked spheres comprise the piperazine molecules.

Compound (2) was further characterised by IR spectroscopy and TGA analysis. The infrared spectrum of compound (2) is shown in Figure 4.9. Similarly to compound (1), the inseparable intense broad bands in the 3400-2400 cm^{-1} region can be assigned to the vibrational modes of *v*(O-H), *v*(N-H) and *v*(C-H) groups which are associated with the water molecules and piperazinium cations.[8] The strong band detected at 1628 cm^{-1} can be attributed to the $\delta(OH_2)$ of lattice water, whilst the broad band occurred in the region 1460-1380 cm^{-1} can be assigned to the very characteristic modes of the piperazine ring. These include the stretching vibrations of C-C and C-N bonds in combination with the deformation vibration of C-N-H groups. In the low frequency region, a very strong band is detected at 979 cm^{-1} which can be attributed to the ν(V=O) group, followed by the ν(As-O) stretching modes that can be detected as the doublet broad band occurred at 849 cm^{-1}/810 cm^{-1}.[9]

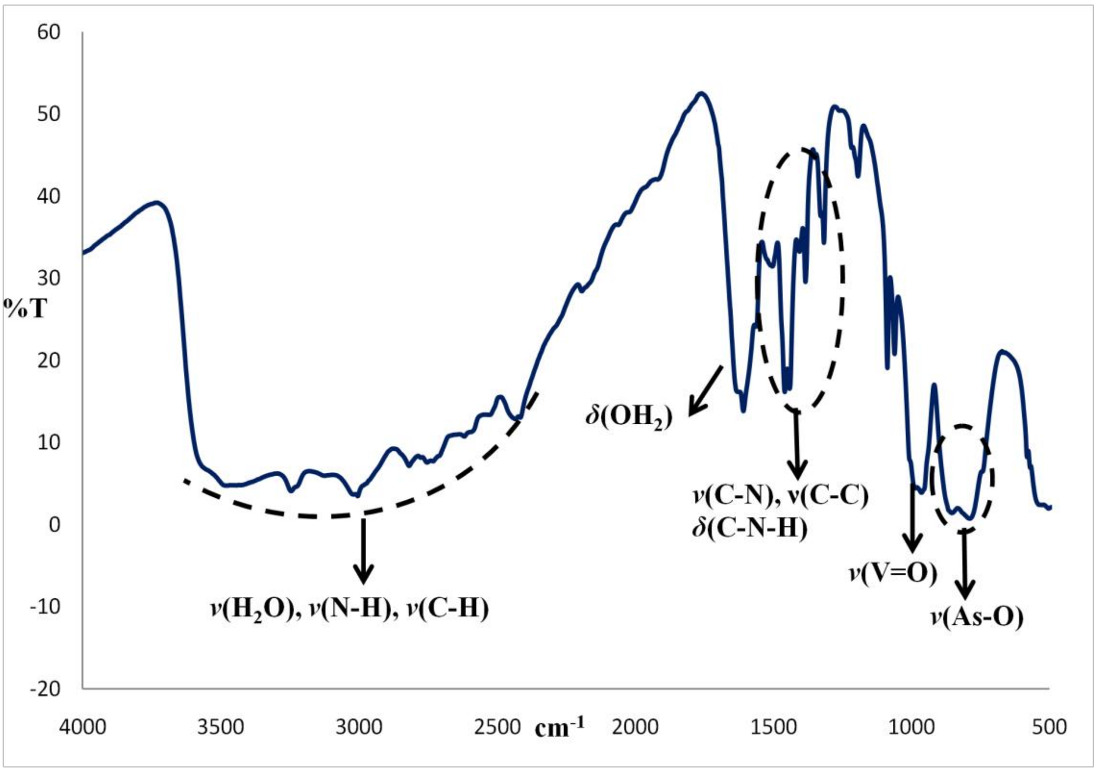

Figure 4.9: Infrared spectrum of compound (2) showing the characteristic bands for each group.

TGA and DTA analysis of the compound (2) (8.973 mg) showed a sharp decrement of mass (total loss ~ 8.52%), divided in two main steps, in the region of 80-240°C because of the evaporation of four water molecules from one molecule of compound (2) (calculated mass loss ~ 8.31%). The presence of endothermic peaks at 130 °C and 200 ° C is due to the energy for breaking the strong hydrogen bonds between the water molecules and the framework structure. The second obvious decrease of mass (loss ~ 10.04%) occurred in the region of 240-305 °C, followed by a small loss of ~ 5.59 % until 400°C where the framework then collapses. Both steps indicate the calcinations of 1.5 molecules of piperazine cations, and the total mass loss of 15.63 % is in a good agreement with the calculated value (16.64%). The presence of an exothermic peak at ~500 °C is consisted with the collapsing of the framework structure and the formation of the inorganic residue. X-ray powder diffraction analysis on this residue indicated the same product phases as compound (1), showing the presence of V_2O_5 and As_2O_5 compounds in addition to a few unidentified peaks.

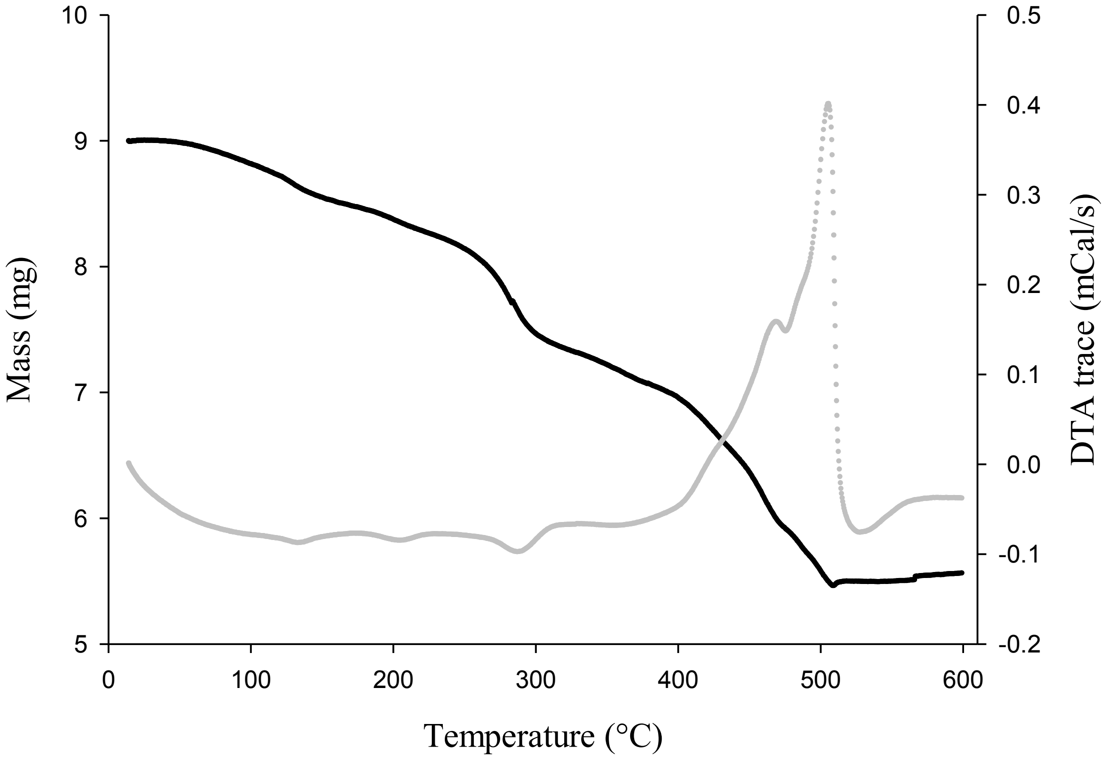

Figure 4.10: TGA pattern of compound (2). Mass loss was recorded as a function of temperature and is shown by the black line. DTA trace is the grey line.

4.1.3 Conclusions

Two piperazinium oxyfluorinated vanadoarsenate compounds have been synthesized and characterised by single crystal X-ray diffraction. From a structural point of view, they embrace framework topologies that appear to be unique, although the number of vanadoarsenate compounds that have been reported in the literature so far. The successfully incorporation of fluoride into the framework structure has led to the discovery of new architectures, particularly in case of compound (2) which is comprised of entirely new vanadium trinuclear units containing double- and triply-bonded fluoride ligands. Attempts to incorporate other amino templates in the system, such as ethylenediamine and dabco, have been less fruitful compared to the piperazine system.

4.2 Oxyfluorinated vanadoarsenates (*via* the VF_3 route)

Research within this chapter is now shifted towards the investigation of an alternative fluoride ion source. Stimulated by recent interest in the use of metal fluorides for the preparation of several phosphate-based compounds,[10] synthetic work here involves vanadium fluoride VF_3 as a starting material source. This approach led to the discovery of much different framework topologies to those described earlier in Section 4.1. A three-dimensional framework interleaved with piperazine cations and an unusual one-dimensional tubular structure have been produced and further described in detail here.

4.2.1 Experimental

I. Synthesis

The general procedure consisted of the hydrothermal treatment of vanadium fluoride with phosphoric or arsenic acid in the presence of water. The preparation of the precursor was followed by the addition of the organic amine. The reaction mixture was stirred for about one hour at room temperature before being added to a 23 mL Teflon-lined steel autoclave and heated to 418 K for four days.

Three main systems were set up based upon the utilization of a different organic amine (piperazine, dabco and ethylenediamine). Reactions in each system were performed by varying the molar composition of the amines in solutions of constant V:(P, As) molar ratios = 1:1 or 1:2. Isolated products were characterised by single X-ray diffraction, TGA, IR and EDS analysis; Bond Valence calculations were also carried out (as previously described in Section 4.1.1).

- ✓ Detailed reaction conditions for the compounds isolated within this work

$[H_2N(C_2H_4)_2NH_2]_{0.5}\{(VO)_4V(HAsO_4)_2(AsO_4)F_2(H_2O)_4\}.2(H_2O)$ (3): Vanadium (III) fluoride (0.0621 g, 0.575 mmol) was mixed with 70% orthoarsenic acid solution (0.06 mL, 0.575 mmol), piperazine (0.0248 g 0.288 mmol) and distilled water (4 mL, 222.2 mmol). Heated to 418 K and held for 4 days. Product occurred as dark green fragments.

$[H\text{-}Dabco]_xV_{27}As_{24}O_{200}F_{54}.nH_2O,\{[(VO)_3F_4(AsO_4)_{1+2/2}][V_2O_8F]_{1/2}[V_4O_4]_{1/2}\}_{12}$ (4): Vanadium (III) fluoride (0.0621 g, 0.575 mmol) was combined with 70% orthoarsenic acid solution (0.06 mL, 0.575 mmol), dabco (0.0645 g 0.575 mmol) and distilled water (4 mL, 222.2 mmol). Heated to 418 K and held for 4 days. Product crystallized as green needles up to 1 mm in length.

4.2.2 Results and discussion

I. Synthesis overview

Synthetic work in this section was concentrated on the preparation of fluorinated vanadium phosphate and arsenate compounds by utilizing VF_3 as an alternative fluoride ion source, instead of the more commonly used HF. The goal was essentially to achieve incorporation of fluoride into the framework structure by introducing high levels of fluoride ions into the reaction mixture, while also to provide safer working conditions.

Three main systems were carried out in presence of three different organic amines: piperazine, ethylenediamine and dabco. Reactions that involved arsenate species were rather fruitful, leading to the isolation of three distinct structure types in each case. These include the three-dimensional framework interleaved with piperazinium cations, the one-dimensional tube-like structure obtained in the presence of dabco, and the previously-reported $[H_2N(C_2H_4)NH_2]_{0.5}[(VO)(HAsO4)F]$ compound [5] whose structural features will be further discussed in a subsequent chapter (Chapter 5, Section 5.1.2-IV). Looking at the phosphate system it would appear that this remains quite ambiguous, with a number of unidentified products being produced. Reactions in the presence of piperazine and dabco yielded polycrystalline powders with no large crystals, suitable for X-ray single crystal diffraction, within the samples. X-ray powder analysis carried out on all samples, however, X-ray patterns seemed very complicated and any attempts to identify the containing phases proved unsuccessful. In the case of ethylenediamine, the system led to the isolation of the organically-templated structure belonging to the family of structures $M(H_2O)\{VO(F)[AsO_4]\}$ which will be discussed in the later Chapter five. Unfortunately, aggregates consisting of complex twin crystals were produced, and therefore the crystal structure exhibited similar problems with data collection as the two rubidium-templated compounds (details of which are given in Chapter 5, Section 5.1.2-I).

II. Characterization of compound (3)

Compound (3) crystallised from initial reactions aimed at investigating the templating effect of piperazine into the present system. X-ray structural analysis of the crystals revealed a building unit analogous to the previously reported compound, $[H_2N(C_2H_4)_2NH_2]_{0.5}\{(VO)_4V(HPO_4)_2(PO_4)F_2(H_2O)_4\}.2(H_2O)$.[1b] Compound (3) crystallises in the same monoclinic, *C*2/*m* space group and exhibits a slightly larger unit cell compared to the analogous phosphate compound. Crystallographic data are listed in Table 4.5.

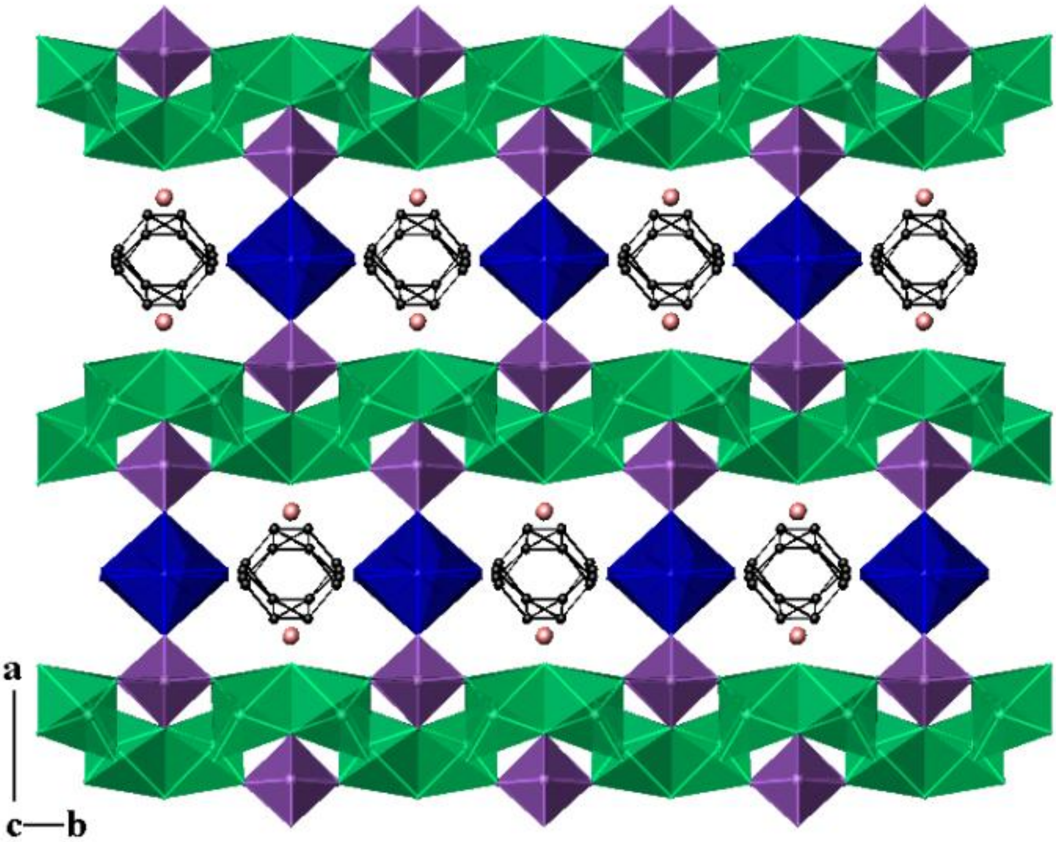

Figure 4.11: Overall view of the 3D framework structure of compound (3). Green polyhedra represent the vanadium octahedra of the bioctrahedral units $(V^{+4}O)_2FO_6$ and blue polyhedra represent the bridging $V^{+3}O_2(OH_2)_4$ octahedra; purple represent the arsenate. Pink spheres show lattice water molecules and grey-black linked spheres comprise the piperazine molecules.

The framework structure of compound (3) can be considered as derived from layers of alternating confacial bioctrahedral $(V^{+4}O)_2FO_6$ units and $[AsO_4]$ tetrahedra that are connected together by bridging isolated $V^{+3}O_2(OH_2)_4$ octahedra (shown in Figure 4.11). The $[V_2O_8F]$ confacial bioctrahedral units are situated on an inversion centre. The one crystallographically distinct vanadium atom (V1) adopts the classic distorted octahedral environment, consistent with the presence of a vanadyl group (V=O), two oxo groups and three apices shared with the symmetry equivalent octahedron *via* bridging O and F atoms, to complete the dimer. V(1) is preferentially occupied by +4 oxidation state and exhibits the very characteristic short V=O bond (1.600(8) Å) *trans* to the lengthened V-F bond (2.153(7) Å), whilst the remaining four equatorial V-O bonds are of intermediate length (1.940(8)-2.087(8) Å).

Bond valence calculations showed values close to two for all the oxygens and close to unity for the bridging fluoride anions. The V-F bond distances are in good agreement with bond lengths found in the two related phosphate compounds that contain isotypical bioctrahedral units (V-F = 2.163(5) Å BV(F) = 0.572/ V-F = 2.135(3) Å, BV(F) = 0.618).[1b] In comparing the bond lengths found in correlated confacial bioctrahedral units which include a bridging aqua ligand instead, it can be observed that very much longer distances and thus slightly lower bond valence values normally occurred. ($V-O_W$ = 2.350(6) Å, $BV(O_W)$ = 0.434 / $V-O_W$ 2.301(1) Å, $BV(O_W)$ = 0.494/ $V-O_W$ = 2.324(1) Å, $BV(O_W)$ = 0.464).[11]

Viewing down the *a* axis, it can be seen how these $[V_2O_8F]$ dimers are connected throughout the structure to six arsenate groups by generating layers running parallel to the *cb* plane (Figure 4.12). There are two crystallographically independent arsenic sites, As(1) and As(2), which both share three oxo groups with vanadium dimers through di-μ-(O,O')AsO_4 (μ^2-links) and di-μ-(O)AsO_4 (μ^3-links) bridges. Additionally, As(1) has its fourth apical unshared and pendant, providing As-OH units, whilst As(2) share its fourth oxygen with a bridging vanadium octahedron to connect adjacent layers into a three-dimensional network. In comparing the two types of arsenate bridges, it is noticeable that the V-O-As bond angles at the μ^3 bridges ($124.7° \leq \alpha_{V-O-As} \leq 126.14°$) are smaller than the bond angles at the μ^2 links ($134.40° \leq \alpha_{V-O-As} \leq 138.79°$). Both arsenate groups show bond distances of similar length for all the bridging oxygen atoms. However, in the case of As(1), there is an exceptional significantly lengthened bond distance (As(1)-O(7) = 1.718(11) Å) that shows much lower bond valence value (BV(O7) = 1.142) compared to the rest bridging oxygens. The lack of electron density around this oxygen site implies the presence of a terminal hydroxyl group.

Table 4.5: Crystal and diffraction data for compound (3)

Empirical formula	$H_{20}C_2NO_{26}F_2V_5As_4$
Formula weight	1109.64
Temperature	120(2) K
Appearance	dark green
Wavelength	0.71073 Å (Mo K_α)
Crystal system	Monoclinic
Space group	$C2/m$
Unit cell dimensions	a = 18.7392(8) Å, b = 7.5382(4) Å c = 9.1659(4) Å, β = 93.461(3)°,
Volume	1292.37(10) $Å^3$
Z	2
D_c	2.852 $g.cm^{-3}$
Θ range for data collection	3.02°-25.03°
Reflections collected	6062
Independent reflections	1227
Data/Restraints/Parameters	1227/36/91
R indices	R_1 = 0.0640, wR_2 = 0.1485

Table 4.6: Selected bond lengths (Å) and bond valences for compound (3).

Polyhedra	Bond lengths	Σs_{ij}	Polyhedra	Bond lengths	Σs_{ij}
$V(1)O_5F$			$HAs(1)O_4$		
V(1)-O(1)	2.087(8)	0.441	As(1)-O(1)	1.697(11)	1.208
V(1)-O(2)	2.073(8)	0.458	As(1)-O(4)	1.663(8)	1.325
V(1)-O(4)	1.961(8)	0.612	As(1)-O(4)	1.663(8)	1.325
V(1)-O(5)	1.600(8)	1.644	As(1)-O(7)	1.718(11)	1.142
V(1)-O(6)	1.940(8)	0.656			**ΣAs1**=5.00
V(1)-F(1)	2.153(7)	0.294			
		ΣV1=4.11	$As(2)O_4$		
			As(2)-O(2)	1.691(11)	1.228
$V(2)O_2(OH_2)_4$			As(2)-O(6)	1.673(8)	1.289
V(2)-O(8)	1.990(11)	0.513	As(2)-O(6)	1.673(8)	1.289
V(2)-O(8)	1.990(11)	0.513	As(2)-O(8)	1.678(11)	1.272
V(2)-O(2)$_W$	2.040(22)	0.448			**ΣAs2**=5.08
V(2)-O(2)$_W$	2.040(22)	0.448			
V(2)-O(3)$_W$	1.958(22)	0.559			
V(2)-O(3)$_W$	1.958(22)	0.559			
		ΣV2=3.04			

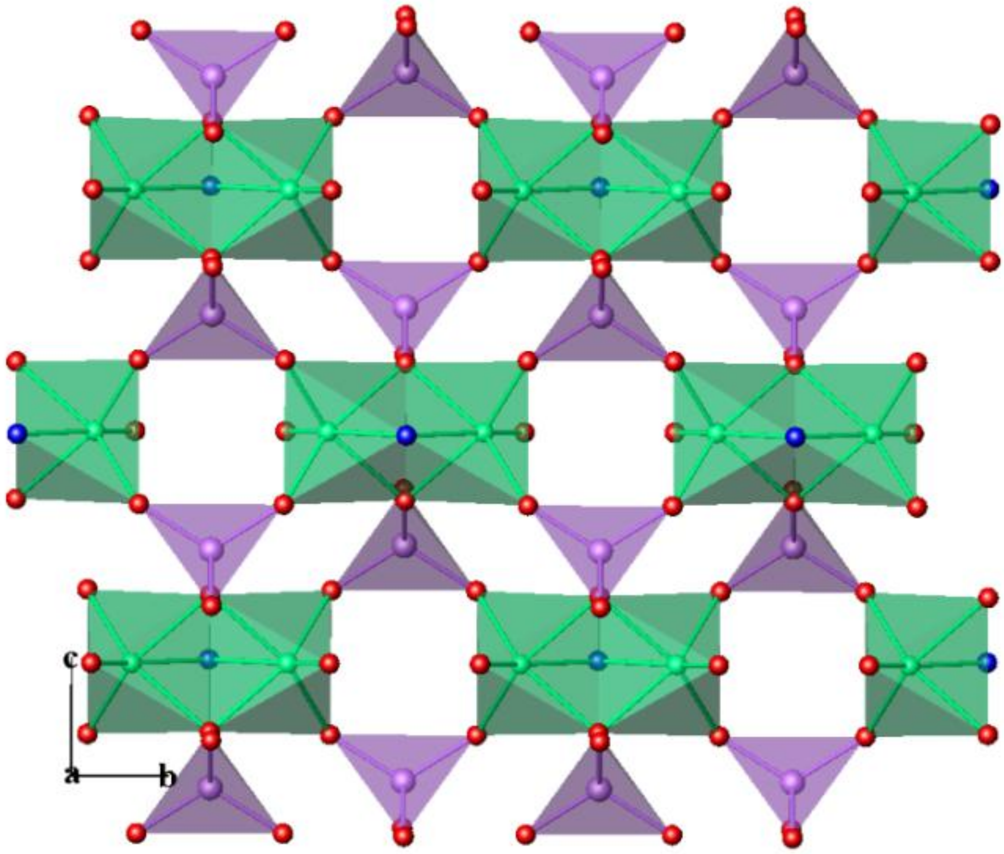

Figure 4.12: View of the layered part of the 3D framework in (3). Green polyhedra represent the vanadium octahedra of the bioctrahedral units $(V^{+4}O)_2FO_6$ and purple represent the arsenate groups.

The layered topology discussed here resembles the well known vanadyl phosphate $VO(HPO_4).0.5H_2O$ compound which comprises layers of alternating linked $(V^{+4}O)_2(H_2O)O_6$ dimers and HPO_4 tetrahedra.[11b] In contrast to the dimers identified in compound (3), the dimers of $VO(HPO_4).0.5H_2O$ have a bridging aqua ligand instead of a fluoride, and the common face is defined by two bridging oxygens and a water molecule. In a similar manner, dimers are connected to six HPO_4 groups through μ^2 and μ^3 oxo bridges to form layers which are weakly held together through strong hydrogen bonding. In attempts to break the bidimensionality and produce three-dimensional frameworks, other metals that promote interlayer connectivity can be incorporated into the framework. This was seen in the case of $(NH_4)Zn(H_2O)(VO)_2(PO_4)_2(H_2PO_4)$ compound[11a] which exhibits layers identical to the $VO(HPO_4).0.5H_2O$ and shows interconnectivity along the third axis through $[H_2PO_4]$ and $ZnO_3(H_2O)$ groups.

In a similar motif, compound (3) exhibits interlayer connectivity through V^{+3} metal centres, resulting in a three-dimensional framework structure. The bridging $V^{+3}O_2(OH_2)_4$ octahedra serve to connect adjacent layers by generating 10–ring pores that run through the structure along the c axis. There is only one distinct vanadium site, V(2) that shares two corners through O(8) atoms on the vertical plane with $As(2)O_4$ groups and has aqua ligands in all equatorial positions. X-ray single crystal diffraction showed that the octahedron of V(2) is rotationally disordered around the O(8)-V(2)-O(8) axis, and the equatorial oxygen atoms (of which there are eight when symmetry is taken into account) are refined at half occupancy. The central vanadium atom has an elongation to its thermal parameter indicating a degree of distortion in the coordination sphere.

Bond valence calculations completed at the V(2) site showed this vanadium to adopt the +3 oxidation state (BV(V2) = 3.04). Indeed, its octahedral geometry is characterised by the absence of strongly bonded oxo groups (V=O), having a regular octahedral geometry with nearly equal V-O bond distances. Crystal structures consisting of isolated bridging V(III) octahedra frequently represent structures with high degree of dimensionality; such species show great tendency for bridging adjacent chains or layers and allow the polyhedral connectivity to be much enhanced into three-dimensional networks.[12]

Projection of the structure down the c axis shows how the polyhedra form channels filled with piperazine cations and water molecules (Fig 4.11). Regarding the piperazinium cation, they appeared to be disordered around the conjunction of an inversion centre, a 2-fold rotation axis and a mirror plane. Through the refinement process, the nitrogen atom has been modelled as split between the four carbons that have closest interactions with the framework oxygens. No hydrogen atoms have been included in this model and the atoms of this molecule were refined with a global temperature factor.

Due to the required positive charge, piperazine molecules were assigned to have both nitrogen atoms diprotonated in order to act as H-bond donors and also to provide a charge-neutral compound. Nitrogen and oxygen atoms from piperazine cations and water molecules are within hydrogen bonding distance of a number of the framework O and F atoms. The N(H)···O distances ranged from 2.7152 to 3.1592 Å, the N(H)···F = 2.6739 Å, and the O_W(H)···O, O_W(H)···F distances found to be 2.6964 Å and 2.9440 Å, respectively.

Compound (3) was characterised by Infrared spectroscopy and TGA analysis. The infrared spectrum, shown in Figure 4.13, exhibits an inseparable broad band in the 3500-2800 cm^{-1} region which can be assigned to the hydroxyl stretching modes (antisymmetric and symmetric stretching) of both lattice and coordinated water in combination with the stretching modes of the N-H and C-H groups of piperazine cations. The present IR spectrum shows overlap of broad bands in this region. Bands in the high frequency region (3500-3200 cm^{-1}) must belong to water molecules and to N-H groups of the protonated piperazine cations, whereas bands in the low frequency region (3100-2800 cm^{-1}) belong to the stretching modes of C-H groups of the piperazine ring.

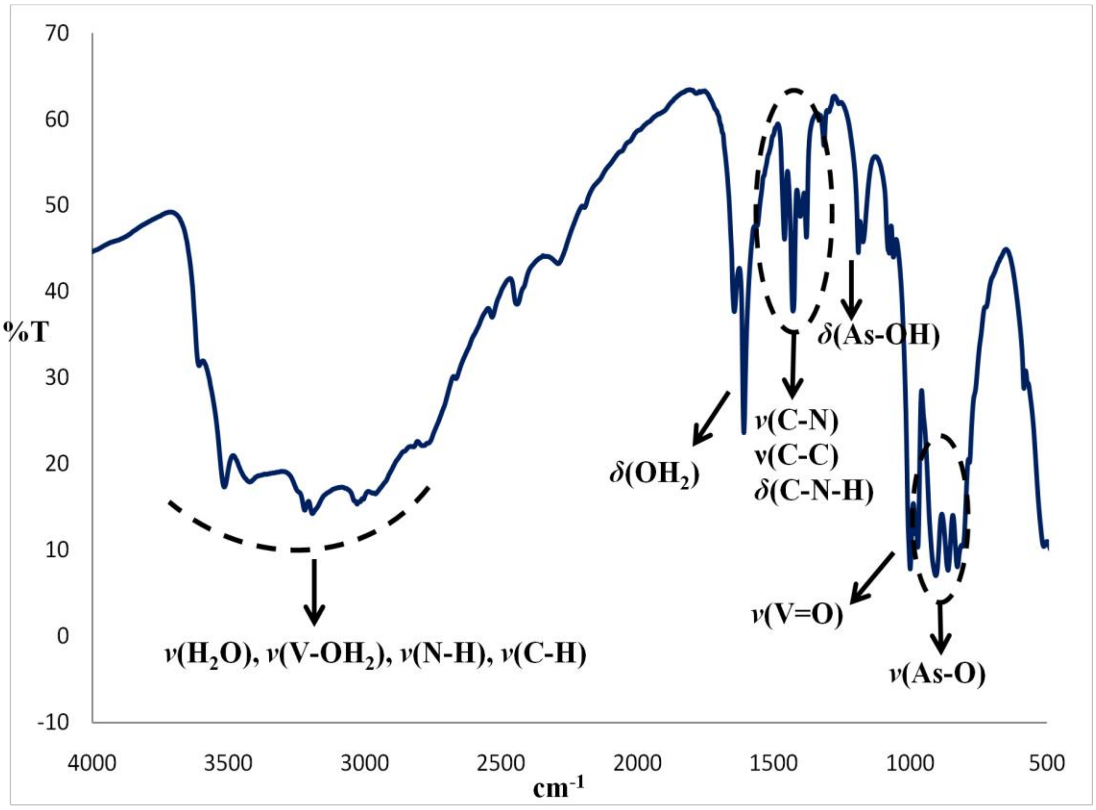

Figure 4.13: Infrared spectrum of compound (3) showing the characteristic bands for each group.

The presence of water in compound (3) can be clearly seen from the hydroxyl stretching vibration δ(O-H) which is observed as a strong doublet band at 1645 and 1610 cm^{-1}. The existence of the doublet band might be due to the presence of two types of water molecules (lattice and coordinated), thus bound water is expected to absorb at relatively higher frequencies.[13] The broad band that occurred in the region (1460-1380 cm^{-1}) can be attributed to the characteristic modes of the piperazine ring.[8] This includes the stretching vibration of C-C and C-N bonds in combination with the deformation vibration of C-N-H groups. In the low frequency region, a strong band is detected at 1170 cm^{-1} which can be assigned to the deformation vibration mode of the protonated arsenate groups.[7] The following absorption band at 972 cm^{-1} is very characteristic for the V^{+4}=O oxo groups. And finally, the intense band well resolved in three components at 906 /861 / 827 cm^{-1} can be assigned to the $\nu_3(T_2)$ stretching vibrations of arsenate groups.[9]

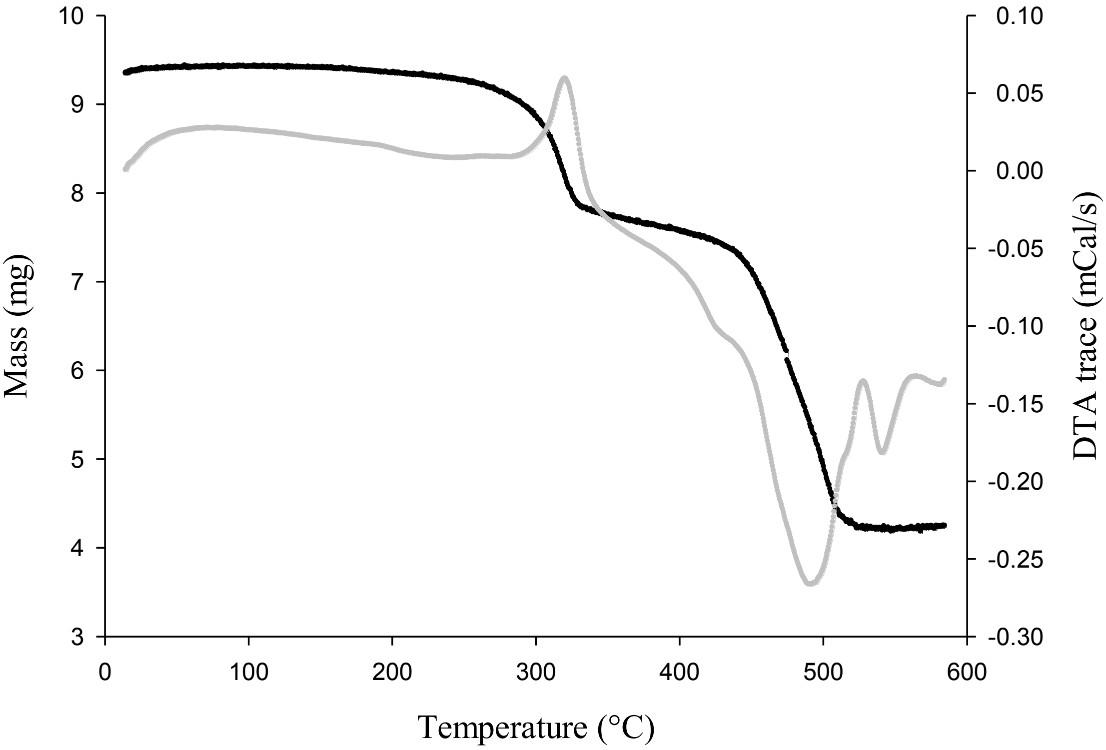

Figure 4.14: TGA pattern of compound (3). Mass loss was recorded as a function of temperature and is shown by the black line. DTA trace is the grey line.

The TGA pattern of compound (3), shown in Figure 4.14, exhibits mass loss in two main steps. The first decrement of mass (loss~17.42%) occurred in the region of 180-350 °C because of the evaporation of half a molecule of piperazine, two lattice and four bound water molecules in addition to the two fluorine ligands from one molecule of compound (3). The calculated value (~ 17.32%) is in good agreement with the observed mass loss. The presence of the exothermic peak at 320 °C is consisted with the collapse of the framework structure during the first step and the formation of the inorganic residue. The second obvious decrease of mass (~43.25%) occurred in the region of 400-520 °C because of the decomposition of the arsenate groups, thus X-ray powder diffraction on the product identified the presence of V_2O_5 as the only residue.

III. Characterization of compound (4)

The main structural features of compound (4) (details of which are summarized in Table 4.7) were initially identified from single crystal X-ray diffraction while further analysis including bond valence calculations and EDS analysis carried out to confirm the location of oxide and fluoride anions. The framework of (4) consists of crown-shaped rings formed of $V(O,F)_n$ and AsO_4 polyhedra producing two types of secondary building that are linked in alternating up-down orientations to form massive tubes, with a ring size consisting of 42 linked polyhedra, parallel to the *c* axis. The vanadium fluoroarsenate tubes are packed in a hexagonal array that resembles the theoretical crystalline form of carbon nanotubes (shown in Figure 4.15).[14] Water and H-dabco molecules are disordered inside and between the vanadoarsenate tubes.

The main secondary building unit, type I, comprises of $[(VO)_3F_4(AsO_4)_{1+2/2}]^{4-}$ units identical to those identified in compound (2) (shown in Figure 4.16). The central $[V_3O_9F_4]$ blocks are bridged by arsenate tetrahedral to form chains that extend along the tube axis. A second type of building unit (BU), type II, present in (4), is composed of a basal $[V_2O_8F]$ confacial dioctahedral unit, with the confacial atoms consisting of 2 x O and 1 x F; the two oxygen atoms of the shared face also bridge to two AsO4 tetrahedra units linking to type I units. The remainder of this BU, which caps the $[V_2O_8F]$ base and two arsenate groups, displays disorder across the full structure which may result from local disorder or differences in the *c*-axis stacking arrangement of the non-connected tubes (Figures 4.17 and 4.18). Possible vanadium and oxygen/fluorine atoms within the disordered unit were identified in an electron density map and modeled using partially occupied sites for all but one atom type. The disordered unit consists of a group of four vertex sharing vanadium polyhedra forming a distorted quadrilateral that bridges to four of the oxygen atoms of the basal [V_2O_8F] confacial unit (two oxygen atoms on each vanadium) and two on AsO_4 (one oxygen on each). This generates a large highly puckered tube consisting of 42 polyhedral units with an internal diameter of ~16 Å (note that the type II units adopt alternating up-down positions around the channel so that internally opposing are staggered relative to each other) and an external diameter of ~33 Å. The non-framework electron density distribution modeled using PLATON SQUEEZE[2] indicates highly disordered water molecules within the hollow tubes and a mixture of dabco and water between the tubes.

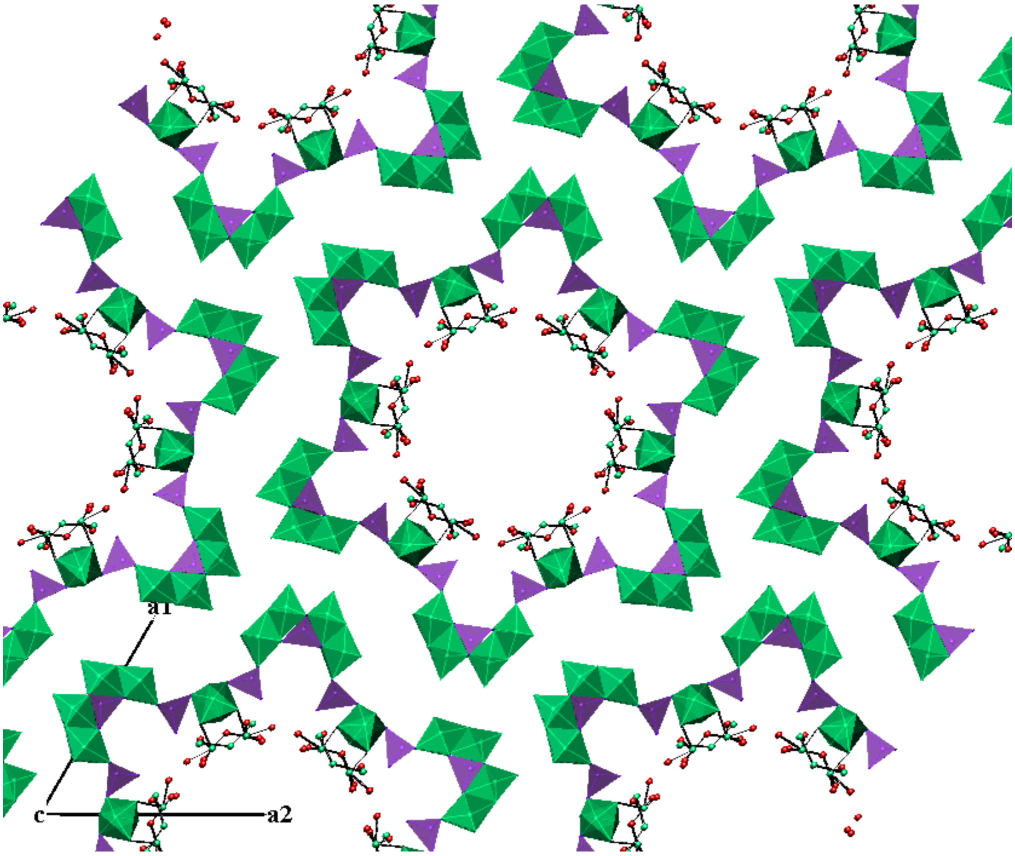

Figure 4.15: A perspective view along the *c* axis showing the hexagonal packing of neighboring tubes in the crystalline structure of (4). Green polyhedra represent vanadium octahedra and purple show the arsenate. Green and red spheres show the vanadium and oxygen atoms that belong to the disordered building blocks.

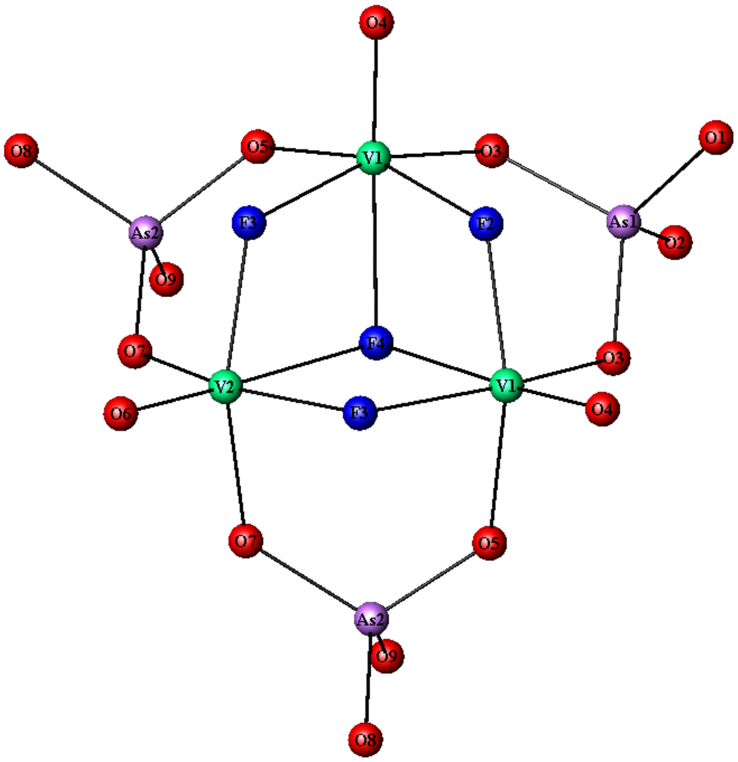

Figure 4.16: Schematic showing the main secondary building unit (type I).

Table 4.7: Crystal and diffraction information of compound (4).

Empirical formula	$As_{12}F_{27}O_{99.69}V_{36}$
Formula weight	4840.92
Temperature	120(2) K
Appearance	green needle
Wavelength	0.71073 Å (Mo K_{α})
Crystal system	Hexagonal
Space group	$P6_3/m$
Unit cell dimensions	a = 32.3426(8) Å, b = 32.3426(8) Å
	c = 10.6928(4) Å
Volume	9686.6(17) $Å^3$
Z	2
D_c	1.660 $g.cm^{-3}$
Θ range for data collection	3.16°-25.03°
Reflections collected	6027
Independent reflections	2644
Data/Restraints/Parameters	2644/90/315
R indices	$R_1 = 0.1006$
	$wR_2 = 0.2950$

Table 4.8: Selected bond lengths (Å) and bond valences for compound (4).

Polyhedra	Bond lengths	Σs_{ij}	Polyhedra	Bond lengths	Σs_{ij}
V(1)O$_3$F$_3$			V(4)O$_3$F$_3$		
V(1)-O(4)	1.618(10)	1.566	V(4)-O(11)	1.605(11)	1.622
V(1)-O(5)	1.940(10)	0.656	V(4)-O(9)	1.951(9)	0.637
V(1)-O(3)	1.974(11)	0.598	V(4)-O(12)	1.988(11)	0.576
V(1)-F(2)	1.861(6)	0.647	V(4)-F(5)	1.894(5)	0.592
V(1)-F(3)	1.929(9)	0.539	V(4)-F(7)	1.923(9)	0.547
V(1)-F(4)	2.183(7)	0.271	V(4)-F(6)	2.177(6)	0.275
		ΣV1=4.27			**ΣV3**=4.25
V(2)O$_3$F$_3$			V(5)O$_5$F		
V(2)-O(6)	1.613(14)	1.588	V(5)-O(15)	1.528(10)	2.103
V(2)-O(7)	1.942(9)	0.652	V(5)-O(16)	1.942(15)	0.687
V(2)-O(7’)	1.942(9)	0.652	V(5)-O(17)	1.974(15)	0.630
V(2)-F(3)	1.907(8)	0.572	V(5)-O(14)	2.051(10)	0.512
V(2)-F(3’)	1.907(8)	0.572	V(5)-O(1)	2.066(11)	0.491
V(2)-F(4)	2.238(12)	0.234	V(5)-F(1)	2.148(11)	0.298
		ΣV2=4.27			**ΣV5**=4.72
V(3)O$_3$F$_3$			As(2)O$_4$		
V(3)-O(10)	1.603(16)	1.717	As(2)-O(5)	1.660(11)	1.335
V(3)-O(8)	1.923(9)	0.723	As(2)-O(7)	1.693(9)	1.221
V(3)-O(8’)	1.923(9)	0.723	As(2)-O(9)	1.698(11)	1.205
V(3)-F(7)	1.885(16)	0.607	As(2)-O(8)	1.704(9)	1.186
V(3)-F(7’)	1.885(9)	0.607			**ΣAs2=4.95**
V(3)-F(6)	2.195(12)	0.262			
		ΣV3=4.64	As(3)O$_4$		
			As(3)-O(13)	1.552(20)	1.788
As(1)O$_4$			As(3)-O(12)	1.649(9)	1.376
As(1)-O(2)	1.670(21)	1.299	As(3)-O(12’)	1.649(9)	1.376
As(1)-O(1)	1.707(12)	1.176	As(3)-O(14)	1.721(12)	1.132
As(1)-O(3)	1.711(11)	1.163			**ΣAs3=5.67**
As(1)-O(3’)	1.711(11)	1.163			
		ΣAs1=4.80			

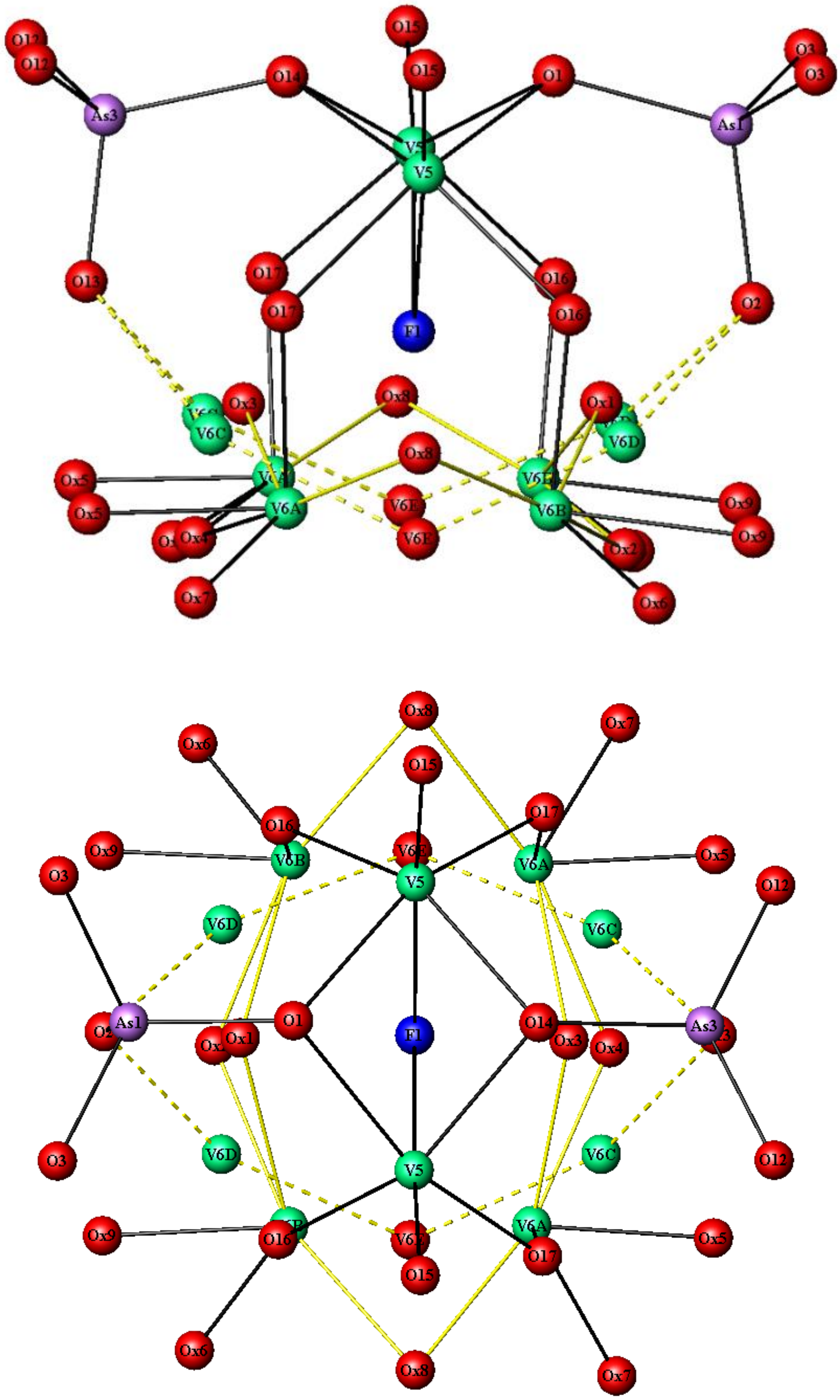

Figure 4.17: Schematic showing the disordered unit, type II, depicted as the reflection of two optical views. Yellow lines highlight the two symmetrically equivalent orientations.

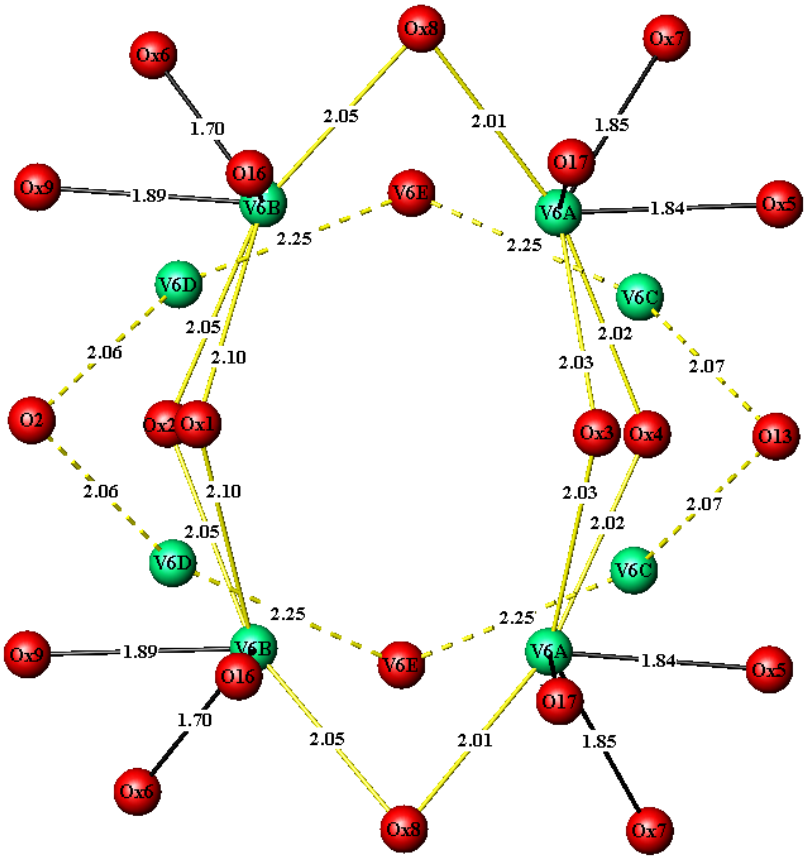

Figure 4.18: Schematic showing details of the two symmetrically equivalent orientations present in BU-type II, where bond lengths are shown in Angstrom units.

Thermogravimetric analysis, differential thermal analysis and variable temperature powder X-ray diffraction studies of compound (4) (details of which are given on the Appendices) showed loss of three dimensional order starting at 160°. The facile destruction of the ordered arrangement of the vanadoarsenate tubes of compound (4) is attributed to loss the solvent species from between the tubes rather than destruction of the tubes themselves. Reduction under hydrogen gas at 400 °C, CARE evolution of HF, yields a black material, with a much lower oxygen/fluorine content than the parent phase but with the same crystal morphology as the needles of (4).

4.2.3 Conclusions

Two amine templated vanadoarsenate frameworks have been synthesised from reactions aimed at investigating the effect of the VF_3 fluorine source. The first compound has been characterised by single crystal X-ray diffraction, revealing a structure which has a phosphate analogue. The second compound exhibits a very unusual framework topology. It comprises open-ended hollow tubes extending along the c axis, built up from entirely new building block units. Single crystal X-ray diffraction data highlight some disorder within the framework structure. Thus, there is a disordered building block unit which exhibits two symmetrically equivalent orientations.

4.3 Overview

The research included in this chapter was aimed at developing the fluoride route for preparing vanadium arsenate and phosphate compounds, as part of an attempt to investigate the role of fluoride into these systems, as well as to discover different framework topologies from those resulting from the more conventional vanadium phosphates. Experimental work reported here has followed two main synthetic routes. Some initial reactions were performed in typical HF fluoride media, and then synthetic work was shifted to the utilization of the VF_3 fluorinated source. Both routes allowed the successful incorporation of fluoride into the coordination sphere of the metal, leading to four distinct oxyfluorinated compounds (details of which are given in the following Table 4.7).

Table 4.7: Summary of the compounds characterised in this investigation.

Formula	Structural features
$[pip]_{1.5}\{[(VO)_2(AsO_4)F_2]O[(VO)(HAsO_4)F]\}.H_2O$ (1)	2D layers of F-F edge-shared $V_2O_8F_2$ dimers ($\rightarrow 2VO_4F_2$) capped on both poles by AsO_4 and $HAsO_4$. Piperazine cations interleaved.
$[pip]_{1.5}\{[(VO)_3(AsO_4)F_4][V(AsO_4)F_3]\}.4H_2O$ (2)	Super corrugated 2D layers of alternating F-F edge-shared $V_2As_2O_8F_4$ ($\rightarrow 2(VO_2F_4) + 2AsO_4$) and $V_6As_2O_{20}F_8$ ($\rightarrow 2(VO_3F_3)_3 + 2AsO_4$). Piperazine cations hosted.
$[pip]_{0.5}\{(VO)_4V(HAsO_4)_2(AsO_4)F_2(H_2O)_4\}.2(H_2O)$ (3)	Layers of confacial V_2O_8F ($\rightarrow 2VO_5F$) and AsO_4 / $HAsO_4$ tetrahedra. These are further connected by bridging $VO_2(H_2O)_4$ octahedra to form the 3D structure. Piperazine cations hosted.
$[Dabco]_xV_{27}As_{24}O_{200}F_{54}.nH_2O,\{[(VO)_3F_4(AsO_4)_{1+2/2}][V_2O_8F]_{1/2}[V_4O_4]_{1/2}\}_{12}$ (4)	1D tubes built up from $As_2V_3O_{15}F_4$ ($\rightarrow 2AsO_4 + 3VO_3F_3$) cube-like blocks and a rotational disordered building block unit. Evidence for water molecules and dabco within the structure.

From the Table above, it can be concluded that fluoride adopts both bridging and terminal sites in vanadium octahedral units, offering topological versatility in the system. A structural comparison of the isolated framework structures shows that fluoride is mostly bound at bridging sites on vanadium polyhedral units, giving rise to the formation of edge- and face-shared vanadium polymeric units, while very rarely, and only in the case of compound (2), fluoride is also found at terminal sites.

The most common building unit within this family is the $V_2As_2O_{10}F_2$ block (type I). This may be described as a vanadium dimmer built up from two F-F edge-shared vanadium octahedra which is capped on both sides by two different arsenate groups. More complex building units have been also identified. These include the unusual confacial $[(VO)_2O_6F]^{4-}$ dioctrahedral units (type II) seen in compound (3), and the new $[(VO)_3F_4(AsO_4)_{1+2/2}]^{4-}$ building blocks (type III) identified in compounds (2) and (4). Building blocks of type I allow for linear linkages between them while coupling two of the new extraordinary blocks of type III produces re-entrant links with an angle of near 160 °C; it is this combination of alternate back-folding and linear linking BUs that generates the highly corrugated structure of compound (2), whereas in compound (4) these are connected through a second re-entrant linking unit, a capped $[V_2O_8F]$ confacial dioctahedron (type II). In this case, the re-entrant angle is slightly larger than 160°, allowing six such repeating units to fold into a complete circular tube.

4.4 References

[1] a) E. Alda, B. Bazan, J. L. Mesa, J. L. Pizarro, M. I. Arriortua and T. Rojo, *Journal of Solid State Chemistry* 2003, *173*, 101-108; b) G. Bonavia, R. C. Haushalter and J. Zubieta, *Journal of Solid State Chemistry* 1996, *126*, 292-299; c) D. Riou and G. Ferey, *Journal of Solid State Chemistry* 1994, *111*, 422-426.

[2] A. L. Spek, *PLATON. A. Multipurpose Crystallographic Tool Utrecht University, UTRECHT, The Netherlands* 2005.

[3] I. D. Brown and D. Altermatt, *Acta Crystallographica Section B-Structural Science* 1985, *41*, 244-247.

[4] G. Huan, M. A. Greaney and A. J. Jacobson, *Journal of the Chemical Society-Chemical Communications* 1991, 260-261.

[5] T. Berrocal, J. L. Mesa, J. L. Pizarro, L. Lezama, B. Bazan, M. I. Arriortua and T. Rojo, *Journal of Solid State Chemistry* 2008, *181*, 884-894.

[6] a) T. Loiseau and G. Ferey, *Journal of the Chemical Society-Chemical Communications* 1992, 1197-1198; b) J. L. Paillaud, B. Marler and H. Kessler, *Chemical Communications* 1996, 1293-1294.

[7] V. Portilla, *American Mineralogist* 1976, *61*, 95-99.

[8] S.Gunasekaran and B.Anita, *Indian Journal of Pure & Applied Physics* 2008, *46*, 833.

[9] E. J. Baran and K. H. Lii, *Zeitschrift Fur Naturforschung Section B-a Journal of Chemical Sciences* 2003, *58*, 485-488.

[10] J. Rouse, K. V. Redrup, E. Kotsapa and M. T. Weller, *Chem Commun (Camb)* 2009, 7209-7211.

[11] a) E. Le Fur, O. Pena and J. Y. Pivan, *Journal of Materials Chemistry* 2002, *12*, 132-136; b) M. E. Leonowicz, J. W. Johnson, J. F. Brody, H. F. Shannon and J. M. Newsam, *Journal of Solid State Chemistry* 1985, *56*, 370-378.

[12] a) V. Soghomonian, Q. Chen, R. C. Haushalter and J. Zubieta, *Angewandte Chemie-International Edition in English* 1993, *32*, 610-612; b) Y. P. Zhang, A. Clearfield and R. C. Haushalter, *Chemistry of Materials* 1995, *7*, 1221-1225.

[13] Ray L. Frost, Kristy Erickson and M. L. Weier, *Spectrochimica acta. Part A* 2004, *60*, 2419-2423.

[14] J. Tersoff and R. S. Ruoff, *Physical Review Letters* 1994, *73*, 676-679.

Chapter Five

Oxyfluorinated Vanadium Phosphates and Arsenates

5.0 Introduction

The quest for structural diversity in inorganic framework materials has led to the use of a variety of synthetic precursors which might affect the relative solubility of the reagents under hydrothermal conditions, or may result in various predominant species that can readily undergo different hydrolysis and condensation processes, or even may act as templating agents or space fillers. Inorganic cations have been traditionally used in the synthesis of many aluminosilicate zeolites and related materials, thus acting as charge-compensating cations, or as structure-directing agents. These are usually introduced into the system in the form of a metal hydroxide source which also provides OH^- mineralizers that serve to enhance the solubility of reactants during the hydrothermal process. Research work within this chapter has attempted to widen the family of the fluoride-containing frameworks obtained *via* the VF_3 synthetic route, as well as to investigate the role of inorganic cations in framework formation under hydrothermal conditions. This approach has involved similar synthetic routes to those reported in the previous chapter with the main difference being the addition of an alkali metal or alkaline earth hydroxide source rather than an organic amine.

5.1 Vanadium phosphates and arsenates (*via* the VF_3 route)

This section of research includes a series of hydrothermal reactions involving vanadium fluoride source, phosphate or arsenate reagents with a variety of inorganic cations acting as templating agents. In presence of NH_4^+, Ba^{2+} and Rb^+ templates, a family of layered structures have been synthesised and discussed in detail here, whilst an exception has occurred in case of Cs^+, resulting in a totally different topology from the others.

5.1.1 Experimental

I. Synthesis

The general procedure entailed dissolution of VF_3 in water followed by the addition of phosphoric acid or arsenic acid and finally the hydroxide agent (NH_4OH, CsOH, RbOH, $Ba(OH_2).8H_2O$). The final reaction mixture was stirred for about one hour at room temperature before being added to a 23 mL Teflon-lined steel autoclave and heated to 418 K for four days.

Investigations were performed by varying the molar composition of the hydroxide source in solutions of constant V: (P, As) molar ratios (V: (P, As) = 1:1 or 1:2). Isolated compounds were characterised by single crystal X-ray diffraction, TGA and IR analysis. Energy-dispersive X-ray spectroscopy and Bond Valence calculations were carried out to clarify the location of near isoelectronic species, such as oxide and fluoride ions.

- ✓ Detailed reaction conditions for the compounds isolated within this work

$NH_4(H_2O)_{0.5}\{VO(F)[PO_4]\}$ (1): Vanadium(III) fluoride (0.0621 g, 0.575 mmol), 85% orthophosphoric acid solution (0.08 mL, 1.15 mmol), 25-30% ammonium hydroxide solution (0.1 mL, 0.77 mmol) and distilled water (4 ml, 222.2 mmol). Heated to 140 °C and held for 96 h. Product crystallised as pale yellow plates.

$Ba(H_2O)_2\{VO(H_2O)[PO_4]\}\{VO(F)[PO_4]\}$ (2): Vanadium(III) fluoride (0.0621 g, 0.575 mmol), 85% orthophosphoric acid solution (0.04 mL, 0.575 mmol),

$Ba(OH_2).8H_2O$ (0.1814 g 0.575 mmol) and distilled water (4 mL, 222.2 mmol). Heated to 140 °C and held for 96 h. Product crystallised as bluish green plates.

$Ba(H_2O)_2\{VO(H_2O)[AsO_4]\}\{VO(F)[AsO_4]\}$ (3): Vanadium(III) fluoride (0.0621 g, 0.575 mmol), 70% orthoarsenic acid solution (0.12 mL, 1.15 mmol), $Ba(OH_2).8H_2O$ (0.091 g 0.288 mmol) and distilled water (4 mL, 222.2 mmol). Heated to 140 °C and held for 96 h. Product occurred as bluish green plates.

$Cs[VO(HAsO_4)F]$ (4): Vanadium(III) fluoride (0.0621 g, 0.575 mmol), 70% orthoarsenic acid solution (0.06 mL, 0.575 mmol), 50% wt CsOH (0.05 mL 0.288 mmol) and distilled water (4 mL, 222.2 mmol). Heated to 140 °C and held for 96 h. Product occurred as green fragments.

II. Characterization

✓ X-ray diffraction studies

Single crystal X-ray diffraction data for each crystal structure were collected on a Bruker Nonius KappaCCD diffractometer (Mo Kα radiation, $\lambda = 0.71073$ Å) at 120 K. Refinements of the structures were carried out using the WinGX system and SHELX-97 (by following direct methods).

✓ Thermogravimetric (TGA) analysis

TGA and DTA data were collected on a Polymer Laboratories STA 1500 system. Samples (mass ~ 10 mg) were heated in flowing air from room temperature to 600 °C at a range of 10° C min^{-1}. Weight loss and heat flow were recorded as a function of temperature.

✓ Infra-red (IR) analysis

Samples were first mixed with KBr and then pressed into thin pellets. IR spectra were collected using a Perkin Elmer Spectrum system over the range 4000-500 cm^{-1}.

✓ Electron microscopy

Energy-dispersive X-ray spectroscopy and Scanning electron microscopy completed on a JOEL JSM-5910 SEM fitted with an Oxford Inca 300 energy dispersive X-ray spectroscopy analysis system.

- ✓ Bond Valence calculations

Bond valence calculations were completed at each atom site using the below equation. The theory behind the equation refers to the valence sum rule for which the valence (V) of each atom must be equal to the sum of its individual bond valences (V_i). The corresponding (V_i) values were calculated using the experimental bond lengths (R) and (R_0, b) parameters from the Tables compiled by Brown and Altermatt.[1]

$$V = \Sigma\ (V_i),\ \text{where}\ V_i = \exp\ [(R_0\text{-}R)/b].$$

5.1.2 Results and discussion

I. Synthesis overview

Five new compounds having related structural building units have been successfully obtained during this course of investigation, in addition there is a sixth compound that turns out to be very different from the others. Isolated products were successfully obtained under quite acidic conditions between the pH range 1 - 4. Attempts to apply basic conditions (pH values greater than six) by introducing higher levels of the hydroxide source into the system proved unsuccessful, leading to mixed phases the majority of which consisted of starting materials and known vanadate salts, such as $Ba(VO)_3H_2O$ and $CsVO_3(H_2O)_{0.5}$.

To begin with the case of the ammonium template, only the phosphate structure was successfully obtained, as the corresponding arsenate based system yielded only clear solutions. Taking into account that the ammonium template can interact strongly with the framework *via* hydrogen bonding, a reasonable explanation for the fact that the arsenate framework is not templating around the 'hard lewis base' ammonium is the softer character of the arsenate anion AsO_4^{3-} compared to phosphate PO_4^{3-}. On the other hand, reactions that involved softer templates such as Ba^{2+} and Rb^{+} cations have been proven fruitful for both arsenate and phosphate based systems, leading to the formation of analogous compounds. Unfortunately, in the case of rubidium the system favoured the formation of aggregates which consisted of complex twin crystals. In an effort to determine the crystal structures by using single crystal X-ray diffraction, structure refinements resulted in unacceptably high R-values, which are believed to be associated with the difficulties encountered in working with data from twinned crystals. However the main structural features, which are likely to be correct, comprise related secondary building units to those found in the two barium-templated compounds. An exception to this general structure type has been identified for reactions that involved the caesium template. The arsenate-based system resulted in the formation of an oxyfluorinated vanadoarsenate compound which showed a completely different layered topology compared to the former compounds. Attempts to synthesise the phosphate analogue of this compound were unsuccessful, leading to the formation of caesium metavanadate salts.

II. Characterization of $NH_4(H_2O)_{0.5}\{VO(F)[PO_4]\}$ (1)

The main structural features of compound (1) $NH_4(H_2O)_{0.5}\{VO(F)[PO_4]\}$(details of which are summarized in Table 5.1) were initially identified from single crystal X-ray diffraction while further analysis including bond valence calculations and EDS analysis carried out to confirm the location of oxide and fluoride anions. In the initial stages, single crystal X-ray diffraction showed the structure to consist of layers of alternating vanadium octahedra and phosphate tetrahedra with hosted interlayer ammonium cations and water molecules (Figure 5.1).

There is only one crystallographically distinct vanadium site V1 that shares its four equatorial oxygen atoms with four different phosphate tetrahedra by generating a repeating four-connected net consisting of vanadium and phosphate polyhedra (shown in Figure 5.2). Axial positions are occupied by vanadyl oxo groups and terminal fluoride ligands that are always perpendicular to the layers and alternate in up-down orientations. Bond valence calculations showed the one unique vanadium site to adopt the highest oxidation state +5 (BV (V) = 4.82). This exhibits the classic distorted geometry, having its four equatorial V-O bond lengths in the range 1.923(6) Å - 1.968(6) Å, and the terminal V-F bond (*trans* to the short V=O) significantly lengthened (V-F: 2.176(7) Å, V-O: 1.580(6) Å). BV calculations completed on all atom sites (compiled in Table 5.2) showed the expected values: BV (P) = 5.05 for the one unique phosphorous site and BV(O)s ~ 2 for all the bridging oxygens. An exception was noticed for the terminal F1 site which exhibits a significantly low bond valence value below the expected unity (BV(F) = 0.276), and thus prompted speculation as to whether this position is likely to be an aqua ligand instead. Based on the electron microscopy analysis which showed the presence of fluorine within the crystalline structure, in addition to the similar low BV value (V-F = 2.1081(5) Å, BV(F) = 0.332) found in the related reported compound $Na_3\{V_2O_2F[PO_4]_2\}$[2], this site was eventually assigned as a terminal fluoride ion. On the other hand, much longer bond distances and thus significantly lower BV(O) values compared to compound (1) were generally observed in related compounds that contained terminal aqua ligands instead ($V-O_w$/ $BV(O_w)$ = 2.335(3)Å/ 0.226[3], 2.439(3) Å/ 0.170[4], 2.366(3) Å/ 0.207, 2.318(2) Å/ 0.236[5]. In both cases, very low BV values were observed for the terminal fluorides or aqua ligands resulting from the strong hydrogen bonding interactions to these sites.

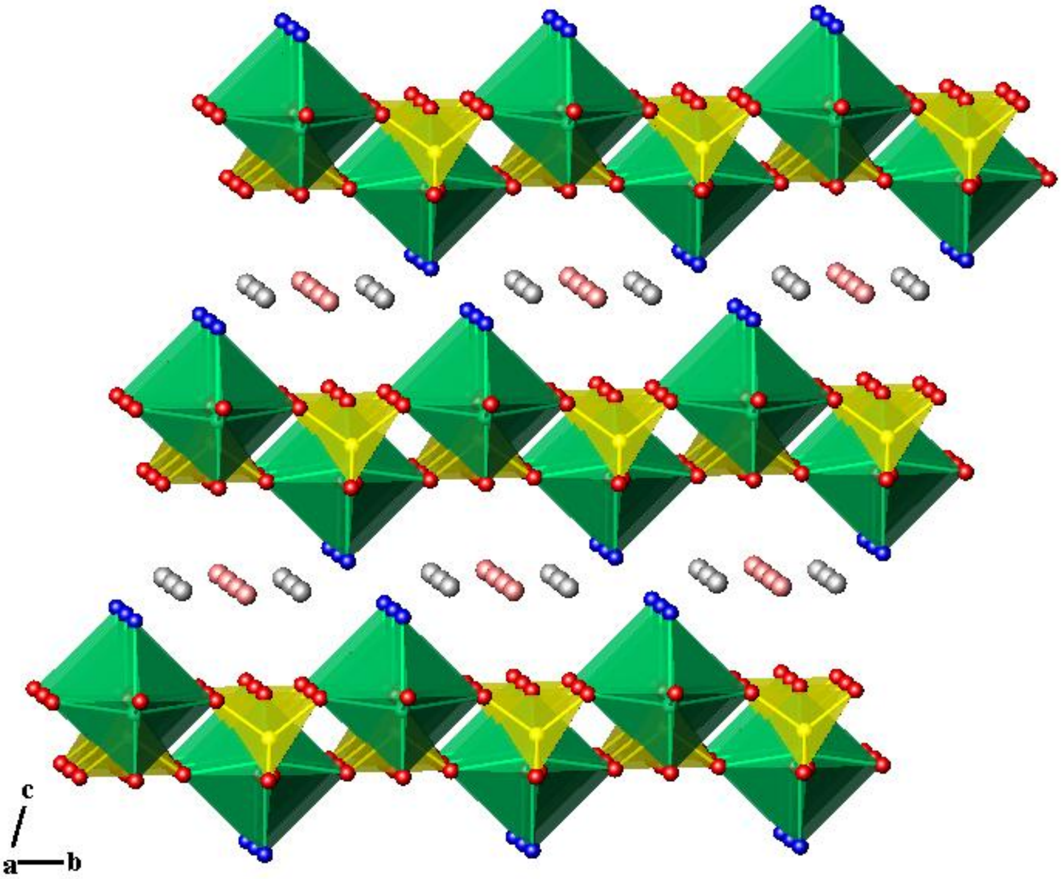

Figure 5.1: Layered structure of compound (1) viewed down the *a* axis. Green polyhedra represent vanadium octahedra and yellow polyhedra represent the phosphate (oxygen and fluorine atoms are shown in red and blue, respectively). Pink spheres show lattice water; grey spheres represent the ammonium cations.

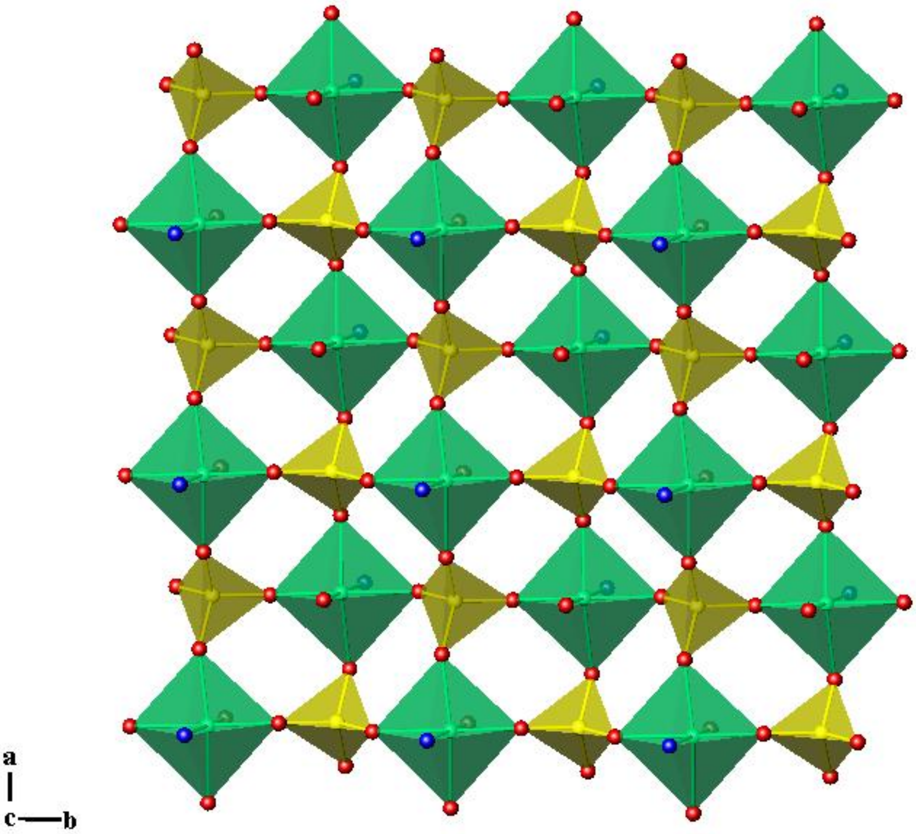

Figure 5.2: Layers built up from repeating four-connected nets of vanadium (shown in green) and phosphate polyhedra (shown in yellow).

Table 5.1: Crystal and diffraction data for compound (1).

Empirical formula	$H_5NO_{5.5}FVP$
Formula weight	207.96
Temperature	120(2) K
Appearance	Pale yellow plates
Wavelength	0.71073Å (Mo K_α)
Crystal system	Triclinic
Space group	$P\bar{1}$
Unit cell dimensions	a = 6.2713(4) Å, b = 6.2824(4) Å c = 7.2128(6) Å, α = 106.748(4)° β = 98.049(4)°, γ = 90.149(5)°
Volume	269.16(3) Å^3
Z	2
D_c	2.566 g.cm^{-3}
Θ range for data collection	2.91°-27.48°
Reflections collected	5441
Independent reflections	958
Data/Restraints/Parameters	958/0/89
R indices	R_1 = 0.0703, wR_2 = 0.1687

Table 5.2: Selected bond lengths (Å) and bond valences for compound (1).

Polyhedra	Bond Lengths	Σs_{ij}	Polyhedra	Bond Lengths	Σs_{ij}
$V(1)O_5F$			$P(1)O_4$		
V(1)-O(1)	1.946 (6)	0.679	P(1)-O(1)	1.531(7)	1.262
V(1)-O(2)	1.950(6)	0.672	P(1)-O(2)	1.528(6)	1.272
V(1)-O(3)	1.923(6)	0.723	P(1)-O(3)	1.542(6)	1.225
V(1)-O(4)	1.968(6)	0.640	P(1)-O(4)	1.524(6)	1.286
V(1)-O(5)	1.580(7)	1.827			**ΣP1=5.05**
V(1)-F(1)	2.176(7)	0.276			
		ΣV1=4.82			

As can be depicted in Figure 5.1, there is a relative displacement of the layers in such a way that fluorine atoms of adjacent layers are not pointing exactly towards each other. In general, insertion of guest species between the layers normally causes displacement of the layers and rotation of the polyhedra. Two non-framework species with different occupancy factors were identified in between the interlamellar space and were assigned as 1 x (NH_4^+) and 1 x $(H_2O)_{0.5}$ based upon the required positive charge of the framework. Moreover, the very characteristic distances between possible hydrogen-bond donors and hydrogen-bond acceptors and thereby their characteristic coordination spheres support this assumption, allowing the ammonium cations and water molecules to adopt the expected tetrahedral geometry and the typical 2-fold coordination, respectively.

Evidence for the presence of water molecules and ammonium cations was clearly seen by IR spectroscopy and was further confirmed by TGA analysis. The infrared spectrum of compound (1) $NH_4(H_2O)_{0.5}\{VO(F)[PO_4]\}$, shown in Figure 5.4, exhibits an inseparable broad band in the 3500-3200 cm^{-1} region assigned to the hydroxyl stretching modes (antisymmetric and symmetric stretching) of the lattice water in combination with the stretching modes of the NH_4^+ groups.[6] Since the stretching modes of both guest species lie in the same region, observation of the bending vibrations could be used in order to distinguish them. Indeed the H-O-H bending mode of the water molecule appears at 1630 cm^{-1}, and the corresponding bending vibration of the ammonium cation is detected at 1415 cm^{-1}. The absorption bands of PO_4^{3-} and V=O groups appear at lower frequencies.[7] The two strong band detected at 1086 cm^{-1} can be attributed to the vibration mode of PO_4^{3-} groups, whilst the second strong broad band observed at 952 cm^{-1} can be assigned to a mixture of P-O and V=O stretching modes.

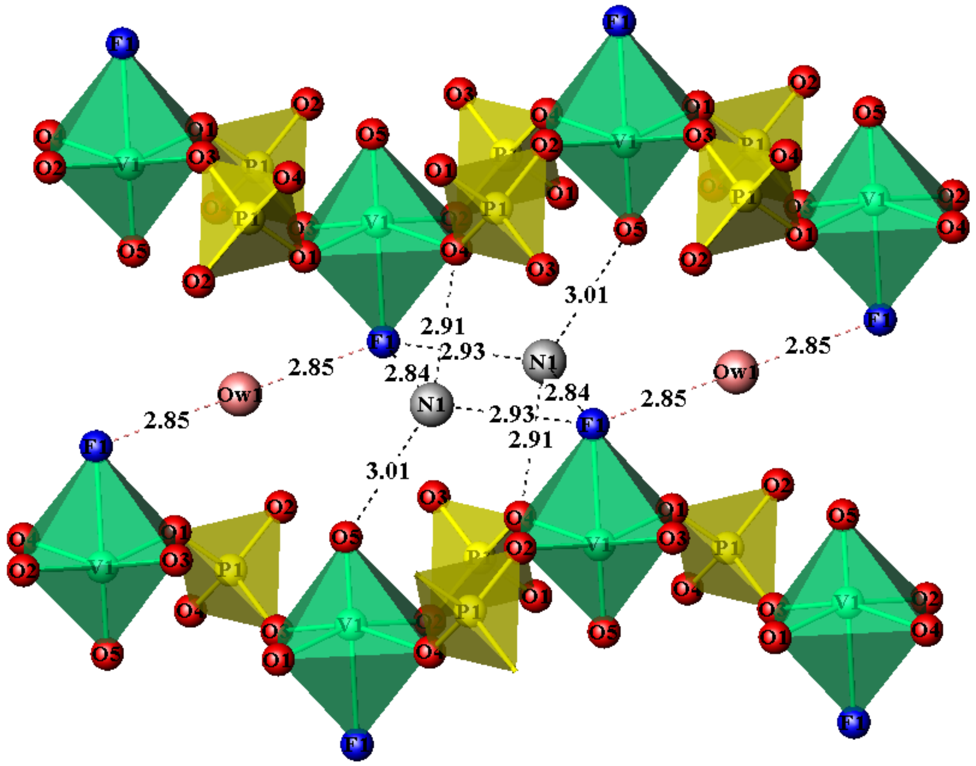

Figure 5:3: Schematic showing the tetrahedral coordination geometry of ammonium cations and the 2-fold coordination of water molecules. Hydrogen atoms are assured to lie on the dotted lines. NH_4^+ (grey spheres) and water molecules (pink spheres) are within hydrogen bonding interactions to a number of framework atoms.

The TGA pattern (shown in Figure 5.5) exhibits mass loss in four main steps, followed by a number of endothermic peaks. The latter can be attributed to the energy for breaking the hydrogen bonds and to the evaporation of the water molecules and the ammonium cations. The first decrement of mass (loss ~ 4.83%) occurred in the region of 80-150 °C because of the evaporation of half a molecule of water from one molecule of compound (1) (calculated value: 4.32%). The second obvious decrease of mass (~5.86%) occurred in the region of 150-275 °C followed directly by the third step which occurs between 150-320 °C (mass loss ~ 3.73%). Both steps can be assigned to the loss of one molecule of ammonium cation from one molecule of compound (1) as the observed total mass (~9.49%) is in a good agreement with the calculated value (9.13%). The final decrement of mass is observed between 320 and 460 °C (loss ~12.74%) and this latter step might be attributed to the elimination of the fluorine ligand attached to the framework (calculated value: 10.46%).

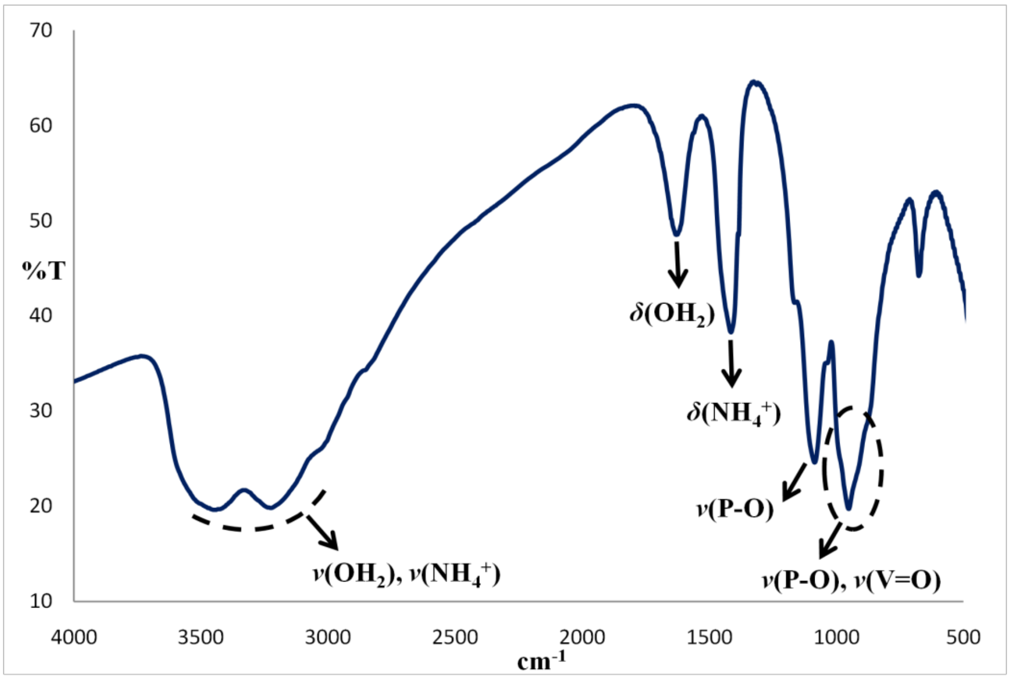

Figure 5.4: Infrared spectrum of compound (1).

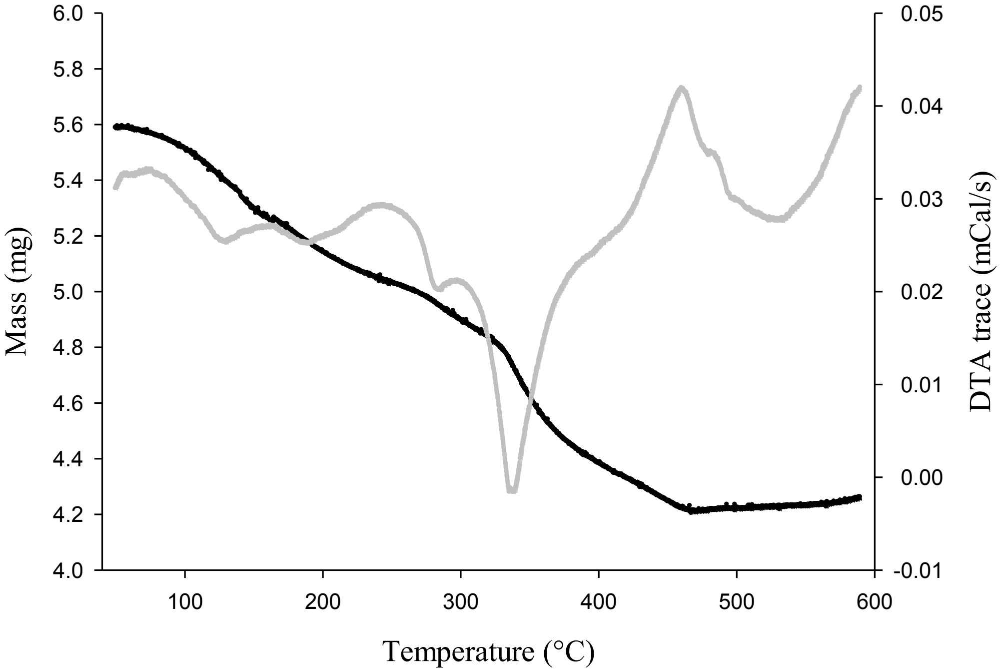

Figure 5.5: TGA pattern of compound (1). Mass loss was recorded as a function of temperature and is shown by the black line. The DTA trace is the grey line.

It is worthwhile pointing out at this stage an important correlation that was observed between compound (1) and a large family of structures reported in the literature. From a structural point of view, compound (1) exhibit similar polyhedral connectivity to the one that occurs in the mineral natisite, Na_2TiSiO_5[8]. Based on a similar bonding motif, natisite is comprised of titanium hemioctahedral which shares four corners with four different SiO_4 units in such a way as to form anionic layers with sodium cations in the interstices. A wide range of compounds, which can be thought as derivatives of the natisite, have been reported in the literature, though here most attention has been paid to the vanadium phosphate derivatives, as they are considered to be the most closely related compounds with compound (1).

To begin with the polymorphic vanadyl phosphate $VO(PO_4)$, the α-form was the first reported vanadium phosphate to adopt this characteristic bonding motif.[9] Its structure can be considered as derived from neutral tetragonal layers of corner-sharing VO_5 square based pyramids and PO_4 tetrahedra. Following a similar motif, VO_5 units share four equatorial oxygens with four PO_4 groups in such a way that the vanadyl oxo groups are always antiparallel. One of the most interesting features is the extraordinary stacking of these layers which allows weak interlayer connectivity along the axial vertices of vanadium polyhedra. Due to this phenomenon, α-$VO(PO_4)$ may undergo intercalation reactions and act as a host for neutral guests such as water molecules.

In the latter case, intercalation of α-$VO(PO_4)$ with water molecules causes expansion of the interlayer space and additionally strongly modifies the vanadium geometry into sixfold coordination, having the aqua ligands attached to vanadium spheres. This is the case for $V^{(V)}OPO_4.2H_2O$ which is comprised of neutral layers of alternating $V^{(V)}O(H_2O)O_4$ octahedra and PO_4 groups with intercalated water molecules.[3] Vanadyl phosphate dihydrate $VOPO_4.2H_2O$ has received considerable interest in the last few years due to its ability to act as a host lattice for redox intercalation reactions with alkali metals and alkaline earth cations. Thus, partial reduction of the vanadium centres allows $V^{(IV)}OPO_4.2H_2O$ to act as a host for cationic species, resulting in a series of alkali metal intercalated compounds, details of which are given in Table 5.3

Table 5.3: Crystallographic data and structure details of a series of vanadophosphate compounds related to compound (1).

Reported Compound[Ref]	Unit cell information	Structural features
$(H_2O)\{VO(H_2O)[PO_4]\}$[3]	Tetragonal, $P4/nmm$ α = 6.202(2) Å, c = 7.410(1) Å,	Neutral layers of alternating $V^{+5}O_5(OH_2)$ and PO_4 polyhedra. H_2O in the interlayer region.
$Ba_{0.5}(H_2O)\{VO(H_2O)[PO_4]\}$[4]	Monoclinic, Pn α = 6.3860(3),b = 12.7796(9)Å, c = 6.3870(5)Å,β = 90.172(6)° V = 521.24(6) $Å^3$	Layers of alternating $V^{+4}O_5(OH_2)$ and PO_4. H_2O and Ba^{+2} in the interlayer region.
$K_{0.5}(H_2O)\{VO(H_2O)[PO_4]\}$[5]	Triclinic, P-1 α = 6.282(2) Å, b = 6.285(1) Å c = 6.679(2)Å, α = 89.11(2)°, β = 72.84(2), °γ = 89.98(2)° V = 251.9(1) $Å^3$	Layers of alternating mixed valence $V^{+4.5}O_5(OH_2)$ octahedral and PO_4 tetrahedra. H_2O and K^+ in the interlayer region.
$Na_{0.5}(H_2O)\{VO(H_2O)[PO_4]\}$[5]	Triclinic, P-1 α = 6.285(7) Å, b = 6.284(1) Å c = 13.262(2)Å, α = 80.30(1)°, β = 87.434(9), °γ = 89.94(1)° V = 515.7(1) $Å^3$	Same structural features as the potassium derivative. In contrast, it exhibits different atomic positions.
$Co_{0.5}(H_2O)\{VO(H_2O)[PO_4]\}$[10]	Tetragonal, $I4/mmm$ α = 6.264(1) Å, c = 13.428(4)Å V = 526.9 (2) $Å^3$	Layers of alternating $V^{+4}O_5$ square pyramids and PO_4. Layers are weakly held through V=O-Co-O=V chains. Coordination sphere of Co^{+2} is defined by two oxo groups (V=O) and four lattice H_2O.
$Ni_{0.5}(H_2O)\{VO(H_2O)[PO_4]\}$[11]	Tetragonal, $I4/m$ α = 6.251(1) Å, c = 13.334(3)Å V = 521.0 (3) $Å^3$	Isostructural to the Co-derivative.
$Ca_{0.5}(H_2O)\{VO(H_2O)[PO_4]\}$[10]	Triclinic, $P1$ α = 6.348(8) Å, b = 6.350(1) Å c = 6.597(1)Å, α = 106.81(2)° β = 94.09(1)°, γ = 90.02(1)° V = 253.86(8) $Å^3$	Layers of alternating $V^{+4}O_5(OH_2)$ and PO_4. Coordination sphere of Ca^{+2} is defined by one oxo group (V=O), two lattice H_2O, two coordinated H_2O-V and two oxygens from V-O-P bridge.
$Sr_{0.5}(H_2O)\{VO(H_2O)[PO_4]\}$[10]	Monoclinic, Cc α = 9.026(2) Å, b = 9.010(3) Å c = 12.841(3) Å,β = 100.19(2)° V = 1027.8(1) $Å^3$	Same structural features with Ca derivative. In contrast, it exhibits different stacking of the layers.
$Pb_{0.5}(H_2O)\{VO(H_2O)[PO_4]\}$[10]	Monoclinic, Cc α = 9.030(3) Å, b = 9.021(2) Å c = 12.874(4) Å, β =100.16(2)° V = 1032.3(5) $Å^3$	Isostructural to the Sr derivative.

From the Table above, it can be concluded that these compounds exhibit the same polyhedral connectivity as compound (1), having the four equatorial oxygens of each vanadium shared between four different phosphate groups. Vanadium coordination geometries varied from octahedral to square based pyramidal and vanadium sites are preferentially occupied by reduced oxidation states, thus reduction of vanadium seemed to be necessary in order to allow insertion of cationic guests. In contrast, compound (1) exhibits vanadium sites occupied by vanadium in the highest oxidation state +5. Hence, insertion of the terminal fluoride ligand into the vanadium coordination sphere renders the framework negatively charged and allows the successful incorporation of ammonium cations. An additional beneficial effect of the terminal fluoride is its ability to enhance the hydrogen bonding by creating anchoring points for ammonium cations, which facilitates stabilization of the structure. To the best of our knowledge, the ammonium templated derivative from the family displayed in Table 5.3 has not yet been reported. A reasonable explanation might be the unstable nature of the structure due to the absence of strong hydrogen bonding interactions.

III. Characterization of $Ba(H_2O)_2\{VO(H_2O)[TO_4]\{VO(F)[TO_4]\}$ (2), (3)

Two isostructural compounds were obtained when barium was introduced into the present system. Compounds (2) and (3) $Ba(H_2O)_2\{VO(H_2O)[TO_4]\{VO(F)[TO_4]\}$ (where T = P, As), crystallise in the same $P2_1$ space group. Crystal and diffraction data are compiled in Table 5.4. The framework structure of $Ba(H_2O)_2\{VO(H_2O)[TO_4]\}\{VO(F)[TO_4]\}$, shown in Figure 5.6, can be best thought of as being derived from layers of corner-sharing vanadium octahedra and oxotetrahedral groups with Ba^{2+} cations and water molecules occupying the interlamellar space. They exhibit identical bonding motifs to that of compound $NH_4(H_2O)_{0.5}\{VO(F)[PO_4]\}$ (1), however they embrace different vanadium environments, having two types of octahedral units: $V(1)O_5(H_2O)$ and $V(2)O_5F$ with terminal aqua ligands and fluoride ions, respectively. H_2O and F^- terminal ligands are always bonded perpendicular to the layers and alternated in up-down orientations.

Table 5.4: Crystal and diffraction data for compounds (2), (3).

Empirical formula	$H_6BaO_{13}FV_2P_2$	$H_6BaO_{13}FV_2As_2$
Formula weight	534.21	622.11
Temperature	120(2) K	120(2) K
Appearance	dark blue	dark blue
Wavelength	0.71073 Å (Mo K_α)	0.71073 Å (Mo K_α)
Crystal system	Monoclinic	Monoclinic
Space group	$P2_1$	$P2_1$
Unit cell dimensions	a = 7.2225(3) Å b = 8.8870(4) Å c = 8.9007(4) Å β= 108.815(3)°	a = 7.3380(5) Å b = 9.0448(6) Å c = 9.1177(7) Å β= 108.244(4)°
Volume	540.78(4) $Å^3$	574.73(7) $Å^3$
Z	2	2
D_c	3.281 $g.cm^{-3}$	3.595 $g.cm^{-3}$
Θ range for data collection	2.92°-25.02°	2.92°-25.02°
Reflections collected	5124	6506
Independent reflections	1796	1965
Data/Restraints/Parameters	1796/19/94	1965/79/101
R indices	R_1 = 0.0790,wR_2 =0.1702	R_1 = 0.0632,wR_2 = 0.129

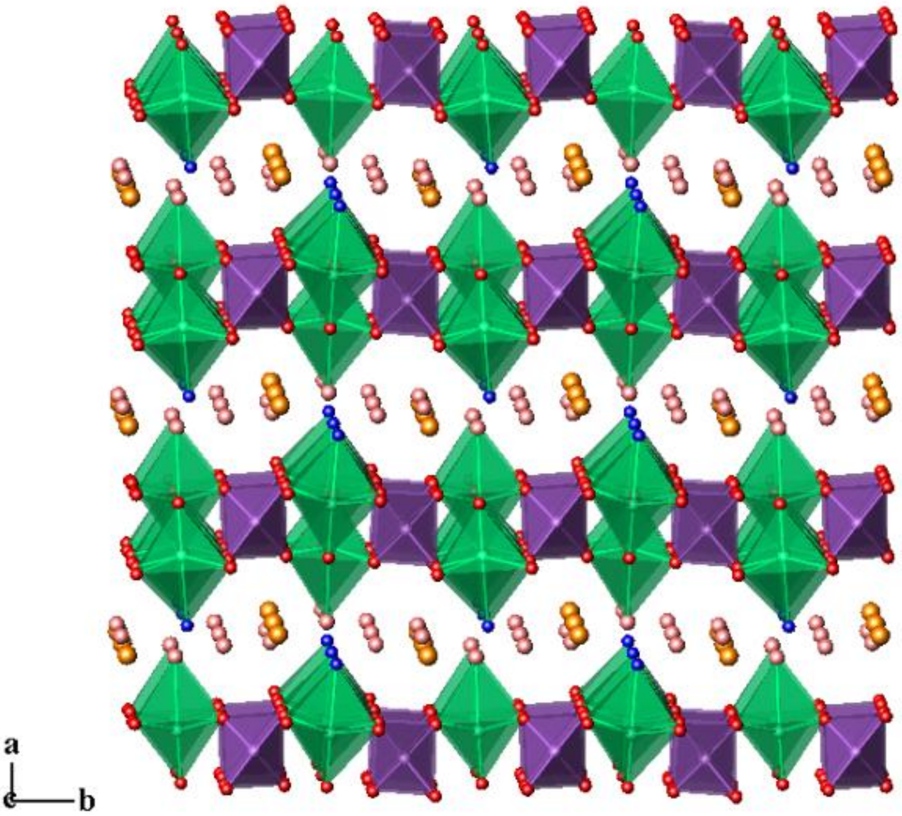

Figure 5.6: Layered structure of compounds (2) and (3). Green and purple polyhedra represent the VO_6 and the TO_4^{3-} groups, respectively (H_2O and F^- terminal ligands are shown in pink and blue); orange spheres represent the barium cations.

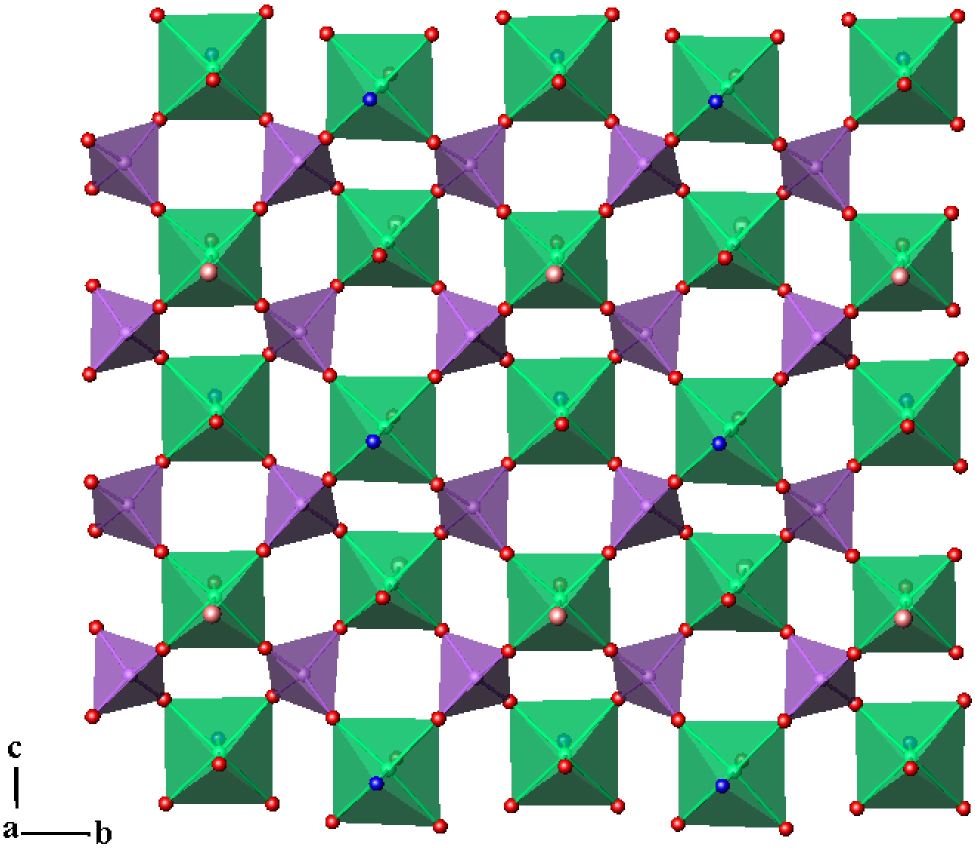

Figure 5.7: Layers built up from a repeating four-connected net of vanadium and phosphate/arsenate polyhedra; this is an identical bonding motif to that of compound (1), but two types of vanadium environments [(V(1)O_5(H_2O) / V(2)O_5F] occur here.

Ba(H_2O)$_2${VO(H_2O)[TO_4]}{VO(F)[TO_4]} compounds display framework structures based on mixed-oxidation vanadium states. Bond valence calculations showed V(1) to adopt the highest oxidation state +5 (BV(V1)$_{T=P}$ = 5.26 / BV(V1)$_{T=As}$ = 5.34). V(1) exhibits the classic distorted octahedral environment due to the presence of a short V=O bond opposite to a significantly lengthened V-H_2O bond. Additionally, the four equatorial V-O bond lengths are within the expected ranges 1.899(18)-1.928(14) Å and 1.850(14)-1.922(15) Å for phosphate and arsenate based compounds, respectively. Bond valence calculations at the V(2) site showed much lower bond valence values compared to V(1), (BV(V2)$_{T=P}$ = 4.24 / BV(V2)$_{T=As}$ = 4.13), suggesting the reduced +4 oxidation state for this site. V(2) adopts the classic distorted octahedral geometry with the presence of an oxo V=O group opposite to a significantly lengthened V-F bond in the vertical plane, whilst the four equatorial V-O distances are intermediate bonds of similar lengths (1.992(14)-2.010(14) Å / 2.005(14)-2.019(4) Å for phosphate and arsenate compounds respectively). Selected bond distances and bond valence calculations for both barium templated structures are given in Table 5.5.

BV calculations were performed on all atom sites and EDS analysis carried out on selected crystals from both compounds in order to confirm the atoms present within the crystalline structures as well as to verify the location of fluoride and water terminal ligands. When comparing the terminal bond lengths (V-F/O_W) in both types of vanadium octahedra, very much shorter bond distances and thus slightly higher BV values have been generally observed when the terminal ligand is a fluoride ion. Hence, due to its highly electronegative character, fluoride is expected to be strongly bonded to vanadium sites. [*T* = P: V(1)-F = 2.082(11) Å / BV(F) = 0.356, V(2)-O_W = 2.222(14) Å / BV(O_W) = 0.322], [*T* = As: V(1)-F = 2.089(10) Å / BV(F) = 0.350, V(1)-O_W = 2.232(12) Å / BV (O_W) = 0.314]. Nevertheless, in both cases bond valence values were found to be significantly low, especially in the case of fluoride, suggesting the strong interactions between these sites and the barium cations and lattice water molecules.

According to the literature, related compounds which include either terminal fluorides or aqua ligands, exhibit comparable bond lengths to those reported here. Concerning the case of the water ligand, similar bond distances (V^{+5}- O_W = 2.233(5) Å, BV(O_W) = 0.30) were observed in compound $(H_2O)\{V^{(V)}O(H_2O)[PO_4]\}$[3], and when accommodating lower oxidation states of vanadium then even longer distances were observed ~ 2.3-2.5 Å.[4-5]. In a similar way, the V^{+4}-F bond lengths are in good agreement with the characteristic bond distances found in the related structure $Na_3\{V_2O_2F[PO_4]_2\}$[2], (V-F = 2.1081(5) Å, BV(F) = 0.332). Finally, EDS analysis confirmed the presence of fluoride within the crystalline structures, and the determined atomic ratios are in line with the chemical formula sum (Ba/V/P/F = 1:1.8:1.9:0.9 – Ba/V/As/F = 1.6:1.8:0.7).

Table 5.5: Selected bond lengths (Å) and bond valences for compounds (2), (3).

Octahedra	Bond lengths	Σs_{ij}	Bond lengths	Σs_{ij}
	T = P		*T = As*	
$V(1)O_5OH_2$				
V(1)-O(8)	1.551(13)	1.976	1.576(13)	1.847
V(1)-O(4)	1.899(18)	0.771	1.850(14)	0.881
V(1)-O(7)	1.904(14)	0.761	1.869(14)	0.837
V(1)-O(1)	1.927(15)	0.715	1.922(15)	0.725
V(1)-O(6)	1.928(14)	0.713	1.917(15)	0.735
V(1)-OW(1)	2.222(14)	0.322	2.232(12)	0.314
		ΣV1=5.26		**ΣV1=5.34**
$V(2)O_5F$				
V(2)-O(9)	1.554(12)	1.862	1.607(12)	1.613
V(2)-O(3)	2.010(14)	0.543	2.009(16)	0.544
V(2)-O(5)	1.993(15)	0.568	2.007(15)	0.547
V(2)-O(2)	1.992(14)	0.569	2.005(14)	0.550
V(2)-O(10)	2.022(13)	0.525	2.019(14)	0.530
V(2)-F(1)	2.082(11)	0.356	2.089(10)	0.350
		ΣV2=4.24		**ΣV2=4.13**

	T = P		*T = As*	
$T(1)O_4$				
T(1)-O(5)	1.539(15)	1.235	1.647(14)	1.383
T(1)-O(10)	1.535(13)	1.248	1.666(13)	1.314
T(1)-O(6)	1.537(15)	1.241	1.667(13)	1.310
T(1)-O(7)	1.522(13)	1.293	1.681(13)	1.262
		ΣP1=5.02		**ΣAs1=5.27**
$T(2)O_4$				
T(2)-O(2)	1.527(14)	1.275	1.664(13)	1.321
T(2)-O(3)	1.516(14)	1.314	1.656(14)	1.350
T(2)-O(1)	1.533(15)	1.255	1.668(14)	1.307
T(2)-O(4)	1.527(17)	1.275	1.709(13)	1.170
		ΣP2=5.12		**ΣAs2=5.15**
$Ba(1)\cdots O_7, F_2$				
Ba(1)···O(2)	3.184(14)	0.088	2.725(12)	0.304
Ba(1)···O(9)	2.778(14)	0.264	2.779(14)	0.263
Ba(1)···O(5)	2.841(14)	0.222	2.824(14)	0.233
Ba(1)···O(3)	2.739(12)	0.293	3.010(14)	0.141
Ba(1)···OW(2)	2.887(16)	0.197	2.920(18)	0.180
Ba(1)···OW(2)	3.084(15)	0.115	3.081(16)	0.116
Ba(1)···OW(3)	2.812(14)	0.241	2.814(12)	0.239
Ba(1)···F(1)	2.745(13)	0.222	2.779(12)	0.202
Ba(1)···F(1)’	2.663(12)	0.277	2.705(12)	0.247
		ΣBa1=1.92		**ΣBa1=1.93**

Noticeably, there is a relative displacement of the layers and rotation of the polyhedra, in such a way that coordinated aqua ligands are not pointing exactly toward the fluoride anions of adjacent layers. Barium cations are located in between these anionic layers and occupy a unique crystallographic site. The coordination sphere is defined by two fluoride ligands, three bridging oxygens and one vanadyl oxo group of two adjacent layers in addition to three lattice water molecules. As can be depicted in Figure 5.8, an irregular geometry occurs with average bond distances: d_{av}(Ba···O/F) = 2.848, d_{av}(Ba···O/F) = 2.859 Å; Bond valence values: BV(Ba)$_{av}$ = 1.92, BV(Ba)$_{av}$ = 1.93 (expected = 2.00).

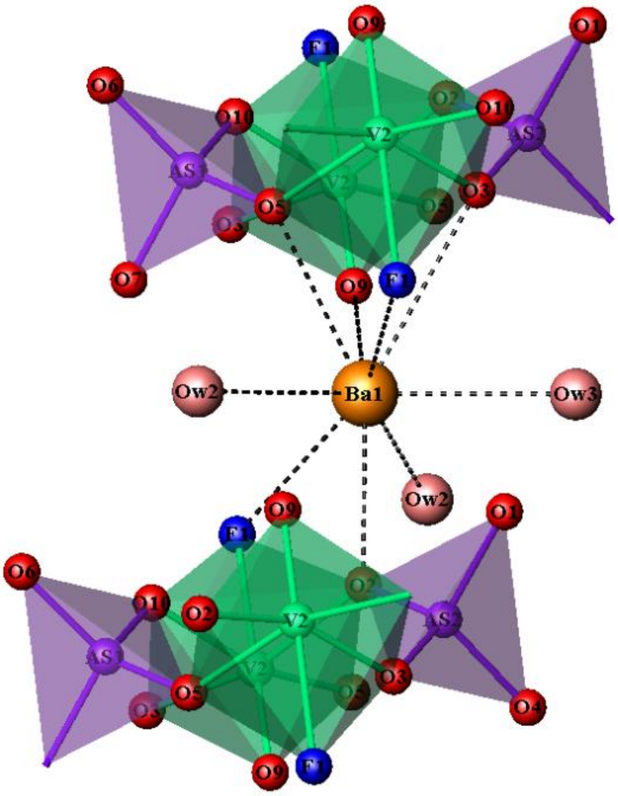

Figure 5.8: Coordination environment of barium in compounds (2), (3).

Evidence for the interlayer and coordinated water molecules within the crystalline structures was clearly seen by IR spectroscopy and was further confirmed by TGA analysis. The infrared spectra of $Ba(H_2O)_2\{VO(H_2O)[TO_4]\}\{VO(F)[TO_4]\}$, shown in Figure 5.9, exhibit intense inseparable broad bands in the 3500-3200 cm^{-1} region which can be assigned to the hydroxyl stretching modes (antisymmetric and symmetric stretching) of water molecules. The hydroxyl bending modes are detected in lower frequencies compared to the stretching modes and thus the strong bands observed at 1604 cm^{-1} and 1607 cm^{-1} (for arsenate and phosphate compounds respectively) can be assigned to the H-O-H bending mode.[7b] It should be noted that stretching and bending modes lie on the same region for both lattice and coordinated water. Thus, the present infrared spectra provide no direct information about the aqua ligand attached to the framework structures.

The arsenate compound, referred to as the blue spectrum in Figure 5.9, exhibits two strong bands at 994 cm^{-1} and 971 cm^{-1} attributed to the short V=O bond and a broad intense band well resolved into two components (one single band at 868 cm^{-1} and one doublet at 800/788cm^{-1}). The latter is attributed to the $\nu_3(T_2)$ stretching vibration of the As-O bond.[12] In contrast, the phosphate analogous compound (shown as the red spectrum) exhibits overlap of broad bands in the P-O and V=O stretching region.[7a, 13] The V=O absorption band cannot not be readily distinguished, but rather two strong bands at 1074 cm^{-1} and 1073 cm^{-1} can be observed, and these can be assigned to the vibration mode of PO_4^{3-} groups. The following broad band is well resolved in two components: one doublet band at 972/967 cm^{-1} and one singlet peak at 919 cm^{-1} attributed to a mixture of P-O and V=O stretching modes.

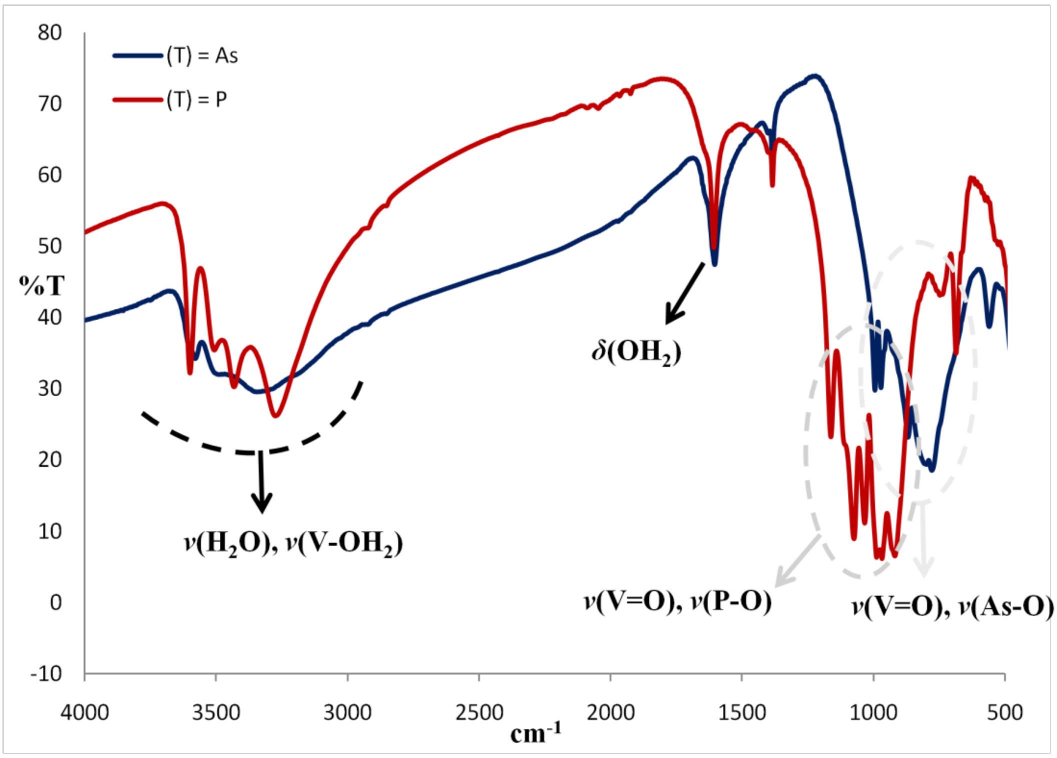

Figure 5.9: IR spectra of compounds (2), (3). Blue and red lines represent the arsenate and phosphate compounds, respectively.

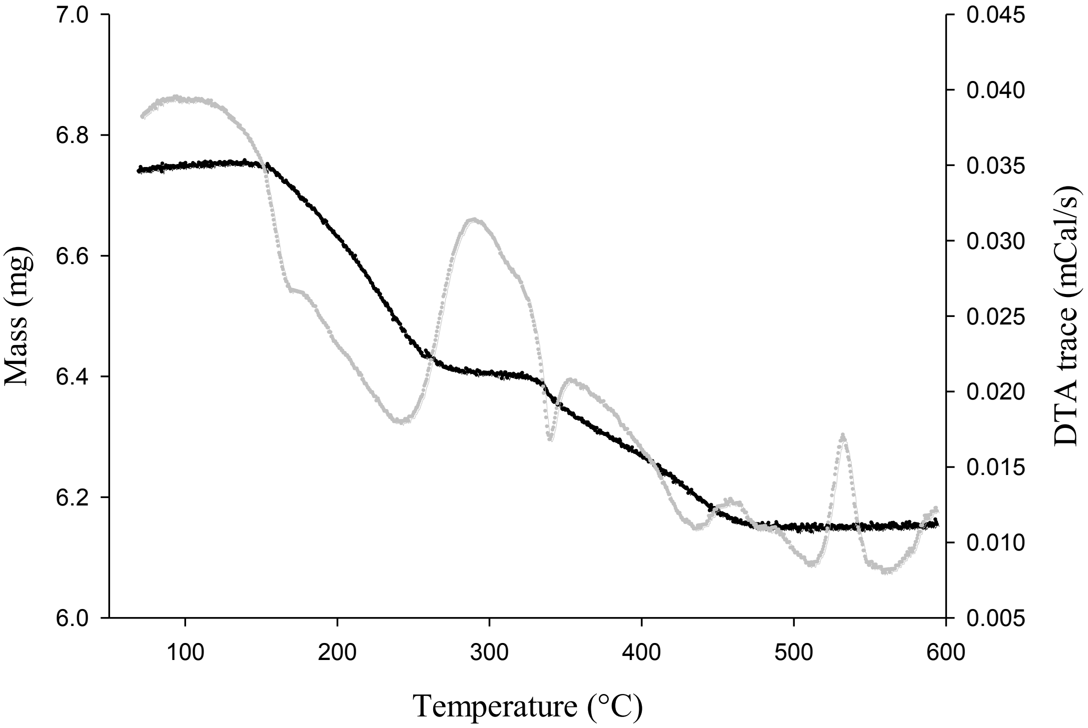

Figure 5.10: TGA pattern of compound (2). Mass loss was recorded as a function of temperature and is shown by the black line. DTA trace is the grey line.

The TG analysis of the arsenate derivative is shown in Figure 5.10. It exhibits water loss in two main steps followed by the corresponding endothermic peaks which are attributed to the energy required for the evaporation of both lattice and bound water and to the additional energy for breaking all the weak interactions between the Ba cations and water molecules. The first sharp decrement of mass (loss ~ 5.22%) occurred in the region of 120 - 280 °C because of the evaporation of two lattice water molecules from one molecule of compound (2) (expected to be 5.76%). The second obvious decrease of mass (~3.85%) occurred in the temperature region 320-480 °C and can be assigned to the evaporation of the water ligand attached to the framework and to the partial elimination of the fluoride ligand, since higher energy is required for breaking stronger bonds. Its thermal behavior above 500 °C is quite uncertain. The presence of an exothermic peak at 530 °C in DTA analysis indicates the recrystallization process of the inorganic residues. The TG curve of the phosphate derivative (shown in Figure 5.11) shows a smooth decrease, in the temperature range 80-510 °C, separated in three mass losses. The total mass loss estimated to be ~ 10.98%. Similarly, compound (3) shows mass loss due to the evaporation of two interlayer water molecules and one coordinated water, in addition to the elimination of the fluoride ligand from one molecule of compound (3).

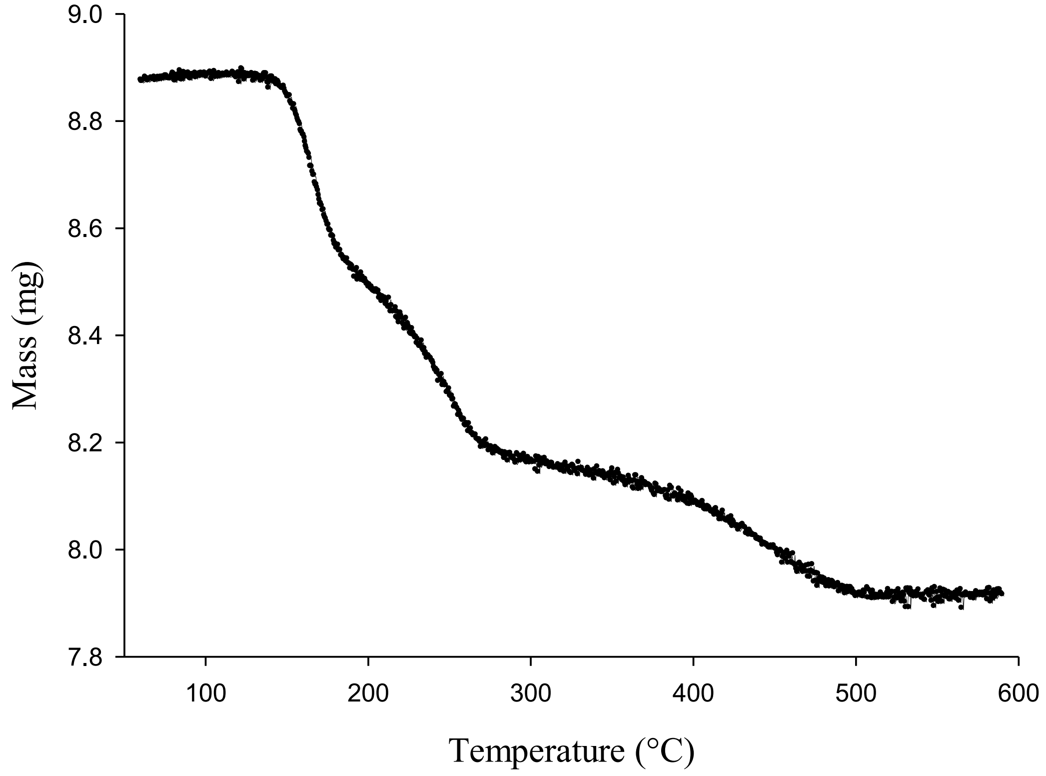

Figure 5.11: TGA pattern of compound (3). Mass loss was recorded as a function of temperature and is shown by the black line.

IV. Characterization of Cs[VO(HAsO$_4$)F] (4)

Selected crystals from the reaction mixture VF$_3$/H$_3$AsO$_4$/CsOH/H$_2$O, were characterised by single crystal X-ray diffraction, revealing a structure isotypical with the previously reported layered compounds, (R)$_{0.5}$[(VO)(HAsO$_4$)F] (where R: ethylenediamine, piperazine).[14] Compound (4), Cs[VO(HAsO$_4$)F] crystallises in the same monoclinic, $P2_1/c$ space group and exhibits a slightly smaller unit cell compared to the organically-templated compounds. Crystallographic data are listed in Table 5.6.

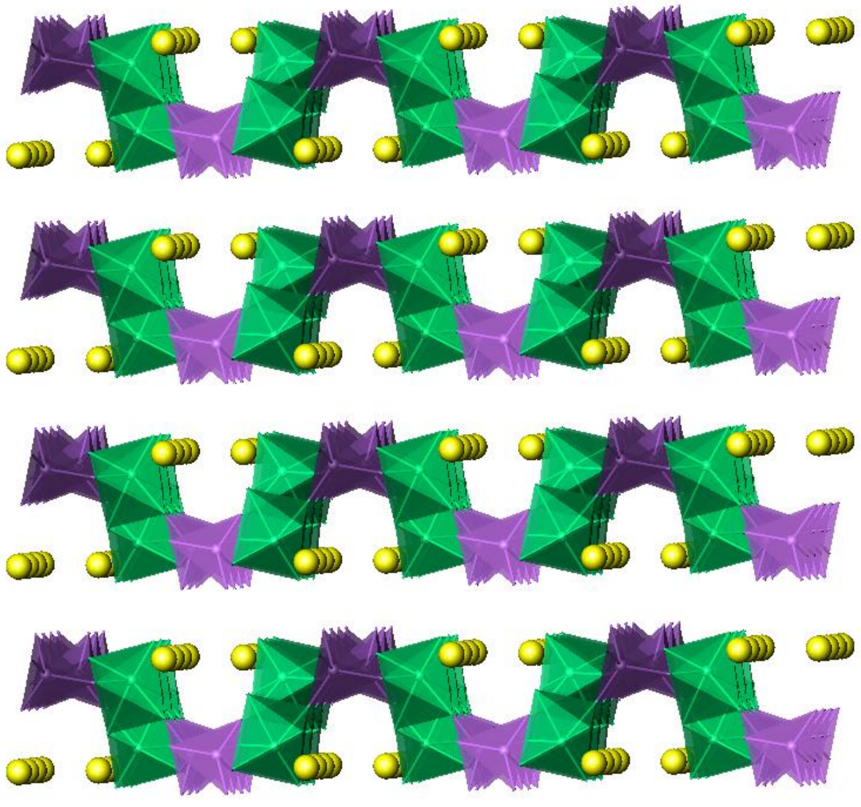

Figure 5.12: View down the *c* axis shows the undulating layers of compound (4). Green polyhedra represent the vanadium octahedra; purple represent the arsenate tetrahedra. Yellow spheres show caesium cations.

Compound (4) consists of undulating $[VO(F)(HAsO_4)]^{-1}$ layers running parallel to the *ab* plane with interleaved Cs^+ cations, as depicted in Figure 5.12. It exhibits an identical layer motif to $(R)_{0.5}[(VO)(HAsO_4)F]$ compounds, built up from tetrameric units of F-F edge-shared $[V_2O_8F_2]$ dimmers, capped on both sites by di-μ-(O,O')-arsenate bridges. There is only one distinct vanadium site which adopts the typical distorted +4 oxidation state. V(1) exhibits the typical set of one intermediate and one long V-F distance for the bridging F-F edge shared octahedra, whilst the remaining V-O bonds include a short bond assigned to a vanadyl oxo group (V=O) and three intermediate bond lengths in the range of 1.994(8) – 2.003(8) Å. The $HAsO_4$ tetrahedra show relatively characteristic bonds, having three bridging As-O bonds of similar length in addition to the one significantly lengthened bond assigned to the hydroxyl group. BV values for all atoms are within the expected range, showing values close to two for all the oxygens and close to unity for the bridging fluoride atoms. Bond lengths and bond valence calculations are summarised in Table 5.7.

Table 5.6: Crystal and diffraction data for compound (4).

Empirical formula	$HCsO_5FVAs$
Formula weight	358.78
Temperature	120(2) K
Appearance	Green fragments
Wavelength	0.71073 Å (Mo K_α)
Crystal system	Monoclinic
Space group	$P2_1c$
Unit cell dimensions	a = 7.8579(4) Å, b = 9.8022(7) Å c = 8.5517(6) Å, β = 117.35°,
Volume	585.06(7) $Å^3$
Z	4
D_c	4.073 $g.cm^{-3}$
Θ range for data collection	2.92°-25.01°
Reflections collected	3254
Independent reflections	824
Data/Restraints/Parameters	824/42/53
R indices	R_1 = 0.1194, wR_2 = 0.2770

Table 5.7: Selected bond lengths (Å) and bond valences for compound (4).

Polyhedra	Bond Lengths	Σs_{ij}	Polyhedra	Bond Lengths	Σs_{ij}
$V(1)O_4F_2$			$Cs(1)\cdots O_8,F_1$		
V(1)-O(1)	2.003(8)	0.553	Cs(1)···F(1)	3.146(6)	0.110
V(1)-O(2)	1.581(8)	1.731	Cs(1)···O(5)	3.184(9)	0.126
V(1)-O(3)	1.994(8)	0.567	Cs(1)···O’(3)	3.193(8)	0.123
V(1)-O(4)	1.990(8)	0.573	Cs(1)···O’(1)	3.210(7)	0.117
V(1)-F(1)	2.178(6)	0.275	Cs(1)···O’(4)	3.220(8)	0.114
V(1)-F’(1)	1.938(6)	0.526	Cs(1)···O’(2)	3.255(8)	0.104
		ΣV(1)=4.22	Cs(1)···O(3)	3.283(7)	0.096
			Cs(1)···O(2)	3.327(8)	0.085
$HAs(1)O_4$			Cs(1)···O’(4)	3.335(8)	0.083
As(1)-O(1)	1.680(7)	1.265	Cs(1)...O’(2)	3.388(8)	0.055
As(1)-O(3)	1.653(7)	1.361			**ΣCs(1)=1.01**
As(1)-O(4)	1.679(7)	1.269			
As(1)-O(5)	1.729(8)	1.108			
		ΣAs(1)=5.00			

Viewing the structure down the *a* axis (Figure 5.13), it can be seen how these tetramers are linked together, producing tunnels running along the direction perpendicular to the layers. Four alternating [$V_2As_2O_{12}F_2$] units are connected through oxygen atoms in order to form eight-sided roughly rectangular tunnels. Single crystal X-ray refinements showed the presence of high electron density within the channels and therefore this one unique crystallographic site was assigned to the Cs^+ ion in order to charge balance the negatively-charged framework. When comparing both structures, compound (4) and the reported compounds $(R)_{0.5}[(VO)(HAsO4)F])$, it is noticeable that the replacement of organic amines with the caesium cations does not change the layer topology or the monoclinic symmetry of the structure. However, the location of the guest species is much different. Organic amines are located at the centre of the channel, unlike caesium cations that were found to be off centre with respect to the tunnels and occupy preferentially sites which are very close to the vanadoarsenate polyhedra. There is only one crystallographically independent caesium atom that is coordinated by ten framework oxygen and fluorine atoms with Cs-O, F distances within the expected range (3.1-3.4 Å). Figure 5.14 illustrates the coordination environment of the Cs^+ cations and shows the weak linking between two adjacent layers.

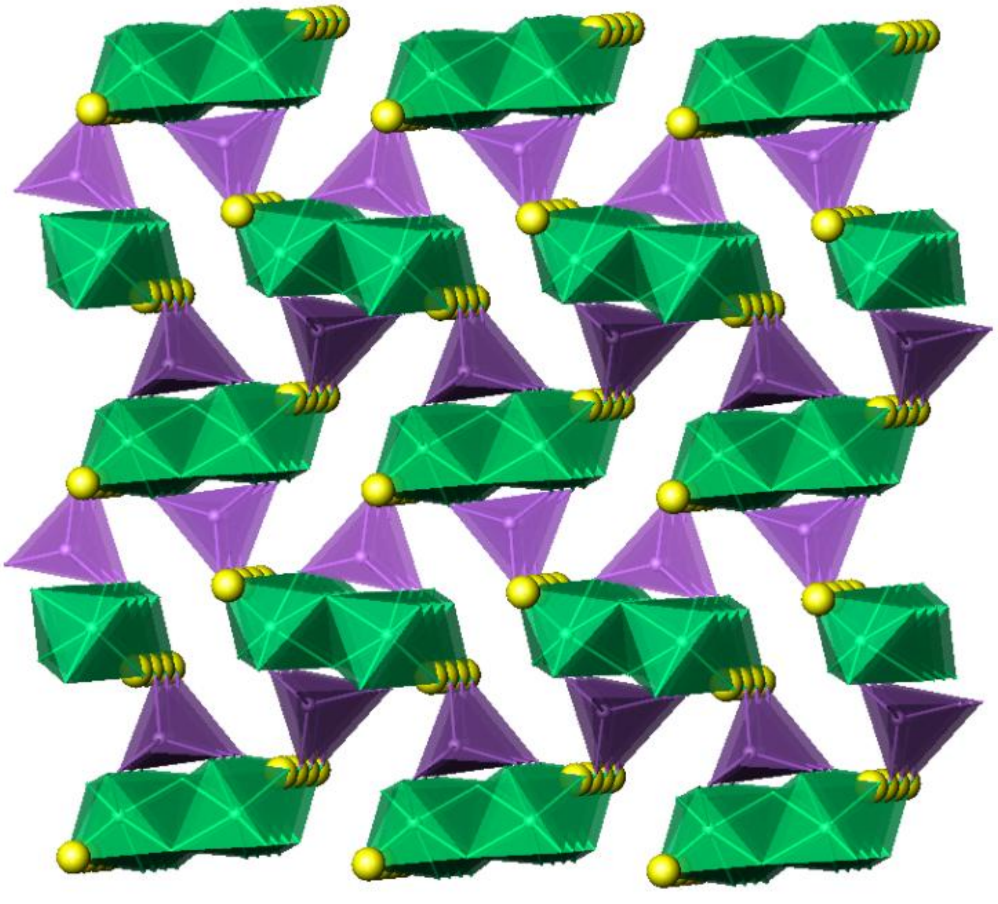

Figure 5.13: View of the layer down the *a* axis shows details of the channels in the structure of compound (4).

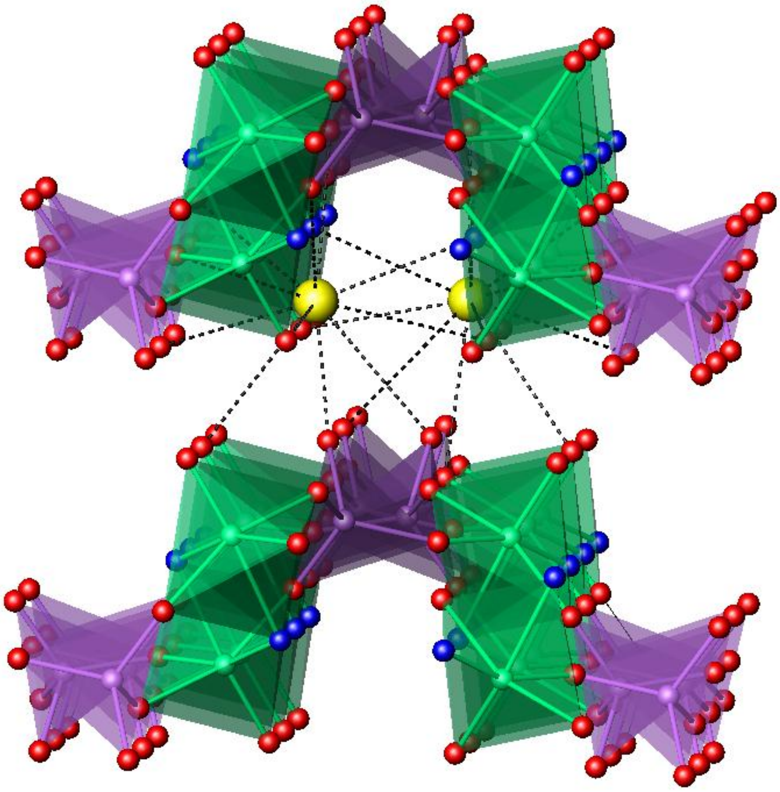

Figure 5.14: Adjacent layers are weakly held together through caesium cations. Green polyhedra represent the vanadium octahedra; purple represent the arsenate tetrahedra. Yellow spheres show caesium cations.

Compound (4) was further characterised by Thermogravimetric analysis and IR spectroscopy. Looking at the thermal analysis of compound (4), (shown in Figure 5.15), it would appear that the structure is stable up to 290 °C, since no significant mass loss is observed. Above this temperature, the first significant decrement of mass is observed (loss ~ 4.04%) between 290 and 460 °C. The mass continues decreasing up to 540 °C with a total mass loss estimated to be ~ 4.71%. Both steps may be assigned to the elimination of the fluoride anion since the estimated value is quite close to the calculated one (~5.29%). Unfortunately the product was spread into the crucible and therefore further identification using X-ray powder diffraction method was unable.

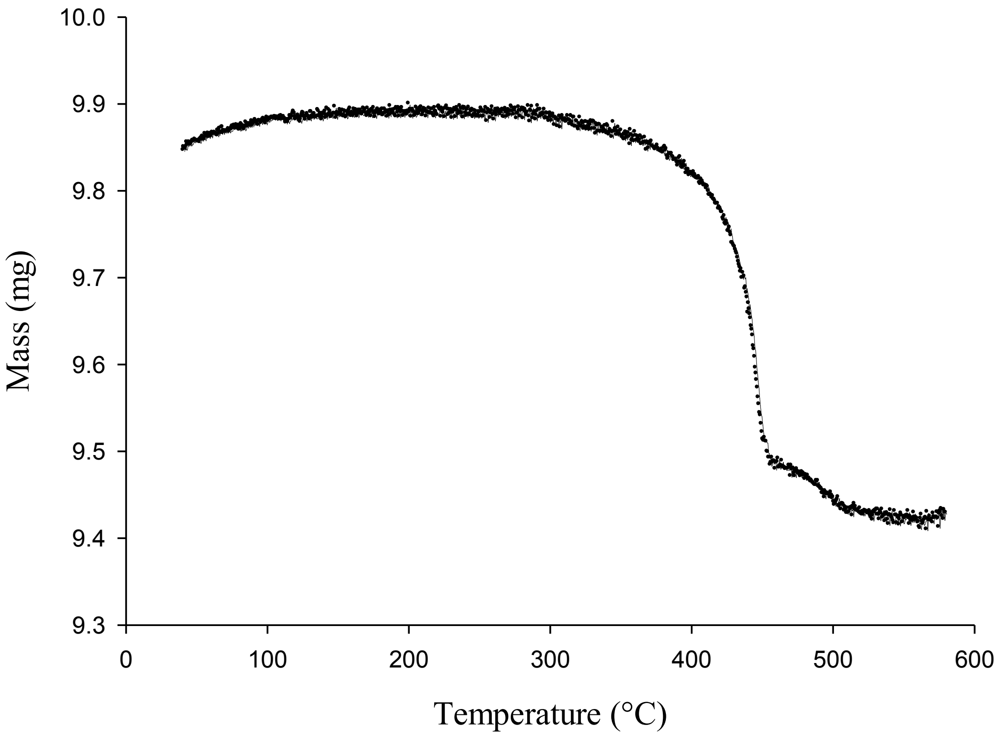

Figure 5.15: TGA pattern of compound (4). Mass loss was recorded as a function of temperature and is shown by the black line.

The Infrared spectrum of compound (4) is illustrated in Figure 5.16. What is being demonstrated here is the absence of the vibration modes associated with water molecules but rather the detection of the hydroxyl groups attached to the arsenate tetrahedra. The hydroxyl stretching mode of the $HAsO_4$ group in this spectrum is detected at much lower frequencies (~ 3022 cm^{-1}) compared to the typical stretching mode of water which usually lies in the 3550-3200 cm^{-1} region. Moreover, the present IR spectrum lacks the very characteristic H-O-H bending mode near 1600 cm^{-1} but exhibits a strong band at 1163 cm^{-1} which can be attributed to the bending mode of the As-OH group.[12] In the low frequency region, a very strong band is detected at 976 cm^{-1} which can be attributed to the ν(V=O) group followed by the complex ν(As-O) stretching modes.[7a, 13] The latter mode consists of an intense broad band well resolved into two components at 879 cm^{-1} / 841 cm^{-1} ($\nu_3(T_2)$ stretching vibrations) and a strong single band at 740 cm^{-1} ($\nu_1(A_1)$ stretching vibration). It is worth mentioning that the splitting of the $\nu_3(T_2)$ band and the presence of the $\nu_1(A_1)$ stretching vibrations implies the presence of more than two types of side symmetry for the arsenate groups.

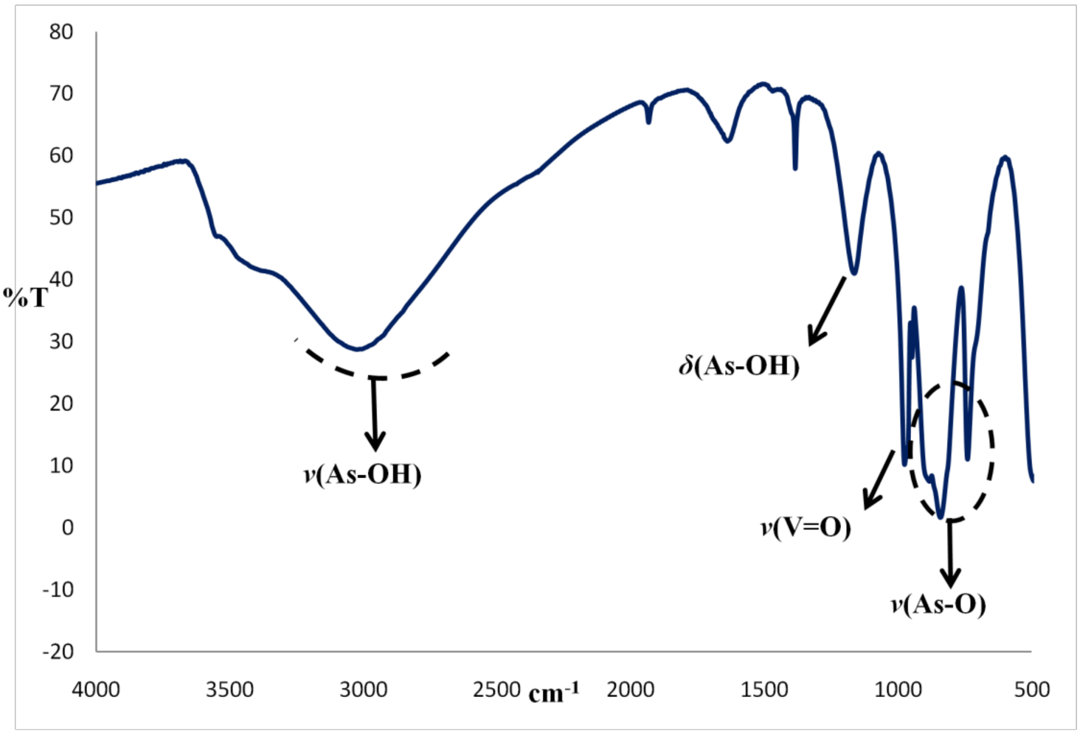

Figure 5.16: Infrared spectrum of compound (4) showing the characteristic bands for each group.

From a general structural point of view, compound (4) and the related organically-templated compounds $(R)_{0.5}[(VO)(HAsO4)F])$ are based on tetrameric units that strongly resemble those usually found in most oxyfluorinated alumino- and gallophosphate microporous compounds. Following a similar bonding motif, these tetramers are built up from dimers of Al or Ga octahedra that share a common edge through fluorine atoms, and are capped on both poles by two different phosphate tetrahedra.[15] A related bonding motif has been frequently identified in many non-fluorinated compounds which contain similar dimers of vanadium octahedra but share an edge through bridging oxygens instead. One such example is $BaVO_2AsO_4$ which exhibits a closely-related structural unit to compound (4).[16] Following the same characteristic bonding motif, layers are constructed from edge sharing $V^{+5}{}_2O_{10}$ dimeric units which are connected through arsenate tetrahedra in such a way that six of the ten vertices of a dimer are shared with four tetrahedral groups. Enhancing the polyhedral connectivity leads to the tunnel structures of two isotypical compounds, $A_{0.5}VOAsO_4$ (where A= Sr, Ba)[17], which exhibit common structural features with the compound described above. In a similar way, their framework structure is based on dimers of edge sharing $V^{+4}O_6$ octahedra, capped on both sites by arsenate groups.

However, dimers are now connected to six arsenate tetrahedra resulting in an extended three dimensional network. Another example belonging to the same family is the previously reported compound $(H_3NC_2H_4NH_3)_{0.5}[VO(H_2O)(AsO_4)]$, which exhibits chains built up from $[V^{+4}{}_2O_8(H_2O)_2]$ bioctrahedral units and arsenate tetrahedra.[18] In this case, each vanadium centre of the dimers provides one unshared aqua ligand opposite to the V=O oxo group and so the polyhedral connectivity is extended into opposite directions, leading to one dimensional chains. A more detailed structural comparison of both types of edge-shared vanadium dimmers, O-O and F-F type, shows that the shortening of the shared edge compared to the unshared ones was found to be relatively increased in the F-F type dimer. Thus, one might expect that incorporation of fluoride into the layered structure of (4) makes the structure essentially more ionic.

5.1.3 Conclusions

During the investigation of VF_3 as an alternative fluoride source, four inorganic templated compounds were successfully obtained and have been characterised by single crystal X-ray diffraction. All compounds exhibit layered structures, and two main structural topologies generally occurred. The first layer type has been observed in ammonium and barium templated compounds and can be described as a four connected net of alternating oxyfluorinated vanadium octahedral units and $TO_4{}^{n-}$ oxotetrahedral groups. This very characteristic bonding motif resembles that found in the mineral natisite Na_2TiSiO_5 and an extensive family of vanadophosphate derivatives. What is being distinguished here is the participation of the terminal fluoride ligand into the vanadium coordination sphere which in some cases, renders the framework negative and thus allows the insertion of cationic guests, enhances the hydrogen bonding or provides new framework topologies. The second layer type involves the caesium-templated compound that incorporates a layer motif identical to the recently-reported amino-templated compounds $(R)_{0.5}[(VO)(HAsO_4)F]$. In this case, layers are constructed by F-F edge shared vanadium bioctrahedral units capped on both sides by arsenate bridges; remarkably the incorporation of bridging fluoride ligands into these vanadium bioctrahedral units has facilitated more ionic structures.

5.2 References

[1] I. D. Brown and D. Altermatt, *Acta Crystallographica Section B-Structural Science* 1985, *41*, 244-247.

[2] W. Massa, O. V. Yakubovich and O. V. Dimitrova, *Solid State Sciences* 2002, *4*, 495-501.

[3] H. R. Tietze, *Australian Journal of Chemistry* 1981, *34*, 2035-2038.

[4] M. Roca, M. D. Marcos, P. Amoros, J. Alamo, A. BeltranPorter and D. BeltranPorter, *Inorganic Chemistry* 1997, *36*, 3414-3421.

[5] S. L. Wang, H. Y. Kang, C. Y. Cheng and K. H. Lii, *Inorganic Chemistry* 1991, *30*, 3496-3499.

[6] a) D. G. Tuck, *Progr. Inorg. Chem* 1968, *9*, 161; b) T. C. Waddington, *Journal of the Chemical Society* 1958, 4340-4344.

[7] a) E. Y. Borovikova, V. S. Kurazhkovskaya, D. M. Bykov and A. I. Orlova, *Journal of Structural Chemistry* 2010, *51*, 40-44; b) Ray L. Frost, Kristy Erickson and M. L. Weier, *Spectrochimica acta. Part A* 2004, *60*, 2419-2423.

[8] H. Nyman, M. Okeeffe and J. O. Bovin, *Acta Crystallographica Section B-Structural Science* 1978, *34*, 905-906.

[9] B. D. Jordan and C. Calvo, *Acta Crystallographica Section B-Structural Science* 1976, *32*, 2899-2900.

[10] H. Y. Kang, W. C. Lee, S. L. Wang and K. H. Lii, *Inorganic Chemistry* 1992, *31*, 4743-4748.

[11] K. H. Lii, L. S. Wu and H. M. Gau, *Inorganic Chemistry* 1993, *32*, 4153-4154.

[12] V. Portilla, *American Mineralogist* 1976, *61*, 95-99.

[13] E. J. Baran and K. H. Lii, *Zeitschrift Fur Naturforschung Section B-a Journal of Chemical Sciences* 2003, *58*, 485-488.

[14] T. Berrocal, J. L. Mesa, J. L. Pizarro, L. Lezama, B. Bazan, M. I. Arriortua and T. Rojo, *Journal of Solid State Chemistry* 2008, *181*, 884-894.

[15] a) T. Loiseau and G. Ferey, *Journal of the Chemical Society-Chemical Communications* 1992, 1197-1198; b) J. L. Paillaud, B. Marler and H. Kessler, *Chemical Communications* 1996, 1293-1294.

[16] F. Gagnard, C. Reisner and W. Tremel, *Inorganic Chemistry* 1997, *36*, 352-355.

[17] S. L. Wang and C. Y. Cheng, *Journal of Solid State Chemistry* 1994, *109*, 277-280.

[18] A. H. Liu and S. L. Wang, *Inorganic Chemistry* 1998, *37*, 3415-+.

Chapter Six

Vanadium Phosphate and Borate Structures

6.0 Introduction

Incorporation of boron into framework structures has led to the discovery of numerous new framework topologies as a result of its multi co-ordinate linking ability. Borophosphate frameworks have been extensively studied over the past few years. Much of this work has been undertaken by Kniep and co-workers, with a diverse range of novel structure types being produced.[1] Following the success with the vanadium borophosphate system,[2] research included within the first part of the chapter has aimed at expanding this family of compounds in terms of investigating other boron and phosphorous sources in the framework formation. A series of hydrothermal reactions involving different combinations of starting material sources were carried out. It appears as the resulting products exhibit building units consisting of vanadium polyhedra and phosphate tetrahedra that incorporation of boron within these crystalline products was unsuccessful. Among the structures isolated in this investigation, a new framework topology has been identified and further discussed in Section 6.1.

Synthetic work within the second part of the chapter has been focused on the investigation of vanadium borate cluster polyanions. Following similar synthetic procedures to those used for the vanadium borate cluster types: $[(VO_6)\{B_{10}O_{16}(OH)_6\}_2]^{4-}$ and $[V_6B_{20}O_{38}(OH)_{12}]^{4-}$,[3] a series of hydrothermal reactions were carried out to produce the complete series of the analogous alkali metal templated compounds. In the cases of rubidium and caesium cations reactions were successful, whilst in presence of smaller cations such as sodium, potassium and lithium difficulties were encountered in producing bigger size crystallites, suitable for single-crystal X-ray diffraction analysis.

6.1 Vanadium phosphates

In the course of the study of vanadium borophosphate framework materials, different combinations of phosphate and borate sources have been investigated under mild hydrothermal routes in the presence of piperazine acting as a template. A new vanadium phosphate compound has been prepared. This comprises of layers built up from infinite chains of corner-sharing vanadium octahedra and phosphate tetrahedra that are further interconnected by isolated vanadium octahedra to form a three-dimensional framework.

6.1.1 Experimental

I. Synthesis

✓ System (1): $V_2O_5 + H_3PO_4 + H_3BO_3 + \mathit{M}Cl$ + piperazine

(M = Rb, Cs, K, Na, Li)

The reagents: vanadium pentoxide (0.750 g, 4.12 mmol), 85% orthophosphoric acid solution (2.42 ml, 34.7 mmol), boric acid (1.002 g, 16.2 mmol) and the corresponding alkali metal chloride source (26.8 mmol) were first dispersed into 20 ml of distilled water and stirred for about one hour. Then, piperazine (0.1397 g, 1.62 mmol) was added to the solution and the final mixture was transferred into a 23 mL Teflon-lined steel autoclave and heated under autogenous pressure for three days at 453 K. Once cool the products were filtered, washed with distilled water and air dried.

✓ System (2): $V_2O_5 + H_3PO_4$ + Borate salt + piperazine

(Borate source: $NaB_4O_7.5H_2O$)

Vanadium pentoxide (0.375 g, 2.06 mmol), 85% orthophosphoric acid solution (1 ml, 14.3 mmol), borax pentahydrate (0.501 g, 1.72 mmol) were first dispersed into 10 ml of distilled water and stirred for about one hour. Then, piperazine (0.1397 g, 1.62 mmol) was added to the solution and the final mixture was transferred into a 23 mL Teflon-lined steel autoclave and heated under autogenous pressure for three days at 453 K. Once cool the products were filtered, washed with distilled water and air dried. The product consisted of light green crystals and microcrystalline powder of the new compound. Compound (1), $[H_2N(C_2H_4)_2NH_2]\{[VO(PO_4)(HPO_4)]_2[VO(H_2O)_3][VO(H_2O)]\}$ was characterised by single crystal X-ray diffraction, TGA and IR analysis.

- ✓ System (3): $V_2O_5 + H_3BO_3$ + Phosphate salt + piperazine

(Phosphate source: $NH_4H_2PO_4$, KH_2PO_4, NaH_2PO_4)

Vanadium pentoxide (0.375 g, 2.06 mmol), boric acid (0.499 g, 8.08 mmol) and MH_2PO_4 (1.84 mmol) were first dispersed into aqueous solution (10 ml distilled water) and stirred for about one hour. Then, piperazine (0.1397 g, 1.62 mmol) was added to the solution and the final mixture was transferred into a 23 mL Teflon-lined steel autoclave and heated under autogenous pressure for three days at 453 K. Once cool the products were filtered, washed with distilled water and air dried.

II. Characterization

- ✓ X-ray diffraction studies

Single crystal X-ray diffraction data for each crystal structure were collected on a Bruker Nonius KappaCCD diffractometer (Mo Kα radiation, $\lambda = 0.71073$ Å) at 120 K. Refinements of the structures were carried out using the WinGX system and SHELX-97 (by following direct methods).

- ✓ Thermogravimetric (TGA) analysis

TGA and DTA data were collected on a Polymer Laboratories STA 1500 system. Samples (mass ~ 10 mg) were heated in flowing air from room temperature to 600 °C at a range of 10° C min^{-1}. Weight loss and heat flow were recorded as a function of temperature.

- ✓ Infra-red (IR) analysis

Samples were first mixed with KBr and then pressed into thin pellets. IR spectra were collected using a Perkin Elmer Spectrum system over the range 4000-500 cm^{-1}.

- ✓ Electron microscopy

Energy-dispersive X-ray spectroscopy and Scanning electron microscopy studies completed on a JOEL JSM-5910 SEM fitted with an Oxford Inca 300 energy dispersive X-ray spectroscopy analysis system.

- ✓ Bond Valence calculations

Bond valence calculations were completed at each atom site using the following equation: $V = \Sigma\ (V_i)$, where $V_i = \exp\ [(R_0\text{-}R)/b]$. The theory behind the equation refers to the valence sum rule for which the valence (V) of each atom must be equal to the sum of its individual bond valences (V_i). The corresponding (V_i) values were calculated using the experimental bond lengths (R) and (R_0, b) parameters from the Tables compiled by Brown and Altermatt.[4]

6.1.2 Results and discussion

I. Synthesis overview

Three systems were set up to investigate different combinations of starting material sources in reactions that entailed hydrothermal treatment of vanadium pentoxide with the boron and phosphorous sources in the presence of piperazine. The first system aimed at investigating the combination of phosphoric and boric acid. In all cases, a series of the previously reported compounds $M_{0.5}(H_2O)\{VO(H_2O)[PO_4]\}$ (where M = Rb, Cs, K, Na)[5] was obtained, except in the case of lithium where only glassy products were produced. The fundamental building block unit can be described as a tetragonal net consisted of corner-sharing vanadium octahedra and phosphate tetrahedra (details of which is given in Chapter 5, Subsection 5.1.2).

The second system attempted to investigate the combination of the borate salt, $NaB_4O_7.5H_2O$ with phosphoric acid. This approach led to the discovery of compound (1) whose structural features are discussed in the following subsection. Finally, the third system involved reactions in the presence of a phosphate salt and boric acid. The majority of the reactions resulted in mixed powder product phases which could not be identified using X-ray powder diffraction analysis. In a few cases, a minor phase of black crystals was obtained. Single crystal X-ray diffraction identified the previously reported compound $(H_2N(C_2H_4)_2NH_2)[V_4O_{10}]$.[6] This consists of vanadium oxide layers built up from alternating edge-shared VO_5 square pyramids and VO_4 tetrahedra with piperazine cations located in the interlayer region.

II. Characterization of compound (1)

Compound (1) crystallises in the monoclinic *Cm* space group and its structure is demonstrated in Figure 6.1. Crystal and diffraction information for compound (1) are given in Table 6.1. The framework structure may be considered as composed of $\{[VO(PO_4)(HPO_4)]_2[VO(H_2O)_3]\}_\infty$ layers built up from infinite chains of corner-sharing vanadium octahedra and phosphate tetrahedra which are connected together by bridging $VO_4(H_2O)$ groups.

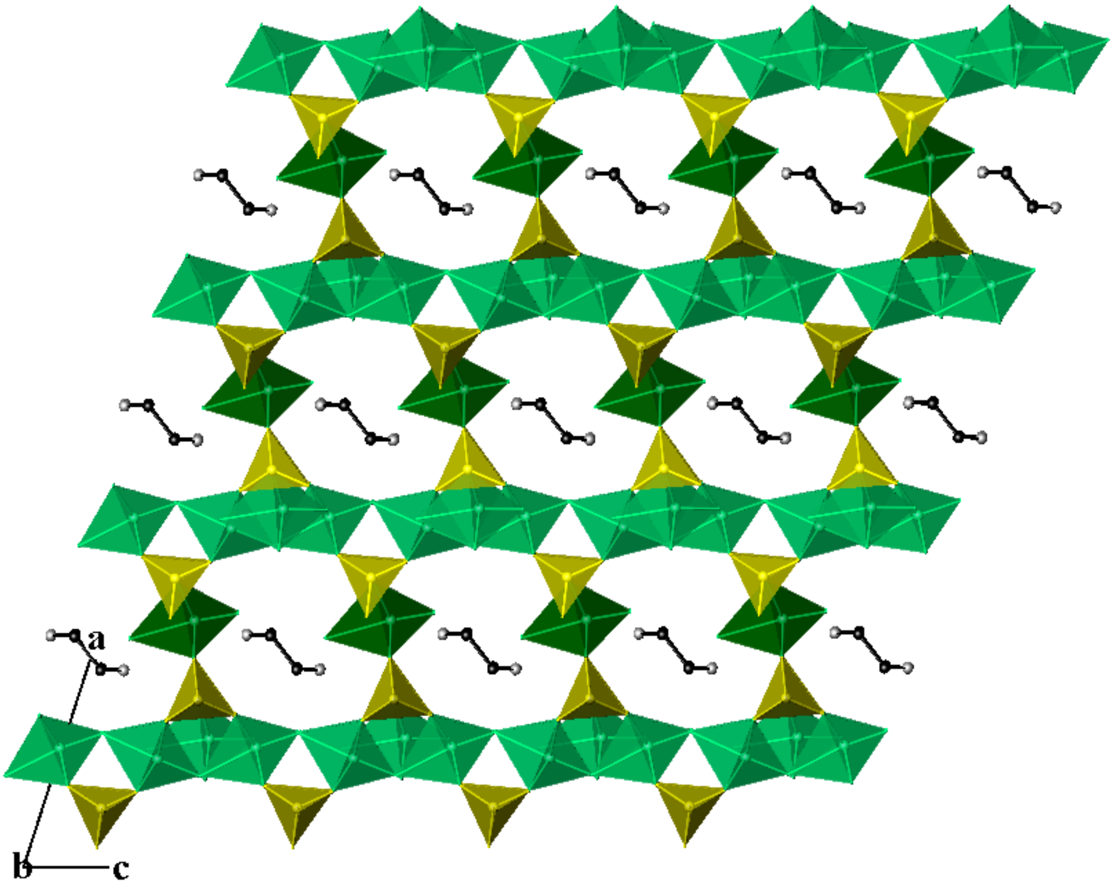

Figure 6.1: A perspective view of the structure of compound (1) along the *b* axis. Light green polyhedra represent the vanadium octahedra of the layers, dark green polyhedra represent the bridging $V(4)O_5(H_2O)$ octahedra. Phosphates are shown in yellow colour. The grey-black linked spheres comprise the piperazine molecules.

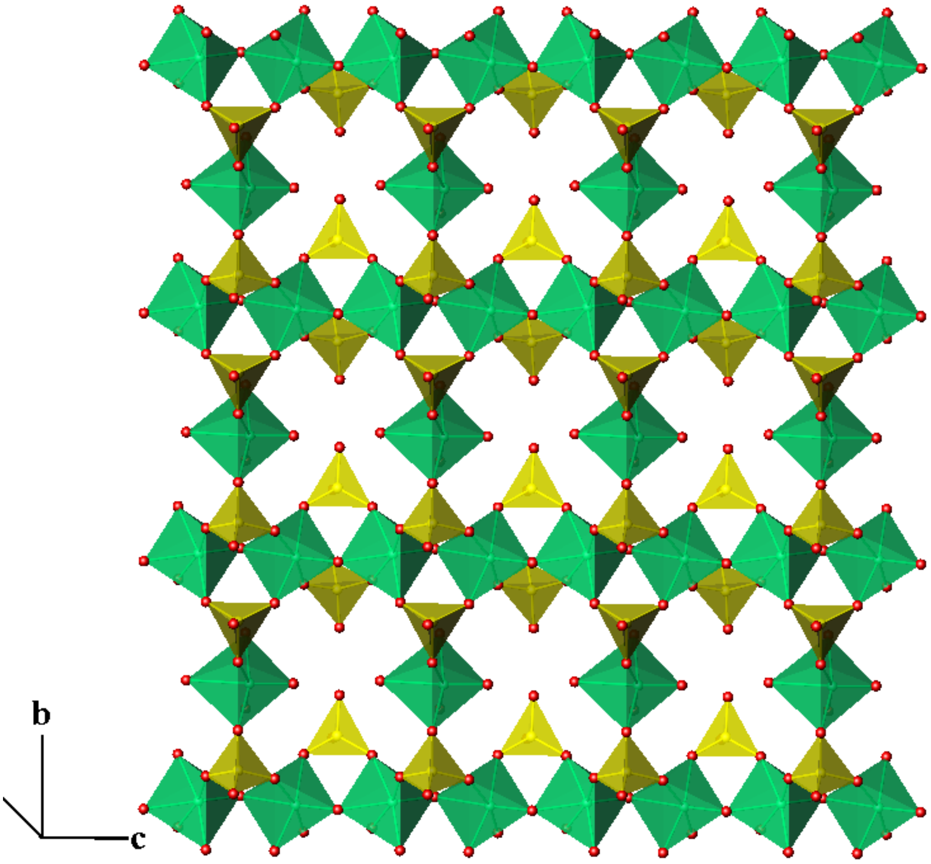

Figure 6.2: View of the $\{[VO(PO_4)(HPO_4)]_2[VO(H_2O)_3]\}_\infty$ layers showing details of the bonding motif. Green polyhedra represent the vanadium octahedra and yellow polyhedra show the phosphate tetrahedra.

Table 6.1: Crystal and diffraction information for compound (1).

Empirical formula	$H_{22}C_4N_2V_4P_4O_{24}$
Formula weight	809.88
Temperature	120(2) K
Appearance	Green-blue polyhedral crystals
Wavelength	0.71073 Å (Mo K_α)
Crystal system	Monoclinic
Space group	*Cm*
Unit cell dimensions	*a* = 17.3691(15) Å, *c* =9.4648(9) Å b = 7.0433(4) Å, β = 107.986(5)°
Volume	1102.30(15) $Å^3$
Z	2
D_c	2.442 $g.cm^{-3}$
Θ range for data collection	3.04°-25.02°
Reflections collected	7701
Independent reflections	2023
Data/Restraints/Parameters	2023/2/190
R indices	$R_1 = 0.0569$, $wR_2 = 0.1587$

A number of vanadium phosphate compounds can be considered as derived from layers built up from identical –V-O-V-O- infinite chains to those discussed here.[7] However, different bonding motifs have been identified concerning the bridging manner of adjacent layers. In the structure discussed here the difference derives from the presence of bridging isolated octahedral units which enhance the connectivity into a three-dimensional array, giving rise to a channel system filled with piperazine molecules.

Figure 6.2 shows details of the polyhedral connectivity identified in the $\{[VO(PO_4)(HPO_4)]_2[VO(H_2O)_3]\}_\infty$ layers of compound (1). There are two crystallographically independent vanadium sites, V(2) and V(3), forming infinite chains of alternating octahedra. Each vanadium site of the chains is coordinated to four oxygen donors from four different phosphate groups in addition to a pair of oxygens which exhibit *trans* corner-sharing between adjacent vanadium sites. Bond valence calculations showed the two distinct vanadium sites to be preferentially occupied by the reduced +4 oxidation state. Both adopt the classic distorted octahedral geometry of V(IV) having the four equatorial distances within the expected intermediate range (V-O = 1.947(8)-2.077(8) Å) and a pair of one short axial vanadyl bond (~1.6 Å) *trans* to a significantly lengthened V-O bond (~2.2 Å).

Adjacent vanadium octahedra within a single {–V-O-V-O-} chain are capped on both sites by phosphate tetrahedra through di-μ-(O,O')PO_4 bridges. There are two crystallographically independent phosphorous sites, P(1) and P(2), which provide two oxygen donors for the di-μ-(O,O') bridges. In addition, P(1) shares one corner with the isolated $V(1)O_3(H_2O)_3$ octahedra so as to bridge adjacent chains into layers, whilst its remaining fourth apical is shared with the isolated $V(4)O_4(H_2O)$ octahedra. In a similar manner, P(2) shares a corner with the isolated $V(1)O_3(H_2O)_3$ octahedra, but in this case the remaining fourth apical contributes a terminal hydroxyl group. Investigations of the P-O bond lengths (given in Table 6.2) showed that both unique phosphate tetrahedra pose characteristic bond distances for all the bridging oxygen atoms. Additionally, $P(2)O_4$ exhibits an exceptionally long bond distance (P(2)-O(6): 1.570(9) Å) with a much lower bond valence value (1.135) compared to the rest bridging oxygens owing to lack of electron density around this oxygen site.

There are two types of bridging vanadium octahedral units within the framework structure of (1): V(1)O$_3$(H2O)$_3$ and V(4)O$_4$(H$_2$O). The former provides connectivity of adjacent chains into layers by sharing two corners with two different P(1)O$_4$ groups, while the remaining apices are occupied by a vanadyl oxo group and three terminal water ligands. The second type serves to link together the vanadophosphate layers by sharing four equatorial oxygens with the phosphate groups, whereas the two remaining apices are occupied by a short vanadyl group opposite to a terminal water molecule. Both vanadium sites adopt the classic distorted octahedral geometry. Comparison of the bond distances in both vanadium sites shows that the V(4)O$_4$(H$_2$O) unit exhibits a much longer bond distance (~2.5 Å) for its terminal water molecule (the one located opposite to the short vanadyl oxo group), thus forming an elongated octahedral geometry.

Table 6.2: Selected bond lengths (Å) and bond valences for compound (1).

Polyhedra	Bond lengths	Σs_{ij}	Polyhedra	Bond lengths	Σs_{ij}
V(1)O$_3$(O$_w$)$_3$			V(4)O$_5$(O$_w$)		
V(1)-O(4)	1.591(11)	1.685	V(4)-O(2)	1.592(13)	1.680
V(1)-O(10)	1.986(8)	0.579	V(4)-O(12)	2.005(8)	0.550
V(1)-O(10’)	1.986(8)	0.579	V(4)-O(12)	2.005(8)	0.550
V(1)-O$_w$(2)	2.070(8)	0.462	V(4)-O(11)	2.006(9)	0.549
V(1)-O$_w$(2’)	2.070(8)	0.462	V(4)-O(11)	2.006(9)	0.549
V(1)-O$_w$(3)	2.334(12)	0.226	V(4)··O$_w$(1)	2.484	0.151
		ΣV1=3.99			**ΣV4=4.03**
V(2)O$_6$			P(1)O$_4$		
V(2)-O(3)	1.637(10)	1.488	P(1)-O(1)	1.485(9)	1.429
V(2)-O(1)	1.967(9)	0.610	P(1)-O(9)	1.527(8)	1.275
V(2)-O(1’)	1.967(9)	0.610	P(1)-O(10)	1.535(8)	1.248
V(2)-O(5)	1.982(10)	0.586	P(1)-O(12)	1.549(8)	1.202
V(2)-O(5’)	1.982(10)	0.586			**ΣP1=5.15**
V(2)-O(7)	2.192(9)	0.332			
		ΣV2=4.21	HP(2)O$_4$		
			P(2)-O(5)	1.498(9)	1.379
V(3)O$_6$			P(2)-O(11)	1.505(10)	1.354
V(3)-O(7)	1.612(10)	1.592	P(2)-O(8)	1.518(8)	1.307
V(3)-O(9)	1.947(8)	0.643	P(2)-O(6)	1.570(9)	1.135
V(3)-O(9)	1.947(8)	0.643			**ΣP1=5.18**
V(3)-O(8)	2.027(8)	0.519			
V(3)-O(8)	2.027(8)	0.519			
V(3)-O(3)	2.256(10)	0.279			
		ΣV3=4.20			

A further unique structural feature is the channel system running along the *b* axis. There is a ten-membered ring consisting of two VO_6 octahedra of the {–V-O-V-O-} chains, four PO_4 tetrahedra and the two bridging $VO_4(H_2O)$ units. Diprotonated piperazine cations are hosted inside, and they are involved in strong hydrogen bonding with the anionic vanadophosphate framework. There is one crystallographically unique piperazine molecule within the crystalline structure of compound (1) which contains two distinct nitrogen atoms. The nitrogen atom N(1) makes two hydrogen bond links with the framework, connecting to O(6) and Ow(3) (N(1)-O(6)/Ow(3) = 2.886 Å/ 2.928 Å) , whilst N(2) is connected with two oxygen donors of type O(6) (N(2)-O(6) = 3.118 Å).

Compound (1) was further characterised by IR spectroscopy and TGA analysis. The infrared spectrum of compound (1), shown in Figure 6.3, exhibits an inseparable intense broad band in the 3400-2400cm^{-1} region attributed to the hydroxyl stretching modes (antisymmetric and symmetric stretching) of the coordinated water molecules and the HPO_4 groups as well as to the stretching modes of the N-H and C-H groups of piperazinium cations.[8]

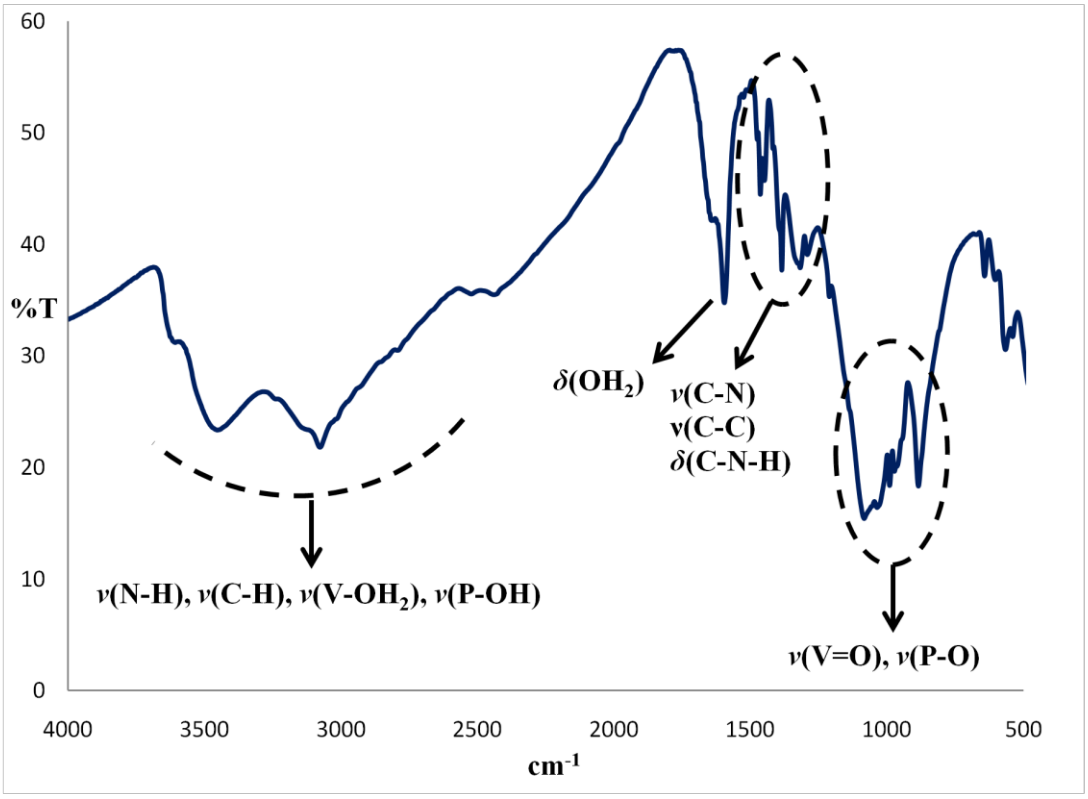

Figure 6.3: Infrared spectrum of compound (1) showing the characteristic bands for each group.

The strong band detected at 1598 cm^{-1} can be attributed to the $\delta(OH_2)$ of the coordinated water, and the broad band occurred in the region 1460-1380 cm^{-1} can be assigned to the characteristic modes of the piperazine ring. These include the stretching vibrations of C-C and C-N bonds in combination with the deformation vibration of C-N-H groups. The broad band resolved into two components: one triplet band at 1032/1019/986 cm^{-1} and a singlet band at 878 cm^{-1} can be assigned to a mixture of P-O and V=O stretching modes.

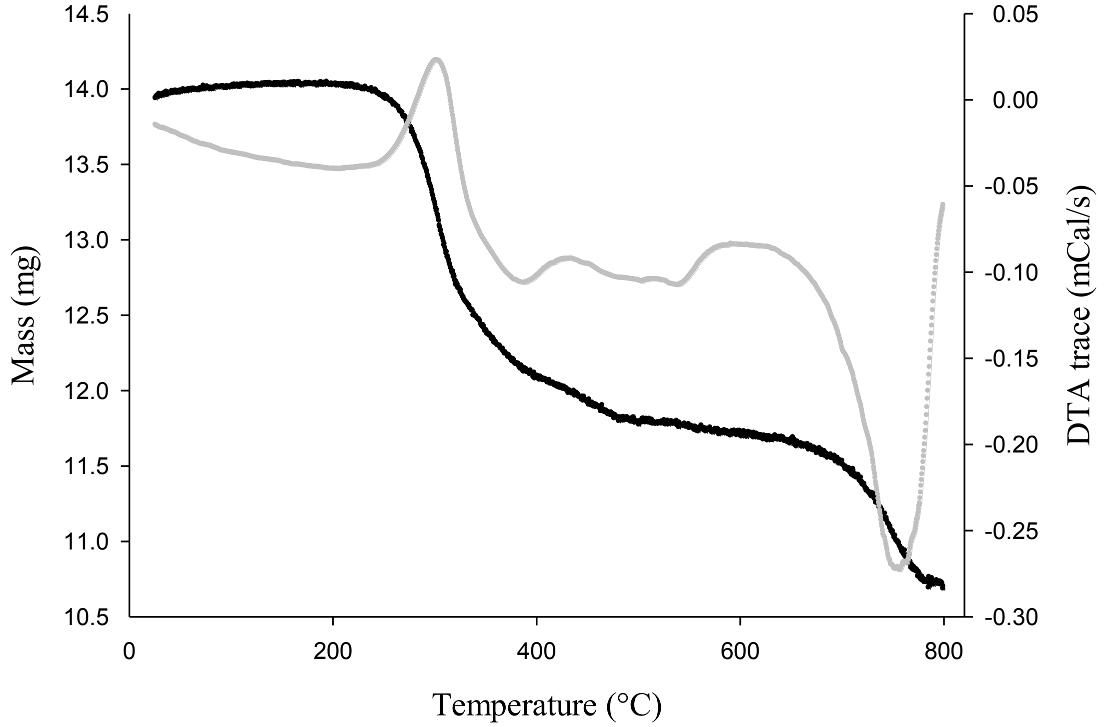

Figure 6.4: TGA pattern of compound (1). Mass loss was recorded as a function of temperature and is shown by the black line. The corresponding DTA trace is the grey line.

Figure 6.4 shows the TGA and DTA analysis of compound (1) (13.952 mg). As can be seen, the framework structure of compound (1) is stable up to 200 °C. Above this temperature, a sharp decrement of mass (total loss ~ 16.23%) occurred between the region 200-540 °C because of the evaporation of the four coordinated water molecules and the calcination of one molecule of piperazine (calculated total mass loss ~ 19.77%). Between this temperature range, one might expect the decomposition of the structure after the elimination of the coordinated water ligands. The presence of the exothermic peak at 300 °C is consisted with the collapsing of the framework structure and the formation of the inorganic residue. A further decrement of mass occurred between the temperature range 650 and 800 °C (loss~ 8 %). In this region, the thermal behavior of compound (1) seems very unclear, as the product was spread into the crucible and the identification of the resulting phase by X-ray powder diffraction proved unsuccessful.

6.1.3 Conclusions

Research included in this section has aimed at investigating the formation of vanadium containing frameworks where both the anionic units, phosphate and borate moieties, can be used together to link vanadium metal centres. Different combinations of starting material sources were investigated in systems that entailed hydrothermal treatment of vanadium pentoxide with phosphate and borate sources in the presence of piperazine. When phosphoric and boric acids were combined together, the system favoured the formation of one particular layered structure type based on alternating linked vanadium and phosphate polyhedra, whereas the combination of a phosphate salt with boric acid yielded vanadium oxide layered structures. Compound (1) has been synthesised under mild hydrothermal conditions from reaction mixtures consisted of phosphoric acid and borax pentahydrate source, and characterised by single crystal X-ray diffraction. Its framework structure embraces layers built up from infinite chains of corner-sharing vanadium octahedra and phosphate tetrahedra; layers are connected together by isolated vanadium octahedra units to form a three-dimensional framework consisting of channels filled with piperazine cations.

6.2 Vanadium borate structures

This section of research includes a series of hydrothermal reactions aimed at investigating the templating effect of the complete series of alkali metal cations in the vanadium clusters formation. Two similar but rather distinct vanadoborate cluster types were synthesized and further described here.

6.2.1 Experimental

I. Synthesis

✓ Synthesis of alkali metal metavanadates MVO_3 (M = Rb, Cs, K, Na, Li)

Alkali metal metavanadates were prepared from the stoichiometric mixture of the corresponding alkali metal carbonate salt and vanadium pentoxide.

$$M_2CO_3 + V_2O_5 \rightarrow 2MVO_3 + \uparrow CO_2$$

The carbonate sources were first heated at a temperature of 200 °C for 2 h in the furnace before being transferred to a glove box where they were weighed and ground together with the vanadium pentoxide source. Reaction mixtures were then transferred into a platinum crucible and heated for 10 hours at the corresponding temperature: $T_{Rb, Cs}$ = 570 °C, T_K = 365 °C, $T_{Li, Na}$ = 300 °C. Once the reaction had finished, products were allowed to cool to room temperature inside the furnace. Products consisted of a single phase of microcrystalline powder of the corresponding MVO_3. The purity of the phases was verified using X-ray powder diffraction.

✓ Synthesis of the vanadium borate clusters

The general procedure entailed hydrothermal treatment of the MVO_3 source with the borate source $(NH_4)_2B_4O_7.4H_2O$ and an organic amine in distilled water. Reaction mixtures were stirred for about one hour at room temperature before being added to a 23 mL Teflon-lined steel autoclave and heated to 448 K for five days. A series of reactions performed by varying the molar composition of the borate source in mixtures of constant $[V]/[B]/[Amine]/[H_2O]_{\text{molar ratios}} = 1/X/2/135$ (1 = 0.618 mmol, and X = any integer number in the range of 1-8). Ethylenediamine was used in all cases; piperazine and diethylenetriamine (deta) was introduced only in the rubidium system.

6.2.2 Results and discussion

I. Synthesis overview

The rubidium templated vanadoborate cluster $Rb_4[(VO_6)\{B_{10}O_{16}(OH)_6\}_2].0.5H_2O$ was reproduced as previously described.[3b]The synthesis yielded a mixed phase consisted of the title compound and a minor phase of orange crystals of the $[(VO)_{12}O_6\{B_3O_6(OH)\}_6]^{10-}$ cluster polyanion. When ethylenediamine was replaced by diethylenetriamine, the relevant phases of green and orange crystals were obtained for any given value of the $[B]/[V]_{molar\ ratio}$. However, when the cyclic piperazine amine was used, a single phase of the $Rb_4[(VO)_6\{B_{10}O_{16}(OH)_6\}_2].0.5H_2O$ product was produced.

A series of hydrothermal reactions was carried out to investigate the templating effect of other alkali metal ions. During this project, the borate content was decreased in different steps from 8 to 1 mol equivalents based on the amount of MVO_3 so as to examine the influence of the amount of boron in the synthesis procedure. Reactions with cesium cations resulted in the analogues crystalline phases. It was observed that nearly a single phase of green crystals of $[(VO_6)\{B_{10}O_{16}(OH)_6\}_2]^{4-}$ was obtained when $[B]/[V]_{molar\ ratio} = 8\text{-}6$. Further decrease of the borate source ($[B]/[V]_{molar\ ratio} = 5\text{-}3$) yielded equal amounts of the two different crystalline phases, whereas for any values $[B]/[V]_{molar\ ratio} < 2$ only the orange crystalline phase was isolated. In the cases of potassium and sodium alkali metals, products were obtained as microcrystalline powders, when the $[B]/[V]_{molar\ ratio} = 8\text{-}5$. Investigation of the resulting products using X-ray powder diffraction identified the analogues compounds, $M[(VO)_6\{B_{10}O_{16}(OH)_6\}_2].0.5H_2O$ where M = K, Na. Further decrease of the borate source ($[B]/[V]_{molar\ ratio} < 4$) resulted to the single phase of orange crystals. Finally, reactions that involved lithium template ions yielded a very different product phase.

II. Structural features of the vanadium borates isolated in this investigation

Selected green plate crystals from the present system were characterised by single crystal X-ray diffraction, revealing a structure consisting of discrete vanadium borate $[V_6B_{20}O_{38}(OH)_{12}]^{4-}$ cluster anions, alkali metal cations and water molecules. The previously reported $[V_6B_{20}O_{38}(OH)_{12}]^{4-}$ cluster polyanion[3b] (shown in Figure 6.5) is derived from a hexavanadate ring, build up from edge-shared VO_5 square pyramids, which is caped on both sides by two polyborate $B_{10}O_{16}(OH)_6^{8-}$ ligands.

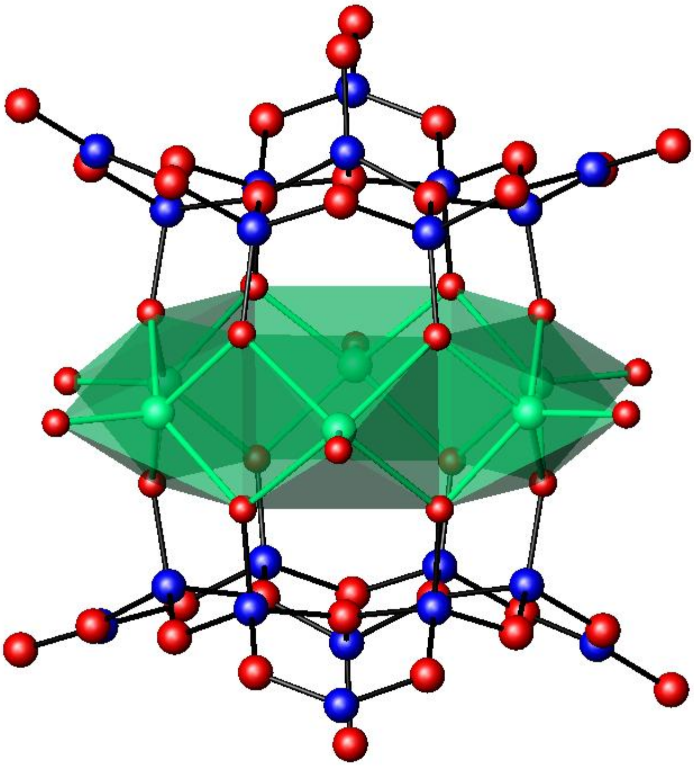

Figure 6.5: Schematic showing the $[V_6B_{20}O_{38}(OH)_{12}]^{4-}$ cluster polyanion. Green spheres represent the vanadium, red spheres show the oxygens; blue the boron.

Figure 6.6 shows the nearly perfect hexagonal vanadium ring which exhibits an approximate diameter of 6 Å. There are three crystallographically independent vanadium sites that adopt the classic distorted pyramidal geometry of V(IV) and show interactions with oxygens comparable to those reported in related structures ($V\text{-}O_{terminal}$ ~ 1.6 Å, $V\text{-}O_{basal}$ ~ 1.95-1.97 Å). The polyborate ligand (shown in Figure 6.6) can be best described as a triangular arrangement of three $[B_3O_5(OH)_3]^{4-}$ units that are linked into a central tetrahedral borate group. Each of the $[B_3O_5(OH)_3]^{4-}$

block contains two tetrahedral borate groups which show very characteristic B-O distances for all the bridging oxygens (B-O: 1.43-1.45 Å), and a planar HBO_3 group that exhibit B-O distances in the range of 1.35-1.39 Å. The central BO_4 tetrahedral group shows intermediate B-O bonds for all the bridging oxygens in the range of 1.47-1.49 Å, in addition to a relatively shorter distance ($B\text{-}O_{terminal}$ ~ 1.42 Å) which is attributed to the terminal oxo group.

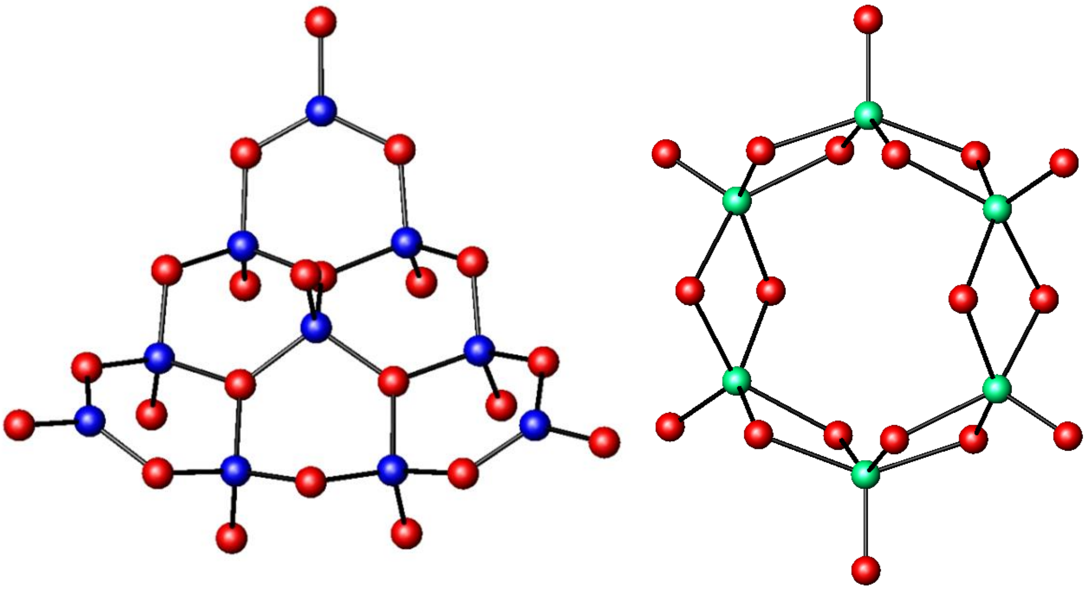

Figure 6.6: Schematic showing parts of the building unit of $M_4[(VO)_6\{B_{10}O_{16}(OH)_6\}_2].0.5H_2O$ analogous compounds, the $B_{10}O_{16}(OH)_6^{8-}$ polyborate ligand (LHS), the $[V_6O_{18}]^{12-}$ hexavanadate ring (RHS). Green spheres represent the vanadium, red spheres show the oxygen atoms; blue the boron atoms.

Projection of the structure along the *a* axis shows how discrete vanadium borate $[V_6B_{20}O_{38}(OH)_{12}]^{4-}$ cluster anions are connected with alkali metal cations into a three-dimensional array through an intricate intermolecular bonding. There are four crystallographically distinct metal atoms (*M* = Rb or Cs), refined at half occupancies, which were found to be located in the intercluster space. Each site adopts an irregular geometry having a coordination sphere defined by nine framework oxygens (d_{av}(Cs-O) = 3.147 Å, d_{av}(Rb-O) = 3.108 Å). As can be depicted in Figure 6.7, a complex bonding motif occurs such as metal cations are couple together by sharing common edges and corners through oxygen bridges. Within the intracluster space there is one crystallographically independent water molecule partially occupied which resides in between the hexacore vanadate ring, and this is within hydrogen bonding distance of a number of the framework oxygens with the $O(H)_w{\cdots}O$ distances ranging from 2.993 to 3.088 Å.

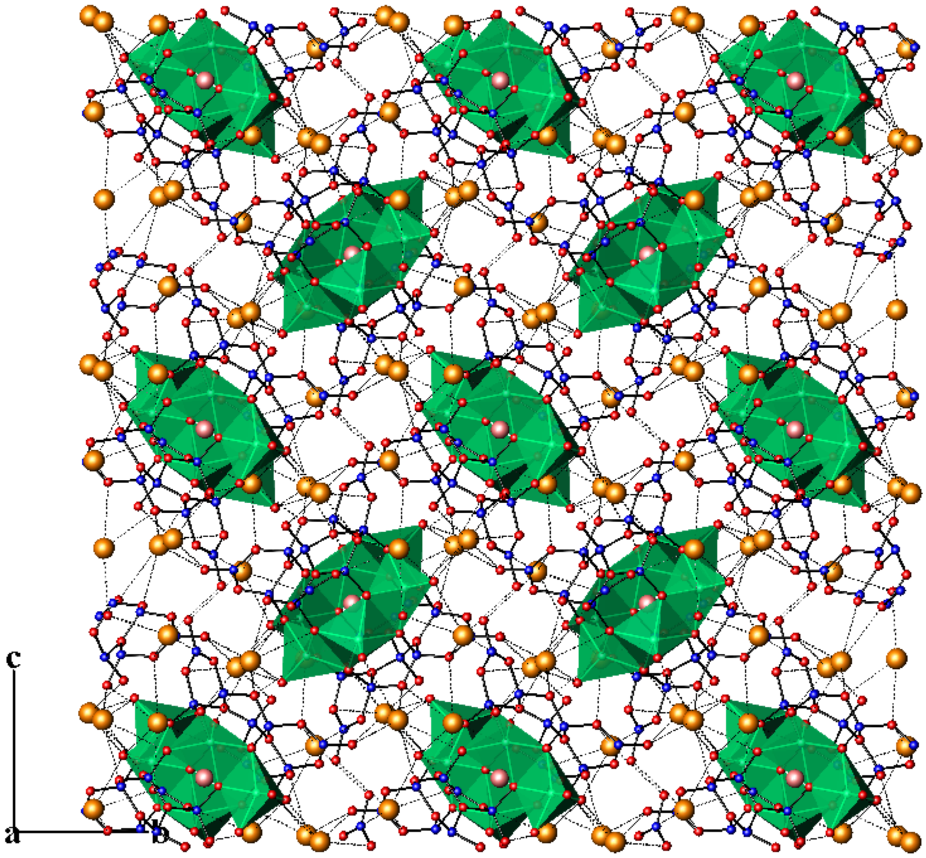

Figure 6.7: A perspective view of the structure of $M_4[(VO)_6\{B_{10}O_{16}(OH)_6\}_2].0.5H_2O$ compound along the *a* axis. Green polyhedra represent the vanadium octahedra forming the hexavanadate ring. Blue spheres represent the boron; red spheres show the oxygen atoms; pink and orange spheres show the hosted lattice water and alkali metal cations (rubidium and caesium) respectively.

The $[(VO)_{12}O_6\{B_3O_6(OH)\}_6]^{10-}$ vanadoborate cluster type, which corresponds to the phase of orange crystals coexisted in the present investigation, consists of an unusual polyborate ligand $B_{18}O_{36}(OH)_6$ coordinated to two isotypical hexacore vanadate rings. As can be observed in the following Figure 6.8, this unique polyborate ligand adopts a chair-like configuration, in such a way as to succeed at being sandwiched between the two detached triangular vanadate rings. Figure 6.9 shows details of the

$B_{18}O_{36}(OH)_6$ ligand. It derives from six $[B_3O_6(OH)_4]^{4-}$ building blocks which share corners through oxygens, forming a B_{18}-ring like arrangement. Each $[B_3O_6(OH)_4]^{4-}$ block is constructed by two corner-sharing borate tetrahedra that share two corners with one HBO_3 group. Investigations on the bond lengths showed very characteristic B-O distances for all the bridging oxygens (B-O = 1.425(11)-1.522(11) Å and 1.349(12)-1.371(12) Å for the BO_4 and HBO_3 groups, respectively) in addition to one slightly lengthened B-O distance ~ 1.39 Å which can be attributed to a terminal hydroxyl group.

The hexavanadate ring (shown in Figure 6.10) can be best described as a triangle arrangement of three alternating pairs of edge-shared vanadium pyramids. There are two isotypical vanadate rings within one molecule of the cluster unit; each one consists of six crystallographically independent vanadium sites. Bond valence calculations completed on the vanadium sites showed the presence of mixed oxidation states. Hence, four out of six vanadium sites have reduced V(IV) oxidation states, and the rest two adopt the highest oxidation state V(V).

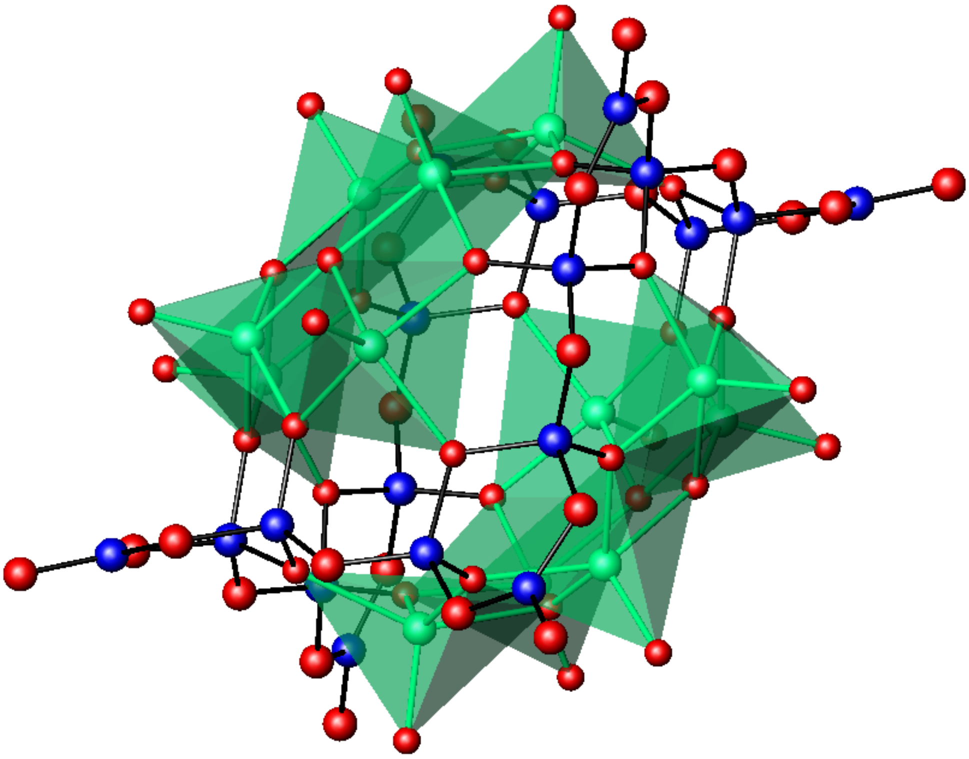

Figure 6.8: Schematic showing the $[(VO)_{12}O_6\{B_3O_6(OH)\}_6]^{10-}$ vanadoborate cluster polyanion.

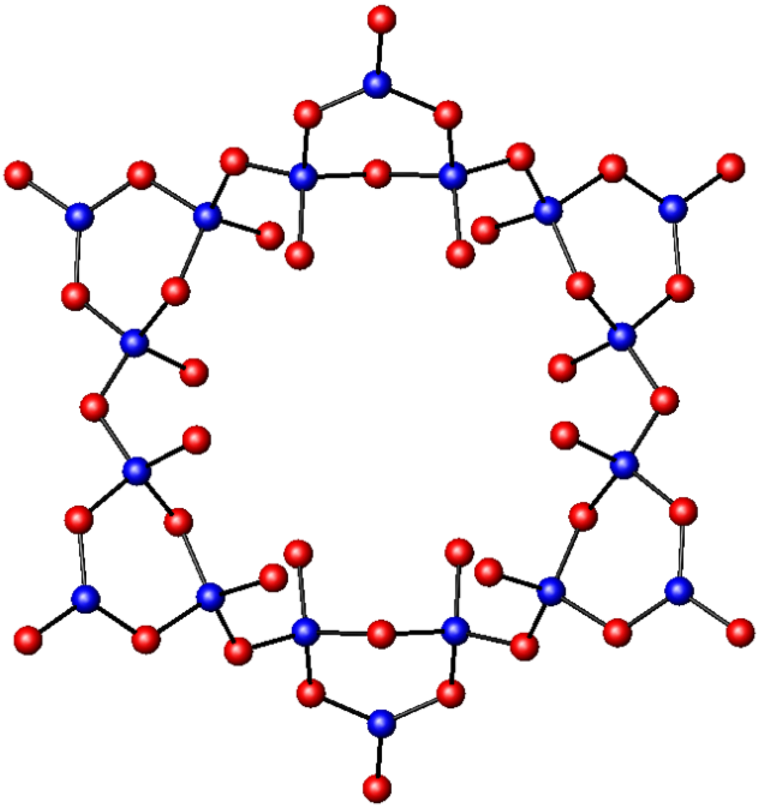

Figure 6.9: Schematic showing the $B_{18}O_{36}(OH)_6$ polyborate ligand.

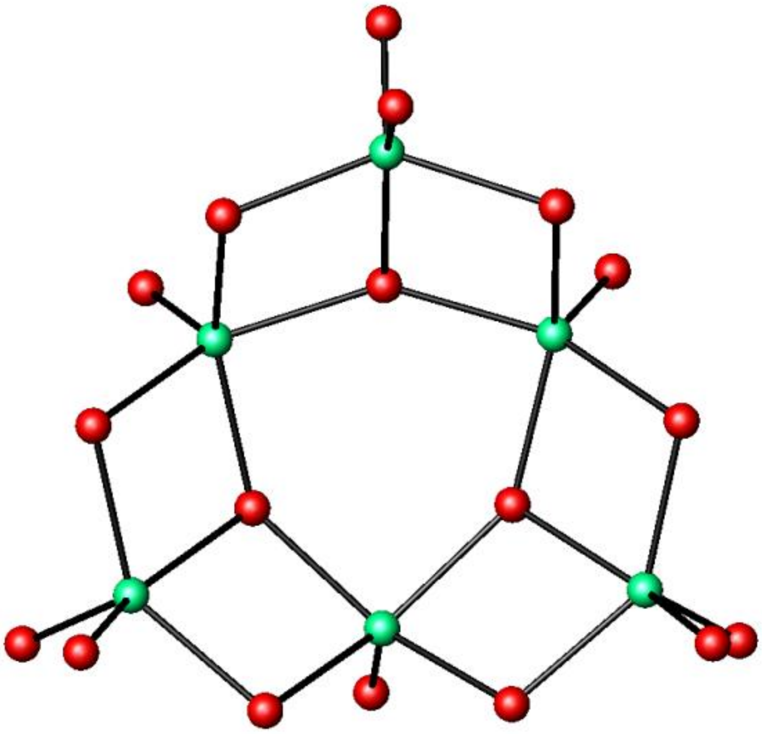

Figure 6.10: Schematic showing the $[V_6O_{18}]^{12-}$ hexavanadate ring.

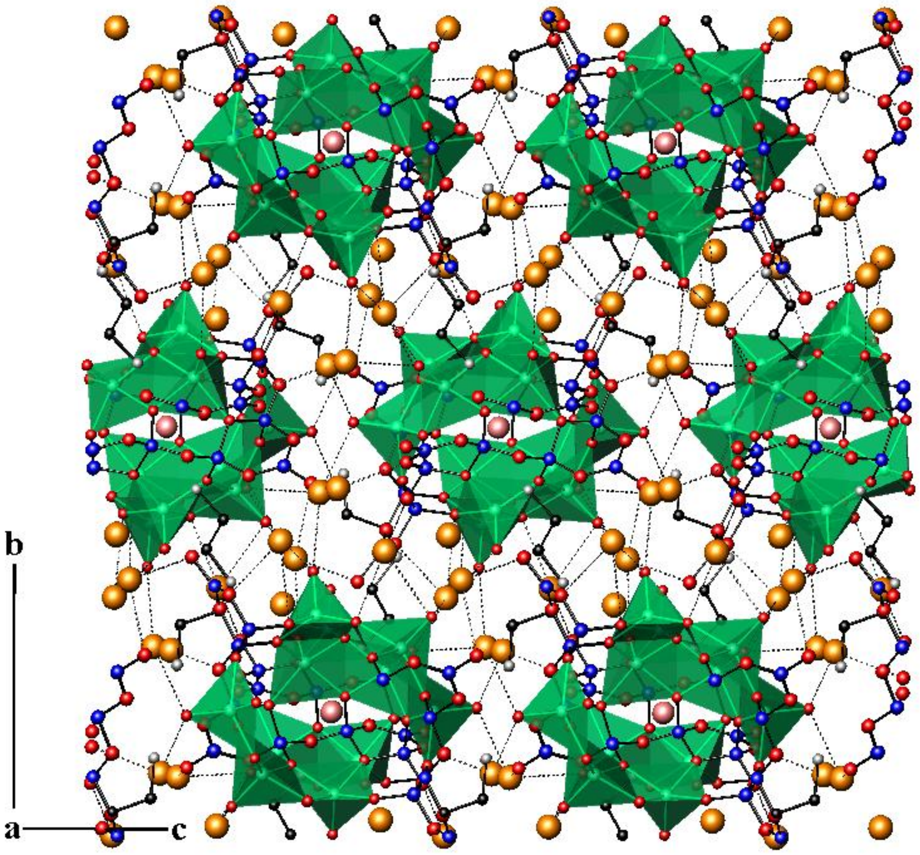

Figure 6.11: A perspective view of the structure of $Rb_6(deta)_2[(VO)_{12}O_6\{B_3O_6(OH)\}_6].0.5H_2O$ compound along the *a* axis. Green polyhedra represent the vanadium octahedra forming the hexavanadate ring. Blue spheres represent the boron; red spheres show the oxygen atoms; pink and orange spheres show the hosted lattice water and alkali metal cations (rubidium and caesium).

Adjacent $[(VO)_{12}O_6\{B_3O_6(OH)\}_6]^{10-}$ vanadoborate cluster anions are connected with rubidium cations and the diethylenetriamine molecules through an intricate intermolecular bonding (illustrated in Figure 6.11). The diethylenetriamine molecules bridge adjacent cluster units *via* an extensive hydrogen bonding, forming layers running along the direction parallel to *ac* plane. There is one crystallographically unique deta molecule within the crystalline structure that contains three distinct nitrogen atoms. As it might have been expected, the two terminal nitrogen atoms act as hydrogen bond donors for a number of the framework oxygens with the N(H)···O distances ranging from 2.885 Å to 3.161 Å. Rubidium cations are located in between the vanadoborate layers. There are six crystallographically independent rubidium atoms, of which two are fully occupied and the other four are partially occupied so as to form a complete site in total. Each rubidium site adopts an irregular geometry with the coordination number varying from five to seven (Rb···O = 2.888-3.137 Å). An intricate bonding occurs such as rubidium cations are coupled together by sharing common edges and corners through oxygen bridges.

6.2.3 Conclusions

The series of the alkali metal templated vanadoborate cluster types, $[(VO_6)\{B_{10}O_{16}(OH)_6\}_2]^{4-}$ and $[V_6B_{20}O_{38}(OH)_{12}]^{4-}$, have been produced and further investigated using X-ray diffraction techniques. The former type consists of a hexavanadate ring, built up from edge-shared VO_5 square pyramids, which is caped on both sides by two polyborate $B_{10}O_{16}(OH)_6^{8-}$ ligands, and the latter comprises of a $B_{18}O_{36}(OH)_6$ ligand sandwiched between two $[V_6O_{18}]^{12-}$ hexavanadate rings.

6.3 Overview

Research included in this chapter has been mainly focussed on the formation of vanadium containing frameworks, where phosphate and borate anionic units can be combined together to link vanadium metal centres. The first part of this chapter was concentrated on the formation of vanadium borophosphate frameworks. A series of hydrothermal reactions were carried out to examine different phosphate and borate starting material sources. As appeared, the incorporation of boron into the resulting crystalline structures proved to be unsuccessful, leading to structural building units consisted of vanadium polyhedra and phosphate tetrahedra. Isolated products include a series of layered structures based on a four-connected net of alternating corner-sharing vanadium octahedra and phosphate tetrahedra, the layered vanadium oxide structure type $(H_2N(C_2H_4)_2NH_2)[V_4O_{10}]$, in addition to the new vanadium phosphate framework $[H_2N(C_2H_4)_2NH_2]\{[VO(PO_4)(HPO_4)]_2[VO(H_2O)_3][VO(H_2O)]\}$ (1). The latter consists of layers of –V-O-V-O- infinite chains and phosphate tetrahedra which are connected with isolated vanadium octahedra to form a three-dimensional framework penetrated by channels where piperazine cations are hosted.

Synthetic work within the second part aimed at investigating the templating effect of the complete series of alkali metal cations in the formation of two previously reported vanadoborate clusters, $[(VO_6)\{B_{10}O_{16}(OH)_6\}_2]^{4-}$ and $[V_6B_{20}O_{38}(OH)_{12}]^{4-}$. Reactions that involved rubidium and cesium cations yielded crystals of the analogous compounds, whereas reactions with sodium and potassium resulted in microcrystalline powder phases of the derivative structures, and reactions with lithium were unsuccessful.

6.4 References

[1] a) K. Bluhm and C. H. Park, *Zeitschrift Fur Naturforschung Section B-a Journal of Chemical Sciences* 1997, *52*, 102-106; b) C. Hauf and R. Kniep, *Zeitschrift Fur Naturforschung Section B-a Journal of Chemical Sciences* 1997, *52*, 1432-1435; c) R. Kniep, H. Engelhardt and C. Hauf, *Chemistry of Materials* 1998, *10*, 2930-2934; d) R. Kniep, G. Gozel, B. Eisenmann, C. Rohr, M. Asbrand and M. Kizilyalli, *Angewandte Chemie-International Edition in English* 1994, *33*, 749-751; e) C. H. Park and K. Bluhm, *Zeitschrift Fur Naturforschung Section B-a Journal of Chemical Sciences* 1995, *50*, 1617-1622; f) S. C. Sevov, *Angewandte Chemie-International Edition in English* 1996, *35*, 2630-2632.

[2] a) R. P. Bontchev, J. Do and A. J. Jacobson, *Inorganic Chemistry* 1999, *38*, 2231-2233; b) R. P. Bontchev, J. Do and A. J. Jacobson, *Angewandte Chemie-International Edition* 1999, *38*, 1937-1940; c) H. Engelhardt, H. Borrmann, W. Schnelle and R. Kniep, *Zeitschrift Fur Anorganische Und Allgemeine Chemie* 2000, *626*, 1647-1652; d) Y. N. Zhao, Z. Shi, S. H. Ding, N. Bai, W. Liu, Y. C. Zou, G. S. Zhu, P. Zhang, Z. H. Mai and W. Q. Pang, *Chemistry of Materials* 2000, *12*, 2550-2556; e) Y. N. Zhao, G. S. Zhu, W. Liu, Y. C. Zou and W. Q. Pang, *Chemical Communications* 1999, 2219-2220.

[3] a) J. T. Rijssenbeek, D. J. Rose, R. C. Haushalter and J. Zubieta, *Angewandte Chemie-International Edition in English* 1997, *36*, 1008-1010; b) C. J. Warren, J. T. Rijssenbeek, D. J. Rose, R. C. Haushalter and J. Zubieta, *Polyhedron* 1998, *17*, 2599-2605.

[4] I. D. Brown and D. Altermatt, *Acta Crystallographica Section B-Structural Science* 1985, *41*, 244-247.

[5] S. L. Wang, H. Y. Kang, C. Y. Cheng and K. H. Lii, *Inorganic Chemistry* 1991, *30*, 3496-3499.

[6] Y. P. Zhang, R. C. Haushalter and A. Clearfield, *Inorganic Chemistry* 1996, *35*, 4950-4956.

[7] a) P. Amoros and A. Lebail, *Journal of Solid State Chemistry* 1992, *97*, 283-291; b) R. C. Haushalter, Z. W. Wang, L. M. Meyer, S. S. Dhingra, M. E. Thompson and J. Zubieta, *Chemistry of Materials* 1994, *6*, 1463-1464; c) V. Soghomonian, R. C.

Haushalter, J. Zubieta and C. J. Oconnor, *Inorganic Chemistry* 1996, *35*, 2826-2830; d) V. Zima and K. H. Lii, *Journal of Solid State Chemistry* 2003, *172*, 424-430.

[8] a) Ray L. Frost, Kristy Erickson and M. L. Weier, *Spectrochimica acta. Part A* 2004, *60*, 2419-2423; b) S.Gunasekaran and B.Anita, *Indian Journal of Pure & Applied Physics* 2008, *46*, 833; c) D. G. Tuck, *Progr. Inorg. Chem* 1968, *9*, 161.

Chapter Seven

Molybdenum Phosphonates

7.0 Metal organophosphonates

In the context of designing new functional materials, the use of organophoshonate anions to link inorganic oxides into extended frameworks has received considerable attention over the past few years. Utilizing a variety of functionalized diphosphonate linkers, the proof of concept was first given through the successful preparation of organically pillared materials. Examples include most zirconium phosphonate materials that encompass corrugated[1] or flat porous layers[2] bridged by diphosphonate anions as well as ordered three dimensional open frameworks.[3] Since then, the family of metal phosphonate materials has been greatly expanded and is no longer limited to pillared materials associated with only bifunctional linkers. The potential to build a variety of rigid and flexible ligands and thereby to direct the connectivity of the functional groups with a vast number of metal oxide frameworks has generated an enormous family of distinct framework topologies. Examples involve infinite inorganic chains [4] or tubular framework structures [5] linked through organophoshonate anions, as well as many layered and open framework structures.[6]

Research included in this chapter has been directed towards the exploration of the molybdenum phosphonate frameworks during a three month placement at the University of Kiel (Germany) working with Prof. Stock. The project mainly involved the utilization of the previously reported diphosphonate ligand,[7] $H_2O_3P\text{-}CH_2\text{-}NC_4H_8N\text{-}CH_2\text{-}PO_3H_2$ (H_4L), which has been extensively used in the past few years for forming coordination frameworks with several transition metals such as Ti,[8] Ni,[9] V,[10] Zn,[11] Mn and Co[12] as well as coordination polymers with lanthanide anions.[13]

Investigations on the molybdenum system were performed on a custom-made high throughput reactor system, allowing a systematic study of compositional and process parameters. The first step was to set up a discovery library with the purpose of doing a general examination of the system, as detailed in Section 7.1. During this investigation, the isolation of a particular phase, which was obtained in a microcrystalline powder form, was thought of as being the starting point for setting up further focused libraries. In an effort to grow bigger crystals of this phase so as to allow further analysis using single crystal X-ray diffraction, four libraries were carried out, and these are discussed in Section 7.2. Finally, research within this project shifted at investigating the reactivity of sodium molybdate with the smallest phosphonate anion (H_3PO_3) in presence of an organic templating agent. An amine templated molybdenophosphite polyanion has been obtained from reactions that involved 4,4'-bipyridine (details of which are given in Section 7.3).

7.1 Discovery Library-System: $Mo_{source}/H_4L/NaOH\text{-}HCl/H_2O$

A discovery library was set up so as to allow a general exploration of the system $Mo/H_4L/NaOH\text{-}HCl/H_2O$. By utilizing high-throughput methods, it has become possible to systematically investigate the effect of different starting material sources ($Na_2MoO_4.2H_2O$, MoO_3, and MoO_2) as well as compositional and experimental conditions on the current system. During this investigation, a particular phase was successfully obtained from mild hydrothermal treatment of $Na_2MoO_4.2H_2O$ source with the phosphonate ligand (H_4L) in presence of HCl.

7.1.1 Experimental

I. Synthesis

✓ Synthesis of the $H_2O_3P\text{-}CH_2\text{-}NC_4H_8N\text{-}CH_2\text{-}PO_3H_2$ ligand (H_4L)

N,N'-piperazinebismethylphosphonic acid was synthesised as previously reported using a typical Mannich type reaction. Piperazine hexahydrate (19.4 g, 0.1 mol) and phosphorous phosphoric acid (16.4 g, 0.2 mol) were dissolved in a solution consisted of distilled water (10 mL) and HCl (10 mL of concentrated 37% hydrochloric acid solution). The mixture was heated to reflux when formaldehyde was slowly dropped into the solution (22 mL of 37% solution, 0.222 mol). The final mixture continued to be heated for two hours and then the reaction stopped. Once cool, the product was filtered, washed with distilled water and air dried. The product consisted of the white microcrystalline powder of the ligand.

✓ High-throughput experiments

The system $Mo_{source}/ H_4L/$ NaOH or HCl/ H_2O was investigated *via* high-throughput methods. Reaction mixtures were placed in a custom-made HT reactor system, consisted of 48 PTFE inserts with a maximum volume of 300 μL, and then transferred to an autoclave and heated under autogenous pressure for two days. During this course of investigation, three main systems were set up using a different metal source every time ($Na_2MoO_4.2H_2O$, MoO_3, or MoO_2). Each system was hydrothermally treated at various temperatures (120 °C, 140 °C and 180 °C). When the reaction was finished, the furnace was cooled down over a period of 6 h.

Summary of the discovery library is given in Table 7.1, in which the ligand concentration was always kept constant (0.15M or 0.30M) and the molar ratios of the Mo sources varied accordingly. NaOH or HCl was then added to the mixture in order to obtain an approximate range of acidic or basic conditions. The NaOH and HCl content was varied in two steps for each given value of $[Mo]/[L]_{ratio}$. Note that soluble starting materials, such as $Na_2MoO_4.H_2O$, NaOH and HCl, were first dissolved in distilled water (preparing concentrated solutions of C (mol/L) = 2M), which then were automatically dispensed into the HT array; insoluble sources including the H_4L, MoO_3 and MoO_2 were solid dosed.

Table 7.1: Summary of the discovery library.

$[H_4L]$ (mol/L)	$[NaOH]$ or $[HCl]/[H_4L]_{ratio}$	$[M]/[H_4L]_{ratio}$
0.15	1	4
0.30	2	3
		2
		1.5
		1
		0.750

$[H_4L]$ (mol/L) = Ligand: N'N-piperazine bismethylene phosphonate

[M] (mol/L) = Mo sources: $Na_2MoO_4.2H_2O$, MoO_3, and MoO_2

Total volume (μL) = 240

FW_{H4L}(g/mol) = 274.15, FW_{MoO3} (g/mol) = 143.94, FW_{MoO2} (g/mol) = 127.94

C (mol/ L) = 2M (NaOH, HCl and $Na_2MoO_4.2H_2O$ aqua solutions)

7.1.2 Results and discussion

For the exploration of the system $Mo/H_4L/NaOH\text{-}HCl/H_2O$, a discovery library was set up to allow a general study of the reaction parameter space concerning starting material sources as well as compositional and process parameters. In this investigation, three molybdenum sources ($Na_2MoO_4.2H_2O$, MoO_3, or MoO_2) have been tested, and each one yielded different products. High-throughput reactions that involved $Na_2MoO_4.2H_2O$ showed many difficulties in forming a product phase. Particularly, reactions that took place at the very high temperatures (160 °C and 180 °C) resulted in having no solid products in their solutions. Similarly, lower temperatures (140 °C and 120 °C) tended to produce clear solutions, however in only very few cases two distinct microcrystalline powder phases (denoted here as phase ‘A’ and ‘B’) were discovered. Phase ‘A’ was obtained from the following reaction mixtures: [H_4L]/[M]/HCl] = 0.15/0.30/0.30, 0.15/0.15/0.15 and 0.30/0.30/0.30, and Phase ‘B’ was obtained from the mixtures: [H_4L]/[M]/[HCl] = 0.15/0.225/0.30, 0.15/0.15/0.30, 0.30/0.30/0.60 and 0.30/ 0.225/0.60. Investigation of the isolated product phases using powder X-ray diffraction showed Phase ‘B’ to contain both the H_4L ligand and Phase ‘A’, with the latter being an unidentifiable material. Figure 7.1 shows the powder patterns of these phases, where it can be observed that Phase ‘A’ shows a sensible powder diffraction pattern with reflections occurred at relatively low 2θ angles. In addition, EDS analysis carried out on the samples has shown the presence of both molybdenum and phosphorus elements within the crystalline phase. Phase ‘A’ was found to be very homogenous and the determined atomic ratios were Mo/P/O/N = 1/0.77/2.49/0.75.

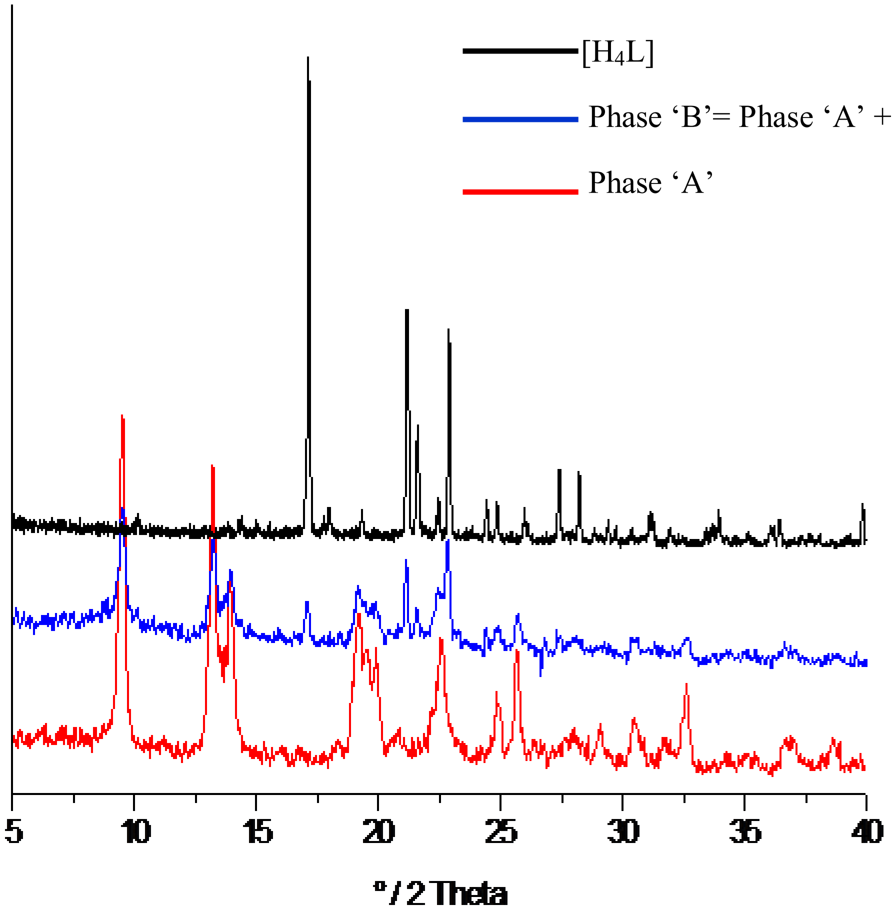

Figure 7.1: Powder X-ray diffraction patterns of H_4L, Phase ‘A’, and Phase ‘B’.

When MoO_3 was introduced into the system, reactions resulted in mixed phases mostly consisting of white microcrystalline powders and black crystals. X-ray powder diffraction identified the presence of the ligand in most cases and very rarely the formation of molybdenum oxide which are the black isolated crystals. Particularly, only the following reaction mixtures: $[H_4L]/[M]/HCl]$ = 0.15/0.225/0.15, $[H_4L]/[M]/NaOH]$ = 0.15/ 0.225/0.15, 0.10/0.225/0.10 yielded Phase 'B'. Finally, reactions that entailed MoO_2 source proved to be very unsuccessful. Despite varying the reaction temperature and the composition parameter, powder X-ray diffraction on the products identified the presence of the starting materials MoO_2 and H_4L, assuming that reagents did not involve in any reaction.

7.1.3 Conclusion

A discovery library was set up in an effort to investigate general parameters, such as starting material sources as well as compositional and process parameters, for the previously unknown system $Mo/H_4L/NaOH\text{-}HCl/H_2O$. From a general point of view, $Na_2MoO_4.2H_2O$ appears to be the best starting material source compared to the other molybdenum oxide sources investigated. During this study, a particular phase (identified as Phase 'A') was successfully obtained under mild hydrothermal routes (120 °C) and always under acidic conditions (reactions that involved addition of HCl). This particular phase can be thought of as being the starting point for setting up further focused libraries, thus the quest now is to grow bigger size crystallites, suitable for single-crystal X-ray diffraction analysis.

7.2 Focused libraries-System: $Na_2MoO_4.2H_2O/H_4L/HCl/H_2O$

Following the isolation of Phase 'A' during the earlier discovery library, synthetic work in this part includes four main focused libraries that aimed to grow bigger crystals of this particular phase. The first library involved a closer study on the compositional parameters of the reaction mixtures that yielded this phase previously, the second one attempted to perform more dilute reaction mixtures, and the third one applied very low temperatures by using a TGradient Thermocycler. Finally, the fourth library introduced a mixed-solvent system containing isopropanol and water.

7.2.1 Experimental

I. Synthesis

✓ System (1): $Na_2MoO_4.2H_2O$/ H_4L/ HCl/ H_2O, 120°C, 48 HT-array

Reaction mixtures were placed in a custom-made HT reactor system which consisted of 48 PTFE inserts with a maximum volume of 300 µL (volume filled = 240 µl), and then transferred to an autoclave and heated at 120 °C under autogenous pressure for two days and cooled down for a period of 12 h. Summary of the focused library is given in the below Table 7.2. The ligand concentration was always kept constant ($[H_4L]$ = 0.075M-0.15M) as well as the amount of HCl ($[HCl]/[H_4L]$ = 1 or 2), whilst the [M] was varied according to the $[H_4L]$. Note that soluble starting materials, such as $Na_2MoO_4.H_2O$, and HCl, were first dissolved in distilled water (preparing concentrated mixtures of C (mol/ L) = 2M), which then were automatically dispensed into the HT array; only H_4L was solid dosed.

Table 7.2: Summary of the focused library for System (1).

$[H_4L]$ (mol/L)	$[HCl]/[H_4L]_{ratio}$	$[M]/[H_4L]_{ratio}$
0.075	1	1
0.10	2	1.2
0.125		1.4
0.15		1.6
		1.8
		2

✓ System (2): $Na_2MoO_4.2H_2O$/ H_4L/ HCl/ H_2O, 120°C, 24 HT-array

Reaction mixtures were placed in a custom-made HT reactor system which consisted of 24 PTFE inserts with a maximum volume of 1.5 mL, and then transferred to an autoclave. The reaction time was set up for 48 h and the cooling period for 12 h. Two focused libraries were performed for System (2) (summarized in the Tables 7.3) in which the H_4L (0.027 mmol, 6.58 mg) and $Na_2MoO_4.2H_2O$ (0.024 mmol, 0.012 ml of 2M solution) content kept constant, whilst the amount of water was increased in every step. In the first library (a) the amount of HCl was also kept constant (0.048 mmol, 0.024 ml of 2M solution); the molar concentrations of the resulting solutions are given in the following Table. In the second library (b), the amount of HCl was varied in every step in order to adjust the C_{final} of HCl at 2M. The required V_{HCl} (ml) was calculated from the following equation: $(V_{H2O} + V_{Mo} + V_{HCl}).C_{final} = V_{HCl}.\ C_{initial}$

Tables 7.3: LHS: Focused library (a), RHS: Focused library (b).

V_{H2O}(ml)	C_{final}HCl (mol/L)
0.204	0.2
0.214	0.192
0.224	0.185
0.234	0.177
0.244	0.172
0.254	0.166
0.264	0.160
0.274	0.155
0.284	0.150
0.294	0.145
0.304	0.141
0.354	0.123
0.404	0.109
0.454	0.098
0.504	0.089
0.554	0.081
0.604	0.075
0.654	0.069
0.704	0.065
0.754	0.061
0.804	0.057
0.854	0.054
0.904	0.051
0.954	0.048

V_{H2O}(ml)	V_{HCl} (ml)
0.204	0.024
0.214	0.025
0.224	0.026
0.234	0.027
0.244	0.028
0.254	0.030
0.264	0.031
0.274	0.032
0.284	0.033
0.294	0.034
0.304	0.035
0.354	0.041
0.404	0.046
0.454	0.052
0.504	0.057
0.554	0.063
0.604	0.068
0.654	0.074
0.704	0.080
0.754	0.085
0.804	0.091
0.854	0.096
0.904	0.102
0.954	0.107

- ✓ System(3): $Na_2MoO_4.2H_2O/H_4L/NaOH-HCl/H_2O$ TGrad.Thermocycler

System (3) entailed reactions that took place in a TGradient Thermocycler where different temperatures can be tested within a single row between the range 55-100 °C. Thermocycler is dived into six rows and eight columns, for every column a different temperature was set up (T_1 = 55, T_2 = 60, T_3 = 65…T_8 = 100 °C). Samples within the same row differ in reagents composition, details of which are shown in Table 7.4. The reaction time was set up for 48 h and the cooling period for 12 h.

Table 7.4: Compositional details of the samples placed in each row.

Row No	$[H_4L]$(mol/L)	$[M]/[H_4L]$	$[HCl]/[H_4L]_{ratio}$	$[NaOH]/[H_4L]_{ratio}$
1	0.15	1	—	—
2	0.15	1	1	—
3	0.15	1	2	—
4	0.15	1	4	—
5	0.15	1	—	1
6	0.15	1	—	2

- ✓ System (4): $Na_2MoO_4.2H_2O/H_4L/HCl/H_2O$-isopropanol, 48 HT-array

Reaction mixtures were placed in a custom-made 48-HT reactor system, then transferred to an autoclave and heated at 120 °C for two days. The $[H_4L]$ was always kept constant ($[H_4L]$ = 0.10M or 0.20M), as well as the amounts of [M] and [HCl] ($[M]/[\ H_4L]_{ratio}$ = 1, $[HCl]/\ [H_4L]_{ratio}$ = 1 or 2). In this mixed solvent system containing isopropanol and water, different mixtures were prepared by varying the solvents % parts (detailed in Table 7.5).

Table 7.5: Summary of the focused library for System (4).

$[H_4L]$ (mol/L)	$[M]/[H_4L]_{ratio}$	$[HCl]/[H_4L]_{ratio}$	$[P]/[H_2O]_{parts}$
0.10	1	1	10/90
0.20		2	20/80
			30/70
			40/60
			50/50
			60/40
			70/30
			80/20
			90/10
			100/0

7.2.2 Results and discussion

The first library has been focused on the detailed examination of the three reaction mixtures that had yielded Phase 'A' during the earlier discovery library. These were the reactions consisting of $[H_4L]/[M]/HCl]$ = 0.15/0.30/0.30, 0.15/0.15/0.15 and 0.30/0.30/0.30, in which $[H_4L]/[M]$ and $[H_4L]/HCl]$ ratios can only take the values 1 or 2. In this investigation, much less concentrated mixtures were performed by decreasing the $[H_4L]$ (mol/L) in the range of 0.075 - 0.15M. Also, the cooling rate was increased from 6 h to 12 h so as to facilitate the crystal growth process. As a result, reaction mixtures with $[H_4L]/ [M]$ ratios in the range of 1.2-1.4 yielded Phase 'A', whilst the rest samples resulted either in Phase 'B' or gave clear solutions. All the products were obtained as microcrystalline powders, however, an exception occurred in the case of $[H_4L] = [M] = 0.10M$, $[HCl] = 0.20M$ in which very tiny small crystals were obtained. Unfortunately, the small crystallite size hinders efforts to analyse this product using single crystal X-ray diffraction analysis.

Following the occurrence of small crystals within the former sample, the second library aimed at preparing even more dilute mixtures by increasing the amount of water in the system. This took place in a larger-volume custom-made HT reactor system (consisting of 24 PTFE inserts with a maximum volume of 1.5 mL). Two series of experiments were carried out, in which samples were prepared by keeping constant the reagents ratios but adding more water in the system. Phase 'A' was successfully obtained from all samples but unfortunately crystallites present in the samples were not big enough for single crystal X-ray diffraction.

In the meantime, a series of experiments took place in a TGradient Thermocycler where different temperatures can be tested within a single row between the range 55-100 °C. Unfortunately system (3) was very unsuccessful, since all reactions ended up either in clear solutions or in the precipitation of the ligand. Finally, a mixed-solvent system containing isopropanol and water was designed, thus one might expect that larger crystals can be formed when increasing the viscosity of the solvent. Unfortunately this investigation was also unsuccessful, as the ligand was precipitated from reactions that had $[H_4L]/[M]/HCl]$ ratio = 1/1/1 and Phase 'B' was formed by reactions that had $[H_4L]/[M]/HCl]$ ratios = 1/1/2. It was generally observed that the different % parts of H_2O-isopropanol did not have an effect on the products formation. Furthermore, reactions that took place only in the presence of isopropanol and in absence of water gave no products in their solutions.

7.2.3 Conclusions

In an effort to investigate the formation of an unidentified phase which was obtained from the earlier discovery library and termed as Phase ‘A’, four main libraries were set up and discussed here. The first library involved a detailed examination of the compositional parameters of mixtures that had yielded this phase before, showing the successful reproduction of the phase when the $[H_4L]/[M]$ and $[H_4L]/HCl]$ ratios take the values 1 or 2. The successful formation of some really small crystallites (identified as Phase ‘A’) in one particular reaction mixture was the main reason for setting up the second library. The second library attempted to decrease the total concentration of the reagents in this specific reaction mixture, as more dilute mixtures might facilitate the crystals growth process. However, all attempts were unsuccessful and no crystals were grown out of this project. Moreover, lower temperatures were applied by using a TGradient Thermocycler. This study has either led to the precipitation of ligand or ended up in clear solutions. Finally, the fourth library aimed at investigating the crystal growth process using a mixed-solvent system (isopropanol-water). During this investigation, Phase ‘B’ (consisting of Phase ‘A’ and ligand) was mainly observed, and this was isolated in the form of crystalline powder.

7.3 System: $Na_2MoO_4.2H_2O/H_3PO_3$/organic amine/HCl

The present investigation includes a series of hydrothermal reactions involving sodium molybdate with the smallest phosphonate anion (H_3PO_3) in the presence of an organic templating agent (dabco, 4,4'-bipyridine). Reactions took place in a 24-HT array, allowing verification of the compositional parameters in the current system. An amine templated molybdenophosphite polyanion has been successfully obtained when 4,4'-bipyridine was introduced into the system.

7.3.1 Experimental

I. Synthesis

Reaction mixtures were placed in a custom-made HT reactor system, consisting of 24 PTFE inserts with a maximum volume of 1.5 ml (volume filled 0.5 ml) and then transferred to an autoclave and heated under autogenous pressure at 120 °C for two days. Once the reaction was finished, the oven was cooled down over a period of 12 h. Two main series of experiments (12 reactions each) were carried out based upon two different organic amines (dabco and 4,4'-bipyridine). Table 7.6 shows the compositional details of the 12 samples in the HT reactor in which the phosphorous source [P] was always kept constant at 0.15M, whilst the other reagents ($Na_2MoO_4.2H_2O$ = [M], organic amine = [A] and HCl) varied according to the ligand. Note, that all soluble starting materials were first dissolved in distilled water (preparing concentrated solutions of C_{H3PO3}, $C_{Na2MoO4}$ = 1M, C_{HCl} = 1M, C_{dabco} = 0.55M) which were then automatically dispensed into the HT array; 4,4'-bipyridine was solid dosed.

Table 7.6: Compositional details of the 12 samples placed in 24-HT.

[P](mol/L)	$[M]/[P]_{ratio}$	$[HCl]/[P]_{ratio}$	$[A]/[P]_{ratio}$
0.15	1 or 1.5	0	1
0.15	1 or 1.5	1	1
0.15	1 or 1.5	2	1
0.15	1 or 1.5	0	2
0.15	1 or 1.5	1	2
0.15	1 or 1.5	2	2

7.3.2 Results and discussion

In an effort to investigate the reactivity of $Na_2MoO_4.2H_2O$ molybdenum source with the smallest phosphonate ligand (phosphorus acid), we have carried out a programme of work in systems that entailed hydrothermal treatment of the above reagents in presence of an organic templating agent (dabco or 4,4'-bipyridine). In most cases, the system led to the formation of the disodium phosphonate salt Na_2HPO_3 (when $[P]/[Mo]/[HCl]/[A]_{ratio}$ = 1/1-1.5/1-2/1). By increasing the concentration of amine in the final reaction mixture ([A]/[P] = 2), the system yielded a crystalline product but only in the presence of 4,4'-bipyridine. Single crystal X-ray analysis of the crystalline phase revealed a structure consisting of discrete $\{Mo_5O_{15}(HPO_3)_2\}^{4-}$ cluster polyanions, 4,4'-bipyridine cations and water molecules (demonstrated in Figure 7.2). Crystal and diffraction data of $(4,4'\text{-biy})_2\{Mo_5O_{15}(HPO_3)_2\}.H_2O$ (1) is given in Table 7.7.

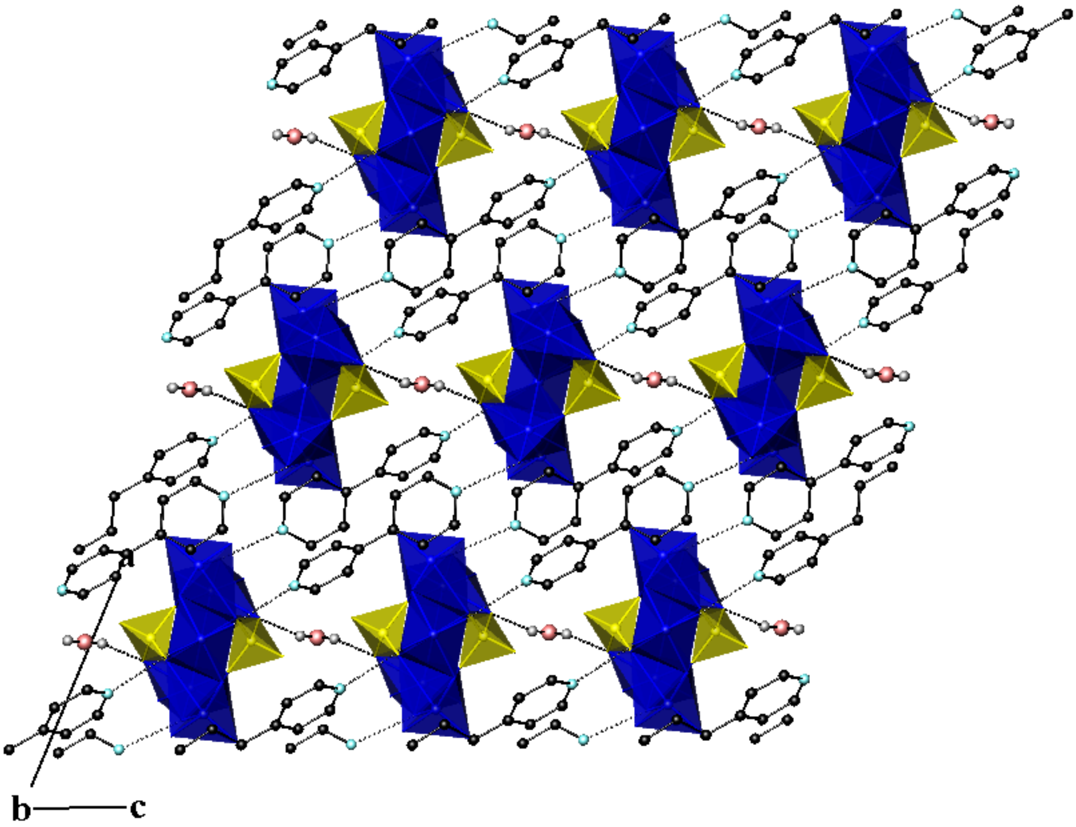

Figure 7.2: View of the structure of compound (1). Blue polyhedra represent the molybdenum octahedra and yellow polyhedra show the phosphite groups. Pink spheres show lattice water; black and turquoise small spheres show the carbon and nitrogen atoms of 4,4'-bipy, respectively.

The $\{H_2Mo_5P_2O_{21}\}^{4-}$ polyanion is built up from five MoO_6 octahedra that share four common edges and one corner through oxygen atoms to form a five-membered ring which is capped on both poles by two $[HPO_4]^{2-}$ phosphite groups. Similar $[Mo_5O_{15}(PO_4)_2]^{6-}$ polyanions, consisting of $[HPO_4]^{2-}$ tetrahedra instead, have been extensively studied in the past, however relatively little work has been carried out on the analogous molybdenum phosphite system.[14] Figure 7.3 shows the $\{H_2Mo_5P_2O_{21}\}$ cluster polyanion found in compound (1).

There are three crystallographically independent molybdenum sites that adopt the classic distorted octahedral geometry of Mo(VI) and show interactions with oxygens comparable to those reported in related compounds. The phosphite group contains one crystallographically independent phosphorous atom that is coordinated to three bridging oxygen donors from MoO_6 octahedra, forming a pseudo-pyramidal $(HPO_3)^{2-}$ oxoanion. The $(HPO_3)^{2-}$ group shows very characteristic bond distances (P-O: 1.507(6) – 1.547(5) Å) and bond angles (O-P-O: 110.29(3)-112.70(3)°) for all the bridging oxygen donors, and as can be seen, these do not differ much from those reported in related polyanions consisting of phosphate tetrahedra instead. The hydrogen attached to the phosphite group was identified in the difference map and from bond elongation (P-H: 1.396 Å), this was then fixed in calculated positions, treated as riding on the parent atom and the torsion angle allowed to refine.

Looking at the bond distances displayed in Table 7.8, it would appear that oxygen atoms can be divided into three main groups according to the coordination mode they adopt. The first group includes the terminal oxo groups of MoO_6 octahedra which show relatively short Mo-O bond distances in the range of 1.685(6) – 1.727(5) Å. The second group involves the bridging oxygens between two Mo centres that exhibit intermediate distances in the range of 1.887(2)-1.960(6) Å, whereas the third group includes the oxygens of the phosphite groups that are shared between two Mo centres and show significantly lengthened bond distances in the range of 2.197(5)-2.423(6) Å.

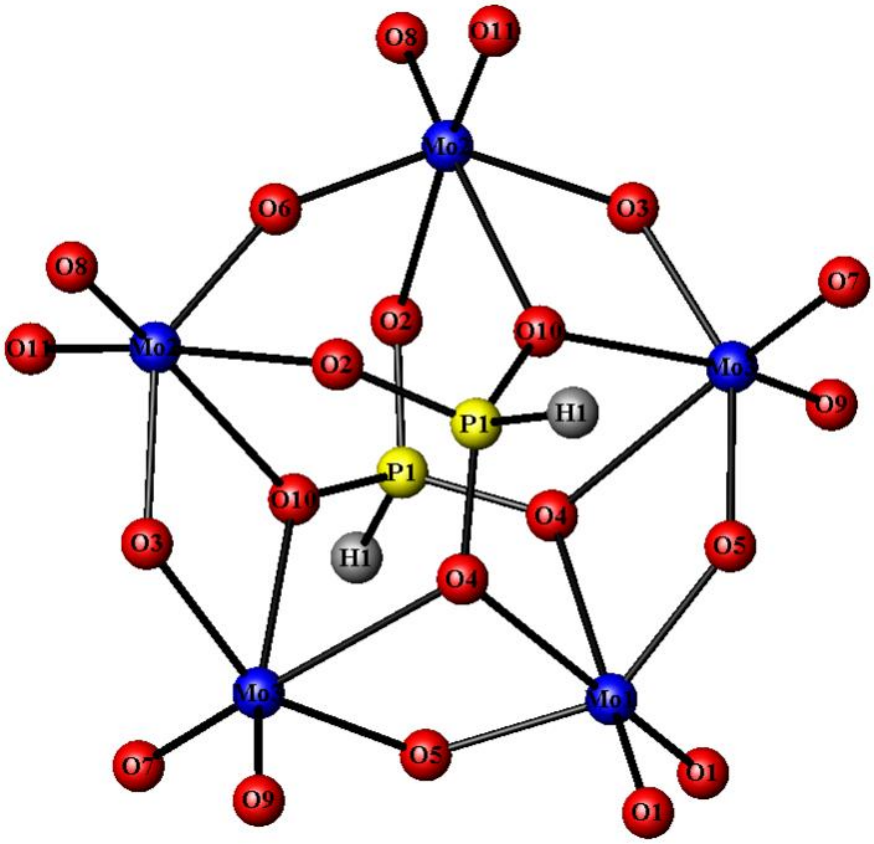

Figure 7.3: Schematic showing the $\{H_2Mo_5P_2O_{21}\}^{4-}$ cluster polyanion.

Table 7.7: Crystal and diffraction information of compound (1).

Empirical formula	$C_{20}H_{24}N_4Mo_5P_2O_{22}$
Formula weight	1214.07
Temperature	120(2) K
Appearance	Colourless needle
Wavelength	0.71073 Å (Mo K_α)
Crystal system	Monoclinic
Space group	$C2$
Unit cell dimensions	a = 20.3974(5) Å, b = 10.6862(4) Å c = 8.6562(2) Å, β = 113.718(2)°
Volume	1727.43(9)
Z	2
D_c	2.334 g.cm^{-3}
Θ range for data collection	3.03-27.49
Reflections collected	11026
Independent reflections	3769
Data/Restraints/Parameters	3769/67/249
R indices	R_1 = 0.0409 wR_2 = 0.0821

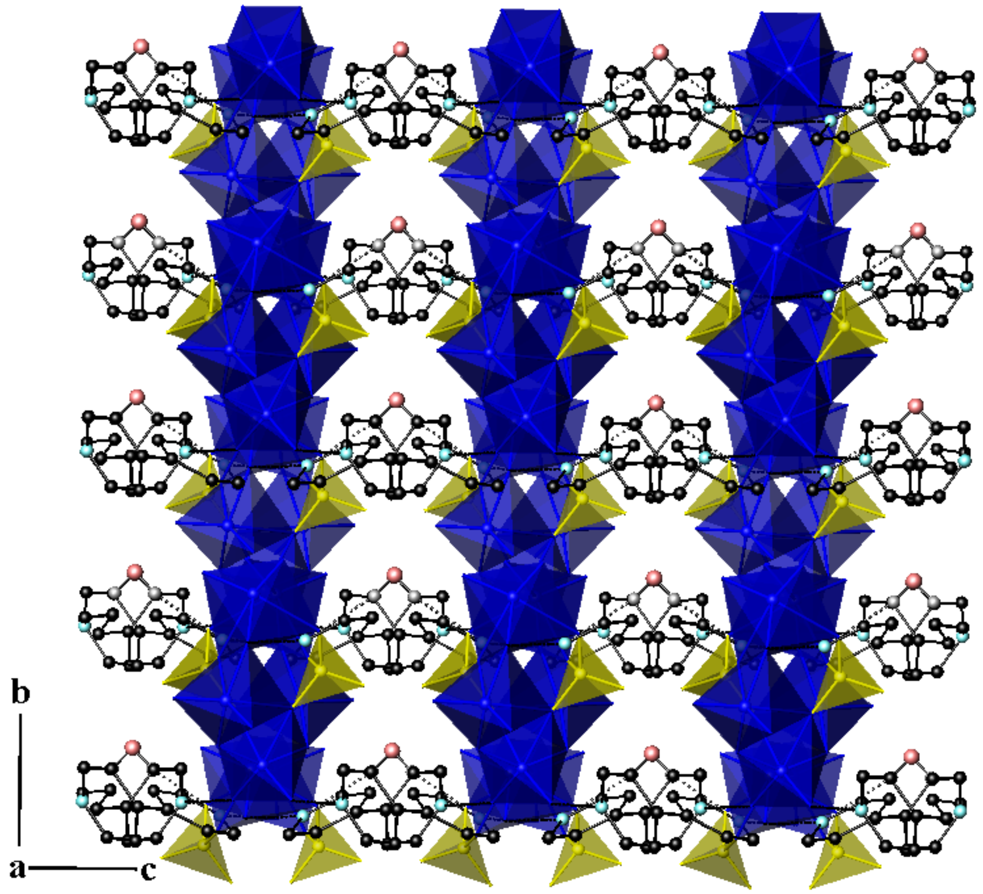

Figure 7.4: A perspective view of the structure of compound (1) along the *a* axis.

Table 7.8: Selected bond lengths (Å) and bond valences for compound (1).

Polyhedra	Bond lengths	Σs_{ij}	Polyhedra	Bond lengths	Σs_{ij}
Mo(1)O$_6$			Mo(3)O$_6$		
Mo(1)-O(1)	1.727(5)	1.627	Mo(3)-O(7)	1.692 (5)	1.788
Mo(1)-O(1’)	1.727(5)	1.627	Mo(3)-O(9)	1.709(6)	1.708
Mo(1)-O(5)	1.901(5)	1.016	Mo(3)-O(5)	1.936(6)	0.925
Mo(1)-O(5’)	1.901(5)	1.016	Mo(3)-O(3)	1.960(6)	0.867
Mo(1)-O(4)	2.316(5)	0.331	Mo(3)-O(10)	2.197(5)	0.457
Mo(1)-O(4’)	2.316(5)	0.331	Mo(3)-O(4)	2.423(5)	0.248
		ΣMo1=5.95			**ΣMo3=5.99**
Mo(2)O$_6$			HP(1)O$_3$		
Mo(2)-O(8)	1.685(6)	1.822	P(1)-O(2)	1.507(6)	1.346
Mo(2)-O(11)	1.694(5)	1.778	P(1)-O(4)	1.533(5)	1.255
Mo(2)-O(6)	1.887(2)	1.056	P(1)-O(10)	1.547(5)	1.208
Mo(2)-O(3)	1.946(6)	0.899			**ΣP1=3.81**
Mo(2)-O(2)	2.330(5)	0.319			
Mo(2)-O(10)	2.423(6)	0.248			
		ΣMo2=6.12			

A further unique structural feature is the layered packing arrangement of these {$H_2Mo_5P_2O_{21}$} polyanions along the *a* axis (illustrated in Figure 7.4). Diprotonated 4,4’-bipyridine cations and water molecules are located in the interlayer space, and bridge adjacent layers as a result of strong hydrogen bonding. There is one unique crystallographic 4,4’-bipy molecule that contains two distinct nitrogen atoms. Each nitrogen atom makes one hydrogen bond link with the polyanions connecting to O(3) and O(1) in such a way as to form bridges running along the direction perpendicular to the layers ((N(1)···O(3) = 2.587 Å, (N(2)···O(1) = 2.689 Å). Water molecules also act as hydrogen bond donors, forming bond links with the bridging oxygen donors, with the Ow(1)···O(2) distance = 2.858 Å.

Compound (1) was further characterised by Infrared spectroscopy and TGA analysis. The infrared spectrum shown in Figure 7.5 exhibits overlap of broad bands in the 3500-2800 cm^{-1}. Bands in the high frequency region (3500-3200 cm^{-1}) can be assigned to water molecules and to the amino groups of the protonated 4,4’-bipy cations, whereas bands in the low frequency region (3100-2800 cm^{-1}) can be attributed to the stretching modes of C-H groups of the 4,4’-bipy ring and to the P-H bond. The latter shows a very characteristic absorption band clearly detected at 2373 cm^{-1}.[15] The band detected at 1617 cm^{-1} is assigned to the corresponding H-O-H bending mode of water molecule, and the following intense single bands at 1492, 1383 cm^{-1} in addition to the doublet band at 1239/1206 cm^{-1} can be attributed to the very characteristic modes of the 4,4’-bipy ring.[16] These include the stretching vibration of C-C and C-N bonds in combination with the deformation vibration of C-N-H groups. The absorption bands of HPO_3^{2-} and Mo-O groups appear in lower frequencies. The three strong bands at 1119 cm^{-1}, 1058 cm^{-1} and 988 cm^{-1} are attributed to the asymmetric vibration, the deformation vibration of P-H bond and the symmetric vibration of the phosphite group respectively. The following doublet band at 935/908 cm^{-1} is assigned to the characteristic stretching mode of Mo=O oxo groups, and the two medium absorptions at 856 cm-^{1} and 806 cm^{-1} are assigned to the Mo-O-Mo bridges.

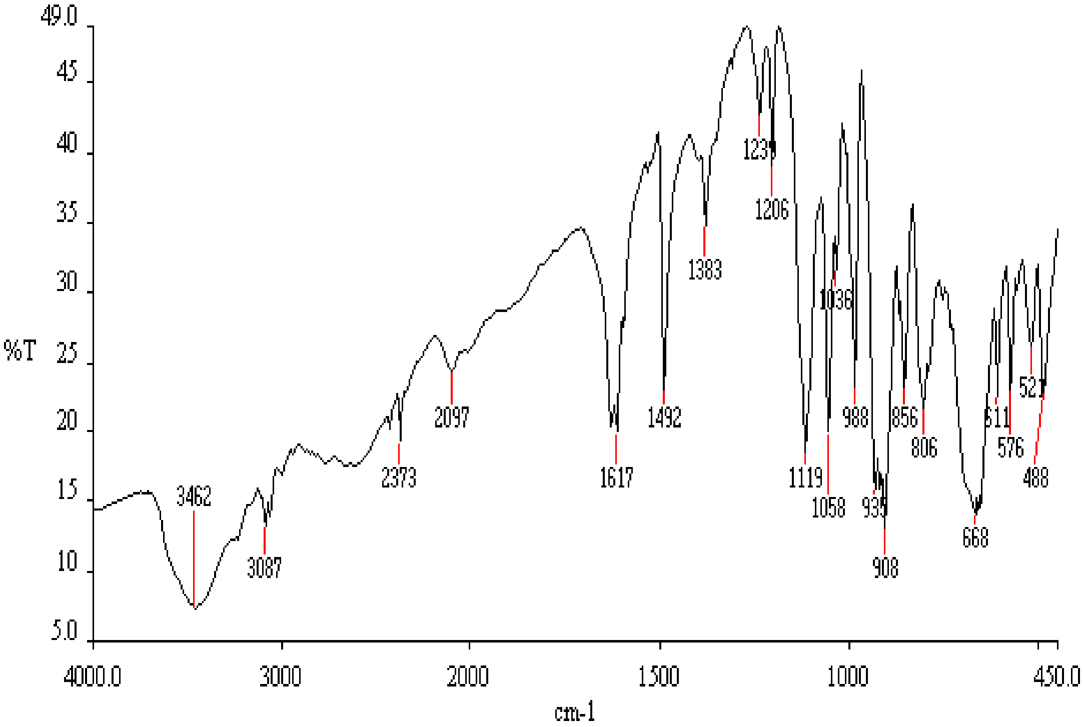

Figure 7.5: Infrared spectrum of compound (1) shows the characteristic bands for each group.

Figure 7.6 shows analysis of compound (1) (of 7.1449 mg) by TGA. A small mass loss (~1.14 %) occurred in the region of 140-260 °C, followed by a sharp decrement of mass in the region of 260-285 °C (~ 1.97 %). Both steps indicate the evaporation of one molecule of water from one molecule of compound (1) (calculated value ~ 1.48 %) and the beginning of the calcination process of the 4,4’-bipy molecules. The TG curve continues decreasing up to 500 °C where there is a big mass loss estimated to be ~ 13%. As can be depicted in the figure below, DTA analysis of compound (1) shows one very small exothermic peak at 280 °C and one very sharp exothermic peak at 430 °C, indicating the release of energy. These exothermic peaks might be attributed to the collapse of the framework and the formation of the inorganic residue.

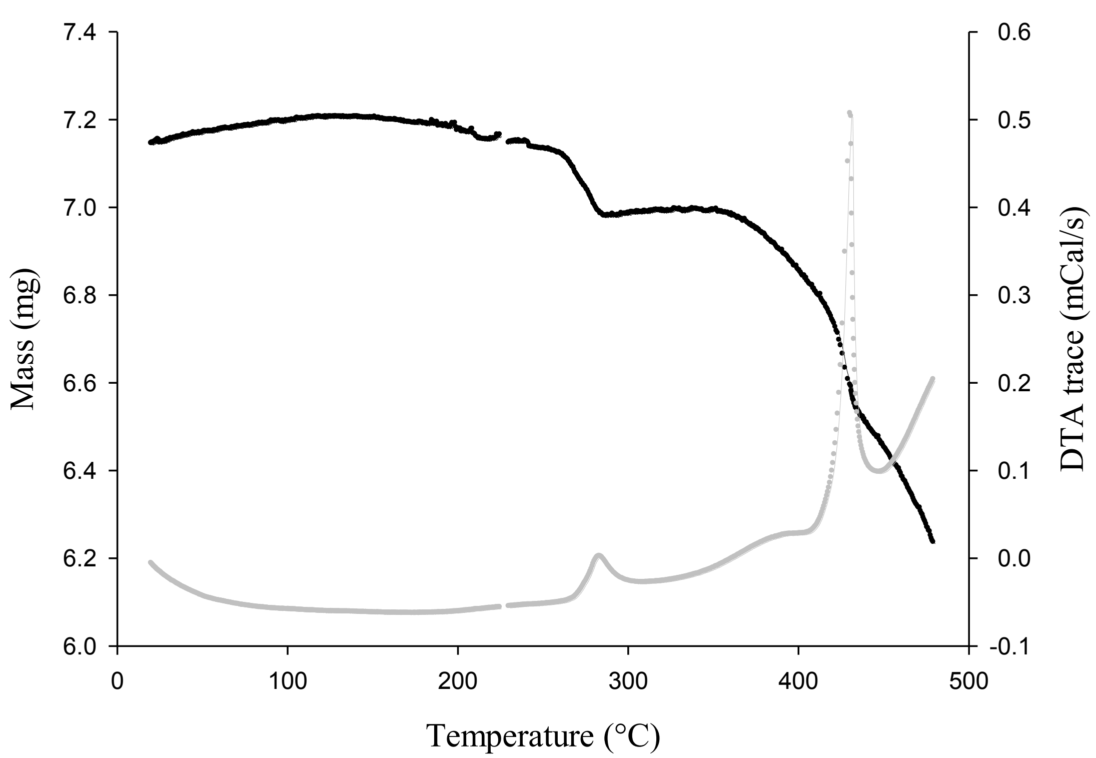

Figure 7.6: TGA pattern of compound (1). Mass loss was recorded as a function of temperature and is shown by the black line. DTA trace is the grey line.

7.3.3 Conclusions

Compound (1) has been prepared under mild hydrothermal routes and characterised by single crystal X-ray diffraction, IR spectroscopy and TGA analysis. The asymmetric unit of (1) consists of isolated $\{H_2Mo_5P_2O_{21}\}$ cluster polyanions, diprotonated 4,4'-bipyridine cations and water molecules. An extensive hydrogen bonding occurs between the N-H groups of the organic amine, water molecules and the framework oxygens, allowing further stabilization of the framework structure.

7.4 Overview

The three month placement in University of Kiel (Germany), working with Prof. Stock, offered the opportunity to investigate the molybdenum phosphonate system by applying high-throughput methods. Research included in this project has been mainly focused on forming molybdenum containing frameworks coordinated by the previously reported diphosphonate ligand $H_2O_3P\text{-}CH_2\text{-}NC_4H_8N\text{-}CH_2\text{-}PO_3H_2$ (H_4L).

At the initial stage, a discovery library was designed to gain a general exploration of the system in terms of investigating molybdenum starting material sources as well as compositional and process parameters. This library involved a series of hydrothermal reactions of different molybdenum sources with the diphosphonate ligand (H_4L) under acidic or basic conditions at various temperatures. From a general point of view, sodium molybdate source seemed to be the best starting material source, thus yielded a particular product phase (termed as Phase 'A') in only a very few cases. Investigations were then directed in forming bigger crystals of this phase so as to allow further analysis using single crystal X-ray diffraction. Four focused libraries were carried out which have mainly involved less concentrated reaction mixtures, much lower temperatures and slower cooling rates as well as mixed-solvent systems. However, the presence of Phase 'A', in the form of powder, within all samples hindered efforts to elucidate this further.

Besides the H_4L organophosphonic ligand, some reactions were carried out using the smallest phosphonate anion, H_3PO_3. The general procedure entailed mild hydrothermal treatment of sodium molybdate with phosphorous acid in presence of an organic templating agent. This approach led to the discovery of an amine templated molybdenophosphite polyanion obtained in presence of 4,4'-bipyridine acting as a templating agent.

7.5 References

[1] D. M. Poojary, B. L. Zhang and A. Clearfield, *Chemistry of Materials* 1999, *11*, 421-426.

[2] a) G. Alberti, U. Costantino, F. Marmottini, R. Vivani and P. Zappelli, *Angewandte Chemie-International Edition in English* 1993, *32*, 1357-1359; b) M. B. Dines, R. E. Cooksey, P. C. Griffith and R. H. Lane, *Inorganic Chemistry* 1983, *22*, 1003-1004.

[3] a) S. Drumel, P. Janvier, P. Barboux, M. Bujolidoeuff and B. Bujoli, *Inorganic Chemistry* 1995, *34*, 148-156; b) S. Drumel, P. Janvier, D. Deniaud and B. Bujoli, *Journal of the Chemical Society-Chemical Communications* 1995, 1051-1052; c) G. B. Hix, A. Turner, B. M. Kariuki, M. Tremayne and E. J. MacLean, *Journal of Materials Chemistry* 2002, *12*, 3220-3227.

[4] a) A. Distler and S. C. Sevov, *Chemical Communications* 1998, 959-960; b) M. Riou-Cavellec, M. Sanselme and G. Ferey, *Journal of Materials Chemistry* 2000, *10*, 745-748; c) M. Riou-Cavellec, M. Sanselme, M. Nogues, J. M. Greneche and G. Ferey, *Solid State Sciences* 2002, *4*, 619-625; d) A. Turner, P. A. Jaffres, E. J. MacLean, D. Villemin, V. McKee and G. B. Hix, *Dalton Transactions* 2003, 1314-1319.

[5] a) B. A. Adair, N. Guillou, M. Alvarez, G. Ferey and A. K. Cheetham, *Journal of Solid State Chemistry* 2001, *162*, 347-353; b) G. Bonavia, R. C. Haushalter, C. J. O'Connor, C. Sangregorio and J. Zubieta, *Chemical Communications* 1998, 2187-2188; c) D. M. Poojary, A. Cabeza, M. A. G. Aranda, S. Bruque and A. Clearfield, *Inorganic Chemistry* 1996, *35*, 1468-1473; d) D. M. Poojary, D. Grohol and A. Clearfield, *Angewandte Chemie-International Edition in English* 1995, *34*, 1508-1510.

[6] a) D. Riou and G. Ferey, *Journal of Materials Chemistry* 1998, *8*, 2733-2735; b) D. Riou, C. Serre, J. Provost and G. Ferey, *Journal of Solid State Chemistry* 2000, *155*, 238-242; c) V. Soghomonian, Q. Chen, R. C. Haushalter and J. Zubieta, *Angewandte Chemie-International Edition in English* 1995, *34*, 223-226.

[7] N. Choi, I. Khan, R. W. Matthews, M. McPartlin and B. P. Murphy, *Polyhedron* 1994, *13*, 847-850.

[8] C. Serre, J. A. Groves, P. Lightfoot, A. M. Z. Slawin, P. A. Wright, N. Stock, T. Bein, M. Haouas, F. Taulelle and G. Ferey, *Chemistry of Materials* 2006, *18*, 1451-1457.

[9] R. L. LaDuca, M. Desciak, M. Laskoski, R. S. Rarig and J. Zubieta, *Journal of the Chemical Society-Dalton Transactions* 2000, 2255-2257.

[10] V. Soghomonian, R. Diaz, R. C. Haushalter, C. J. Oconnor and J. Zubieta, *Inorganic Chemistry* 1995, *34*, 4460-4466.

[11] J. A. Groves, P. A. Wright and P. Lightfoot, *Dalton Transactions* 2005, 2007-2010.

[12] R. LaDuca, D. Rose, J. R. D. DeBord, R. C. Haushalter, C. J. Oconnor and J. Zubieta, *Journal of Solid State Chemistry* 1996, *123*, 408-412.

[13] P. Lightfoot, J. A. Groves, N. F. Stephens and P. A. Wright, *Solid State Sciences* 2006, *8*, 397-403.

[14] a) X. He, P. Zhang, T. Y. Song, Z. C. Mu, J. H. Yu, Y. Wang and J. N. Xu, *Polyhedron* 2004, *23*, 2153-2159; b) B. Hedman, *Acta Chemica Scandinavica* 1973, *27*, 3335-3354; c) R. Strandberg, *Acta Chemica Scandinavica* 1973, *27*, 1004-1018; d) Q. Sun, *Acta Crystallographica Section E* 2003, *E59*, 729-730.

[15] M. Tsuboi, *Contribution from the Randall Laboratory of Physics, University of Michigan* 1956.

[16] D.-H. Sun, J.-L. Zhang, H.-J. Ren, Z.-F. Cui and D.-X. Sun, *Acta Physico-Chimica Sinica* 2010, *26*, 1264-1270.

Chapter Eight

Conclusions

8.0 Conclusions

The research included in this thesis was mainly focused on the synthesis and characterisation of new molybdenum and vanadium framework structures with the aims of increasing structural diversity in open-framework materials and of producing new framework architectures that contain additional structural motifs beyond the tetrahedral co-ordination.

In the search for new open-framework materials the family of transition metal phosphates has attracted considerable attention because of the diverse range of porous architectures, the redox abilities and rich magnetic properties observed in these materials. The molybdenum and vanadium phosphates have been extensively studied for several years, with a diverse range of framework typologies being reported. The quest for structural diversity has led to the use of alternative primary building units, thus offering greater potential of different framework topologies from those found with the more conventional phosphate systems.

Hydrothermal syntheses were mainly employed for the production of molybdenum and vanadium containing frameworks, whereas high-temperature flux growth technique was rarely used in this project. A range of appropriate analytical techniques was used for the characterization of the inorganic materials prepared in this project. Single crystal X-ray diffraction was the main method of identification employed, allowing a methodical structural characterization to be performed.

Initially, interest was concentrated on developing new molybdenum phosphate compounds by introducing borate building blocks into the framework, with the aim of increasing structural diversity owing to the multi co-ordinate linking ability of boron. Though this approach proved unsuccessful, and the materials produced lack borate moieties, this allowed a variety of other molybdenum phosphate compounds with different bonding motifs to be identified. The novel ammonium templated material, $[NH_4]_{12}[(MoO_2)_2O(HPO_4)_2]_4[PO_4]X$, ($X$ = Cl, Br), constructed from molybdenophosphate layers of unique topology with embedded multiple anionic and cationic guests was discovered. Hydrothermal syntheses that involved organic amines instead, resulted in a series of molybdenophosphate polyanions. The bonding of these systems consisted of various types of Mo_n-membered rings built up from edge- or face- shared bioctahedral units that are capped by di-μ-(O)PO_4 phosphate bridges.

One other approach involved attempts to incorporate fluoride anions into the molybdenum phosphate frameworks, since halide containing compounds are currently poorly investigated. This study resulted in the production of the first oxyfluorinated molybdenum phosphate. The material exhibited very common structural pattern, consisted of alternating molybdenum octahedral and phosphate tetrahedral, however what distinguished the structure obtained was the participation of fluoride into the molybdenum sphere that allowed for terminator points to be occurred, leading in a decrease of the dimensionality.

A further development involved the use of organophosphonate anions to link molybdenum oxide units into extended framework structures. This investigation was part of a collaboration project during a three month placement in University of Kiel (Germany). High-throughput methods were employed, allowing a systematic study of compositional and process parameters. This approach resulted in the formation of a particular phase, however unsuccessful attempts to grow bigger crystals of this phase, so as to allow further analysis using single crystal X-ray diffraction, hindered efforts to elucidate this further.

Research within this project was then shifted towards the investigation of vanadium containing frameworks. Synthetic plans were concentrated on producing vanadium borophosphate compounds. A series of hydrothermal reactions involving different combinations of starting material sources were carried out. It appeared as the resulting products exhibited building units consisting of vanadium polyhedra and phosphate tetrahedra that incorporation of boron within these crystalline products was unsuccessful.

The project's aim involved increasing structural diversity, and this was achieved with incorporation of fluoride anions into vanadium framework structures. Experimental work followed two main synthetic routes. Some reactions were performed in typical HF fluoride media, and some were attempted to use VF_3, as an alternative fluoride ion source. Different organic amines were introduced into the synthesis in order to achieve an increase of the pH of the reaction mixture, while also to facilitate directional interactions between the amino groups of the organic amine and the framework F and O atoms as a result of strong hydrogen bonding. Four amine templated vanadium arsenate frameworks were produced. These exhibited similar but rather distinct framework topologies. It was observed as fluoride was mostly bound at bridging sites on vanadium polyhedral units, giving rise to the formation of F-F edge- and face-shared vanadium bioctrahedral units.

Reactions were also carried out using inorganic templates, and a number of new structure types were produced with ammonium, rubidium, barium and caesium. The series of materials included two-dimensional layer structures, and two main structural topologies were generally observed. Fluoride was found to adopt both bridging and terminal sites in vanadium octahedral units, offering topological versatility in the system. Participation of the terminal fluoride ligand into the metal coordination sphere, in some cases rendered the framework negative and thus allowed the insertion of cationic guests, or enhanced the hydrogen bonding, or offered new framework topologies. Alternatively, incorporation of bridging fluorides into common edges of vanadium bioctrahedral units favored effectively more ionic structures. Further common features of the materials produced are the presence of d^1 vanadium metal centres and the di-μ-(O)TO_4, di-μ-(O, O')TO_4 oxo bridges (where T = P, As), showing the possibility of such compounds to exhibit active pathways for magnetic exchange interactions.

Materials produced within this project are worthy of further investigation, since properties such as amine or metal templating and porous channel systems are potentially useful in many applications as ion exchangers as well as for their use in many adsorption and catalytic processes. It is hoped that research into the synthesis of these materials has constituted a vital step in gaining a fundamental understanding of the formation process behind complex inorganic frameworks, and has offered new synthetic approaches that can be used to prepare crystalline structures with special characteristics and useful properties.